

Springer Water

Shailesh Kumar Singh
C. T. Dhanya *Editors*

Hydrology in a Changing World

Challenges in Modeling

 Springer

Springer Water

The book series Springer Water comprises a broad portfolio of multi- and interdisciplinary scientific books, aiming at researchers, students, and everyone interested in water-related science. The series includes peer-reviewed monographs, edited volumes, textbooks, and conference proceedings. Its volumes combine all kinds of water-related research areas, such as: the movement, distribution and quality of freshwater; water resources; the quality and pollution of water and its influence on health; the water industry including drinking water, wastewater, and desalination services and technologies; water history; as well as water management and the governmental, political, developmental, and ethical aspects of water.

More information about this series at <http://www.springer.com/series/13419>

Shailesh Kumar Singh · C. T. Dhanya
Editors

Hydrology in a Changing World

Challenges in Modeling

 Springer

Editors

Shailesh Kumar Singh
Hydrological Processes
National Institute of Water
and Atmospheric Research
Christchurch, New Zealand

C. T. Dhanya
Department of Civil Engineering
Indian Institute of Technology (IIT) Delhi
New Delhi, India

ISSN 2364-6934

ISSN 2364-8198 (electronic)

Springer Water

ISBN 978-3-030-02196-2

ISBN 978-3-030-02197-9 (eBook)

<https://doi.org/10.1007/978-3-030-02197-9>

Library of Congress Control Number: 2018966838

© Springer Nature Switzerland AG 2019

This work is subject to copyright. All rights are reserved by the Publisher, whether the whole or part of the material is concerned, specifically the rights of translation, reprinting, reuse of illustrations, recitation, broadcasting, reproduction on microfilms or in any other physical way, and transmission or information storage and retrieval, electronic adaptation, computer software, or by similar or dissimilar methodology now known or hereafter developed.

The use of general descriptive names, registered names, trademarks, service marks, etc. in this publication does not imply, even in the absence of a specific statement, that such names are exempt from the relevant protective laws and regulations and therefore free for general use.

The publisher, the authors and the editors are safe to assume that the advice and information in this book are believed to be true and accurate at the date of publication. Neither the publisher nor the authors or the editors give a warranty, express or implied, with respect to the material contained herein or for any errors or omissions that may have been made. The publisher remains neutral with regard to jurisdictional claims in published maps and institutional affiliations.

This Springer imprint is published by the registered company Springer Nature Switzerland AG
The registered company address is: Gewerbestrasse 11, 6330 Cham, Switzerland

Contents

Integration of GRACE Data for Improvement of Hydrological Models	1
Chandan Banerjee and D. Nagesh Kumar	
An Analysis of Spatio-Temporal Changes in Drought Characteristics over India	23
Ganeshchandra Mallya, Shivam Tripathi and Rao S. Govindaraju	
Urban Hydrology in a Changing World	73
James A. Griffiths and Shailesh Kumar Singh	
Uncertainty in Calibration of Variable Infiltration Capacity Model	89
Ankita Pradhan and J. Indu	
Predictability of Hydrological Systems Using the Wavelet Transformation: Application to Drought Prediction	109
Rajib Maity and Mayank Suman	
Land–Atmosphere Interactions in Indian Monsoon at Sub-seasonal to Seasonal Scale	139
Amey Pathak and Subimal Ghosh	
Assessment of Climate Change Impacts on IDF Curves in Qatar Using Ensemble Climate Modeling Approach	153
Abdullah Al Mamoon, Ataur Rahman and Niels E. Joergensen	
River Water Temperature Modelling Under Climate Change Using Support Vector Regression	171
Shaik Rehana	
Assessing the Impact of Climate Change on Water Resources: The Challenge Posed by a Multitude of Options	185
Riddhi Singh and Basudev Biswal	

Streamflow Connectivity in a Large-Scale River Basin 205
Koren Fang, Bellie Sivakumar, Fitsum M. Woldemeskel
and Vinayakam Jothiprakash

**Climate Change Impacts on Four Agricultural, Headwater
Watersheds from Varying Climatic Regions of New Zealand**..... 225
M. S. Srinivasan, Shailesh Kumar Singh and R. J. Wilcock

Integration of GRACE Data for Improvement of Hydrological Models



Chandan Banerjee and D. Nagesh Kumar

1 Introduction

Observation is the first and most primary step in various disciplines of geosciences such as hydrology, meteorology, oceanography, geology, glaciology, and other planetary sciences. Hydrology or hydrological sciences which essentially deals with the question “What happens to the rain?” largely depends on gauge observations, which have been the longest running bastion furnishing long time series of datasets. Hydrological studies require datasets of both meteorological and hydrological variables such as temperature, humidity, precipitation, streamflow, etc. to monitor, understand, and model the complex physical processes which convert precipitation to surface water, soil moisture, groundwater, or streamflow. For a long time, hydrological studies were completely driven by datasets produced only by gauge measurements and to some extent field surveys. Although gauge measurements and field datasets are indispensable tools to understand the natural processes even today, they suffer from several limitations [6] such as

- (i) localized nature of the gauges provides information only for a particular location;
- (ii) gauges cannot provide data at locations inaccessible to humans;
- (iii) data procured by gauges are not easily available due to political control over data sharing policies; and
- (iv) management and maintenance of gauges are big challenges faced by concerned authorities.

Moreover, from hydrological modeling perspective, gauge datasets are quite limiting and do not help incorporate mathematical modeling of many physical processes. Consequently, development of a systematic framework that provides us with observational datasets of the Earth having the desired properties such as global coverage,

C. Banerjee · D. N. Kumar (✉)
Department of Civil Engineering, Indian Institute of Science, Bengaluru, India
e-mail: nagesh@iisc.ac.in

© Springer Nature Switzerland AG 2019
S. K. Singh and C. T. Dhanya (eds.), *Hydrology in a Changing World*, Springer Water,
https://doi.org/10.1007/978-3-030-02197-9_1

continuously available in time, and accessible across political boundaries, specifically of hydrological and meteorological variables, was necessary. As a result, Earth-observing satellite remote sensing has been developed to complement the gauge-based observations and enhance our knowledge and understanding of various physical processes [52, 55, 57]. This has not only enhanced our ability to model complex hydrological processes [36, 53, 86] to a large extent but also improved our capabilities to predict and forecast hydrological extremes which have now reached new levels.

The journey of remote sensing observations started in 1972 with Earth Resources Technology Satellite (ERTS) 1 [14] launched by National Aeronautics and Space Administration (NASA), USA, which later came to be known as Landsat 1. It carried a multispectral scanner (MSS) recording data in four spectral bands, viz., red, green, and two infrared bands. Since then the technology used for remote sensing has grown by leaps and bounds. Remote sensing satellites now record not only in the optical and near-infrared bands but also in thermal and microwave bands. The spatial, spectral, temporal as well as radiometric resolutions have improved with each new satellite. New data acquisition techniques are being developed such as the synthetic-aperture radar (SAR) used to procure terrain and land cover information [44], satellite altimeters used to measure depth of seabed, radiometers used to estimate surface soil moisture [63], and hyperspectral imagers having a very high spectral resolution are used for various applications in the fields of agriculture, mineralogy, and environmental sciences [46].

The Terrestrial Water Storage (TWS) estimate derived from the Gravity Recovery and Climate Experiment (GRACE) satellite data is a remarkable addition to the vast set of remote sensing observations [76, 83]. Compared to the previous satellites, GRACE uses a completely different technique of data acquisition. While most of the previous satellites can observe only surface features of the land, GRACE satellites are able to acquire information about water storages in any form at any depth. TWS refers to the total water storage in a column of land present in the form, be it snow, ice, surface water, soil moisture, and groundwater. Although the spatial and temporal resolution of the GRACE data is coarse as compared to many other satellites, the unique nature of the data makes it an invaluable tool to observe terrestrial hydrological processes [79, 93]. The water storage that is the most difficult to observe and monitor is groundwater and *in situ* well observations were the only way to monitor them until the advent of GRACE. Well observations suffer from the obvious limitations of consistency, unavailability of data for the required period, inadequate spatial distribution of observation wells, and above all, political control over data for transboundary aquifers. GRACE on the other hand provides a global observational dataset periodically for the past 15 years. Using GRACE-derived datasets, scientists have identified depleting groundwater levels in different parts of the world such as Sacramento and San Joaquin River basins, California's Central Valley, and High Plains aquifer in USA [12, 23, 64, 65], Bengal Basin of Bangladesh [68] and Ganga–Brahmaputra–Meghna River basin [34] in South Asia, transboundary river basins in the Middle East [32, 88], Northern China [31] and Southern Murray Darling River basin [15] in Australia.

GRACE data is being used to solve a host of scientific problems other than the numerous studies related to groundwater. GRACE-derived TWS, also known as TWS Anomaly (TWSA) and its derivative TWS Change (TWS C), are used to study the dynamics of the terrestrial part of the hydrologic cycle and unravel its complex nature [5, 27, 45, 80]. It is used to understand water budget at the spatial scale of large river basins or continents [38, 79]. Terrestrial water budget, atmospheric water budget, or a coupling of the two is used to estimate evapotranspiration or river discharge [60, 59, 70, 79, 78]. Evapotranspiration is an important part of the terrestrial hydrological cycle as it is the terrestrial feedback to the atmosphere and affects the climate. However, it is a complex hydrological variable which is difficult to estimate by the various energy balance and aerodynamic methods as they are highly data intensive. GRACE provides a rather simple method of its estimation. River discharge is an equally important parameter affecting the seas and oceans, determining the freshwater input to the system. Ocean salinity, sea surface temperature, and various other parameters are dependent on the amount of freshwater that comes into the oceans in the form of river discharge. The GRACE-based method of river discharge estimation is specifically helpful for large rivers which do not have a defined stream but forms a large delta system as it meets the ocean, as in case of the rivers Ganga–Brahmaputra, Indus, Irrawaddy, Mekong, and Yangtze. GRACE also finds application in drought-related studies [29, 84]. Precipitation is typically used for drought identification, monitoring, and management. Recently, a few studies have also used soil moisture to monitor droughts. However, TWS data which is the total of all the water storages helps improve the impact assessment of a drought by providing a holistic estimate of the total amount of water lost during a drought and the time taken to regain.

The area of application of GRACE data which would be of interest for the present discussion is its integration into hydrological models, which are sophisticated tools used for prediction of various hydrological parameters. Prediction of river discharge has been the sole objective of hydrologic models for a long time due to the limited number of hydrological variables observed (as discussed earlier). However, with the increasing number of observations, specifically satellite-based observations and huge improvement in the computational capabilities, the structure and functions of hydrological models have also evolved. They now represent more complex processes at finer spatial and temporal scales and predict various hydrological parameters along with streamflow [17]. Integration of GRACE data into a hydrological model should further improve the representation of the physical processes and prediction of complex parameters such as evapotranspiration, soil moisture, and snow accumulation. In this chapter, we discuss in detail the various ways of integrating GRACE data into a hydrological model. We elaborate on the physics behind acquisition of TWS data through GRACE satellites and the available data products. We also review various hydrological models used for GRACE-based studies discussing models which are more often chosen over the others.

2 GRACE Data and Gravity Recovery

Before divulging into the details of integrating GRACE data with hydrological models, it is important to understand the science of gravity recovery. The GRACE satellite mission is a joint venture by the US and German space agencies, NASA and DLR (Deutsches Zentrum für Luft- und Raumfahrt), respectively, under the NASA Earth System Science Pathfinder Program. The mission which was launched on March 17, 2002 consists of a pair of small and identical satellites (Fig. 1) orbiting at an altitude of 500 km from the Earth's surface with a separation between them of about 220 km along track. The satellites are connected by a highly accurate inter-satellite microwave K band ranging system constantly measuring the minute changes in the inter-satellite distance/range of the order of 10 μm . The distance between the two satellites changes due to the changes in earth surface features, which vary in density. Higher density relates to high mass, thus culminating into greater gravitational force and vice versa. If the Earth was homogenous in nature, the range between the two satellites would remain constant. However, the mass distribution is highly heterogeneous as well as constantly changing in time. The most dynamic constituent of the planet is water that circulates through the oceans, atmosphere, lithosphere, cryosphere, and biosphere. As a result, the time variable gravity signal acquired by the GRACE satellites through the measurement of the inter-satellite range rate mainly consists of the temporal variations of water as it moves from one storage compartment to another. After removing the fluctuations in the mass of the atmosphere and oceans, also known as Atmosphere and Ocean De-aliasing (AOD) from the total gravity signal, the seasonal and inter-annual fluctuations in TWS are obtained, expressed as centimeters of Equivalent Water Thickness (EWT) [73, 75, 76, 89].

The inter-satellite range rate, the primary variable observed by the GRACE satellites, must go through a long course of data processing to be converted to TWS. There are three primary centers constituting the Science Data System (SDS) which perform the processing of the Level 1 dataset to provide Level 2 and Level 3 datasets. These centers are the Center for Space Research (CSR) at the University of Texas at Austin, Jet Propulsion Laboratory (JPL), NASA and the German Research Center for Geosciences (GFZ) Helmholtz Center, Potsdam. The Level 1 data from GRACE consists of the inter-satellite range, range rate, range acceleration, and non-gravitational accelerations from each satellite. The Level 2 data product is the monthly gravity field estimates available in the form of spherical harmonic coefficients, whereas the Level 3 dataset is mass anomaly expressed in terms of EWT of TWS [39, 77]. The three data processing centers use different data processing techniques which include distinct static gravity models, different de-aliasing schemes and varied order and degree of the spherical harmonic coefficients to produce three separate datasets commonly known as CSR, JPL, and GFZ datasets. However, there are other research groups which also use other varieties of processing techniques to produce Level 2 and Level 3 data products such as the Delft Mass Transport (DMT) model of Delft University of Technology (TU Delft) [35, 43], ITG-Grace2010 of Bonn University, and a host of datasets produced by NASA's Goddard Space Flight Center (GSFC). JPL's TELLUS

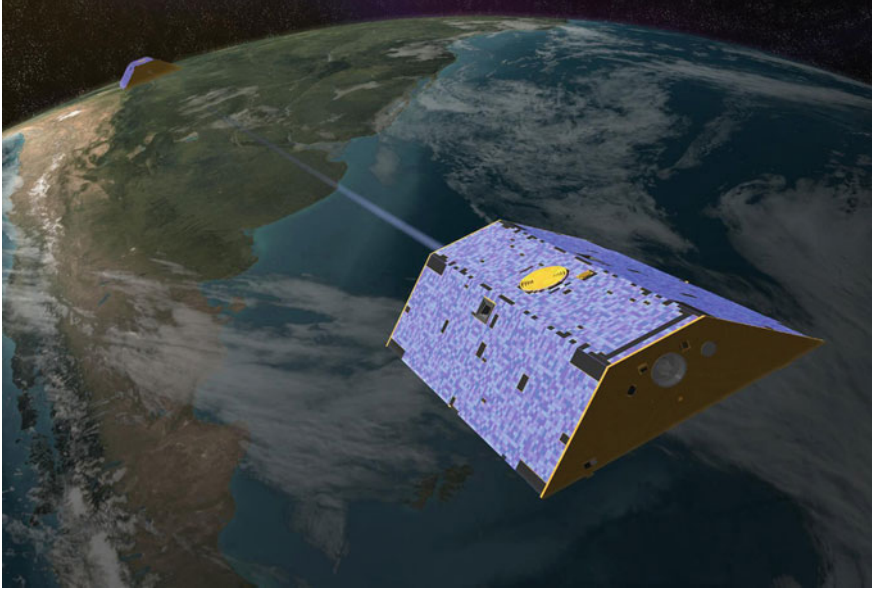


Fig. 1 Illustration of the twin satellites of the GRACE mission, connected by the along-track K-band microwave ranging system (Credits: NASA/JPL-Caltech)

website provides Level 3 monthly gridded as well as mascon products of GRACE TWS estimate derived from Level 2 dataset of the three primary data centers viz CSR, GFZ, and JPL. These products are easily accessible, available along with the error estimates and are ready to use for hydrologists [39].

3 Large-Scale Hydrological Models

Mathematical models of the hydrological processes, commonly known as hydrological models, have a long history as they evolved from simple lumped models with a single output to much more sophisticated stochastic distributed hydrological models which use several input variables and estimate wide range hydrologic responses [69]. Most of the primitive models are known as rainfall–runoff models which take rainfall and very primary land surface characteristics to estimate runoff. However, these models were an improvement over statistical models used for the prediction of runoff because the former contains representation of some physical processes and their usability in real time when forced with real-time precipitation [11]. With advancement in computational capabilities and proliferation of remotely sensed data, the hydrological models have hugely improved in terms of the simulation time steps, number of climatological forcings and land surface characteristics, spatial resolution, and number of output variables. These developments finally culminated to an

increased number of physical processes represented within the models as well as the accuracy with which they are represented. Thus, the hydrological models of the new generation are of great use for prediction of various hydrologic variables such as runoff, streamflow, evapotranspiration, etc. which help for water resources management [8, 42, 71]. Moreover, they also provide a robust framework to run numerical experiments to understand the effects of various natural and anthropogenic changes in the land surface properties and climate such as deforestation, urbanization, expansion of agricultural land, global warming, increasing extreme rainfall, etc. [7, 24].

Another aspect of hydrological models that has changed with improvement in various technologies as well as the urge to improve the accuracy in prediction of large-scale hydrological processes is the expanse of the land surface modeled within a single framework. Most hydrological models refer to catchment or river basin scale modeling where the primary output variable of interest is the streamflow at the mouth of the river basin. However, these models are calibrated for a single catchment such that the model parameters are tuned to represent hydrologic and climatic processes occurring only within that catchment. A new variety of models are the Land Surface Models (LSMs) which are included within the atmospheric General Circulation Models (GCMs) to represent the interaction of the atmosphere with the land surface in the form of mass and energy exchange [10, 21].

As discussed earlier, the river discharges from the land surface into the oceans alter several of its physical properties which in turn affect the climate. As a result, these LSMs are coupled with a River Routing Model (RRM) to convert the runoff produced by the LSM to streamflow and finally the river discharge into the oceans. LSMs have evolved greatly over the past few decades to accurately represent the partitioning of the incoming net radiative energy into latent and sensible heat fluxes and the partitioning of precipitation into runoff, evaporation, and water storage. One such LSM is the Community Land Model (CLM), part of the Community Earth System Model (CESM) of the National Center for Atmospheric Research (NCAR), USA [10]. The hydrologic processes represented in the model (shown in Fig. 2) include interception of precipitation by canopy, throughfall, transpiration, soil evaporation, canopy evaporation, infiltration, runoff, soil moisture, aquifer recharge, snow accumulation, melt, and sublimation. Other than the hydrologic cycle, the model includes other physical processes such as land biogeophysics, biogeochemistry, ecosystem dynamics, and anthropogenic interventions (Fig. 2). A similar framework is the Noah-Multi-parameterization Land Surface Model (Noah-MPLSM) which includes detailed vegetation dynamics including canopy shading and under-canopy snow dynamics along with the capability to differentiate between C3 and C4 pathways of photosynthesis [51, 92]. The Noah-MP LSM version 1.6 was implemented in Weather Research and Forecasting (WRF) Model version 3.6. WRF is a numerical weather prediction model developed mainly by NCAR and National Centers for Environmental Prediction (NCEP).

LSMs coupled within a GCM framework are not the only large-scale hydrological models simulating the water and energy cycles along with geochemical processes and vegetation dynamics. There are many large-scale uncoupled or stand-alone LSMs, sometimes also known as the Global Hydrological Models (GHMs) simulating phys-

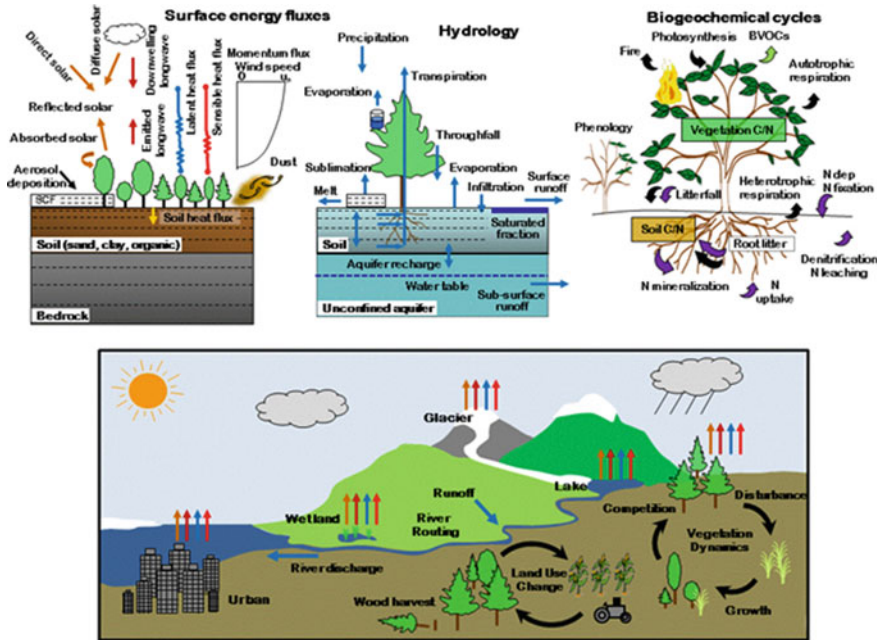


Fig. 2 A schematic diagram showing the energy cycle, hydrological cycle, biogeochemical, vegetation dynamics, and land use change represented within the Community Land Model (CLM) (Credits: <http://www.cesm.ucar.edu/models/clm/>)

ical processes at global scale such as the WaterGAP model (Water—Global Analysis and Prognosis model) [2], developed by University of Kassel and University of Frankfurt, Germany, PCR-GLOBWB (PCRaster GLOBAL Water Balance model) [96] conceived by Utrecht University, The Netherlands, ISBA-TRIP (Interactions between Soil, Biosphere, Atmosphere—Total Runoff Integrating Pathways) [3, 19] created by Centre National de Recherches Météorologiques, France and the Global Land Data Assimilation System (GLDAS) framework [61], developed by GSFC and NCEP. The WaterGAP model is designed for the assessment of macro-scale processes of the terrestrial hydrological cycle, taking into consideration anthropogenic component to simulate freshwater availability and irrigation water use. PCR-GLOBWB includes subgrid schemes for partitioning of rainfall into runoff, infiltration, interflow, groundwater recharge, and baseflow, as well as routing of the generated runoff. The model includes detailed anthropogenic effects to the extent that it includes more than 6000 manmade reservoirs. Thus, the human water use is completely integrated into the hydrological model at time step, calculating water demand, surface and groundwater abstraction, consumptive water use, and return flow. ISBA is a relatively simple LSM calculating variability in energy and water budgets with a saturation excess overland flow approach to simulate runoff based on TOPMODEL hydrological model [9]. This is coupled with TRIP, a simple RRM which converts runoff simulated by ISBA

into river discharge for a global river network. The GLDAS framework consists of four different LSMs, viz., Mosaic, CLM, Noah, and Variable Infiltration Capacity (VIC) models forced by a single forcing dataset. These four models differ mainly in the depth of soil considered for the simulation of soil water interaction and storage as well as the number of layers into which the total depth is divided. It should be noted that both the ISBA-TRIP model and the GLDAS set of models do not include any anthropogenic effects of water storage and water use. Although the LSMs are of great use, a major challenge lies in the calibration of these models which can only be carried out using vegetation indices or streamflow for large river basins by routing the simulated runoff. GRACE provides a very useful data first for the evaluation of such LSMs and eventually can be assimilated into the models for better estimation of various hydrologic variables. In the following sections, these two approaches of integration of GRACE data are discussed in detail.

4 Evaluation of Model Simulations Using GRACE Data

As discussed in the previous section, coupled and uncoupled LSMs try to simulate several hydrological variables by incorporating most complex of the physical processes, mimicking them to the maximum extent possible. Scientists are continuously trying to improve these models by better parameterization and adding more and more hydrological, geophysical, and biophysical processes into these models. A handy dataset for quick evaluation of the hydrological fields simulated by these models is the GRACE dataset. Due to its continuous global coverage, GRACE data could be used for evaluation of LSMs in cold regions affected by snow, arid, and semi-arid regions characterized by very low or no soil moisture conditions as well as areas characterized by a heavy to very heavy monsoonal rainfall. Table 1 provides a detailed chronological list of various studies carried out at global, continental, regional, and river basin scales to compare and evaluate various LSMs to estimate the accuracy with which it simulates various water storages and physical processes affecting them. Some studies tried to improve the estimation of certain variables by incorporating better and more detailed process representation and validated the improvements by comparison with GRACE data. The CLM LSM of NCAR is one such model which has seen continual efforts of betterment and corresponding evaluation using GRACE data. One of the limitations observed with CLM 2.0 was its representation of frozen soil which included completely frozen soil in areas with temperature below 0 °C, resulting in higher and earlier than expected runoff caused by spring season rainfall. The modifications suggested were allowance for the coexistence of ice and water in soil, the concept of a fractional permeable area, and considering both liquid water and ice together as soil moisture for calculating hydraulic conductivity. These modifications improved both the surface runoff and the soil water storage estimates of CLM when the simulations were evaluated for river basins in the cold regions, viz., Lena, Yenisei, Mackenzie, Ob, Churchill-Nelson, and Amur using both streamflow and GRACE data [48, 49]. Another deficiency of the CLM model was its inability

to model the groundwater dynamics as the column of soil considered extends only to 3.8 m below the surface. In another attempt to improve the CLM model, a Simple Groundwater Model (SIMGM) which represents an unconfined aquifer along with the recharge and discharge processes was included within the framework [50]. Although the modification worked out well for all the 12 river basins considered in the study, it is not expected to do well in cold regions where the water table is exposed to freezing conditions due to the obvious differences in the physical processes. In a more recent attempt to accurately represent groundwater dynamics within the CLM model version 4.5, it was found that addition of a no-flux boundary condition at the base of the soil layer improved the estimate. As a result, these simulations from the improved CLM models were found to agree well with GRACE-derived TWS observations [72].

A few studies also tried to improve the ISBA-TRIP hydrological model by comparing modified versions of the model with GRACE data. Initial comparisons of the model with GRACE data outlined some model deficiencies such as the high storage in the form of surface water within the river channel as a part of the routing scheme overestimated the maximum and underestimated the minimum TWS values mainly in the tropical region. Other deficiencies within the ISBA-TRIP model were the calculation of evaporation and snow accumulation. However, the major limitation was identified as the oversimplified routing model and the absence of anthropogenic effects within the model [3, 19, 54, 87]. Although human impact was not included in the modified version, improvements were suggested for TRIP—the routing model which included a simple groundwater reservoir and a variable streamflow velocity calculation. Several other LSMs were evaluated globally or regionally using GRACE data. Inclusion of a water exchange scheme between continents and oceans included in the Organising Carbon and Hydrology in Dynamic Ecosystems (ORCHIDEE) LSM resulted in better simulation of land water storage [Ngo-Duc et al., 2007]. GRACE data when compared to the Australian Water Resource Assessment (AWRA) model suggested a need for improvement in representations of diffuse groundwater discharge processes and interaction between surface and groundwater [van Dijk et al., 2011]. Doll et al. [2014] found that the WaterGAP model version 2.2 underestimates TWS as compared to GRACE with a phase lag of a month observed between the two. Evaluation of the GLDAS framework-versions 1 & 2 carried out for China by Wang et al. [2016] showed inconsistency in the rate of change of TWS. The four land surface models (Noah, SAC-Sacramento Soil Moisture Accounting Model, (VIC) Variable Infiltration Capacity Model, and Mosaic) applied in the newly implemented National Centers for Environmental Prediction (NCEP) operational and research versions of the North American Land Data Assimilation System version 2 (NLDAS-2) were also evaluated using GRACE data [Xia et al., 2016]. A common source of inconsistency observed between the GRACE observation and model simulation was attributed to the error and uncertainty present in the precipitation dataset which is a primary forcing for all hydrologic models.

Table 1 Comparative list of studies evaluating and comparing hydrological models with GRACE data

Authors (Year)	GRACE data	Model	Input data	Study region	Study period
Niu and Yang [49]	Chen et al. [16], Seo and Wilson [67]	CLM 2.0 with SIMTOP	GLDAS 1-degree 3-hourly data (2002–2004)	Lena, Yenisei, Mackenzie, Ob, Churchill-Nelson and Amur	August 2002–July 2004
Niu and Yang [48]	Chen et al. [16], Seo and Wilson [67]	CLM and Modified CLM	GLDAS 1-degree 3-hourly data (2002–2004)	Global and Ob, Yangtze, Amazon, Taz and Ural River Basin	August 2002–July 2004
Swenson and Wahr [74]	Swenson and Wahr [73]	Atmospheric and Terrestrial Water Balance model	GCM output and NCEP/DOE R-2 for atmospheric water balance and GLDAS/Noah LSM for terrestrial water budget	Mississippi and Ohio-Tennessee River basins	June 2002–April 2004
Ngo-Duc et al. [47]	Ramillien et al. [56]	ORCHIDEE modified to include a routing scheme	P: 6-hourly NCEP/NCAR constrained by monthly CMAP; Others: 6-hourly NCC (NCEP/NCAR) corrected by CRU atmospheric forcing	Global and Amazon, Congo, Niger, Mississippi, Yangtze, Ganges, Brahmaputra, Mekong	May 2002–December 2003
Niu et al. [50]	Chen et al. [16], Seo and Wilson [67]	Modified CLM with SIMTOP and SIMGM	1-degree 3-hourly GLDAS dataset (2002–2004)	12 Global river basins not affected by snow or ice	August 2002–December 2004
Alkama et al. [3]	CSR-RL04, JPL-RL 4.1, GFZ-RL04 estimates	ISBA-TRIP	3-hourly 1-degree Princeton University data	Global and 33 large river basins	Aug 2002–Dec 2006
Decharme et al. [19]	CSR-RL04, JPL-RL4.1, GFZ-RL04 estimates	TRIP with groundwater storage and variable flow velocity	Runoff simulated by ISBA of Alkama et al. [3]	Global and 12 large river basins	Aug 2002–Dec 2006
van Dijk et al. [97]	1-degree gridded TWS estimates from CSR	Australian Water Resource Assessment (AWRA)	0.05-degree gridded meteorological forcings obtained by interpolation of Station data	Continental Australia	January 2003–December 2010
Grippa et al. [27]	RL04 of CSR, JPL and GFZ, DEOSDMT, GRGS-EIGEN-GL04 and 10 day, 4° GSFC	HTESSEL, ORCHIDEE-CWRR, ISBA, JULES, SETHYS, NOAH, CLSM, SSiB, SWAP	Rainfall: TRMM 3B42, Atmospheric forcings: ECMWF short-term forecast data Downwell Radiative fluxes: mix of ECMWF and Land Surface Analysis Satellite Applications Facility	West Africa	Jan 2003–Dec 2007

(continued)

Table 1 (continued)

Authors (Year)	GRACE data	Model	Input data	Study region	Study period
Pedinotti et al. [54]	CSR-RL04, JPL-RL4.1, GFZ-RL04 estimates	ISBA-TRIP	TRMM-3B42 and RFE-Hybrid rainfall for ISBA-TRIP CHS, other atmospheric forcings from ECMWF	Niger River Basin	Jan 2003–Dec 2007
Vergnes and Decharme [87]	CSR-RL04, JPL-RL 4.1, GFZ-RL04 estimates	TRIP	Total runoff from ISBA simulation by Alkama et al. [4]	Global and 12 large river basins	August 2002–August 2008
Rosenberg et al. [62]	1-degree gridded CSR dataset	VIC modified to include SIMGM	1/8th-degree Gridded from precipitation and maximum/minimum temperature data from NOAA Cooperative Observer stations and wind data from NCEP-NCAR reanalysis	Colorado River Basin	2002–2010
Cai et al. [13]	1-degree gridded TWS estimates from CSR RL4.0	Noah-MP	NLDAS Phase 2 atmospheric forcing at 1/8° resolution	Mississippi River Basin	2003–2009
Doll et al. [20]	0.5-degree gridded GFZ-RL05, CSR-RL05 and ITG-Grace2010	WaterGAP 2.2	Daily climate dataset WFD (WATCH Forcing Data)/WFDEI (Watch Forcing Data ERA-Interim)	Global	2003–2009
Swenson and Lawrence [72]	CSR RL05	CLM version 4.5 with modification	1.25 longitude × 0.9 latitude ECMWF ERA-Interim Reanalysis data	Lower Colorado River basin, in the southwestern United States, and a region in northeastern Australia	2002–2014
Ahmed et al. [1]	1-degree gridded TWS estimates from CSR RL05	CLM4.5-SP and GLDAS-Noah	GLDAS: NOAA and CPC/CMAP and CLM: CRU/CRUNCEP	Continental Africa (Niger, Zambezi, Okavango, Limpopo)	2003–2010
Wang et al. [90]	GRACE Tellus RL05, CSR, JPL, GFZ	GLDAS1 (Noah, CLM, Mosaic, VIC) GLDAS2 (Noah 3.3)	ECMWF & NCEP–NCAR reanalyses data, NOAA/GDAS and Princeton University atmospheric fields, AGRMET radiation fields,	China	2002–2010

(continued)

Table 1 (continued)

Authors (Year)	GRACE data	Model	Input data	Study region	Study period
Xia et al. [91]	GRACE Tellus RL05 CSR, JPL, GFZ average	NLDAS-2 operation (Mosaic and Noah) and research (SAC-Clim and VIC4.0.5)	CPC, PRISM & NARR precipitation data and 2-m air temperature from NARR	USA	2003–2014
Zhang et al. [95]	GRACE RL05 Level-2 products from GFZ	LSDM, WGHM, JSBACH, MPI-HM	WFDEI dataset based on ERA-Interim reanalysis data	31 largest river basins	2003–2012

5 GRACE Data Assimilation

Data assimilation is a statistical technique of combining the simulations or forecasts from a prediction model with measurements from an observing system to produce improved estimates. Evaluation of LSMs has been one of the most explored techniques of utilizing GRACE data for the improvement of model physics and simulation accuracies. However, it is an indirect method where model deficiencies are figured out by comparing model outputs with GRACE observations followed by improving model physics solely based on our understanding of the intricate details of hydrological processes. This to some extent is limiting since the knowledge and understanding of the hydrological processes are itself limited and the large information hidden within the GRACE observations may be completely overlooked. As an alternate method of data integration, GRACE data assimilation techniques were explored where the observational dataset is directly utilized to improve the model simulation at each time step. Although it apparently does not improve model physics or our understanding of hydrological processes, GRACE data assimilation improves model simulations to a great extent, also facilitating spatial and temporal disaggregation of GRACE data as a byproduct. Table 2 gives a detailed chronological list of studies performed in this field of research.

The assimilation of GRACE data into LSMs has two major challenges. The typical temporal and spatial resolution of the GRACE observation is much coarse as compared to the LSMs. The GRACE data provided by NASA JPL's TELLUS website has a spatial resolution of ~ 100 km (1 degree) and a temporal resolution of a month. On the contrary, most LSMs are run at a daily or sub-daily scale, with the spatial resolution varying from 5 km (0.05°) to a maximum of 50 km (0.5°). Hence, the process of data assimilation invariably includes a spatial and temporal disaggregation technique. Consequently, a widely used and efficient data assimilation technique, known as the Ensemble Kalman Filter (EnKF) [22], is used in most of the previous literature (Table 2). The EnKF is a variant of a statistical technique known as the Kalman filter and is used for large problems. It has the inherent assumptions that the probability

Table 2 Comparative list of GRACE data assimilation studies

Authors (Year)	GRACE data	Model	Input data	Study region	Study period	Assimilation method
Zaitchik et al. [94]	CSR (RL01), GFZ (RL03), JPL (RL02)	CLSM	GLDAS forcing database	Mississippi (4 sub-catchments)	January 2003–May 2006	Ensemble Kalman Smoother
Houborg et al. [29]	CSR-RL04	CLSM	NLDAS-2 ad GLDAS data for study period model run and Princeton University data for long-term simulation	North America	August 2002–July 2009	Ensemble Kalman Smoother
Li et al. [41]	CSR-RL04	CLSM	GLDAS forcing database	Western and Central Europe	August 2002–July 2009	Ensemble Kalman Smoother
Huang et al. [30]	CSR-RL05	Noah-MP	0.1-degree, 3-hourly, near-surface meteorological dataset produced by the ITPCAS	Yangtze River basin	Jan 2003–Dec 2010	Proposed framework
Reager et al. [58]	CSR-RL05	CLSM	Same as Zaitchik et al. [94]	Mississippi river basin	April 2002–Dec 2014	Ensemble Kalman Smoother
Tangdamrongsub et al. [82]	CSR-RL05	OpenStreams wflow_hbv model (HBV-96)	European Climate Assessment & Dataset (ECA & D), ENSEMBLES project and Princeton University Dataset	Rhine river basin	Dec 2003–Oct 2007	Ensemble Kalman Filter
Giroto et al. [25]	Gridded CSR-RL05	CLSM	MERRA	USA	Jan 2003–Dec 2013	Sequential Kalman filtering technique

(continued)

Table 2 (continued)

Authors (Year)	GRACE data	Model	Input data	Study region	Study period	Assimilation method
Schumacher et al. [66]	TWS values using WGHM, ITG-GRACE2010 error covariance	WGHM	CRU TS 3.2, GPCC, WFDEI	Mississippi river basin	August 2003	EnKF, SQRA, SEIK
Giroto et al. [26]	Gridded CSR-RL05	CLSM	MERRA	India	Jan 2003–Aug 2015	3D Ensemble Kalman Filter
Khaki et al. [33]	ITSG-Grace2014	W3RA	Princeton University forcing dataset	Australia	Feb 2002–Dec 2012	(stochastic) EnKF, ETKF, SQRA, DEnKF, EnSRF, EnOI and PF with Multinomial (PFMR) and Systematic (PFMR) Resampling
Tangdamrongsub et al. [81]	CSR-RL05	PCR-GLOBWB	ECMWF Era-Interim, TRMM, CRU, Princeton and China Daily Ground Climate Dataset	Hexi corridor in Northern China	April 2002–Dec 2010	EnKF with and without errors
Tian et al. [85]	JPL-RL05 M, 3-degree mascon product	W3 Model	WFDEI forcing data, Global Tree cover fraction map and MODIS white-sky albedo	Australia	Jan 2010–Dec 2013	EnKF and EnKS

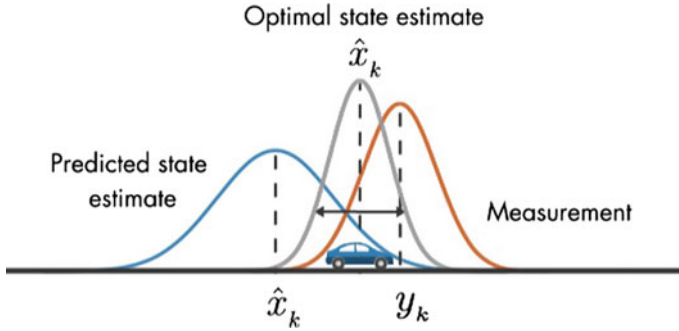


Fig. 3 A schematic diagram showing the concept of a typical Kalman Filter (Credit: Melda Ulusoy, MathWorks)

distributions are all Gaussian and the predictive model is linear. The Kalman filter (Fig. 3) is a recursive filtering mechanism which combines the simulation of a model and a noisy measurement, both of which are assumed to be Gaussian distributions to estimate the most likely state variables. The model estimate is generally less probable and contains more uncertainty than the measurement. However, the use of the EnKF provides an optimal estimate of the state variable which is much more probable and contains less uncertainty as compared to both the model prediction and the measurement, as shown in Fig. 3.

The second challenge is the hydrological variable of interest. GRACE observations result into TWS data which, as discussed earlier, is the aggregation of all the surface and subsurface water storages. To assimilate GRACE TWS data, there needs to be a hydrological variable within the model to which it can be mapped. The problem in this case is that all hydrological models have separate surface and subsurface storages modeled as different processes. Even if all the storages are added up to create a hydrological variable to be mapped against GRACE TWS data, it falls short due to the absence of groundwater storage. Most of the hydrological models incorporate groundwater dynamics as a boundary condition at the bottom of the soil column considered which is typically 2–4 m in depth from the ground surface. To resolve this issue, the catchment land surface model is the most preferred LSM used for assimilation as it contains an unconfined groundwater reservoir. Several studies have assimilated the GRACE TWS data with one of the primary objectives being improvement of groundwater estimation. Zaitchik et al. [2008] assimilated GRACE data into the CLSM using an ensemble Kalman smoother. Results indicated an improved correlation between observed ground-water and data assimilated simulated groundwater. In a similar effort, GRACE data was assimilated into the OpenStreams wflow_hbv model using an ensemble Kalman filter for the Rhine river basins. Results show increase in correlation between observed and simulated ground-water from 0.6 to 0.7 and 15% reduction in RMSE as a result of this data assimilation [Tangdamrongsub et al., 2015]. In both the cases, slight improvement in streamflow simulation was also observed. Tangdamrongsub et al. [2017] showed that assimi-

lation of GRACE data increased the accuracy of groundwater estimate, simulated for a semi-arid region in northern China by PCR-GLOBWB by 25%. GRACE data assimilation was also carried out with the objective of drought assessment because most frameworks lack information of groundwater and soil moisture of deeper layers. Houborg et al. [2012] and Li and Rodell [2015] assimilated GRACE data into CLSM model to derive drought indicators for North America and conterminous US respectively. A similar exercise was carried out for western and central Europe by Li et al. [2012]. These efforts disaggregated GRACE data in both spatial and temporal dimension. GRACE data assimilation was also carried out to estimate human induced changes in TWS and assess regional flood potential [Y Huang et al., 2015a; Reager et al., 2015]. Further studies concentrated on improving the data assimilation using better variants of the ensemble Kalman Filter and other hydrologic dataset such as the soil moisture from Soil Moisture and Ocean Salinity (SMOS) mission [Giroto et al., 2016; Giroto et al., 2017; Khaki et al., 2017; Schumacher et al., 2016; Tian et al., 2017].

6 Conclusions

The hydrological models altogether have improved from the simple lumped models and now include not only hydrological processes but all such physical, chemical, and biological processes that affect or is affected by water (a typical example of which is shown in Fig. 2). Integration of GRACE data into hydrological models has improved their model physics and prediction capabilities. Such models now represent better dynamics of frozen soil, dry soil in arid climate, groundwater, and vegetation. This also improved the estimation of various hydrological and vegetation parameters. Further improvements were achieved by GRACE data assimilation into hydrological models with the added advantage of disaggregation of GRACE TWS observations. Moreover, the GRACE data processing techniques have also improved with the most recent studies using Release 05 dataset which has a much higher accuracy as compared to the initial releases. The GRACE Follow-On (GRACE-FO) mission is scheduled to be launched in 2018 which is expected not only to continue the unique GRACE observations but also to have some improvements as compared to its forerunner [18]. Meanwhile, scientists are still working on the processing techniques of the GRACE data and the new Release 06 of the GRACE dataset having better accuracy is available for use [28]. Thus, there are numerous avenues in which further improvement is possible that will unravel new vistas of knowledge in future.

References

1. Ahmed M, Sultan M, Yan E, Wahr J (2016) Assessing and improving land surface model outputs over africa using GRACE, field, and remote sensing data. *Surv Geophys* 37(3):529–556. <https://>

- doi.org/10.1007/s10712-016-9360-8
2. Alcamo J, Doll P, Henrichs T, Kaspar F, Lehner B, Rosch T, Siebert S (2003), Development and testing of the WaterGAP 2 global model of water use and availability. *Hydrolog Sci J* 48(3):317–337. <https://doi.org/10.1623/hysj.48.3.317.45290>
 3. Alkama R, Decharme B, Douville H, Becker M, Cazenave A, Sheffield J, Voldoire A, Tyteca S, Le Moigne P (2010) Global evaluation of the ISBA-TRIP continental hydrological system. Part I: comparison to GRACE terrestrial water storage estimates and in situ river discharges. *J Hydrometeorol* 11(3):583–600. <https://doi.org/10.1175/2010JHM1211.1>
 4. Alkama R, Decharme B, Douville H, Ribes A (2011) Trends in global and basin-scale runoff over the late twentieth century: Methodological issues and sources of uncertainty. *J. Climate* 24, 3000–3014. <https://doi.org/10.1175/2010JCLI3921.1>
 5. Alsdorf D, Han SC, Bates P, Melack J (2010) Seasonal water storage on the Amazon floodplain measured from satellites. *Remote Sens Environ* 114(11):2448–2456. <https://doi.org/10.1016/j.rse.2010.05.020>
 6. Alsdorf DE, Lettenmaier DP (2003) Tracking fresh water from space. *Science* 301(5639):1491–1494. <https://doi.org/10.1126/science.1089802>
 7. Arnold JG, Fohrer N (2005) SWAT2000: current capabilities and research opportunities in applied watershed modelling. *Hydrol Process* 19(3):563–572. <https://doi.org/10.1002/hyp.5611>
 8. Arnold JG, Srinivasan R, Mutiah RS, Williams JR (1998) Large area hydrologic modeling and assessment-Part 1: model development. *J Am Water Resour Assoc* 34(1):73–89. <https://doi.org/10.1111/j.1752-1688.1998.tb05961.x>
 9. Beven KJ, Kirkby MJ, Schofield N, Tagg AF (1984) Testing a physically-based flood forecasting model (TOPMODEL) for three U.K. catchments. *J Hydrol* 69(1):119–143. [https://doi.org/10.1016/0022-1694\(84\)90159-8](https://doi.org/10.1016/0022-1694(84)90159-8)
 10. Bonan GB, Oleson KW, Verstenstein M, Levis S, Zeng XB, Dai YJ, Dickinson RE, Yang ZL (2002) The land surface climatology of the community land model coupled to the NCAR community climate model. *J Climate* 15(22):3123–3149. [https://doi.org/10.1175/1520-0442\(2002\)015%3c3123:tlscot%3e2.0.co;2](https://doi.org/10.1175/1520-0442(2002)015%3c3123:tlscot%3e2.0.co;2)
 11. Boughton WC (1989) A review of the Usda Scs curve number method. *Aust J Soil Res* 27(3):511–523. <https://doi.org/10.1071/sr9890511>
 12. Brena-Naranjo JA, Kendall AD, Hyndman DW (2014) Improved methods for satellite-based groundwater storage estimates: a decade of monitoring the high plains aquifer from space and ground observations. *Geophys Res Lett* 41(17):6167–6173. <https://doi.org/10.1002/2014GL061213>
 13. Cai XT, Yang ZL, David CH, Niu GY, Rodell M (2014) Hydrological evaluation of the Noah-MP land surface model for the Mississippi River Basin. *J Geophys Res Atmos* 119(1):23–38. <https://doi.org/10.1002/2013JD020792>
 14. Charnell RL, Maul GA (1973) Oceanic observation of New York bight by Ertz-1. *Nature* 242(5398):451–452. <https://doi.org/10.1038/242451a0>
 15. Chen JL, Wilson CR, Tapley BD, Scanlon B, Guntner A (2016) Long-term groundwater storage change in Victoria, Australia from satellite gravity and in situ observations. *Glob Planet Change* 139:56–65. <https://doi.org/10.1016/j.gloplacha.2016.01.002>
 16. Chen JL, Rodell M, Wilson CR, Famiglietti JS (2005) Low degree spherical harmonic influences on Gravity Recovery and Climate Experiment (GRACE) water storage estimates. *Geophys Res Lett* 32(14). <https://doi.org/10.1029/2005gl022964>
 17. Clark MP, Bierkens MFP, Samaniego L, Woods RA, Uijlenhoet R, Bennett KE, Pauwels VRN, Cai XT, Wood AW, Peters-Lidard CD (2017) The evolution of process-based hydrologic models: historical challenges and the collective quest for physical realism. *Hydrol Earth Syst Sci* 21(7):3427–3440. <https://doi.org/10.5194/hess-21-3427-2017>
 18. Darbeheshti N, Wegener H, Muller V, Naeimi M, Heinzl G, Hewitson M (2017) Instrument data simulations for GRACE Follow-on: observation and noise models. *Earth Syst Sci Data* 9(2):833–848. <https://doi.org/10.5194/essd-9-833-2017>

19. Decharme B, Alkama R, Douville H, Becker M, Cazenave A (2010) Global evaluation of the ISBA-TRIP continental hydrological system Part II: uncertainties in river routing simulation related to flow velocity and groundwater storage. *J Hydrometeorol* 11(3):601–617. <https://doi.org/10.1175/2010JHM1212.1>
20. Doll P, Fritsche M, Eicker A, Muller Schmied H (2014) Seasonal water storage variations as impacted by water abstractions: comparing the output of a global hydrological model with GRACE and GPS observations. *Surv Geophys* 35(6):1311–1331. <https://doi.org/10.1007/s10712-014-9282-2>
21. Ek MB, Mitchell KE, Lin Y, Rogers E, Grunmann P, Koren V, Gayno G, Tarpley JD (2003) Implementation of Noah land surface model advances in the national centers for environmental prediction operational mesoscale Eta model. *J Geophys Res-Atmos* 108(D22). <https://doi.org/10.1029/2002jd003296>
22. Evensen G (2003) The ensemble kalman filter: theoretical formulation and practical implementation. *Ocean Dyn* 53(4):343–367. <https://doi.org/10.1007/s10236-003-0036-9>
23. Famiglietti JS, Lo M, Ho SL, Bethune J, Anderson KJ, Syed TH, Swenson SC, de Linage CR, Rodell M (2011) Satellites measure recent rates of groundwater depletion in California's central valley. *Geophys Res Lett* 38. <https://doi.org/10.1029/2010gl046442>
24. Gassman PW, Reyes MR, Green CH, Arnold JG (2007) The soil and water assessment tool: historical development, applications, and future research directions. *Trans ASABE* 50(4):1211–1250
25. Giroto M, De Lannoy GJM, Reichle RH, Rodell M (2016) Assimilation of gridded terrestrial water storage observations from GRACE into a land surface model. *Water Resour Res* 52(5):4164–4183. <https://doi.org/10.1002/2015WR018417>
26. Giroto M, De Lannoy GJM, Reichle RH, Rodell M, Draper C, Bhanja SN, Mukherjee A (2017) Benefits and pitfalls of GRACE data assimilation: a case study of terrestrial water storage depletion in India. *Geophys Res Lett* 44(9):4107–4115. <https://doi.org/10.1002/2017GL072994>
27. Grippa M et al (2011) Land water storage variability over West Africa estimated by Gravity Recovery and Climate Experiment (GRACE) and land surface models. *Water Resour Res* 47. <https://doi.org/10.1029/2009wr008856>
28. Hardy RA, Nerem RS, Wiese DN (2017) The impact of atmospheric modeling errors on GRACE estimates of mass loss in Greenland and Antarctica. *J Geophys Res Solid Earth* 122(12):10440–10458. <https://doi.org/10.1002/2017JB014556>
29. Houborg R, Rodell M, Li BL, Reichle R, Zaitchik BF (2012) Drought indicators based on model-assimilated Gravity Recovery and Climate Experiment (GRACE) terrestrial water storage observations. *Water Resour Res* 48. <https://doi.org/10.1029/2011wr011291>
30. Huang Y, Salama MS, Krol MS, Su ZB, Hoekstra AY, Zeng YJ, Zhou YX (2015a) Estimation of human-induced changes in terrestrial water storage through integration of GRACE satellite detection and hydrological modeling: a case study of the Yangtze River basin. *Water Resour Res* 51(10):8494–8516. <https://doi.org/10.1002/2015wr016923>
31. Huang ZY, Pan Y, Gong HL, Yeh PJF, Li XJ, Zhou DM, Zhao WJ (2015b) Subregional-scale groundwater depletion detected by GRACE for both shallow and deep aquifers in North China Plain. *Geophys Res Lett* 42(6):1791–1799. <https://doi.org/10.1002/2014gl062498>
32. Joodaki G, Wahr J, Swenson S (2014) Estimating the human contribution to groundwater depletion in the Middle East, from GRACE data, land surface models, and well observations. *Water Resour Res* 50(3):2679–2692. <https://doi.org/10.1002/2013WR014633>
33. Khaki M, Hoteit I, Kuhn M, Awange J, Forootan E, van Dijk AIJM, Schumacher M, Pattiaratchi C (2017) Assessing sequential data assimilation techniques for integrating GRACE data into a hydrological model. *Adv Water Resour* 107:301–316. <https://doi.org/10.1016/j.advwatres.2017.07.001>
34. Khandu, Forootan E, Schumacher M, Awange JL, Muller Schmied H (2016) Exploring the influence of precipitation extremes and human water use on total water storage (TWS) changes in the Ganges-Brahmaputra-Meghna River Basin. *Water Resour Res* 52(3):2240–2258. <https://doi.org/10.1002/2015wr018113>

35. Klees R, Revtova EA, Gunter BC, Ditmar P, Oudman E, Winsemius HC, Savenije HHG (2008) The design of an optimal filter for monthly GRACE gravity models. *Geophys J Int* 175(2):417–432. <https://doi.org/10.1111/j.1365-246X.2008.03922.x>
36. Kouwen N, Soulis ED, Pietroniro A, Donald J, Harrington RA (1993) Grouped response units for distributed hydrologic modeling. *J Water Res Plan Manag* 119(3):289–305. [https://doi.org/10.1061/\(Asce\)0733-9496\(1993\)119:3\(289\)](https://doi.org/10.1061/(Asce)0733-9496(1993)119:3(289))
37. Kumar SV et al (2016) Assimilation of gridded GRACE terrestrial water storage estimates in the North American land data assimilation system. *J Hydrometeorol* 17(7):1951–1972. <https://doi.org/10.1175/Jhm-D-15-0157.1>
38. Landerer FW, Dickey JO, Guntner A (2010) Terrestrial water budget of the Eurasian pan-Arctic from GRACE satellite measurements during 2003–2009. *J Geophys Res Atmos* 115. <https://doi.org/10.1029/2010jd014584>
39. Landerer FW, Swenson SC (2012) Accuracy of scaled GRACE terrestrial water storage estimates. *Water Resour Res* 48. <https://doi.org/10.1029/2011wr011453>
40. Li B, Rodell M (2015) Evaluation of a model-based groundwater drought indicator in the conterminous U.S. *J Hydrol* 526:78–88. <https://doi.org/10.1016/j.jhydrol.2014.09.027>
41. Li BL, Rodell M, Zaitchik BF, Reichle RH, Koster RD, van Dam TM (2012) Assimilation of GRACE terrestrial water storage into a land surface model: evaluation and potential value for drought monitoring in western and central Europe. *J Hydrol* 446:103–115. <https://doi.org/10.1016/j.jhydrol.2012.04.035>
42. Liang X, Lettenmaier DP, Wood EF, Burges SJ (1994) A simple hydrologically based model of land-surface water and energy fluxes for general-circulation models. *J Geophys Res Atmos* 99(D7):14415–14428. <https://doi.org/10.1029/94jd00483>
43. Liu X, Ditmar P, Siemes C, Slobbe DC, Revtova E, Klees R, Riva R, Zhao Q (2010) DEOS Mass Transport model (DMT-1) based on GRACE satellite data: methodology and validation. *Geophys J Int* 181(2):769–788. <https://doi.org/10.1111/j.1365-246X.2010.04533.x>
44. Massonnet D, Feigl KL (1998) Radar interferometry and its application to changes in the earth's surface. *Rev Geophys* 36(4):441–500. <https://doi.org/10.1029/97rg03139>
45. Moiwo JP, Yang YH, Tao FL, Lu WX, Han SM (2011) Water storage change in the Himalayas from the Gravity Recovery and Climate Experiment (GRACE) and an empirical climate model. *Water Resour Res* 47. <https://doi.org/10.1029/2010wr010157>
46. Nemmour H, Chibani Y (2006) Multiple support vector machines for land cover change detection: an application for mapping urban extensions. *ISPRS J Photogramm Remote Sens* 61(2):125–133. <https://doi.org/10.1016/j.isprsjprs.2006.09.004>
47. Ngo-Duc, T, Laval K, Ramillien G, Polcher J, Cazenave A (2007) Validation of the land water storage simulated by Organising Carbon and Hydrology in Dynamic Ecosystems (ORCHIDEE) with Gravity Recovery and Climate Experiment (GRACE) data. *Water Resour Res* 43(4). <https://doi.org/10.1029/2006wr004941>
48. Niu GY, Yang ZL (2006a) Assessing a land surface model's improvements with GRACE estimates. *Geophys Res Lett* 33(7). <https://doi.org/10.1029/2005gl025555>
49. Niu GY, Yang ZL (2006b) Effects of frozen soil on snowmelt runoff and soil water storage at a continental scale. *J Hydrometeorol* 7(5):937–952. <https://doi.org/10.1175/jhm538.1>
50. Niu GY, Yang ZL, Dickinson RE, Gulden LE, Su H (2007) Development of a simple groundwater model for use in climate models and evaluation with gravity recovery and climate experiment data. *J Geophys Res Atmos* 112(D7). <https://doi.org/10.1029/2006jd007522>
51. Niu GY et al (2011) The community Noah land surface model with multiparameterization options (Noah-MP): 1. Model description and evaluation with local-scale measurements. *J Geophys Res Atmos* 116. <https://doi.org/10.1029/2010jd015139>
52. Njoku EG (1977) Theory for passive microwave remote-sensing of near-surface soil-moisture. *J Geophys Res* 82(20):3108–3118. <https://doi.org/10.1029/Jb082i020p03108>
53. Palaciosvelez OL, Cuevasrenaud B (1986) Automated river-course, ridge and basin delineation from digital elevation data. *J Hydrol* 86(3–4):299–314. [https://doi.org/10.1016/0022-1694\(86\)90169-1](https://doi.org/10.1016/0022-1694(86)90169-1)

54. Pedinotti V, Boone A, Decharme B, Cretaux JF, Mognard N, Panthou G, Papa F, Tanimoun BA (2012) Evaluation of the ISBA-TRIP continental hydrologic system over the Niger basin using in situ and satellite derived datasets. *Hydrol Earth Syst Sci* 16(6):1745–1773. <https://doi.org/10.5194/hess-16-1745-2012>
55. Price JC (1977) Thermal inertia mapping-new view of earth. *J Geophys Res* 82(18):2582–2590. <https://doi.org/10.1029/Jc082i018p02582> *Ocean Atmosphere*
56. Ramillien G, Frappart F, Cazenave A, Güntner A (2005) Time variations of the land water storage from an inversion of 2 years of GRACE geoids. *Earth Planet Sci. Lett* 235, 283–301.
57. Rango A, Salomonson VV (1974) regional flood mapping from space. *Water Resour Res* 10(3):473–484. <https://doi.org/10.1029/Wr010i003p00473>
58. Reager JT, Thomas AC, Sproles EA, Rodell M, Beaudoin HK, Li BL, Famiglietti JS (2015) Assimilation of GRACE terrestrial water storage observations into a land surface model for the assessment of regional flood potential. *Remote Sens* 7(11):14663–14679. <https://doi.org/10.3390/rs71114663> *Basel*
59. Rodell M, McWilliams EB, Famiglietti JS, Beaudoin HK, Nigro J (2011) Estimating evapotranspiration using an observation based terrestrial water budget. *Hydrol Process* 25(26):4082–4092. <https://doi.org/10.1002/hyp.8369>
60. Rodell M, Famiglietti JS, Chen J, Seneviratne SI, Viterbo P, Holl S, Wilson CR (2004a) Basin scale estimates of evapotranspiration using GRACE and other observations. *Geophys Res Lett* 31(20). <https://doi.org/10.1029/2004gl020873>
61. Rodell M et al (2004b) The global land data assimilation system. *B Am Meteorol Soc* 85(3):381–394. <https://doi.org/10.1175/bams-85-3-381>
62. Rosenberg EA, Clark EA, Steinemann AC, Lettenmaier DP (2013) On the contribution of groundwater storage to interannual streamflow anomalies in the Colorado River basin. *Hydrol Earth Syst Sci* 17(4):1475–1491. <https://doi.org/10.5194/hess-17-1475-2013>
63. Sandwell DT, Smith WHF (1997) Marine gravity anomaly from Geosat and ERS 1 satellite altimetry. *J Geophys Res Solid Earth* 102(B5):10039–10054. <https://doi.org/10.1029/96jb03223>
64. Scanlon BR, Faunt CC, Longuevergne L, Reedy RC, Alley WM, McGuire VL, McMahon PB (2012a) Groundwater depletion and sustainability of irrigation in the US high plains and central valley. *P Natl Acad Sci USA* 109(24):9320–9325. <https://doi.org/10.1073/pnas.1200311109>
65. Scanlon BR, Longuevergne L, Long D (2012b) Ground referencing GRACE satellite estimates of groundwater storage changes in the California Central Valley, USA. *Water Resour Res* 48. <https://doi.org/10.1029/2011wr011312>
66. Schumacher M, Kusche J, Doll P (2016) A systematic impact assessment of GRACE error correlation on data assimilation in hydrological models. *J Geodesy* 90(6):537–559. <https://doi.org/10.1007/s00190-016-0892-y>
67. Seo KW, Wilson CR (2005) Simulated estimation of hydrological loads from GRACE. *J Geodesy* 78(7–8):442–456. <https://doi.org/10.1007/s00190-004-0410-5>
68. Shamsudduha M, Taylor RG, Longuevergne L (2012) Monitoring groundwater storage changes in the highly seasonal humid tropics: validation of GRACE measurements in the Bengal basin. *Water Resour Res* 48. <https://doi.org/10.1029/2011wr010993>
69. Singh VP, Woolhiser DA (2002) Mathematical modeling of watershed hydrology. *J Hydrol Eng* 7(4):270–292. [https://doi.org/10.1061/\(Asce\)1084-0699\(2002\)7:4\(270\)](https://doi.org/10.1061/(Asce)1084-0699(2002)7:4(270))
70. Sneeuw N, Lorenz C, Devaraju B, Tourian MJ, Riegger J, Kunstmann H, Bardossy A (2014) Estimating runoff using hydro-geodetic approaches. *Surv Geophys* 35(6):1333–1359. <https://doi.org/10.1007/s10712-014-9300-4>
71. Srinivasan R, Ramanarayanan TS, Arnold JG, Bednarz ST (1998) Large area hydrologic modeling and assessment-Part II: model application. *J Am Water Resour Assoc* 34(1):91–101. <https://doi.org/10.1111/j.1752-1688.1998.tb05962.x>
72. Swenson SC, Lawrence DM (2015) A GRACE-based assessment of interannual groundwater dynamics in the community land model. *Water Resour Res* 51(11):8817–8833. <https://doi.org/10.1002/2015WR017582>

73. Swenson S, Wahr J (2002), Methods for inferring regional surface-mass anomalies from Gravity Recovery and Climate Experiment (GRACE) measurements of time-variable gravity. *J Geophys Res Solid Earth* 107(B9). <https://doi.org/10.1029/2001jb000576>
74. Swenson S, Wahr J (2006a) Estimating large-scale precipitation minus evapotranspiration from GRACE satellite gravity measurements. *J Hydrometeorol* 7(2):252–270. <https://doi.org/10.1175/jhm478.1>
75. Swenson S, Wahr J (2006b) Post-processing removal of correlated errors in GRACE data. *Geophys Res Lett* 33(8). <https://doi.org/10.1029/2005gl025285>
76. Swenson S, Wahr J, Milly PCD (2003) Estimated accuracies of regional water storage variations inferred from the Gravity Recovery and Climate Experiment (GRACE). *Water Resour Res* 39(8). <https://doi.org/10.1029/2002wr001808>
77. Swenson SC (2017) GRACE monthly land water mass grids NETCDF release 5.0| PO.DAAC
78. Syed TH, Webster PJ, Famiglietti JS (2014) Assessing variability of evapotranspiration over the Ganga river basin using water balance computations. *Water Resour Res* 50(3):2551–2565. <https://doi.org/10.1002/2013WR013518>
79. Syed TH, Famiglietti JS, Chen J, Rodell M, Seneviratne SI, Viterbo P, Wilson CR (2005) Total basin discharge for the Amazon and Mississippi River basins from GRACE and a land-atmosphere water balance. *Geophys Res Lett* 32(24). <https://doi.org/10.1029/2005gl024851>
80. Syed TH, Famiglietti JS, Rodell M, Chen J, Wilson CR (2008) Analysis of terrestrial water storage changes from GRACE and GLDAS. *Water Resour Res* 44(2). <https://doi.org/10.1029/2006wr005779>
81. Tangdamrongsub N, Steele-Dunne SC, Gunter BC, Ditmar PG, Sutanudjaja EH, Sun Y, Xia T, Wang ZJ (2017) Improving estimates of water resources in a semi-arid region by assimilating GRACE data into the PCR-GLOBWB hydrological model. *Hydrol Earth Syst Sci* 21(4):2053–2074. <https://doi.org/10.5194/hess-21-2053-2017>
82. Tangdamrongsub N, Steele-Dunne SC, Gunter BC, Ditmar PG, Weerts AH (2015) Data assimilation of GRACE terrestrial water storage estimates into a regional hydrological model of the Rhine River basin. *Hydrol Earth Syst Sci* 19(4):2079–2100. <https://doi.org/10.5194/hess-19-2079-2015>
83. Tapley BD, Bettadpur S, Watkins M, Reigber C (2004) The gravity recovery and climate experiment: mission overview and early results. *Geophys Res Lett* 31(9). <https://doi.org/10.1029/2004gl019920>
84. Thomas AC, Reager JT, Famiglietti JS, Rodell M (2014) A GRACE-based water storage deficit approach for hydrological drought characterization. *Geophys Res Lett* 41(5):1537–1545
85. Tian SY, Tregoning P, Renzullo LJ, van Dijk AIJM, Walker JP, Pauwels VRN, Allgeyer S (2017) Improved water balance component estimates through joint assimilation of GRACE water storage and SMOS soil moisture retrievals. *Water Resour Res* 53(3):1820–1840. <https://doi.org/10.1002/2016WR019641>
86. Vandegriend AA, Engman ET (1985) Partial area hydrology and remote-sensing. *J Hydrol* 81(3–4): 211–251. [https://doi.org/10.1016/0022-1694\(85\)90033-2](https://doi.org/10.1016/0022-1694(85)90033-2)
87. Vergnes JP, Decharme B (2012) A simple groundwater scheme in the TRIP river routing model: global off-line evaluation against GRACE terrestrial water storage estimates and observed river discharges. *Hydrol Earth Syst Sci* 16(10):3889–3908. <https://doi.org/10.5194/hess-16-3889-2012>
88. Voss KA, Famiglietti JS, Lo M, Linage C, Rodell M, Swenson SC (2013) Groundwater depletion in the middle east from GRACE with implications for transboundary water management in the Tigris-Euphrates-Western Iran region. *Water Resour Res* 49(2):904–914
89. Wahr J, Molenaar M, Bryan F (1998) Time variability of the Earth's gravity field: hydrological and oceanic effects and their possible detection using GRACE. *J Geophys Res Solid Earth* 103(B12):30205–30229
90. Wang W, Cui W, Wang XJ, Chen X (2016) Evaluation of GLDAS-1 and GLDAS-2 forcing data and noah model simulations over china at the monthly scale. *J Hydrometeorol* 17(11):2815–2833. <https://doi.org/10.1175/Jhm-D-15-0191.1>

91. Xia YL et al (2016) Basin-scale assessment of the land surface water budget in the national centers for environmental prediction operational and research NLDAS-2 systems. *J Geophys Res Atmos* 121(6):2750–2779. <https://doi.org/10.1002/2015JD023733>
92. Yang ZL et al (2011) The community Noah land surface model with multiparameterization options (Noah-MP): 2. Evaluation over global river basins *J Geophys Res Atmos* 116. <https://doi.org/10.1029/2010jd015140>
93. Yeh PJF, Swenson SC, Famiglietti JS, Rodell M (2006) Remote sensing of groundwater storage changes in illinois using the Gravity Recovery and Climate Experiment (GRACE). *Water Resour Res* 42(12). <https://doi.org/10.1029/2006wr005374>
94. Zaitchik BF, Rodell M, Reichle RH (2008) Assimilation of GRACE terrestrial water storage data into a land surface model: results for the Mississippi River basin. *J Hydrometeorol* 9(3):535–548. <https://doi.org/10.1175/2007JHM951.1>
95. Zhang LJ, Dobslaw H, Stacke T, Guntner A, Dill R, Thomas M (2017) Validation of terrestrial water storage variations as simulated by different global numerical models with GRACE satellite observations. *Hydrol Earth Syst Sci* 21(2):821–837. <https://doi.org/10.5194/hess-21-821-2017>
96. van Beek LPH, Wada Y, Bierkens MFP (2011) Global monthly water stress: 1. Water balance and water availability. *Water Resour Res* 47. <https://doi.org/10.1029/2010wr009791>
97. van Dijk AIJM, Renzullo LJ, Rodell M (2011) Use of gravity recovery and climate experiment terrestrial water storage retrievals to evaluate model estimates by the Australian water resources assessment system. *Water Resour Res* 47. <https://doi.org/10.1029/2011wr010714>

An Analysis of Spatio-Temporal Changes in Drought Characteristics over India



Ganeshchandra Mallya, Shivam Tripathi and Rao S. Govindaraju

1 Introduction

1.1 Introduction to Droughts

Droughts are among the world's costliest disasters with an annual cost estimated in the range of \$6–\$8 billion [20]. Unlike other natural disasters such as floods and earthquakes, droughts manifest slowly and are already a serious threat before they are detected. Droughts have major impacts on agriculture, natural habitats and ecosystems, and economies of affected regions. Modeled precipitation and temperature results from different climate change scenarios indicate that droughts are likely to intensify over many parts of the world in the next 20–50 years [13], suggesting the need to assess drought impacts more accurately and develop appropriate mitigation strategies.

When a drought event occurs, moisture deficits are identified from many hydrologic variables such as precipitation, streamflow, soil moisture, snowpack, groundwater levels, and reservoir storage [81]. Because drought impacts are experienced differently across the world, no universally accepted definition of drought exists. However, three types of droughts are commonly featured in the scientific literature [17]:

- a. Meteorological droughts result from deficits in precipitation amounts when compared to the long-term average for a region. This shortage in precipitation can develop quickly and also end abruptly.

G. Mallya · R. S. Govindaraju (✉)
Lyles School of Civil Engineering, Purdue University, West Lafayette, IN 47907, USA
e-mail: govind@purdue.edu

S. Tripathi
Department of Civil Engineering, Indian Institute of Technology, Kanpur,
UP 208016, India

- b. Agricultural drought conditions prevail when available soil moisture is insufficient to replace evapotranspiration losses in the root zone [83]. The timing of soil moisture deficit plays a critical role, because deficiencies during the growing season can adversely impact crop yields. During droughts, plants are under stress and cannot fight off pests. Fertilizers and pesticides are also not effective in the absence of moisture resulting in failure of crops. The onset of agricultural droughts depends on antecedent soil moisture conditions and usually lags meteorological droughts.
- c. Hydrologic droughts reflect shortages in water supply mainly in the form of reduced streamflows, reservoir and lake levels, and groundwater levels. Hydrologic droughts persist for longer durations when compared to meteorological and agricultural droughts because precipitation deficits translate to deficit in other hydrologic variables with significant time lags in some instances.

In this chapter, we focus on meteorological droughts. Precipitation deficits are not the only cause of droughts. Industrial and agricultural water demands have increased exponentially over the last few decades leading to water scarcity. With the increase in the emission of greenhouse gases, a steady rise in temperature has been observed over many parts of the globe. Increasing temperatures have affected the global hydrologic cycle leading to spatiotemporal variability of precipitation at different scales [54, 74], thereby affecting drought characteristics.

1.2 Drought Characterization and Monitoring

Drought indicators or indices are commonly used to characterize and monitor droughts and their impacts. Generally, all drought indicators use some measure of water deficit for analysis. Multiple hydrometeorological variables can also be used in a single drought indicator to capture the complex interactions that lead to droughts. Some of the desirable properties of a drought index are: (1) it should be sensitive to the timescale appropriate for the problem at hand; (2) the index should be able to capture the characteristics of both shorter and longer duration droughts; (3) it should be applicable to the problem being studied; (4) it should be possible to identify historical droughts; (5) the index should be capable of monitoring droughts on a near real-time basis [21, 32]; and (6) it should have drought forecasting capability.

Several studies provide comprehensive review of drought indices [32, 55]. *Palmer drought severity index* (PDSI; Palmer [61]) is a popular meteorological drought index that uses precipitation and temperature for estimating demand and supply of soil moisture within a two-layer water balance model. PDSI provides outlooks of moisture conditions that are comparable across regions and over different months. PDSI values typically vary from -4.0 to $+4.0$, negative values indicating drought conditions, while positive values indicate wet conditions. Another drought index that is popular because of its computational simplicity and forecasting ability at different time scales is the *standardized precipitation index* (SPI; McKee et al. [51]). The SPI

is recommended by the World Meteorological Organization as a standard meteorological drought-monitoring index [30]. The SPI first fits a probability distribution to historic precipitation time series data, and then normalizes the fitted distribution using the standard inverse Gaussian function to compute the drought index. SPI values are dimensionless with negative values indicating drought conditions, and the magnitudes of their departures from zero indicating the severity of the drought.

The *crop moisture index* (CMI; Palmer [60]) that monitors short-term moisture supply was developed to monitor agricultural droughts. With the improvements in satellite remote sensing, monitoring crop and vegetation health over large spatial extents have become routine. For example, *vegetation condition index* (VCI; Liu and Kogan [40]) uses the advanced very high-resolution radiometer radiance (AVHRR) data to study drought characteristics (early onset, intensity, frequency, and duration) and vegetation health. Along similar lines, the *normalized difference water index* (NDWI; Gao [23]) uses near-infrared (NIR) and short-wave infrared (SWIR) channels to study the variation of moisture content and spongy mesophyll in vegetation canopies.

Monthly non-exceedance probability computed by compiling weighted values of variables such as reservoir storage, stream flow, snowpack, and precipitation resulted in the development of a hydrologic drought index called the *surface water supply index* (SWSI; Shafer and Dezman [71]). Other popular hydrologic drought indices are standardized streamflow index (SSI) and standardized runoff index (SRI; Shukla and Wood [73]). The SRI is computed and interpreted along similar lines as SPI.

Drought indices have been used for identifying droughts and their triggers [76], assessing drought status [35], forecasting droughts [1], performing drought risk analysis [31], and studying relationship of droughts with local-scale regional hydrological variables such as water quality [75] and large-scale climate patterns like El Niño–Southern Oscillation [11, 41, 69]. Drought indices are also used for classifying droughts and quantifying their temporal trends. These two applications of drought indices are reviewed in the following paragraphs.

1.3 Drought Classification

Drought classification schemes typically classify droughts based on their severity or intensity, and are often based on drought indices that measure degree of departure of hydrometeorological variables, such as precipitation and streamflow, from their long-term averages. Water resource planners rely on drought classification to select drought mitigation strategies. Hence, weather agencies throughout the world routinely issue drought classification bulletins. For example, the US Drought Monitor releases a weekly update of drought status in USA by classifying droughts into five classes—D0 to D4 with the latter representing exceptional drought. Likewise, India Meteorological Department (IMD) issues drought bulletins classifying droughts into three categories, namely, mild, moderate, and severe.

Common quantitative drought classification schemes work in two steps—first, by defining a drought index using hydrometeorological observations of typically 30-year period to establish normal conditions [33] and next, by categorizing droughts based on predefined thresholds on the index value. Examples include IMD classification that uses departure of rainfall from its long-term average as a drought index, and US Drought Monitor classification that, along with other indices, uses standardized precipitation index (SPI) as a drought index. Among several drought classification schemes [13, 32, 55], the scheme based on standardized precipitation index (SPI; McKee et al. [51]) is very popular because of its computational simplicity and versatility in comparing different hydrometeorological variables at different time scales. In SPI, historical observations are used to compute the probability distribution of the monthly and seasonal (4, 6, and 12 months) precipitation totals. The fitted probability distributions are then normalized using the standard inverse Gaussian function to calculate SPI values. A negative value of SPI indicates precipitation less than the median rainfall, and the magnitude of departure from zero represents the severity of a drought.

Standard SPI-based drought classification, though popular, has many weaknesses [48]. It provides discrete classification and ignores uncertainties arising from data errors, model assumptions, and parameter estimates. Thus, users are not aware of inherent uncertainties in drought classification often required for making informed decisions. Further, in the context of SPI, there is an ongoing debate on the selection of the parametric distribution for fitting the data. McKee et al. [50] in their original paper on SPI recommend a gamma distribution. Lloyd-Huges and Saunders [42] found gamma distribution to be an appropriate model for Europe. Guttman [27] suggested Pearson-III distribution as the best universal model for SPI because it provides more flexibility than the gamma distribution. Rossi and Cancelliere [67] found normal, lognormal, and gamma distributions to be suitable for different datasets in their study. Loukas and Vasilades [43] investigated different theoretical distributions using Kolmogorov–Smirnov ($K-S$) test and chi-squared test and found extreme value-I distribution to be the most suitable for studying droughts over Thessaly, Greece. Mishra et al. [53] argue that different distributions may be appropriate for different drought durations (window size), and recommend the $K-S$ test for choosing an appropriate distribution. Bonaccorso et al. [7] used Lilliefors test to choose among normal, lognormal, and gamma distributions while Russo et al. [68] used three parameters generalized extreme value (GEV) distribution for SPI analysis. Thus, there is no consensus on the choice of distribution for SPI analysis.

Mallya et al. [48] used hidden Markov model (HMM) for drought classification by conceptualizing hidden states in the model to represent drought states. Their model avoided the need for specifying thresholds for drought classification and provided probabilistic drought classification by accounting for model uncertainties; however, the number of hidden states (drought classes) was prespecified. To facilitate comparison of HMM drought index (HMM-DI) classification with standard methods, they specified 11 hidden states. Since the number of states is imposed on the model, it is possible that for datasets with short record length the model suffers from an overspecification problem, i.e., the model structure is more complicated than sup-

ported by the dataset. Specifically, in the HMM context, overspecification would occur if the number of specified hidden states is more than that needed to model the data. Overspecification can result in parameter identification problems leading to unreliable results.

Mallya et al. [47] proposed a method that adapts SPI drought classification methodology by employing gamma mixture model (Gamma-MM) in a Bayesian framework. The method alleviates the problem of selecting suitable distribution for SPI analysis, quantifies modeling uncertainties, and propagates them for probabilistic drought classification. Further, it avoids overspecification using a Bayesian approach for optimally selecting the number of hidden states in the model.

1.4 Temporal Trends in Droughts

Temporal trends in droughts are identified by determining changes or sudden shifts in the distributional properties of the underlying hydrological variable. Classical drought indices such as SPI, or even probabilistic drought indices such as HMM-DI or probabilistic SPI, make several model assumptions about the hydrological variables used in their construct. Among them, the most important assumption is that the time series of hydrological variable is stationary, i.e., its distributional properties used to define droughts do not change over time. Thus, temporal trends in droughts cannot be estimated using classical drought indices. Nevertheless, hydrological time series may exhibit nonstationarity due to changes in climate and land use or due to natural cycles that operate over a period of several years to decades, and hence it is important to study temporal trends of droughts.

Several studies in the literature have proposed methods to perform drought analysis under nonstationary conditions. Mishra and Desai [52] used autoregressive integrated moving average (ARIMA) models and variants of artificial neural networks (ANNs), namely, recursive multistep neural network approach (RMSNN) and direct multistep neural network approach (DMSNN) for drought forecasting in presence of nonstationarity. Coulibaly and Baldwin [12] proposed the use of dynamic recurrent neural network (RNN) to model and forecast nonstationary hydrologic time series. Belayneh et al. [4] used wavelet analysis to first denoise the series, and then train ANNs or support vector regressors on the decomposed signals to perform drought forecasting in arid regions of Ethiopia. Türkeş and Tatlı [77] studied droughts in nonstationary precipitation series by modifying the classical SPI using the concepts of empirical mode decomposition. Unlike the classical SPI, the modified SPI accounts for local or higher order statistics in the precipitation time series. Han et al. [29] proposed the use of ARIMA models on potentially nonstationary remote sensing data to predict vegetation temperature condition index for drought forecasting. Verdon-Kidd and Kiem [80] emphasized the need to evaluate risk to water resources systems during drought under a nonstationary climate over Australia. Mitra and Srivastava [56] use

the modified Mann–Kendall test on SPI and SPEI series to study the spatiotemporal variability of meteorological droughts in southeast USA.

The literature review suggests that in the context of SPI, temporal changes in droughts are mostly studied using one of the following two approaches. The first approach divides the study period into smaller intervals or epochs (~30 years) where the underlying rainfall series is assumed to be stationary, and computes relative SPI for each epoch [18], and then compares drought characteristics between different epochs. The second approach allows the distribution of the hydrological variable to change with time, but the parameters of the distribution can follow only a prespecified temporal pattern. For example, the standardized nonstationary precipitation index (SnsPI) proposed by Russo et al. [68] assumes that the scale parameter of the Gamma distribution for rainfall varies linearly with time.

The main objectives of this chapter are as follows:

- (a) To investigate drought characteristics in India using a probabilistic drought classification approach that adapts SPI methodology by employing gamma mixture model (Gamma-MM) in a Bayesian framework [47], and to compare the results with classical SPI.
- (b) To use an alternate methodology for studying temporal changes in droughts [46] that does not require—(i) making stationarity assumption about the precipitation time series and (ii) prespecifying the nature of temporal trend in the precipitation series.
- (c) To study temporal changes in the droughts in India through this alternate methodology, and compare results with existing methods.

The remainder of the chapter is structured as follows. The next section describes the study area, India, and provides an account of its historical droughts. The precipitation datasets available for the study area are described in Sect. 2. Section 3 presents the mathematical formulation of the methods used for classifying droughts and quantifying temporal variation. These methods will be applied to precipitation data over India and the results will be presented and discussed in Sect. 4. The chapter ends with a set of concluding remarks.

2 Study Area and Dataset

The study area, India, receives 80% of its annual precipitation during 4-months long southwest summer monsoon [3, 62]. The monsoon precipitation makes landfall around the first week of June near Kerala, India, and moves northeast toward the Himalayas. By the first week of July, almost the entire country typically receives some precipitation that continues until the end of September [9]. From beginning of October to December, cool and dry winds from Central Asia cross India diagonally from northeast to southwest. These winds humidify the air as they blow over the Bay of Bengal, resulting in northeast monsoon precipitation predominantly over the state of Tamil Nadu, and partly over other states of Odisha, Andhra Pradesh, Karnataka,

and Kerala [36]. Though the Indian monsoon is believed to be one of the most stable monsoon systems [34, 49, 65], it has large inter- and intraseasonal variability that can sometimes result in weak monsoon or droughts over India [37, 59]. Since the country's gross domestic product (GDP), particularly food and power production, is closely linked to monsoon rains, various strategies have been developed over the years to mitigate the effects of droughts (e.g., drought-prone areas programme (DPAP), and desert development programme (DDP)). Implementing effective drought mitigation strategies requires real-time reliable classification of droughts.

2.1 Droughts over India and Their Consequences

Each type of drought has its own consequences, and the effects are felt by the general population. Since India is mainly an agricultural economy, droughts have historically had major impact on farmers. Agricultural droughts result in low crop yield and sometimes a complete failure of the crop. The agricultural fields can quickly turn into large dust bowls thereby leading to topsoil loss. This, in turn, causes stress in maintaining healthy livestock. Scarcity of water also leads to unhygienic conditions—leading to faster spread of diseases among the population. The economic consequences during/following a prolonged drought event can be detrimental to the poor farming community in India. Lack of crop insurance and inadequate financial support from government-backed banks often forces farmers to borrow money from private lenders. This leads to social disputes and mass migration from villages to cities in search of alternate employment opportunities [15, 64]. The non-farming community living in towns and cities face consequences of droughts in the form of shortage of water supply for household and industrial use. Droughts often lead to rise in commodity and fuel prices, thus causing economic stress for lower and middle-income families within the affected region.

In an effort to build a resilient society, the Central and State Governments in India have developed drought mitigation programs such as drought-prone areas programme (DPAP), desert development programme (DDP), and national watershed development programme in rainfed areas (NWDPRRA) that provide material, educational, and financial support for the following:

- i. Lake restoration and capacity building of existing reservoirs.
- ii. Rainwater harvesting, cloud seeding to trigger rains.
- iii. Large-scale desalination plants in major coastal cities to decrease reliance on groundwater and river water for domestic and industrial supply.
- iv. Low-interest agricultural loans to farmers, and guaranteed employment for at least 100 days in a year under National Rural Employment Guarantee scheme.

2.2 *Recent Drought Literature over India*

Niranjan Kumar et al. [58] used SPEI to study the variability of monsoon droughts over India, and found that El Nino/Southern Oscillation (ENSO) as the most influencing factor. They implicate the warming of the equatorial Indian Ocean to the increased droughts over India in the recent decades. Mahajan and Dodamani [44] performed trend analysis of drought events over Upper Krishna Basin in Maharashtra. Kumar et al. [39] used historical rainfall and sea surface temperature (SST) records to show that warmest SST anomalies in the central equatorial Pacific are better indicators of severe droughts over India. Varikoden et al. [78] showed that droughts associated with El Nino are very intense in most parts of the subcontinent, when compared to droughts during non-El Nino years. Mallya et al. [45] used SPI, SPEI, HMM-based drought index, and Gaussian mixture models and found that irrespective of the precipitation dataset or the choice of drought index, the drought severity and frequency over India increased significantly during recent decades. Their study also found that droughts are becoming more regional and are showing a general shift to the agriculturally important coastal South India, central Maharashtra, and Indo-Gangetic plains. Zhang et al. [86] found that the soil moisture and vegetation drought indices were best suited to study the impact on wheat production in India. Naresh Kumar et al. [57] studied the spatiotemporal patterns of droughts over India using SPI and found that area under moderate droughts have increased in recent decades.

2.3 *India Meteorological Department (IMD) Precipitation Dataset*

To analyze meteorological droughts over India, long-term precipitation data are required. Daily rainfall data at a spatial resolution of 1° for both latitude and longitude were obtained from India Meteorological Department (IMD) and are based on a total 1803 stations distributed over India that have at least 90% availability for the period 1901–2004 [63]. The gridded data, consisting of 357 grid points, have been obtained by interpolating rain gage data. The IMD datasets are standard datasets widely used in monsoon-related studies over India [25]. Figure 1 shows the study area along with the grid locations for which rainfall data were available as circular markers. The grids where results are discussed in subsequent sections are denoted as square red-colored markers. Because of its large geographical extent, the study area consists of several streams and rivers (some of which are perennial). Of these streams, some drain into the Arabian Sea or the Bay of Bengal, while few rivers cross international borders into neighboring countries. The main networks of some of the major rivers of India are shown in Fig. 1.

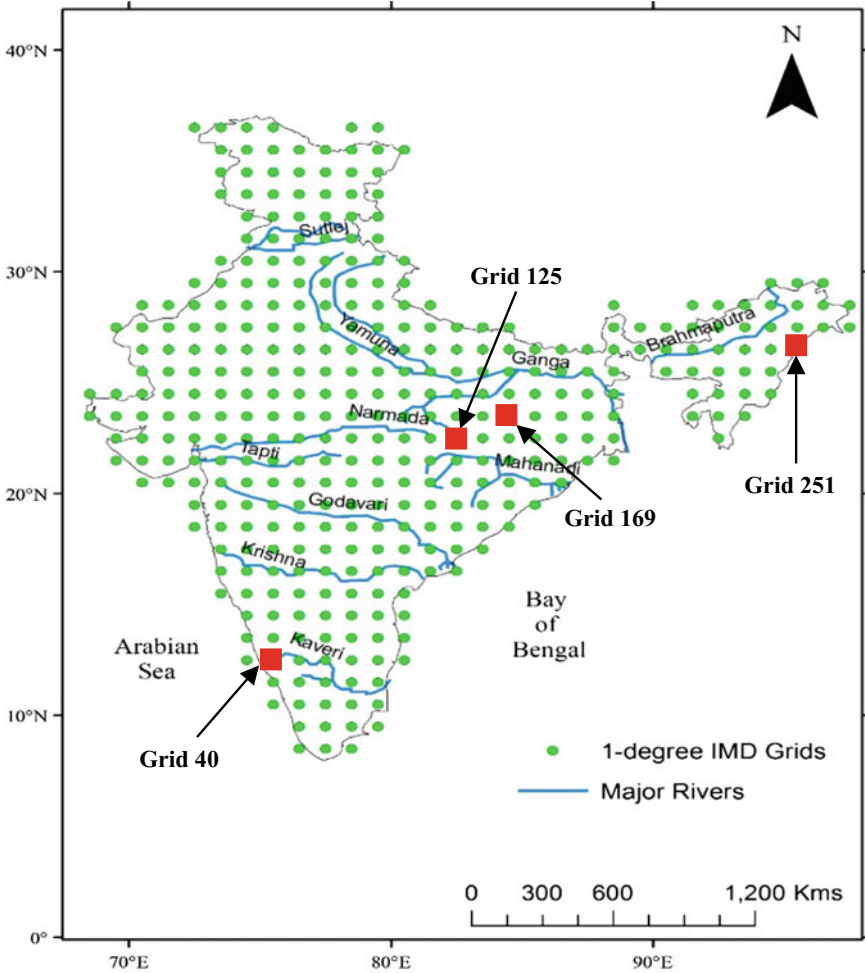


Fig. 1 Map showing the study area along with the location of $1^\circ \times 1^\circ$ grids of India Meteorological Department (IMD) precipitation dataset. Red square markers denote the stations where results are discussed in subsequent sections. The location of major rivers in India are also shown in the map

2.4 Homogenous Monsoon Regions

Based on rainfall characteristics, the Indian Institute of Tropical Meteorology has divided the study area into six homogenous monsoon regions. The geographical extent of each of these regions is shown in Fig. 2. Dividing the entire study area into smaller regions, instead of working with a single representative average precipitation time series for the entire country, is needed to account for large spatiotemporal variability of precipitation across the country. Of the six regions, the hilly region

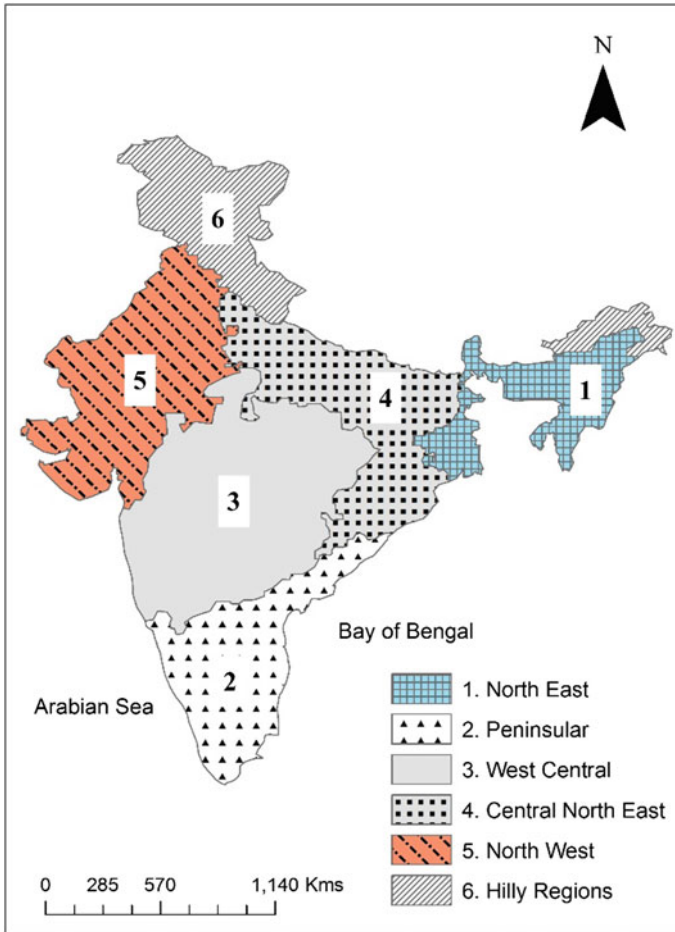


Fig. 2 Map showing homogenous monsoon regions of India Modified from Indian Institute of Tropical Meteorology

(labeled as region 6 in Fig. 2) consists of grids located at high altitudes and often has poor precipitation estimates. The grids belonging to this region are not included in this study, especially when computing or reporting regional or all-India metrics of precipitation or droughts.

The cumulative precipitation time series for different seasons and the water year (June to May of following year) were computed for each of the six regions using the average of precipitation time series recorded at all grids within a region. Figure 3 shows the histogram of water year precipitation series computed over each region. Each panel within Fig. 3 also contains the mean and standard deviation of the water year precipitation time series. The values of mean and standard deviation suggests that region 1 (Northeast monsoon region) is the wettest among the six (mean precipitation

of 208 cm with a standard deviation of 21 cm), while region 5 (Northwest monsoon region spanning over Gujarat and Rajasthan) is the driest (mean precipitation of 52 cm with a standard deviation of 13 cm).

An analysis of previous water year drought events based on SPI values (see Fig. 4) computed using an average representative cumulative precipitation time series over India (without considering grids located over hilly regions) suggested that the most severe conditions persisted during the periods early 1900s, 1918, 1951–52, 1965–68, 1972, late 1980s (Bengal drought), and early 2000s. The most recent drought conditions over India occurred in 2012–2013, with the West Central region—specifically the state of Maharashtra—being severely impacted by the drought.

Figure 5 shows time series of percentage area under drought computed using historical SPI values for water year beginning in June of each year over India. According to this figure, approximately 72% of the grids were under drought during 2002, followed by 69% of the grids in 1972, 68% in 1918, 62% in 1965, and 60% in 1960. Therefore, the combination of Figs. 4 and 5 suggests that 2002 drought was the most severe on record in terms of severity and extent. However, the actual damage caused due to droughts in recent years are much lower compared to some of the previous droughts due to improved drought mitigation programs [14]. The result of Mann–Kendall trend test on the time series of area under drought suggests that the trend is positive (Sen's slope = 0.01, shown as red-dashed line in Fig. 5), although not statistically significant (at $\alpha = 0.05$).

3 Methodology

The mathematical formulations of the two drought classification methods, namely, SPI and Gamma-MM, are presented in Sects. 3.1 and 3.2, respectively. Next, the methods used for studying temporal changes in droughts over India are described.

3.1 Standardized Precipitation Index (SPI)

The method involves the following steps:

1. Decide a drought duration (time window) and estimate cumulative precipitation during that period. For example, to estimate droughts during a summer monsoon season, estimate cumulative precipitation during 4 months of the summer monsoon season (JJAS) for each year. This will yield an annual time series of cumulative precipitation. Likewise, for analyzing water year droughts obtain an annual time series of cumulative precipitation for 12 months starting on June 1 and ending on May 31 of following year.
2. Fit a gamma distribution to the cumulative precipitation series. The cumulative distribution function (CDF) of the gamma distribution is standardized using the

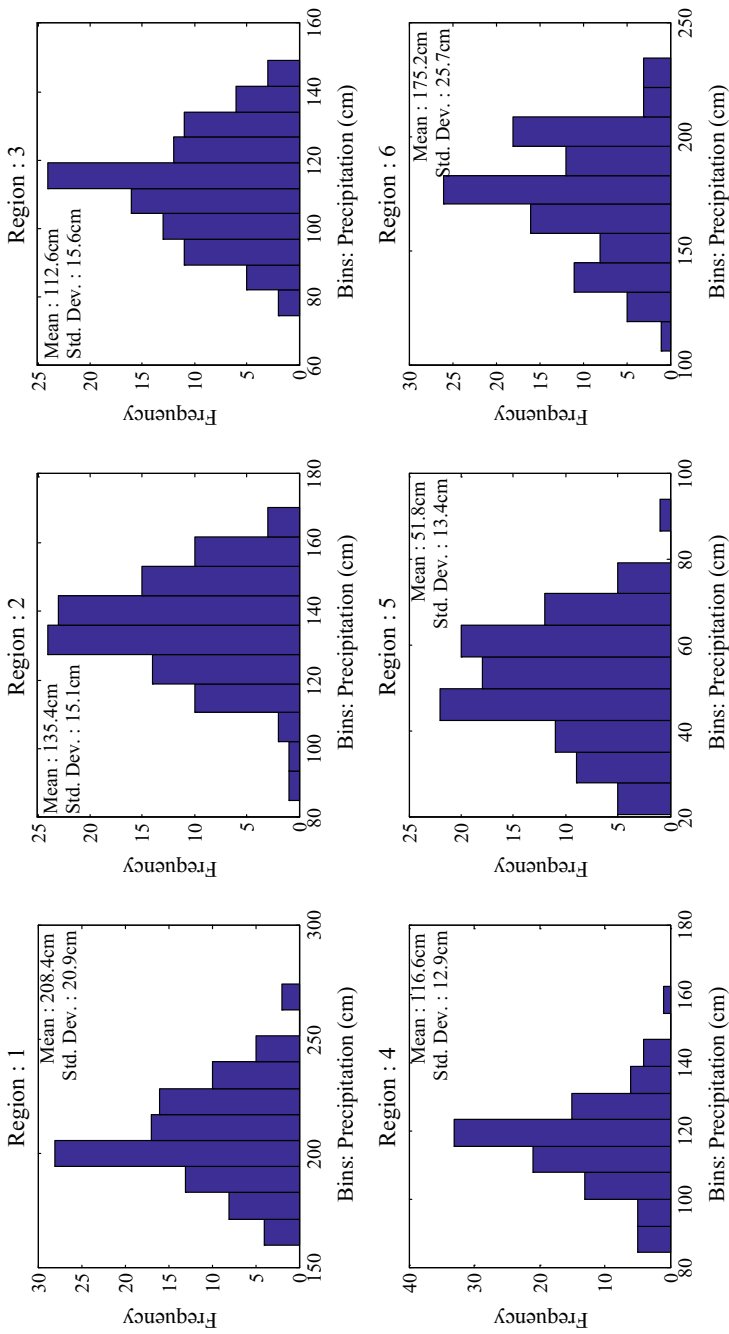


Fig. 3 Histogram of cumulative water year (June to May) precipitation at each homogenous monsoon region over India

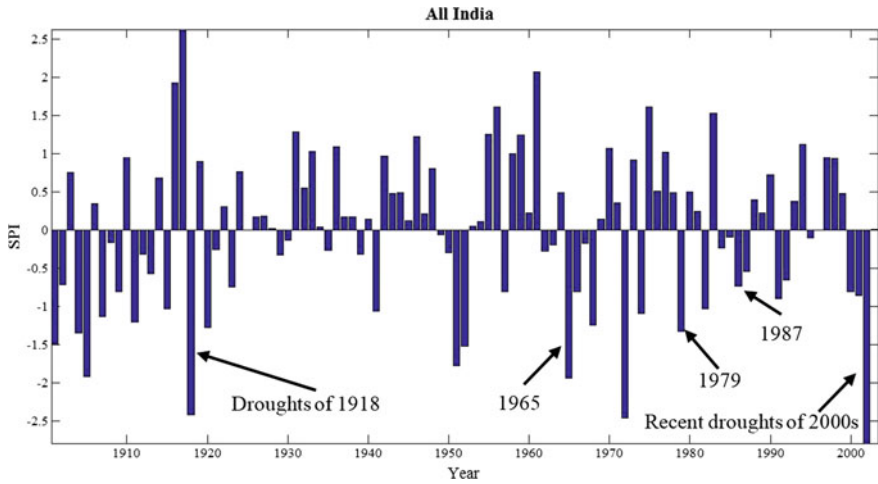


Fig. 4 SPI time series corresponding to water year (June to May) over the Indian monsoon region (IMR, excluding grids over hilly regions shown in Fig. 2)

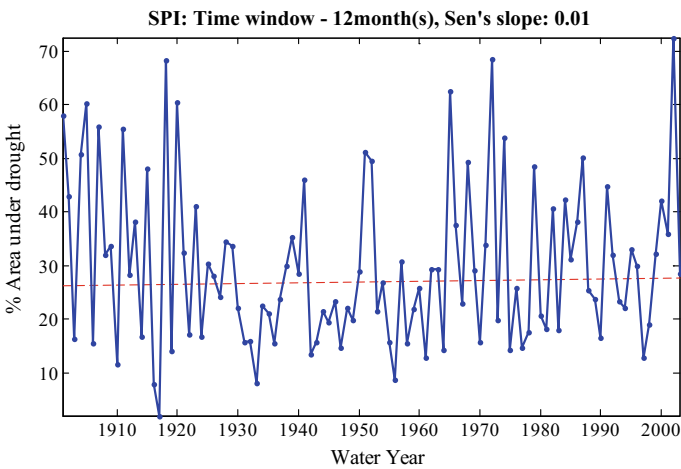


Fig. 5 Time series of percentage area under drought during the period 1901–2003 over India/IMR. The results correspond to water year droughts (12-month time window, June to May) computed using standard SPI. The red-dashed line indicates the Sen's slope

standard inverse Gaussian function to compute the SPI drought index. As stated earlier, a negative value of SPI indicates drought conditions and the magnitude of its departure from zero indicates the severity of a drought.

3. Decide a threshold on CDF to determine drought class. To draw parallels with the US Drought Monitor, we have used the same thresholds as used by them for SPI drought classification (Table 1).

3.2 Gamma Mixture Model (Gamma-MM)

As discussed in the Introduction section, there is an ongoing debate on the choice of a suitable distribution for fitting data in SPI analysis. Mallya et al. [47] addressed this problem using the gamma mixture model (Gamma-MM). Given sufficient number of components in the mixture, the Gamma-MM is proven to provide arbitrarily close approximation to any general continuous distribution in the range $(0, \infty)$ (see, DeVore and Lorentz [16]).

The use of Gamma-MM is not new in hydrology. To model data with multiple modes and different types of skewness, Evin et al. [19] proposed the use of Gamma-MM for strictly positive hydrological data. In the assessment of hydrological droughts for Yellow River in China, Shiau et al. [72] first fitted mixtures of exponential and gamma distributions to drought duration and drought severity, respectively, and then used the copula method to construct a bivariate drought distribution. While the mixtures help represent the subpopulations within an overall population, the copula method describes the dependence between variables of interest. In the following, we provide a brief description of the Gamma-MM. The readers are referred to Wiper et al. [82] and Richardson and Green [66] for details on mixture models. A summary of the mathematical details of the Gamma-MM as described in Mallya et al. [47] is presented below.

Table 1 US Drought Monitor classification scheme. SPI ranges are prescribed for the inverse of the normal distribution. Corresponding thresholds on CDF are given in the last column

Category	Description	SPI range	Threshold on CDF
D0	Abnormally dry	-0.5 to -0.8	0.212-0.309
D1	Moderate drought	-0.8 to -1.3	0.097-0.212
D2	Severe drought	-1.3 to -1.6	0.055-0.097
D3	Extreme drought	-1.6 to -1.9	0.023-0.055
D4	Exceptional drought	-2.0 or less	0.023 or less

Let the cumulative rainfall at time t be denoted by $x_t, t = 1, \dots, N \{x_t \in R \text{ and } X = [x_1, \dots, x_N]^T\}$. If the total number of components of Gamma-MM, M , is known a priori, then the weighted sum of M mixtures of gamma is given by the following equation:

$$P(x_t|\lambda) = \sum_{i=1}^M w_i G\left(x_t|v_i, \frac{v_i}{\mu_i}\right) \quad (1)$$

where w_i are the mixture weights or mixing ratios, and $G\left(x_t|v_i, \frac{v_i}{\mu_i}\right)$ are the components of gamma densities of the form,

$$G\left(x_t|v_i, \frac{v_i}{\mu_i}\right) = \frac{\left(\frac{v_i}{\mu_i}\right)^{v_i}}{\Gamma(v_i)} x_t^{(v_i-1)} \exp\left(-\frac{v_i}{\mu_i} x_t\right), \quad (2)$$

with mean μ_i and shape parameter v_i . Further, the mixture weights satisfy the constraint $\sum_{i=1}^M w_i = 1$. The parameter set is represented as $\lambda = \{\mathbf{w}, \boldsymbol{\mu}, \mathbf{v}\}$ where $\mathbf{w} = [w_1, w_2, \dots, w_M]^T$, $\boldsymbol{\mu} = [\mu_1, \mu_2, \dots, \mu_M]^T$ and $\mathbf{v} = [v_1, v_2, \dots, v_M]^T$.

In the Bayesian framework, the model parameters are obtained by specifying prior distributions to model parameters. Parameter estimation is accomplished by introducing a latent variable $Z = [z_1, \dots, z_N]^T$ for each time step. The variable z_t is an M -dimensional binary random variable, $z_t = [z_{t1}, \dots, z_{tM}]^T$, in which a particular element is equal to 1 and all other elements are zero, i.e., $\sum_{i=1}^M z_{ti} = 1$ and $z_{ti} \in \{0, 1\}$. The variable z_t denotes the component to which the data x_t belongs, and hence it is also called an *indicator variable*. The conditional distribution of x_t given z_t is

$$P(x_t|z_{ti} = 1) \sim G\left(x_t|v_i, \frac{v_i}{\mu_i}\right) \quad (3)$$

The posterior probability of the model parameters and latent variables is obtained by applying Bayes' rule as

$$P(\lambda|X) \propto P(X|\lambda)P(\lambda) \quad (4)$$

where the parameter set λ includes the latent variable as well. The *likelihood function* given the latent variable is

$$P(X|\lambda) = P(X|Z, \boldsymbol{\mu}, \mathbf{v}) = \prod_{t=1}^N \prod_{i=1}^M \left(G\left(x_t|v_i, \frac{v_i}{\mu_i}\right)\right)^{z_{ti}} \quad (5)$$

Following Wiper et al. [82] the *prior distribution* over the model parameter is given as $P(\lambda) = P(Z|\mathbf{w})P(\mathbf{w})P(\boldsymbol{\mu})P(\mathbf{v})$ with

$$P(\mathbf{Z}|\mathbf{w}) = \prod_{t=1}^N \prod_{i=1}^M w_i^{z_{ti}},$$

$$P(\mathbf{w}) = \text{Dir}(\mathbf{w}|\Phi) = C(\Phi) \prod_{i=1}^M w_i^{\phi_i - 1}, \quad \Phi = [\phi_1, \dots, \phi_M]^T,$$

$$P(\mathbf{v}) = \text{Exp}(\mathbf{v}|\theta) = \prod_{i=1}^M \frac{1}{\theta_i} \exp(-\theta_i v_i), \quad \theta = [\theta_1, \dots, \theta_M]^T, \text{ and}$$

$$P(\boldsymbol{\mu}) = \text{GI}(\boldsymbol{\mu}|\boldsymbol{\alpha}, \boldsymbol{\beta}) = \prod_{i=1}^M \frac{\beta_i^{\alpha_i}}{\Gamma(\alpha_i)} \mu_i^{-\alpha_i - 1} \exp\left(-\frac{\beta_i}{\mu_i}\right), \quad \boldsymbol{\alpha} = [\alpha_1, \dots, \alpha_M]^T \text{ and } \boldsymbol{\beta} = [\beta_1, \dots, \beta_M]^T$$

where Dir, Exp, and GI represent Dirichlet, Exponential, and Inverted gamma distributions, respectively, and $C(\Phi)$ is a normalizing constant. The prior distribution is made non-informative by assigning following values to the hyperparameters.

$$\phi_i = 1; \theta_i = 0.01; \alpha_i = \beta_i = 1 \text{ for } i = 1, \dots, M.$$

The posterior distribution $P(\lambda|\mathbf{X})$ does not have a closed form and has to be estimated by either deterministic approximation (variational Bayes' methods) or stochastic approximation (MCMC; Markov chain Monte Carlo methods). In this study, the posterior distribution is estimated using stochastic approximation by sampling the posterior distribution with Gibbs sampler, an MCMC algorithm [24].

The Gibbs sampling algorithm samples posterior distribution of the parameters by sequentially sampling from the conditional distribution of a parameter given all other parameters. The sampling starts with an initial value and proceeds as follows:

1. Set iteration number $j = 0$, and parameters to their initial value $\boldsymbol{\lambda}^{(0)} = [\mathbf{w}^{(0)}, \boldsymbol{\mu}^{(0)}, \mathbf{v}^{(0)}]$. The initial value is obtained by randomly sampling from the prior distribution of the parameters.
2. Sample from $P(\mathbf{z}_t^{(j+1)}|\mathbf{X}, \mathbf{w}^{(j)}, \boldsymbol{\mu}^{(j)}, \mathbf{v}^{(j)}) \sim \text{Multinomial}(\mathbf{z}_t|\mathbf{r}_t)$
 where $\mathbf{r}_t = [r_{t1}, \dots, r_{tM}]^T$, $r_{ti} = \frac{s_{ij}}{\sum_{i=1}^M s_{ii}}$ and $s_{ii} = w_i G\left(x_t|v_i, \frac{v_i}{\mu_i}\right)$ and Multinomial represents multinomial distribution.
3. Sample from $P(\mathbf{w}^{(j+1)}|\mathbf{X}, \mathbf{Z}^{(j+1)}, \boldsymbol{\mu}^{(j)}, \mathbf{v}^{(j)}) \sim \text{Dir}(\mathbf{w}|\hat{\Phi})$ where $\hat{\Phi} = [\phi_i + n_i, \dots, \phi_M + n_M]^T$ and $n_i = \sum_{t=1}^N z_{ti}$.
4. Sample from $P(\boldsymbol{\mu}^{(j+1)}|\mathbf{X}, \mathbf{Z}^{(j+1)}, \mathbf{w}^{(j+1)}, \mathbf{v}^{(j)}) \sim \text{GI}(\boldsymbol{\mu}|\hat{\boldsymbol{\alpha}}, \hat{\boldsymbol{\beta}})$
 where $\hat{\boldsymbol{\alpha}} = [\alpha_i + n_i v_i, \dots, \alpha_M + n_M v_M]^T$ and $\hat{\boldsymbol{\beta}} = \left[\beta_i + v_i \sum_{t=1}^M x_t z_{ti}, \dots, \beta_M + v_M \sum_{t=1}^M x_t z_{tM} \right]^T$.
5. Sample from $P(\mathbf{v}^{(j+1)}|\mathbf{X}, \mathbf{Z}^{(j+1)}, \mathbf{w}^{(j+1)}, \boldsymbol{\mu}^{(j+1)})$. This conditional distribution does not have a closed form. Hence, samples are generated using Metropolis–Hastings algorithm from a proposal distribution $P(\tilde{v}_i|v_i) \sim G(h, h|v_i)$ and are accepted with a probability

$$\min \left\{ 1, \frac{f(\tilde{v}_i)P(v_i|\tilde{v}_i)}{f(v_i)P(\tilde{v}_i|v_i)} \right\},$$

where $f(v_i) \propto \frac{v_i^{n_i v_i}}{\Gamma(v_i)^{n_i}} \exp\left(-v_i \left(\theta_i + \frac{\sum_t x_t z_{ti}}{\mu_i} + n_i \log \mu_i - \log\left(\prod_{t=1; z_{ti}=1}^N x_t\right)\right)\right)$.

If the new sample \tilde{v}_i is rejected, the current value of v_i is retained. The above procedure is repeated to sample v_i for all components $i = 1, \dots, M$. In this study, the parameter of the proposal distribution, h , is set to 2.

6. Set $j = j + 1$ and go to Step 2 until convergence. In this study, 15,000 samples were generated after ignoring initial 500 samples (*burn-in* period). Trace plots of the samples were monitored for convergence.

To keep the notations uncluttered, the iteration number is omitted from the parameters of the conditional distributions.

In the above formulation of Gamma-MM, we have assumed that the number of mixture components, M , is known. However, in a general context, M is not known and should be estimated from data. One approach for estimating M is to consider it as a model parameter, assign prior distribution to it and estimate posterior distribution by MCMC method. Since changing M will result in a different model structure, usual MCMC algorithms such as Gibbs sampler cannot be applied. Instead, reversible jump MCMC (RJCMCMC; Green [26] and Richardson and Green [66]) may be used. In this study, we implemented RJCMCMC for Gamma-MM as described by Richardson and Green [66] and Wiper et al. [82]. The results suggested that RJCMCMC algorithm requires significantly higher number of iterations for convergence compared to a model where M is specified. We found that if we start with a model having sufficiently large number of components, M , the Bayesian algorithm automatically prunes the components that are not relevant by making the mixing ratio (w) very small, thereby determining optimum number of components. We recommend the latter approach for hydrological applications where the number of components is usually limited to 2 or 3.

In the Bayesian framework, mixture models have the *identifiability* problem, i.e., a M component mixture model will have a total of $M!$ equivalent solutions. The problem can be avoided by introducing asymmetry in the likelihood function. For example, in the context of Gamma-MM, Wiper et al. [82] recommended the following restriction on the means of the mixture components, $\mu_1 < \mu_2 < \dots < \mu_M$. However, for finding a good density model, as required in the present application, the problem of identifiability is not relevant because any of the equivalent solutions is as good as another [6].

3.3 Temporal Trends in Droughts

Evaluation of temporal trends associated with retrospective drought events provides a basis to understand regional patterns of severity and duration of droughts. It also provides insight into the nature of possible future droughts and potential vulnerabilities over the study region. In this study, we first investigated trends in precipitation series at each IMD grid and also at each homogeneous monsoon region. A modified Mann–Kendall trend test that accounts for autocorrelation in time series [28, 38] was used to detect trends in summer monsoon and water year precipitation. The trends were tested at 5% significance level (α). The effect of spatial correlations in the data [8, 85] on the trend results was accounted using false discovery rate (FDR) [5, 79].

If the precipitation series exhibits a trend, drought classification methods such as SPI and Gamma-MM are not applicable for drought analysis because they assume the precipitation time series to be stationary. In this study, we apply an alternate method for drought analysis that overcomes this problem by explicitly removing trends from the precipitation series. The method is compared with relative SPI [18] and SnsPI [68] for performing drought analysis of a nonstationary precipitation series. The following paragraphs describe this alternate method and provide a summary of relative SPI and SnsPI methods.

3.3.1 An Alternate Method for Drought Analysis of a Nonstationary Precipitation Series

A precipitation series may exhibit nonstationarity because of any of several reasons [22]—(a) the mean is a function of time, (b) the variance or other higher order moments are functions of time, and (c) the stochastic mechanism generating time series is nonstationary. In this study, we consider nonstationarity arising from first kind. As proposed by Mallya et al. [46], we consider a *trend stationary process* in which the mean trend is deterministic. Once the trend is estimated and removed from the data, the residual series is a stationary stochastic process. A trend stationarity process, y_t , is expressed as

$$y_t = f(t) + z_t \quad (6)$$

where t represents time, z_t denotes a zero-mean stationary process, and $f(t)$ is a function of time representing trend of the process at time t . The trend can be determined either extrinsically by specifying a linear or nonlinear functional form for $f(t)$ [e.g., regression models] or intrinsically by using the data without prespecifying a functional form (e.g., empirical mode decomposition [84]).

Drought classification for nonstationary time series can be approached in one of the following two ways—(a) assuming that the “normal” conditions for a station are evolving, and hence the drought thresholds for different categories are changing with time (similar to SnsPI) and (b) assuming that the “normal” conditions for a station

are fixed (with respect to a reference period, and hence the thresholds for drought classification are fixed), but the frequency of droughts are changing with time (as in relative SPI). The proposed method classifies droughts for nonstationary time series using both the approaches. The steps of the proposed methods are as follows:

- (a) Identify trend in the time series, $f(t)$ using either an extrinsic approach (regression model) or an intrinsic approach (empirical mode decomposition).
- (b) Determine z_t by removing trend from the time series and fit a suitable distribution to obtain the cumulative distribution function $F_Z(z_t) = P(Z \leq z_t)$, where Z is a random variable belonging to a family of stationary stochastic process (for example—normal, lognormal, generalized extreme value, etc.).
- (c) Determine the CDF of the rainfall time series at time t as

$$F_{Y_t}(y_t) = P(Y_t \leq y_t) = P(Z \leq y_t - f(t)) = F_Z(y_t - f(t)). \tag{7}$$

Estimate drought thresholds at each time step using $F_{Y_t}(y_t)$ and the SPI drought definitions given in Table 1.

Select a reference year (t_0), and determine $F_{Y_{t_0}}$ and corresponding drought thresholds. Estimate drought class at time t based on these fixed thresholds for the reference year (t_0).

3.3.2 Standardized Nonstationary Precipitation Index (SnsPI)

The SnsPI method fits a nonstationary model to the precipitation data by linearly varying the scale parameter (s_t) of the gamma distribution with time. Following the notations used in Sect. 3.2, the gamma distribution is represented as $G(x_t|\nu, s_t)$ with scale parameter $s_t = \mu_t/\nu$ and $E(x_t) = \mu_t = b_1 + b_2t$, where b_1 and b_2 are constants. In this study, the parameters ν , b_1 , and b_2 are estimated by the maximum likelihood method.

3.3.3 Relative SPI

The relative SPI is defined with respect to a reference period in which precipitation time series is assumed to be stationary. For estimating relative SPI, the gamma distribution is first fitted to the reference period and to the period for which the temporal changes have to be analyzed. The two distributions are then compared to determine changes in the concerned period with respect to the reference period.

4 Results and Discussion

This section is divided into three subsections. Section 4.1 presents the results for drought classification using SPI and Gamma-MM drought indices. Section 4.2 describes the results for precipitation trend analysis. Section 4.3 presents the results of the proposed methodology for the drought classification of nonstationary precipitation series (detrended-SPI) and compares them with the results of classical SPI, relative SPI, and SnsPI for synthetic and real-world precipitation series.

4.1 Drought Classification

The drought indices described in Sect. 3 are applied to study seasonal (4-month time window) and water year (12-month time window) droughts in India. India has three seasons each spanning about 4 months: Winter (October to January), Summer (February to May), and Summer Monsoon (June to September). The water year in India extends from June to May of the following year. For example, *1999 water year* starts on June 1, 1999 and ends on May 31, 2000. First, an annual time series of cumulative precipitation during any chosen season or water year is computed. Next, droughts are classified using SPI and Gamma-MM methods. The latter method is also referred to as probabilistic SPI. Both the methods assume that the cumulative precipitation time series is stationary, and consists of independent and identically distributed samples. In the following paragraphs, summer monsoon and water year droughts from the two methods are presented for a selected IMD grid over India.

4.1.1 Summer Monsoon Droughts

The results are presented for IMD grid 251 located in northeast India and are among the highest rainfall receiving regions of the world. Figure 6 shows the empirical cumulative distribution function (CDF) obtained using Weibull plotting position formula [10] along with CDFs of fitted gamma distribution (fitted using maximum likelihood approach) and gamma mixture model (Gamma-MM) for summer monsoon precipitation (June–September). The CDF of Gamma-MM is closer to empirical CDF than the CDF of gamma distribution, particularly, for the smaller rainfall values [$F(X) < 0.25$], which are critical for drought classification. The Gamma-MM owes its better fit to the large number of tuning parameters ($3_M - 1$, where M is number of components in Gamma-MM) compared to two-parameter gamma distributions.

Increasing the number of mixture components (M) in Gamma-MM method ensures that the model provides a better fit to the data. However, it may also result in overfitting. The Gamma-MM model addresses this problem using a Bayesian framework that avoids overfitting by marginalizing over the model parameters instead of making point estimates. Figure 7 shows the mixing ratio of a five-component Gamma-

Fig. 6 Empirical CDF along with CDFs obtained by fitting gamma distribution (Gamma CDF) and gamma mixture model (Gamma-MM CDF) to the 4-month cumulative precipitation during summer monsoon (June to September) at IMD grid 251. The gray band shows 5 and 95 percentile of the Gamma-MM CDF and the green-dotted line shows width of its credible interval

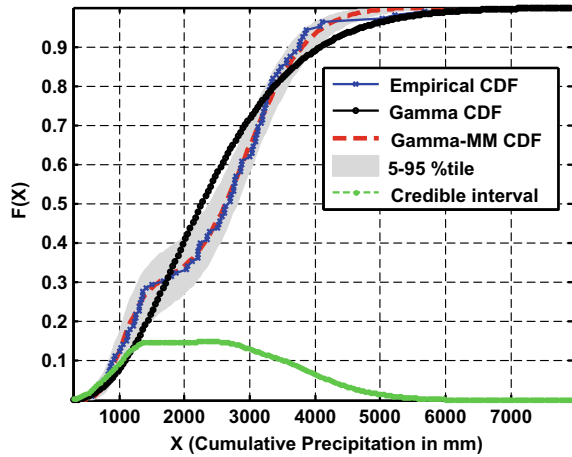
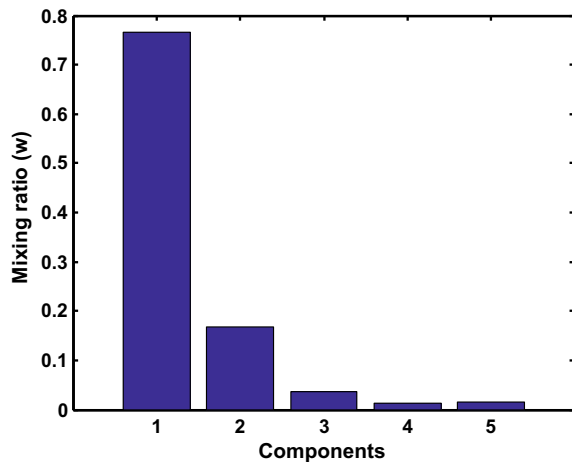


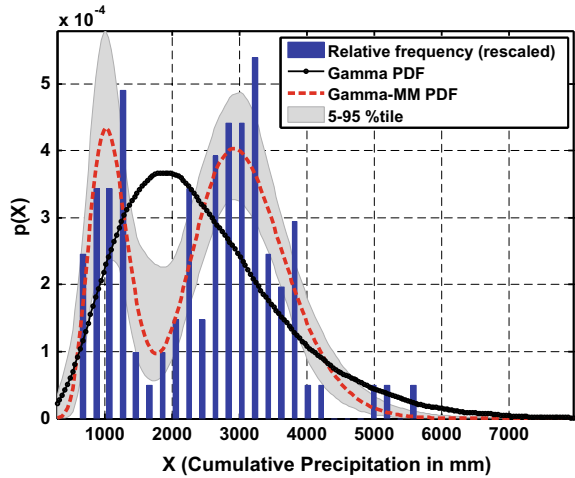
Fig. 7 Mixing ratios of the components of the Bayesian Gamma-MM. Two components are identified as significant for characterizing summer monsoon (June to September) droughts at IMD grid 251



MM fitted to cumulative winter precipitation at this station. The model identifies that three of the five components have negligible contribution and are effectively pruned from the model. Thus, the Bayesian framework identifies optimal number of mixture components needed to fit the data.

The Bayesian framework also allows quantification of model uncertainties and their propagation to model estimates. In the context of Gamma-MM, the posterior distribution of model parameters is estimated from which the CDF is obtained. Unlike maximum likelihood approach that yields a point estimate of CDF, the Bayesian approach treats CDF as a random variable and yields distribution of CDFs for a given value of precipitation. The gray shaded band in Fig. 6 represents 90% credible interval (5 and 95 percentile). The width of the credible interval is not constant but varies with the magnitude of precipitation. It has a maximum value of 0.145 near the

Fig. 8 Relative frequency of the 4-month cumulative precipitation during summer monsoon (June to September) at IMD grid 251, and probability density functions of the fitted gamma distribution (Gamma PDF) and gamma mixture model (Gamma-MM PDF). The gray band shows 90% credible interval (5 and 95 percentile) of the Gamma-MM PDF



median precipitation (120 cm), a plateau near the intersection of two components (~160 cm; Fig. 8), and a monotonic decreasing trend on either side of the median.

The width of the credible interval is large even for smaller values of CDFs that decide drought classes in the SPI methodology. In this study, we attempted to engage credible interval of CDF for drought classification. Figure 9b shows the drought classification using standard SPI method. The empirical CDF along with the fitted CDF and drought classification thresholds are shown in the figure. The SPI drought classification uses fixed thresholds; hence, the boundaries separating two drought classes are vertical lines on the panel. Figure 9a shows probabilistic drought classification using Gamma-MM. The classification uses the same thresholds on CDF as SPI but engages uncertainty in the estimate of CDF resulting in probabilistic drought classification. Unlike standard SPI, the demarcating boundaries in the probabilistic SPI are curves denoting varying classification probabilities.

The probabilities associated with drought classification represent uncertainties in determining drought classes. For example, the D4 category drought represents drought conditions where non-exceedance probability of the cumulative rainfall is less than 0.023 [$F(X) < 0.023$; Table 1]. The probabilistic drought classification acknowledges that, given limited data and model assumptions, such a threshold cannot be determined uniquely but can be estimated probabilistically. The method honors model uncertainty and provides results in a format that could be useful for drought managers.

Figure 10 shows historical drought classes during summer monsoon at IMD grid 251 using standard SPI (Fig. 10b) and probabilistic SPI (Fig. 10a). The droughts classified by the methods are similar; however, the advantages of probabilistic classification are evident in some years. For example, in 1914 and 1915 the cumulative rainfall values were 88 cm and 85 cm, respectively. Considering that the difference in cumulative rainfall among these years is less than 2.7% of their standard deviation

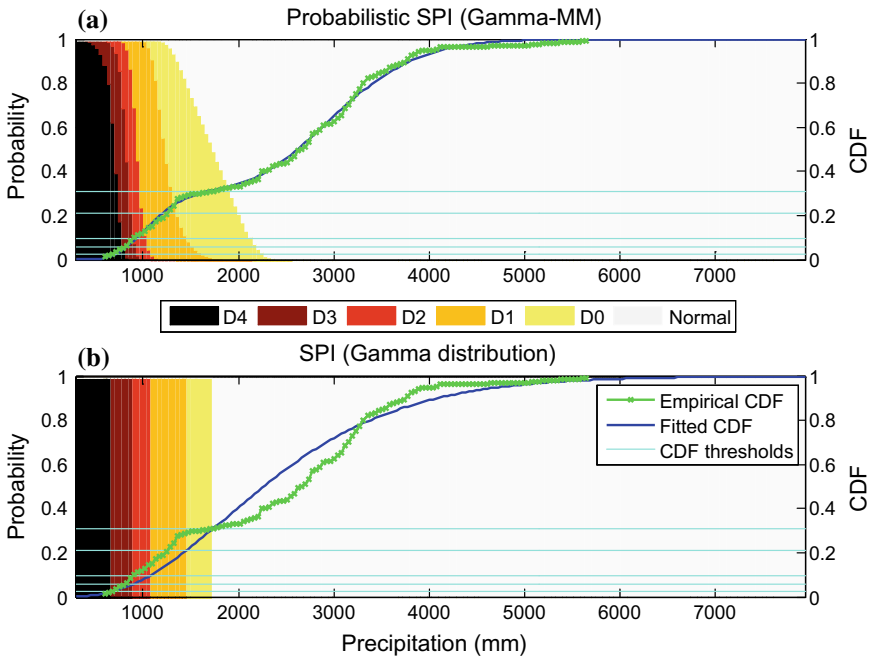


Fig. 9 Drought classification using 4-month cumulative precipitation during summer monsoon (June to September) at IMD grid 251 by **a** the probabilistic SPI (top panel) and **b** standard SPI (bottom panel). The colored patches represent drought classes, the light horizontal lines denote thresholds on CDF specified by US Drought Monitor, and the solid curves represent empirical and fitted CDFs

(110 cm), one would not expect them to belong to two different drought classes as categorized by SPI (1914 in D3, and 1915 in D4). The probabilistic SPI classifies 1914 and 1915 to D3 class with probabilities 66% and 58%, and to D4 class with probabilities 13% and 34%, respectively, (the remaining probability masses being assigned to other drought classes).

4.1.2 Water Year Droughts

Water year droughts were analyzed at all IMD grids in the study area. However, for brevity only the results at IMD grid 125 are discussed below. The grid point is located in the state of Chhattisgarh and belongs to core monsoon region of India. Figure 11 shows the empirical cumulative distribution function (CDF) obtained using Weibull plotting position formula. Figure 11 also shows the CDFs of fitted gamma distribution (fitted using maximum likelihood approach) and gamma mixture model (Gamma-MM). The CDF of Gamma-MM is much closer to empirical CDF compared to CDF of gamma distribution, particularly, for the smaller magnitude of rainfall [$F(x) <$

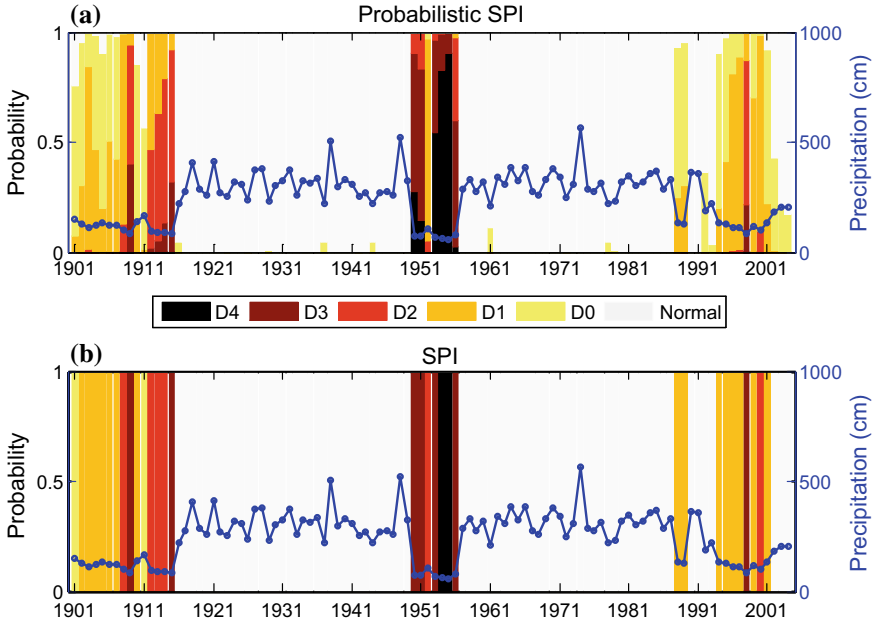


Fig. 10 Classification of historical 4-month time window droughts during summer monsoon (June to September) at IMD grid 251 using **a** probabilistic SPI, and **b** standard SPI approaches. The solid blue line represents cumulative precipitation during summer monsoon months

0.25], which is critical for drought classification. The gray shaded band in Fig. 11 represents 90% credible interval (5 and 95 percentile). The width of the credible interval is not constant but varies with the magnitude of rainfall. It has a maximum value of 0.16 near the median rainfall (1260 mm), a plateau near the intersection of two components (~ 900 mm; Fig. 12), and a monotonic decreasing trend on either side of the median.

The drought classification in the case of Gamma-MM model (shown in top panel of Fig. 13) uses the same thresholds on CDF as SPI but engages uncertainty in the estimate of CDF resulting in probabilistic drought classification. Unlike standard SPI (bottom panel of Fig. 13), the demarcating boundaries in the probabilistic SPI are curves denoting varying classification probabilities. We observe that the demarcating boundaries are slightly curved for D0–D2 classes indicating less uncertainty. However, the demarcating boundaries are more curved for D3 and D4 drought classes indicating higher uncertainty in their classification.

Figure 14 shows the historical drought classification for water year droughts at IMD grid 125. The droughts classified by both probabilistic SPI and standard SPI are similar, however, the advantages of probabilistic classification are evident in some years. For example, in 1998, 1999, and 2000 the cumulative rainfall values were 69 cm, 73 cm, and 66 cm, respectively. Considering that the difference in cumulative rainfall among these years is less than 3% of their standard deviation

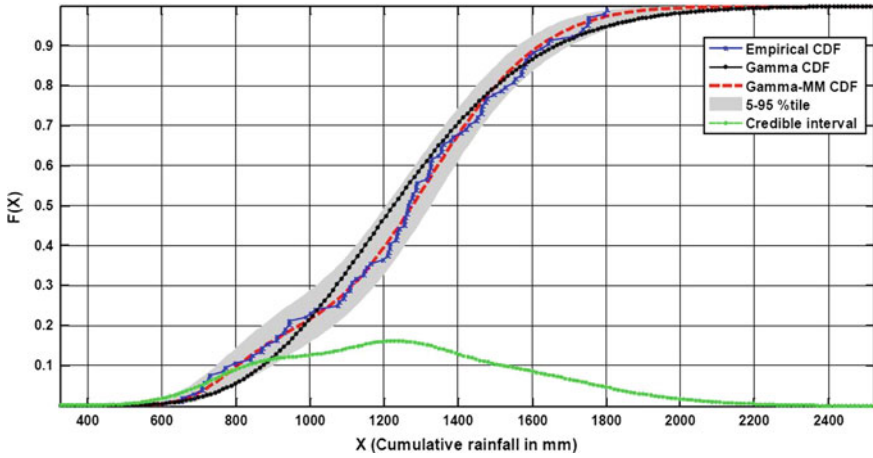


Fig. 11 Empirical CDF along with CDFs obtained by fitting gamma distribution (Gamma CDF) and gamma mixture model (Gamma-MM CDF) to cumulative precipitation during water year (June to May of following year) at IMD grid 125. The gray band shows 5 and 95 percentile of the Gamma-MM CDF and the green-dotted line shows width of its credible interval

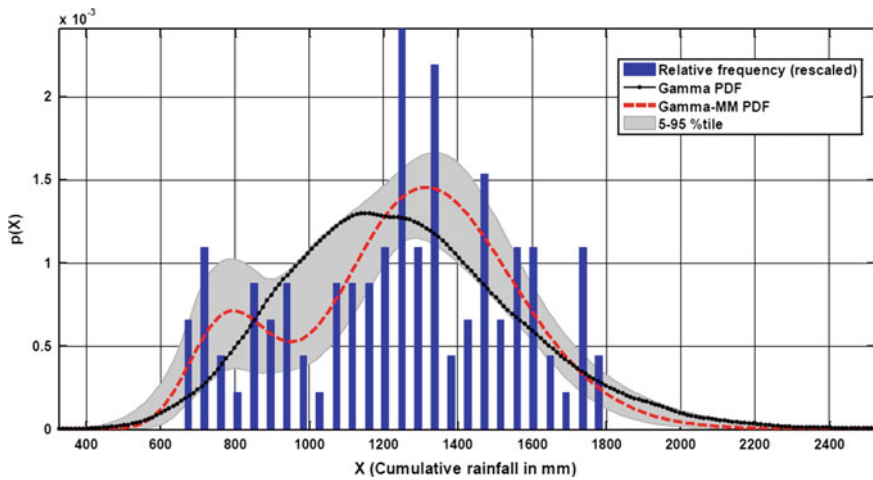


Fig. 12 Relative frequency of the cumulative rainfall in a water year at Grid 125, and probability density functions of the fitted gamma distribution (Gamma PDF) and gamma mixture model (Gamma-MM PDF). The gray band shows 90% credible interval (5 and 95 percentile) of the Gamma-MM PDF

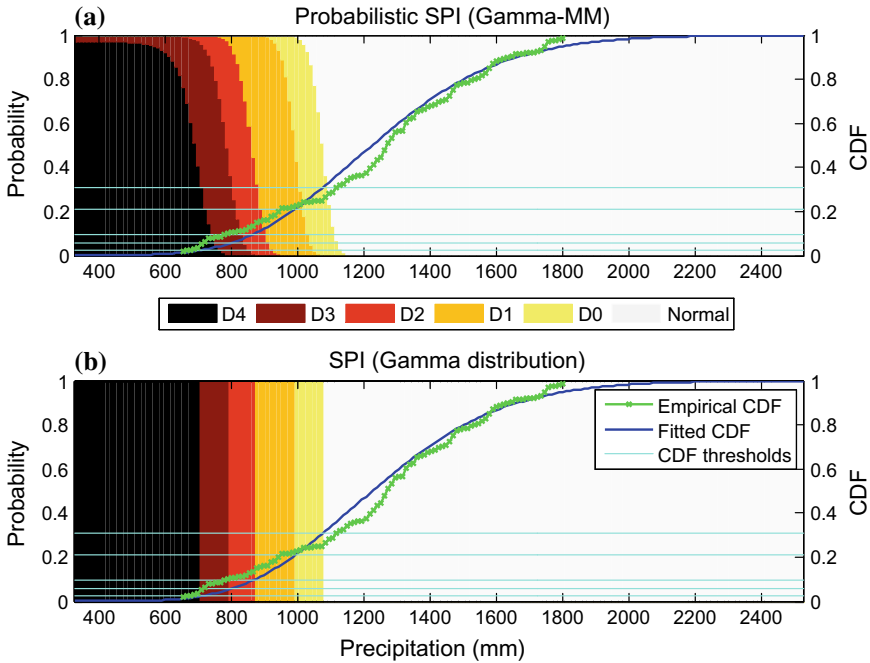


Fig. 13 Drought classification using cumulative precipitation during water year (June to May of following year) at IMD grid 125 by **a** the probabilistic SPI (top panel) and **b** standard SPI (bottom panel). The colored patches represent drought classes, the light horizontal lines denote thresholds on CDF specified by US Drought Monitor, and the solid curves represent empirical and fitted CDFs

(30 cm), we would not have expected them to belong to two different drought classes as categorized by SPI (1998 and 2000 in D4, and 1999 in D3). The probabilistic SPI classifies 1998, 1999, and 2000 to D3 class with probability 46%, 76%, and 23%, and to D4 class with probabilities 53%, 16%, and 75%, respectively, (the remaining probabilities being allocated to other drought classes).

Analyses of historical droughts over the climate divisions in India (see Fig. 15) reveals that the drought characterizations by both standard SPI and Gamma-MM are almost identical for the major drought events. Using fixed thresholds to characterize droughts (as in case of SPI) or when reporting drought class based on average Gamma-MM, we come to similar conclusions. The average Gamma-MM intensities were obtained by taking the probability-weighted sum of average SPI under each drought class. For example, the average Gamma-MM intensity is -1.71 (i.e., $-1.8 * 0.75 + -1.45 * 0.25$) when probabilities under D3 (average SPI -1.8) and D2 (average SPI -1.45) drought categories at a given location are 75% and 25%, respectively. However, if the regions have smaller geographic extent, then some differences in drought classification are possible [46]. Such differences can have significant impact on decision-making. It can result in incorrect assessment of drought impacts, leads to under/over allocation of resources, and affects triggering of miti-

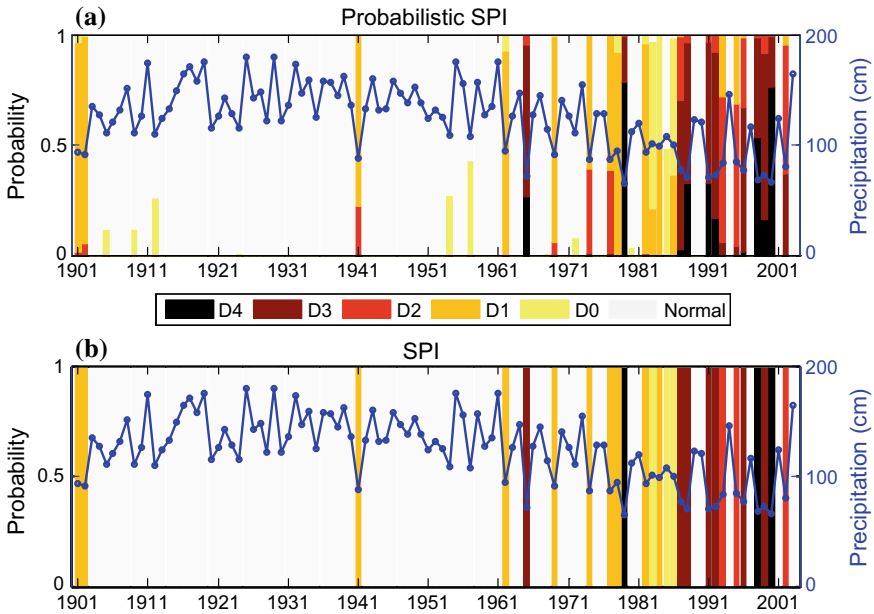


Fig. 14 Classification of historical droughts during water year (June to May of following year) at IMD grid 125 using **a** probabilistic SPI, and **b** standard SPI approaches. The solid blue line represents cumulative precipitation during a water year

gation measures. A probabilistic drought classification provides estimates of uncertainty in drought classification, and thus helps decision-makers to take informed actions.

Figure 16 shows the spatial variation of drought classes computed across all IMD grids over India in May 2003 (or 2002 water year drought) according to standard SPI (Fig. 16a) and average drought intensity values from probabilistic SPI (Fig. 16b). The 2002 water year drought was one of the most severe and widespread drought in the recent decades. Both drought classification methods provide similar results in terms of classifying grids as being in drought, or otherwise. However, upon closer observation, readers may be able to notice subtle differences in the assigned drought classes according to the two methods. For example, IMD grid 58 is classified as D2 and D3 category droughts according to standard SPI and probabilistic SPI, respectively. Similarly, at IMD grid 81 the 2002 water year droughts are classified as D1 and D0 category droughts according to standard and probabilistic SPI, respectively.

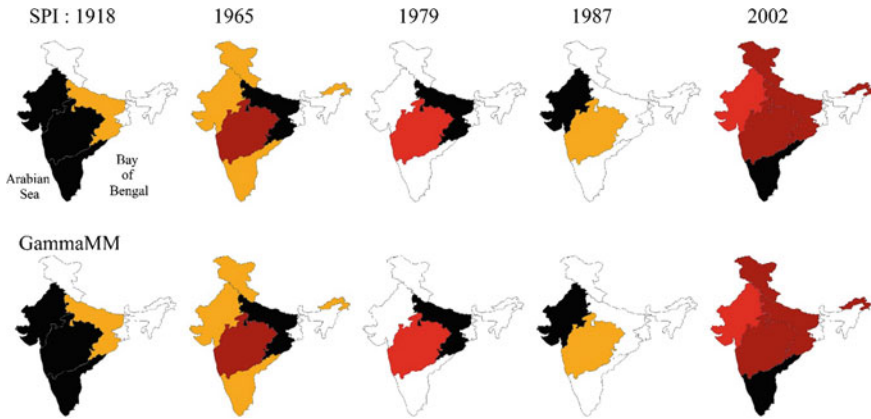


Fig. 15 Spatial variation of historical water year drought classes at each climate division during major drought events over India according to standard SPI (top panel) and Gamma-MM (bottom panel). Color coding for drought classes similar to Fig. 14

4.2 Precipitation Trends

The summer monsoon and water year precipitation series are analyzed for trends. Figure 17a shows the results of Mann–Kendall trend test of summer monsoon precipitation series (i.e., 4-month time window, JJAS) ending month in September at all 1° IMD grids over India. Results indicate that trends in summer monsoon precipitation series are not statistically significant ($\alpha = 0.05$) at most grids (denoted by circles). After ignoring 62 IMD grids located in the hilly regions (see Fig. 2), we find that 34 IMD grids have statistically significant trends with negative slope, indicating that precipitation magnitudes are decreasing with time. These grids are denoted by downward pointing triangles in Fig. 17a and are mostly present within the Central Northeast region and along the western coast of Peninsular monsoon region. Both these regions have either dominant agricultural land use or belong to forested tribal areas, and therefore decreasing magnitudes of summer monsoon precipitation over these regions are of concern. Grids with statistically significant positive trend in precipitation magnitudes are denoted by upward pointing triangular markers. Approximately, 25 grids have positive trends, and these are predominantly located along the western and eastern coasts of West Central and Peninsular monsoon regions, respectively.

Similar analysis was performed for water year precipitation series (12-month cumulative precipitation time series ending in May) at each IMD grid over India. From Fig. 17b, we observe that majority of the grids (235) have no statistically significant trends, 30 grids exhibited statistically significant increase in cumulative precipitation, while another 30 grids showed significant negative trend. The geographic location of the grids with significant positive and negative trends, and their importance within the context of the study area, is similar to that described in the

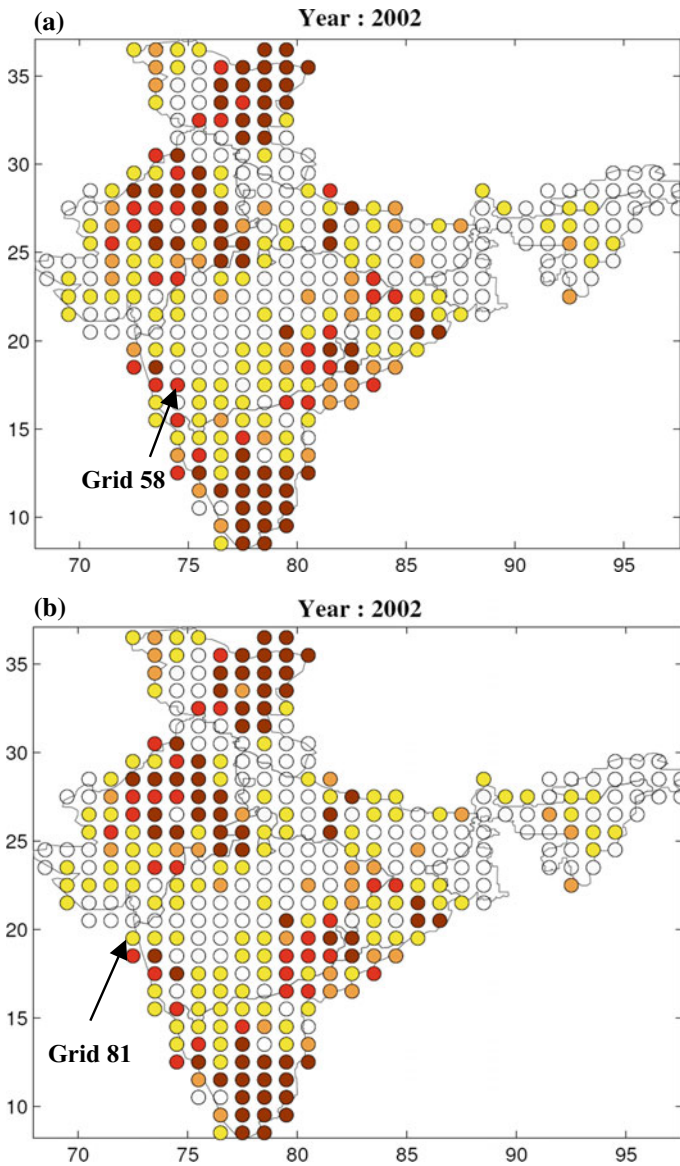


Fig. 16 Spatial variation of water year drought classes at each IMD grid during a recent major drought in 2002 over India according to **a** standard SPI and **b** Gamma-MM. Color coding for drought classes similar to Fig. 14

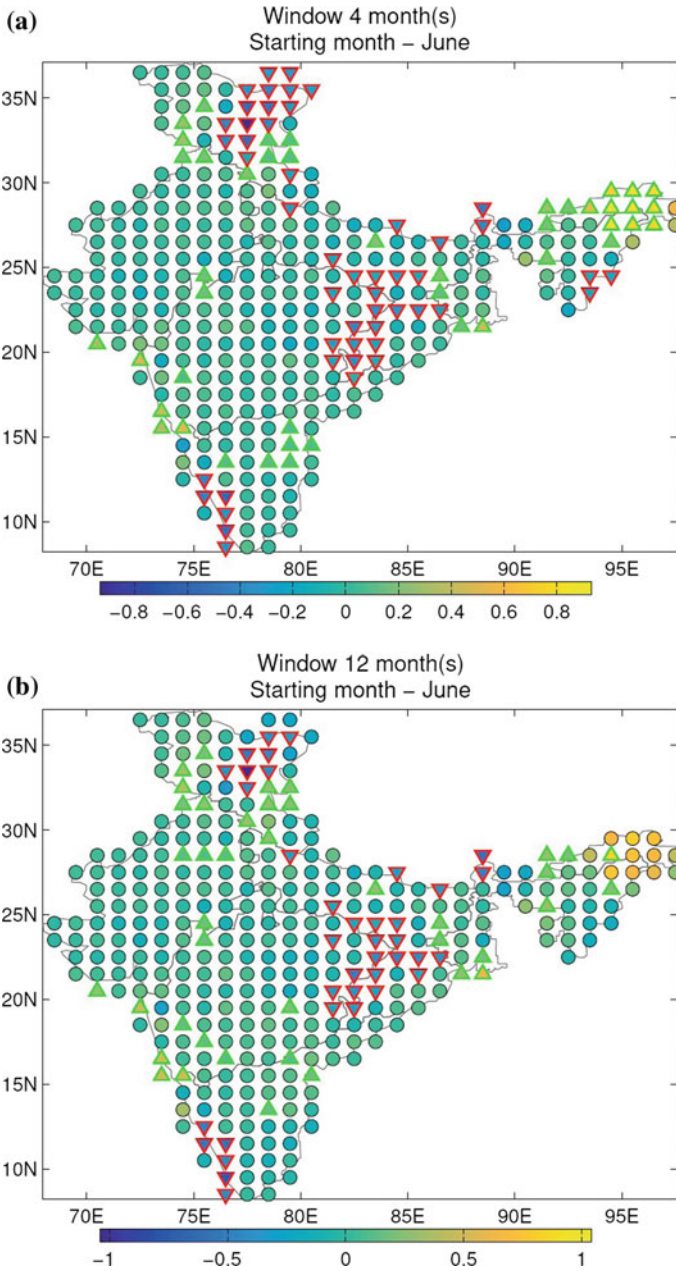


Fig. 17 Mann-Kendall trend test (with $\alpha = 0.05$) of cumulative **a** summer monsoon (4-month time window, JJAS) and **b** water year (12-month time window, June to May) precipitation series at 1° IMD grids over India. Markers are color coded based on the magnitude of Sen's slope. Grids with statistically significant positive slope are denoted by upward pointing triangular markers, while those with significant negative slope are denoted as downward pointing triangular markers

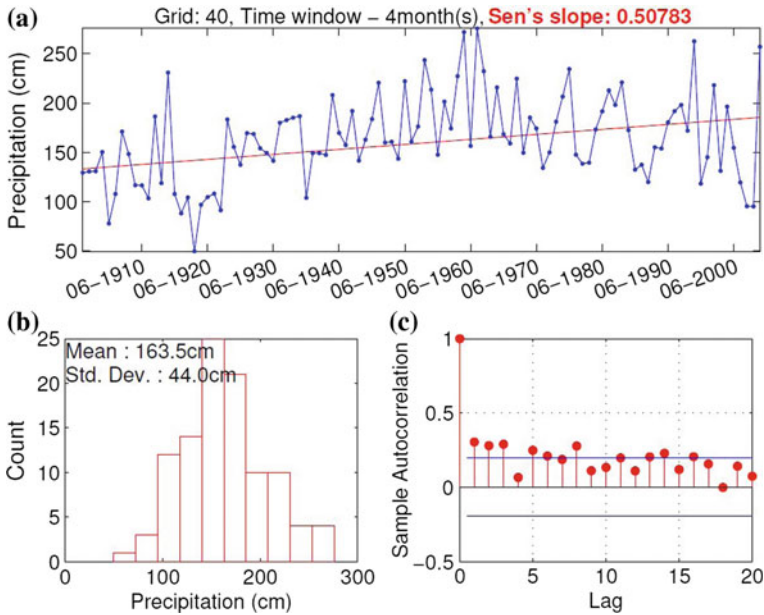


Fig. 18 Mann-Kendall trend test result (with $\alpha = 0.05$) of cumulative summer monsoon precipitation series (June to September) at IMD grid 40 located along the western coast of West Central monsoon region

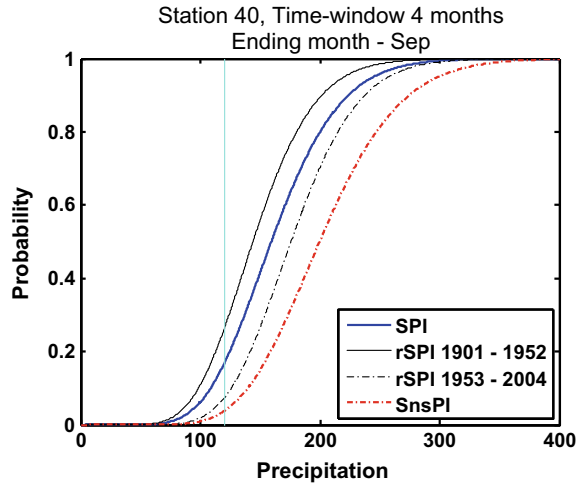
preceding paragraph. The results for other ending months were similar, except for minor differences, and are not shown here for brevity.

4.3 Drought Classification for Nonstationary Precipitation Series

Figure 18a shows the results of Mann-Kendall trend test of cumulative summer monsoon precipitation series at IMD grid 40 located along the western coast of West Central monsoon region. The trend is found to be significant ($\alpha = 0.05$), with a positive Sen's slope of 0.51 cm/year, indicating that summer monsoon precipitation totals are increasing over time. Figure 18b shows the histogram of summer monsoon precipitation at grid 40. The mean value of total summer monsoon precipitation at grid 40 is about 163 cm, with a standard deviation of 44 cm. Figure 18c shows the autocorrelation of summer monsoon precipitation totals at several lags.

As the precipitation series exhibits nonstationarity, classical drought indices such as SPI may not be appropriate. Alternate methods, namely, relative SPI and standardized nonstationary precipitation index (SnsPI) are applied to the precipitation series. Figure 19 shows the comparison of CDFs of three drought analysis methods. The

Fig. 19 Comparison of CDFs of classical SPI, relative SPI (rSPI), and SnsPI obtained for summer monsoon precipitation series (June to September) at IMD grid 40. Blue cyan vertical line represents 4-month cumulative precipitation total of 120 cm



differences in the CDF for different epochs (1901–1952 and 1953–2004) indicate that recent periods are becoming wetter. For example, a cumulative precipitation of 120 cm corresponds to relative SPI of 0.27 and 0.08 for the first (1901–1952) and second half (1953–2004) of the study period, respectively. The corresponding values from standard SPI and SnsPI are 0.18 and 0.03, respectively. These different values of drought index suggest that when precipitation series is nonstationary, standard SPI and its variants that assume stationarity are not reliable.

Figure 20a shows the 12-month cumulative precipitation time series corresponding to the water year at Grid 169 located in Central Northeast monsoon region. The red line indicates the Sen’s slope or the trend in precipitation time series (−0.23 cm/year). The Mann–Kendall trend test at 5% significance level was found to be statistically significant. Figure 20b shows the comparison of CDFs of three drought analysis methods when applied over 12-month water year cumulative precipitation series at IMD grid 169. The differences in the CDF for different epochs (1901–1952 and 1953–2004) indicate that recent periods are becoming drier. For example, a cumulative precipitation of 100 cm corresponds to relative SPI of 0.05 and 0.25 for the first (1901–1952) and second half (1953–2004) of the study period, respectively. The corresponding values from standard SPI and SnsPI are 0.13 and 0.3, respectively. Once again, this highlights the inconsistencies in drought characterization when applying standard methods on nonstationary precipitation series.

The proposed method for classifying nonstationary precipitation series is first applied on two synthetic series, and then to the summer monsoon precipitation series at IMD grid 40 and water year precipitation series at IMD grid 169.

First, we begin by detrending the cumulative precipitation time series. One approach for detrending is to decompose the time series using empirical mode decomposition which separates both deterministic and stochastic trends as intrinsic mode functions (IMFs; Wu et al. [84]). The IMFs consist of amplitude and frequency modu-

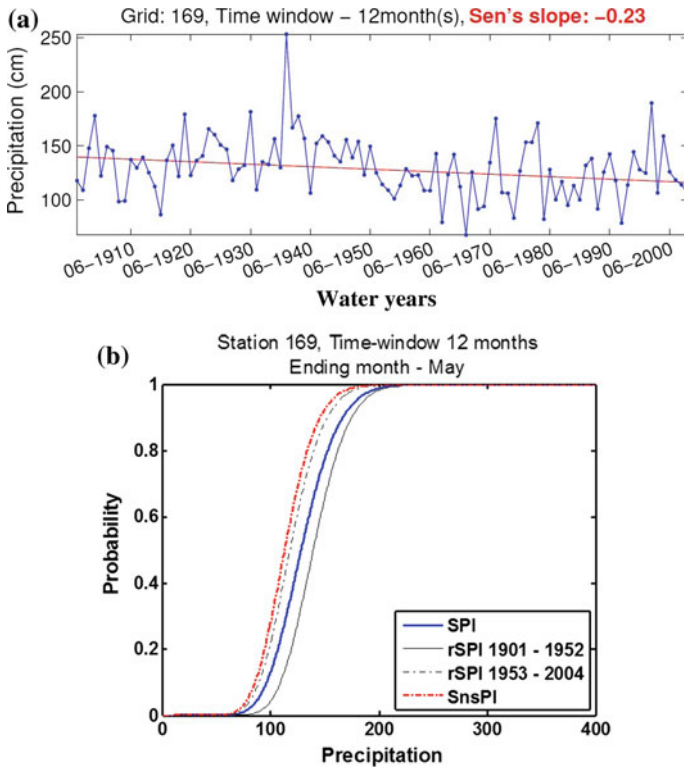


Fig. 20 a Cumulative water year precipitation time series at Grid 169 along with Sen's slope, and b Comparison of CDFs of classical SPI, relative SPI (rSPI), and SnsPI obtained for water year precipitation series (12-month time window, i.e., June to May) at IMD grid 169 located in Central Northeast monsoon region

lations and are extracted from the original time series in a stepwise manner, beginning with high-frequency local oscillations that are superimposed on low-frequency part of the data. These high-frequency oscillations are subtracted from the data to obtain the residual. Then, the next IMF, representing highest frequency oscillations present in the residual, is extracted. The process is repeated until we obtain a residual with no oscillation. Typically, if we have a dataset of length N we can extract about $\log_2 N$ IMFs from the data. Then, those IMFs that are statistically different from white noise are subtracted from the original series to obtain a detrended series.

The second approach for detrending the time series, and the one that is used in this study, is to fit polynomials of several orders to the data, and obtain the best polynomial using either the Akaike information criteria (AIC; Akaike [2]) or Bayesian information criteria (BIC; Schwarz [70]). Trend line is then obtained from the coefficients of the best fitting polynomial.

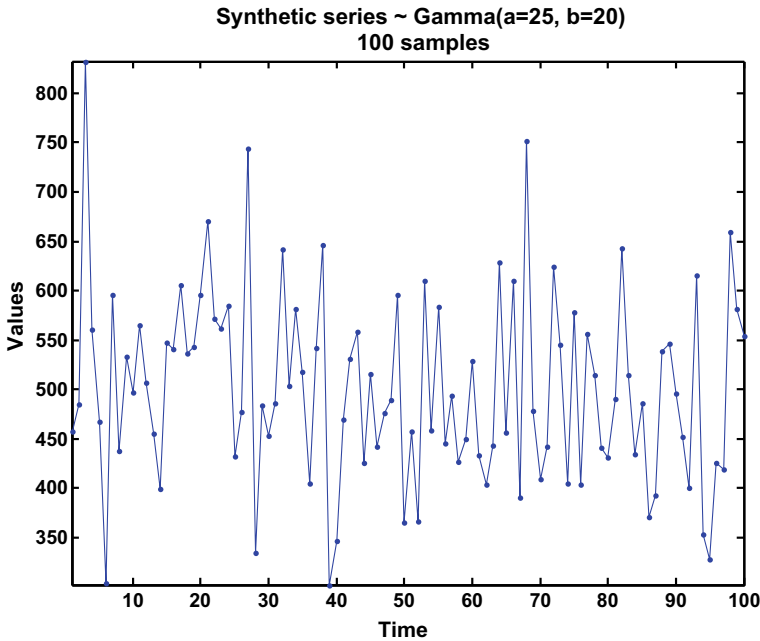


Fig. 21 Synthetic time series generated from a gamma distribution with mean 500 cm and standard deviation equal to 100 cm. No trend is present in the time series

4.3.1 Synthetic Series with Linear Trend

First, 100 samples are drawn from the gamma distribution, $G(x_t|\nu, s_t)$ with scale parameter $s_t = 20$ and shape parameter $\nu = 25$. The time series of the 100 samples is shown in Fig. 21. The mean and standard deviation of the series are around 500 mm and 100 mm, respectively.

For the first synthetic example, a linear trend is added to the mean of the synthetic series. The resulting series is shown in Fig. 22. Drought characterization is then performed using the following methods:

- **SPI**—A gamma distribution is fitted to the synthetic series and SPI values are obtained as described in Sect. 3.1. The drought classes for classical SPI are shown in the top panel of Fig. 23.
- **Standardized nonstationary precipitation index (SnsPI; Russo et al. [68])**—The SnsPI drought indices are obtained using the method presented in Sect. 3.3.2. In this method, the scale parameter of the gamma distribution is assumed to vary linearly with time. Such a model specifies a linear trend for the mean of the series and a quadratic trend for its variance. Drought classes obtained for SnsPI are shown in the second panel of Fig. 23.
- **Detrended-SPI**—First, trend in the mean of the series is obtained by fitting a polynomial. Next, the detrended series is obtained by subtracting the estimated trend

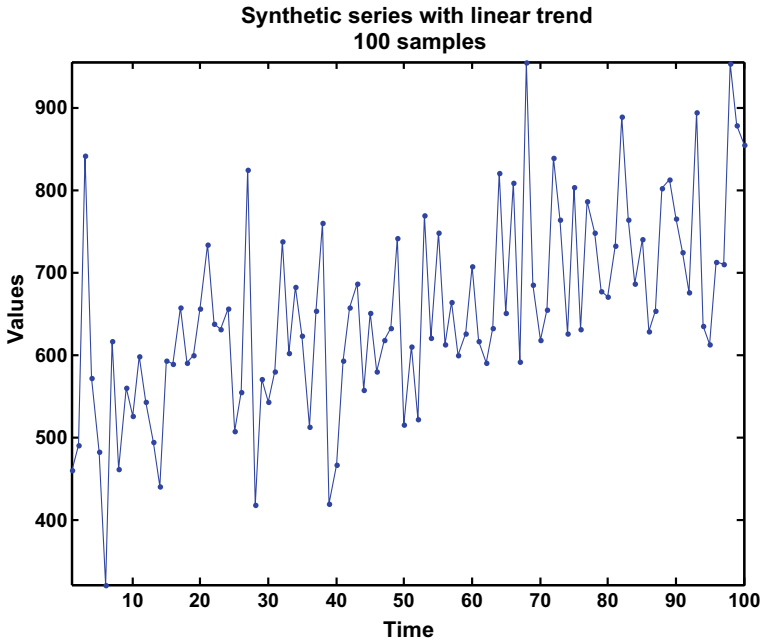


Fig. 22 Synthetic series with linear trend in mean

from the data. Several candidate distributions (beta, Birnbaum–Saunders, exponential, extreme value, gamma, generalized extreme value, generalized Pareto, inverse Gaussian, logistic, log-logistic, lognormal, Nakagami, normal, Rayleigh, Rician, and t location-scale and Weibull distributions) are fitted to the detrended series, and the best distribution is selected based on AIC score (see Fig. 24). The method identifies Gamma distribution to be one of the best distributions to describe the detrended series. The selected distribution is then used for obtaining drought indices shown in the third panel of Fig. 23.

As expected, the standard SPI overestimates drought severities for the earlier time steps, and underestimates it for the later time steps. This is evident from the top panel of Fig. 23 and also by observing that the threshold that defines any drought class is fixed over the entire time period (dashed line in Fig. 25a and first panel of Fig. 25b). For example, the threshold for D4 drought ($F(X) < 0.023$) is about 430 cm, and remains unchanged over the entire period. The SnsPI treats the scale parameter as a time-varying component of the model, and is able to capture the linear trend in the synthetic data. This is evident from the dotted lines of Fig. 25a. For example, the threshold for D4 category drought is close to 380 mm at time step 1 and close to 550 mm at time step 100. The threshold varies linearly between these points (Fig. 25a). As a consequence, the drought classes obtained are markedly different compared to standard SPI approach. In SnsPI, the drought occurrences are

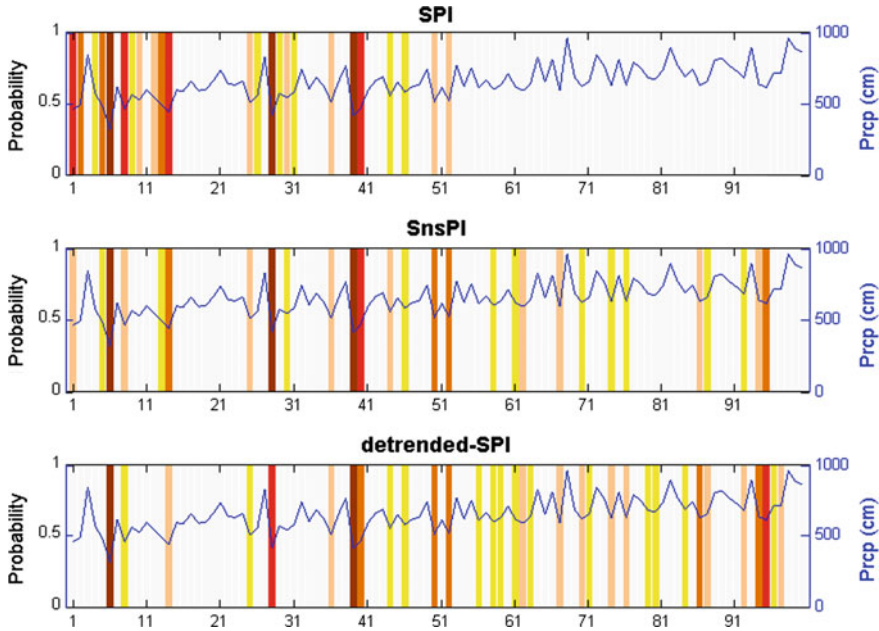


Fig. 23 Droughts classified into D0–D4 classes according to US Drought Monitor classification scheme for SPI (first panel), SnsPI (second panel), and proposed detrended-SPI method (third panel). The blue line represents the original synthetic series that has linear trend

spread evenly across the study period (second panel of Fig. 23), rather than being concentrated in the earlier years like standard SPI (first panel of Fig. 23).

SnsPI prescribes linear trend for mean and a quadratic trend for variance. This property is evident from the second panel of Fig. 25b. The proposed detrended-SPI method, however, specifies linear trend for mean and no trend for variance (see third panel of Fig. 25b).

The second approach for drought analysis of nonstationary series assumes that the “normal” conditions for a station are fixed (with respect to a reference period), but the frequency of droughts are changing with time. Figure 26 shows the drought classes by the new approach when the reference point is time step 1. As expected, the droughts become less severe with time because of the positive trend in the synthetic precipitation series.

4.3.2 Synthetic Series with Nonlinear Trend

For the second synthetic example, a quadratic trend is imposed on a series (see Fig. 27) generated from the same gamma distribution as used in the first example (Sect. 4.3.1). The three methods for drought characterization, standard SPI, SnsPI, and detrended-SPI, are applied again. For the detrended-SPI, gamma distribution

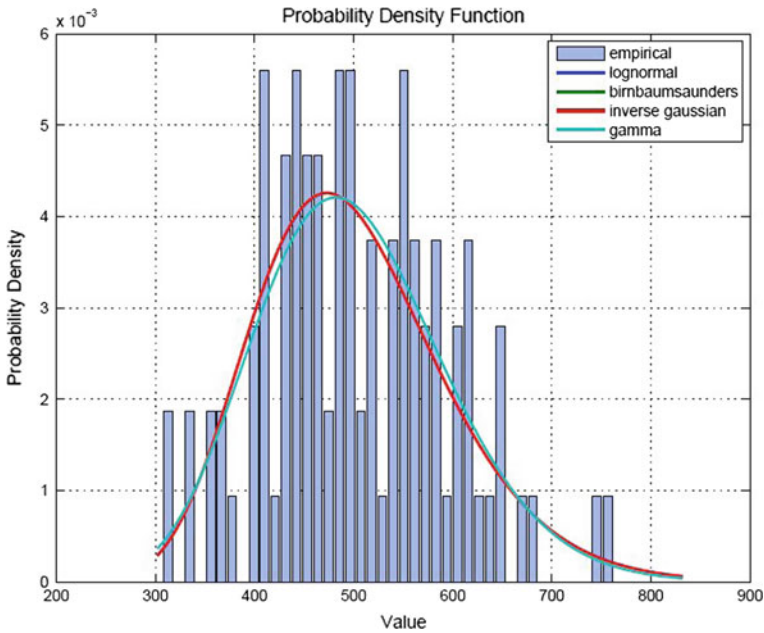


Fig. 24 Top four out of seventeen candidate distributions based on AIC scores that fit the detrended series (original synthetic series had linear trend)

was selected as the best distribution based on AIC score. The results obtained are shown in Fig. 28.

The first panel of Fig. 28 shows the drought classes obtained from standard SPI. Given the significantly positive nonlinear trend of the time series, most drought occurrences are concentrated in the first half of the time period. The results obtained from the detrended-SPI (third panel of Fig. 28) are significantly different from SnSPI (second panel of Fig. 28), specifically, in the second half of the series. These differences can be attributed to the fact that SnsPI can only account for linear trends in mean.

The advantages of proposed detrended-SPI are evident in Fig. 29a and b. Figure 29a shows the variation of precipitation thresholds over time for different drought categories. The SPI thresholds remain constant over time (dashed lines in Fig. 29a), SnsPI thresholds vary linearly (dotted lines in Fig. 29a), while the drought thresholds for the proposed method show a quadratic trend (solid lines in Fig. 29a).

Figure 30 shows the drought classes over the study period according to detrended-SPI when the reference period is selected as time step 1. Again as expected, the drought severities decrease with time, indicating wetter conditions (or positive trend in data).

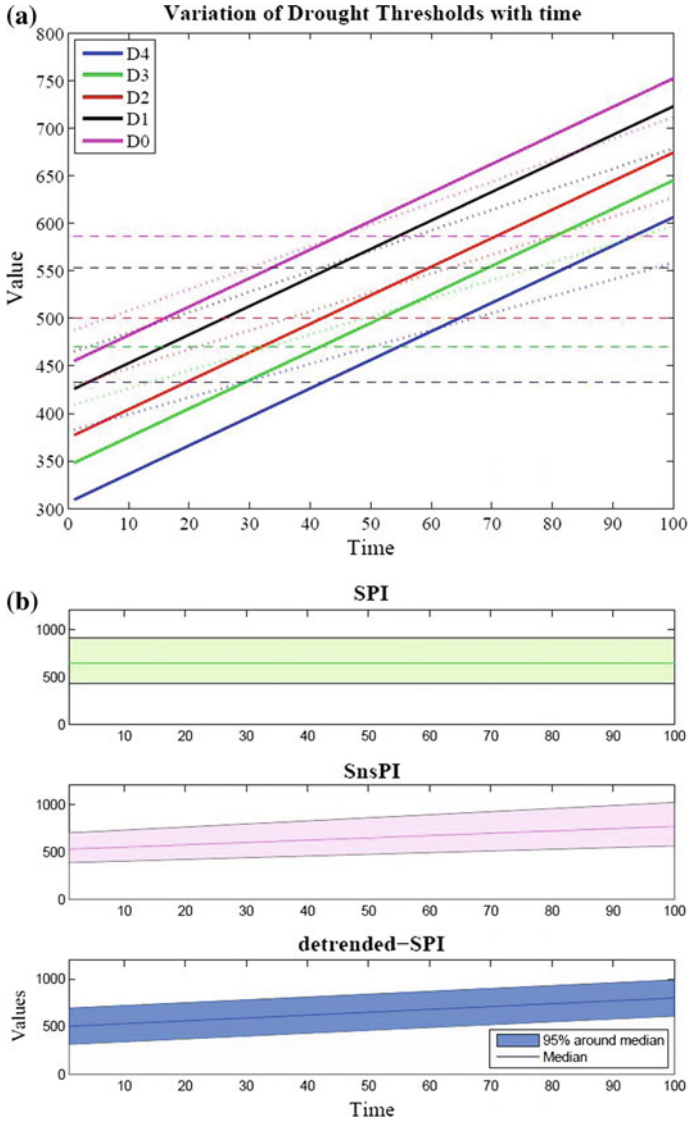


Fig. 25 Variation of fitted model distributions as a function of time for synthetic data with linear trends. Figure **a** shows the variation of data thresholds that define drought classes (D4 to D0) according to SPI (dashed lines), SnsPI (dotted lines), and proposed detrended-SPI (solid lines), **b** shows the median of the distribution and 95% distribution interval around the median for SPI (first panel of Fig. 25b), SnsPI (second panel of Fig. 25b), and detrended-SPI approach (third panel of Fig. 25b)

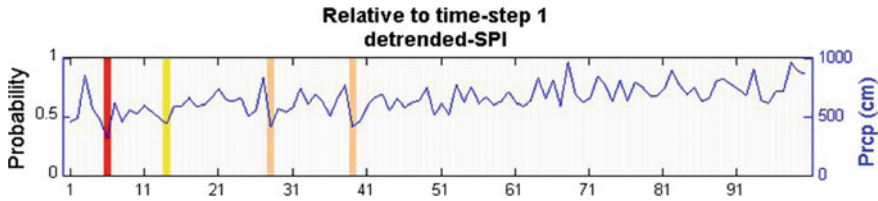


Fig. 26 Drought classes calculated relative to distributional properties at the first time step using detrended-SPI

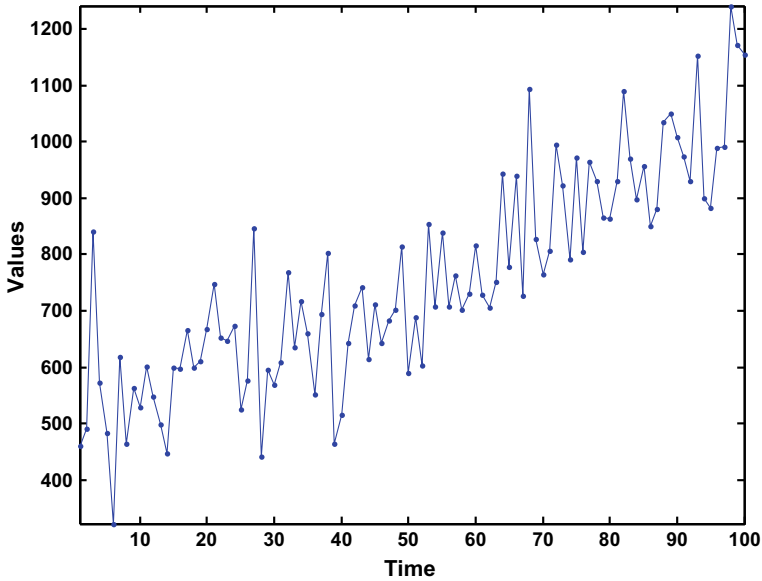


Fig. 27 Synthetic time series with quadratic trend in mean

4.3.3 Observed Precipitation Series

The proposed detrended-SPI method was tested on cumulative (a) summer monsoon precipitation data at IMD grid 40 and (b) water year precipitation data at IMD grid 169. The cumulative precipitation time series at grid 40 (Fig. 18) corresponds to 4-month time window during summer monsoon season (June to September). The red line indicates positive Sen’s slope, indicating increasing precipitation over time (0.51 cm/year). The series exhibits a statistically significant positive trend according to Mann–Kendall trend test ($\alpha = 0.05$).

The results obtained from the three methods, SPI, SnsPI, and detrended-SPI, are shown in Fig. 31. The detrended-SPI identifies linear trend in the precipitation series and selects normal distribution for the detrended series. As in the synthetic time series case (Sect. 4.3.1), the SPI and SnsPI results are markedly different during the

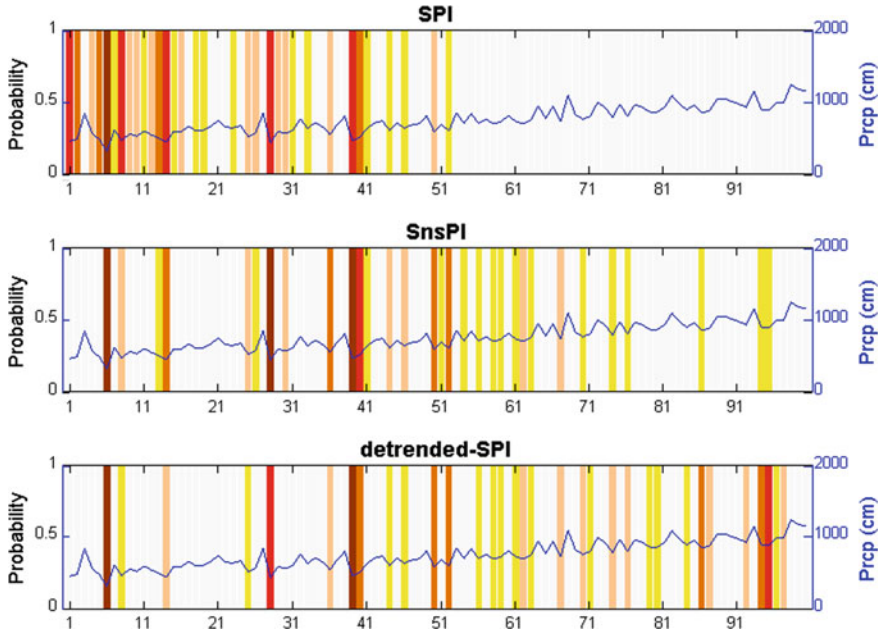


Fig. 28 Droughts classified into D0–D4 classes according to US Drought Monitor classification scheme for SPI (first panel), SnsPI (second panel), and proposed detrended-SPI method (third panel). The blue line represents the original synthetic series that has nonlinear quadratic trend

recent years. The SnsPI assigns drought categories to several time steps in recent years compared to SPI.

The consequences of model assumptions in the three methods become clear in Fig. 32. The dashed lines in Fig. 32a denote the thresholds of D4–D0 classes according to standard SPI. These dashed lines are horizontal indicating that the thresholds on precipitation for different drought classes do not change over time (stationarity assumption). This property of SPI model also becomes evident in the median and variance in the first panel of Fig. 32b. For SnsPI (second panel of Fig. 32b), the median varies linearly with time, whereas the variance varies quadratically. For detrended-SPI (third panel of Fig. 32b), the median varies linearly, while the variance is constant.

Relative drought severity and classes with respect to the first time step are shown in Fig. 33. Since the cumulative summer monsoon precipitation series at IMD grid 40 has positive trend (top panel Fig. 18), the summer droughts relative to the first year become milder over time.

Figure 34a compares the performance of the three drought classification methods on cumulative water year precipitation series at IMD grid 169. Unlike IMD grid 40, the precipitation series shows a significant decreasing trend with a Sen’s slope of -0.23 cm/year (not shown here for brevity). Due to stationarity assumption in standard SPI, the horizontal dashed lines that indicate the thresholds on precipitation

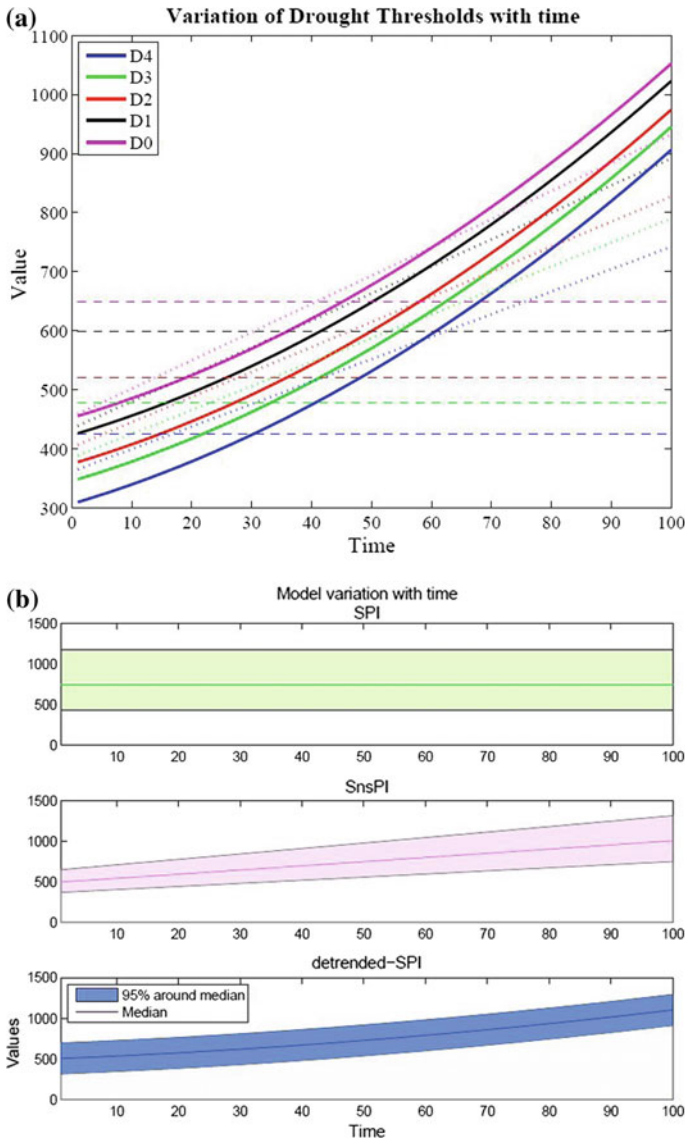


Fig. 29 Variation of fitted model distributions as a function of time for synthetic data with nonlinear trends. Figure **a** shows the variation of data thresholds that define drought classes (D4 to D0) according to SPI (dashed lines), SnsPI (dotted lines), and proposed detrended-SPI (solid lines); **b** shows the median of the distribution and 95% distribution interval around the median for SPI (first panel of Fig. 29b), SnsPI (second panel of Fig. 29b), and detrended-SPI approach (third panel of Fig. 29b)

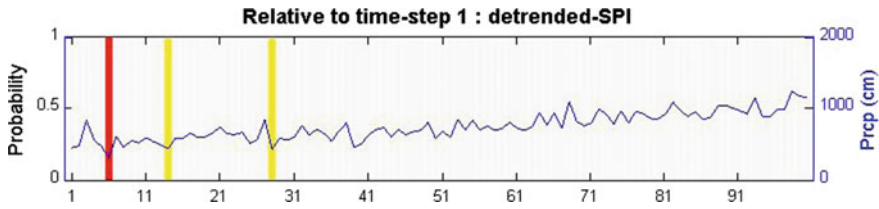


Fig. 30 Drought classes for synthetic series with nonlinear trend in its mean, calculated relative to distributional properties at the first time step using detrended-SPI

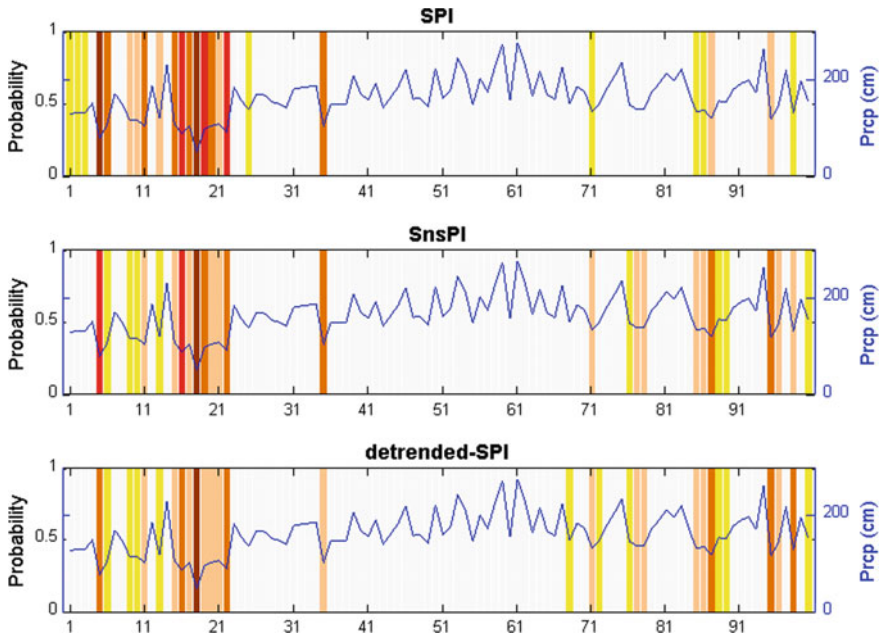


Fig. 31 Droughts classified into D0–D4 classes according to US Drought Monitor classification scheme for SPI (first panel), SnsPI (second panel), and proposed detrended-SPI method (third panel). The blue line represents the cumulative summer monsoon precipitation series at IMD grid 40 in India

for different drought classes (D0–D4) do not change over time (Fig. 34a). On the other hand, the dotted and bold lines in Fig. 34a show that the drought thresholds decrease over time for SnsPI and detrended-SPI, respectively. Figure 34b shows the relative water year drought severity and classes calculated at IMD grid 169 using detrended-SPI and the distributional properties of cumulative water year precipitation time series at time step 1. Since the cumulative water year precipitation series at IMD grid 169 has negative trend, the water year droughts relative to the first year becomes severe over time.

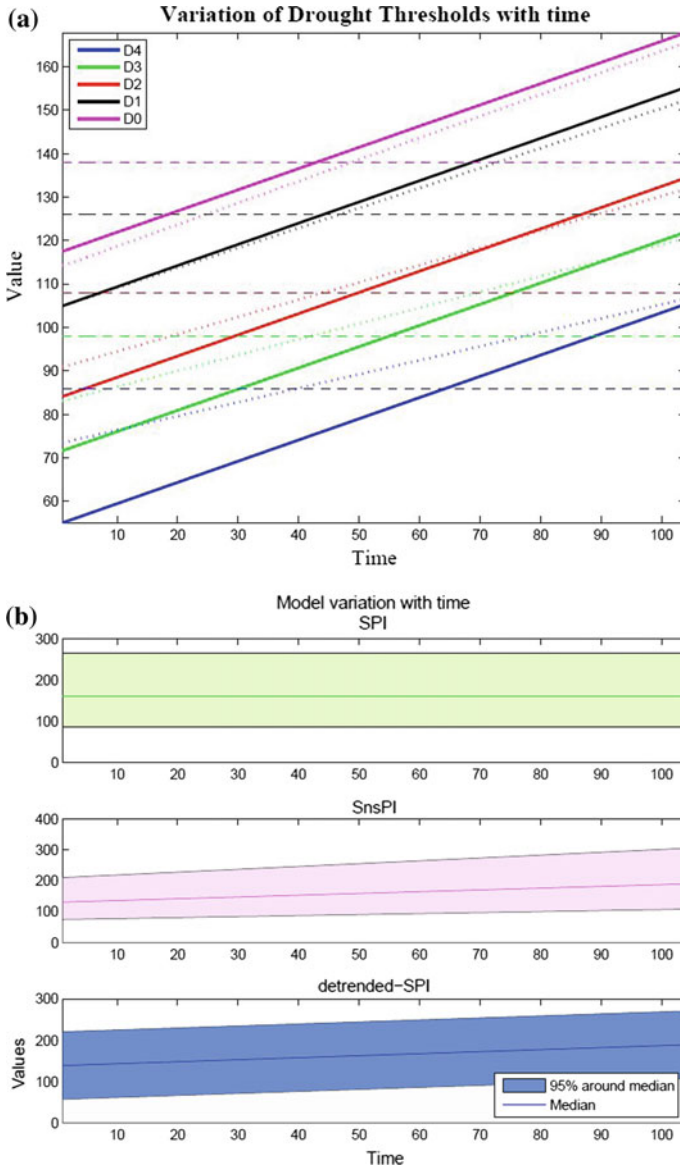


Fig. 32 Variation of fitted model distributions as a function of time for nonstationary cumulative summer monsoon precipitation (4-month time window, June to September) at IMD grid 40 in India. Figure a) shows the variation of data thresholds that define drought classes (D4 to D0) according to SPI (dashed lines), SnsPI (dotted lines), and proposed detrended-SPI (solid lines), b) shows the median of the distribution and 95% distribution interval around the median for SPI (first panel of Fig. 32b), SnsPI (second panel of Fig. 32b), and detrended-SPI approach (third panel of Fig. 32b)

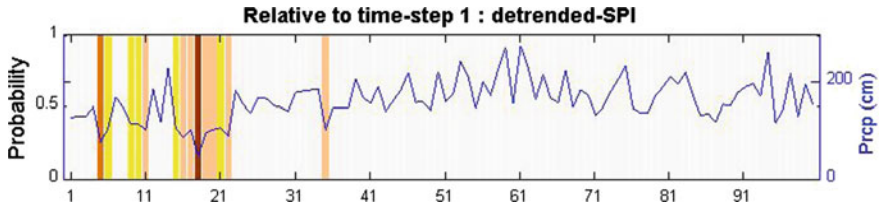


Fig. 33 Drought classes calculated relative to distributional properties of cumulative summer monsoon precipitation series (4-month time window, June–September) at the first time step according to detrended-SPI method. Precipitation data is from IMD grid 40 in India

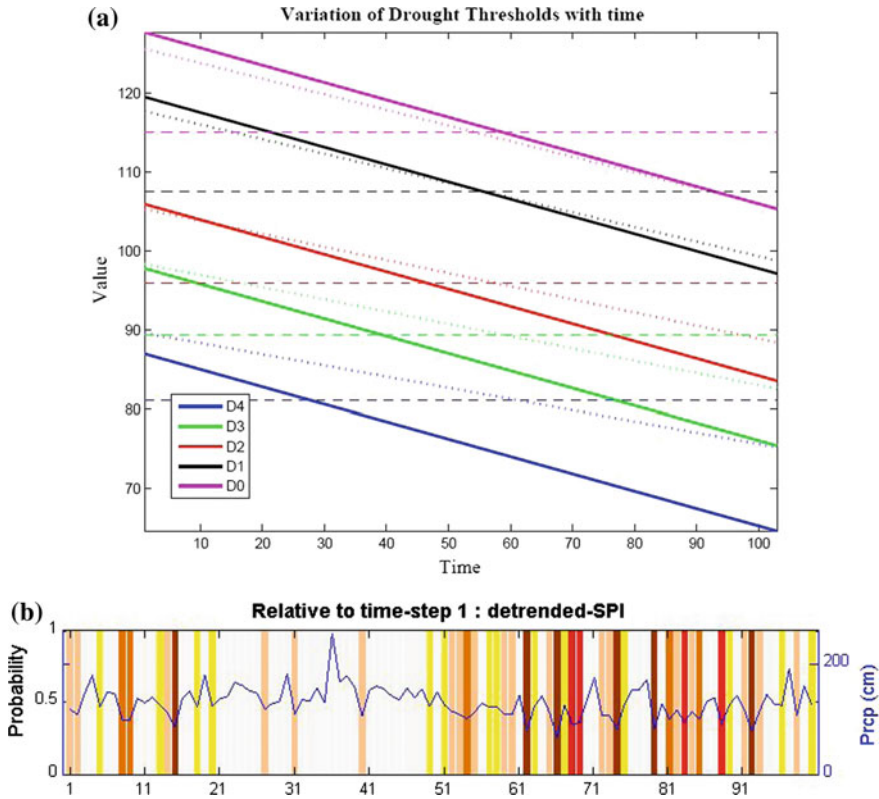


Fig. 34 Using nonstationary cumulative water year precipitation (12-month time window, June to May) at IMD grid 169 in India, **a** shows the variation of data thresholds that define drought classes (D4 to D0) according to SPI (dashed lines), SnsPI (dotted lines), and proposed detrended-SPI (solid lines), and **b** shows the drought classes calculated relative to distributional properties of cumulative water year precipitation series at the first time step according to detrended-SPI method

5 Summary and Concluding Remarks

1. Meteorological droughts over India were studied using two drought classification methods, namely, standardized precipitation index (SPI) and gamma-mixture-model-based drought index (Gamma-MM). The latter provides probabilistic classification of droughts.
2. The Gamma-MM alleviates the problem of adopting a prescribed distribution for SPI analysis by modeling the data with a mixture of gamma distributions. Given sufficient components in the mixture, the Gamma-MM can give arbitrarily close approximation to any general continuous distribution in the range $(0, \infty)$. The problem of overfitting the data is avoided using a Bayesian framework that determines optimum number of components for the model.
3. The results of droughts over India during the water year (June–May) and for each of the three seasons (winter, summer, and summer monsoon) suggest that the drought classification by the Gamma-MM is similar to SPI when the data satisfies SPI assumptions. However, the results of the two methods are significantly different when data violate SPI assumptions.
4. Mann–Kendall trend test of precipitation series indicated that several IMD grids in India have statistically significant trends. IMD grids with significant negative trend in 4-month cumulative precipitation (JJAS) are greater in number (34 grids) compared to grids with significant positive trend (25 grids). Also, similar number of grids with significant positive precipitation trends and negative precipitations trends (30 grids each) are found when analyzing water year precipitation series.
5. An alternate method is proposed for drought analysis of trend stationary precipitation series. The method first explicitly removes trend from the data, and then analyzes detrended series to estimate changes in drought frequency and drought classification thresholds.
6. The application of the proposed method on synthetic and real-world data suggests that it offers flexibility in modeling nonstationary time series compared to standardized nonstationary precipitation index (SnsPI) and relative SPI.
7. The proposed method can be applied only if the trends are deterministic and can be explicitly estimated as a function of time. Future research should explore possibilities to relax this requirement.

References

1. AghaKouchak A (2014) A baseline probabilistic drought forecasting framework using standardized soil moisture index: application to the 2012 United States drought. *Hydrol Earth Syst Sci* 18:2485–2492
2. Akaike H (1974) A new look at the statistical model identification. *IEEE Trans Autom Control* 19:716–723
3. Bagla P (2006) Controversial rivers project aims to turn India's fierce monsoon into a friend. *Science* 313:1036–1037. <https://doi.org/10.1126/science.313.5790.1036>

4. Belayneh A, Adamowski J, Khalil B, Ozga-Zielinski B (2014) Long-term SPI drought forecasting in the Awash River Basin in Ethiopia using wavelet neural network and wavelet support vector regression models. *J Hydrol* 508:418–429. <https://doi.org/10.1016/j.jhydrol.2013.10.052>
5. Benjamini Y, Hochberg Y (1995) Controlling the false discovery rate: a practical and powerful approach to multiple testing. *J R Stat Soc Ser B Methodol* 57:289–300
6. Bishop CM (2006) *Pattern Recognition and Machine Learning*. Springer, New York
7. Bonaccorso B, Peres DJ, Cancelliere A, Rossi G (2013) Large scale probabilistic drought characterization over Europe. *Water Resour Manag* 27:1675–1692. <https://doi.org/10.1007/s11269-012-0177-z>
8. Burn DH, Elnur MAH (2002) Detection of hydrologic trends and variability. *J Hydrol* 255:107–122. [https://doi.org/10.1016/S0022-1694\(01\)00514-5](https://doi.org/10.1016/S0022-1694(01)00514-5)
9. Burroughs WJ (1999) *The climate revealed*. Cambridge University Press
10. Chow VT, Maidment DR, Mays LW (1988) *Applied hydrology*. McGraw-Hill. Ser Water Resour Environ Eng
11. Cole JE, Cook ER (1998) The changing relationship between ENSO variability and moisture balance in the continental United States. *Geophys Res Lett* 25:4529–4532. <https://doi.org/10.1029/1998GL900145>
12. Coulibaly P, Baldwin CK (2005) Nonstationary hydrological time series forecasting using nonlinear dynamic methods. *J Hydrol* 307:164–174
13. Dai A (2011) Drought under global warming: a review. *Wiley Interdiscip Rev Clim Chang* 2:45–65. <https://doi.org/10.1002/wcc.81>
14. De U, Dube R, Rao GP (2005) Extreme weather events over India in the last 100 years. *J Ind Geophys Union* 9:173–187
15. Deshingkar P, Start D (2003) *Seasonal migration for livelihoods in India: coping, accumulation and exclusion*. Overseas Development Institute London
16. DeVore RA, Lorentz GG (1993) *Constructive approximation*. Springer
17. Dracup JA, Lee KS, Paulson EG Jr (1980). On the definition of droughts. *Water Resour Res* 16:297–302. <https://doi.org/10.1029/WR016i002p00297>
18. Dubrovsky M, Svoboda MD, Trnka M, Hayes MJ, Wilhite DA, Zalud Z, Hlavinka P (2009) Application of relative drought indices in assessing climate-change impacts on drought conditions in Czechia. *Theor Appl Climatol* 96:155–171. <https://doi.org/10.1007/s00704-008-0020-x>
19. Evin G, Merleau J, Perreault L (2011) Two-component mixtures of normal, gamma, and Gumbel distributions for hydrological applications (W08525). *Water Resour Res* 47. <https://doi.org/10.1029/2010WR010266>
20. Federal Emergency Management Agency (1995) *National Mitigation Strategy*. FEMA Wash. DC
21. Friedman DG (1957) The prediction of long-continuing drought in south and southwest Texas. *Occasional Pap Meteorol* 1, 182
22. Fuller W-A (1996) *Introduction to statistical time series*
23. Gao B-C (1996) NDWI—A normalized difference water index for remote sensing of vegetation liquid water from space. *Remote Sens Environ* 58:257–266
24. Geman S, Geman D (1984) Stochastic relaxation, Gibbs distributions, and the Bayesian restoration of images. *IEEE Trans Pattern Anal Mach Intell PAMI-6*, 721–741. <https://doi.org/10.1109/TPAMI.1984.4767596>
25. Goswami BN, Venugopal V, Sengupta D, Madhusoodanan MS, Xavier PK (2006) Increasing trend of extreme rain events over India in a warming environment. *Science* 314:1442–1445. <https://doi.org/10.1126/science.1132027>
26. Green PJ (1995) Reversible jump Markov chain Monte Carlo computation and Bayesian model determination. *Biometrika* 82:711–732. <https://doi.org/10.1093/biomet/82.4.711>
27. Guttman NB (1999) Accepting the standardized precipitation index: a calculation algorithm. *JAWRA J Am Water Resour Assoc* 35:311–322. <https://doi.org/10.1111/j.1752-1688.1999.tb03592.x>

28. Hamed KH, Ramachandra Rao A (1998) A modified Mann-Kendall trend test for autocorrelated data. *J Hydrol* 204:182–196. [https://doi.org/10.1016/S0022-1694\(97\)00125-X](https://doi.org/10.1016/S0022-1694(97)00125-X)
29. Han P, Wang PX, Zhang SY, Zhu DH (2010) Drought forecasting based on the remote sensing data using ARIMA models. *Math Comput Model Agric* 51:1398–1403. <https://doi.org/10.1016/j.mcm.2009.10.031>
30. Hayes M, Svoboda M, Wall N, Widhalm M (2011) The Lincoln declaration on drought indices: universal meteorological drought index recommended. *Bull Am Meteorol Soc* 92:485–488
31. Hayes MJ, Wilhelmi OV, Knutson CL (2004) Reducing drought risk: bridging theory and practice. *Nat Hazards Rev* 5:106–113
32. Heim RR (2002) A review of twentieth-century drought indices used in the United States. *Bull Am Meteorol Soc* 83:1149
33. Hogg R, Tanis E, Zimmerman D (2014) Probability and statistical inference. Pearson Higher Ed
34. Houghton JT, Ding Y, Griggs DJ, Nogueira N, van der Linden PJ, Xiaosu D, Maskell K, Johnson CA (eds) (2001) Climate change 2001: the scientific basis. Cambridge University Press
35. Kao SC, Govindaraju RS (2010) A copula-based joint deficit index for droughts. *J Hydrol* 380(1–2):121–134. <https://doi.org/10.1016/j.jhydrol.2009.10.029>
36. Kripalani RH, Kumar P (2004) Northeast monsoon rainfall variability over south peninsular India vis-à-vis the Indian Ocean dipole mode. *Int J Climatol* 24:1267–1282. <https://doi.org/10.1002/joc.1071>
37. Krishnamurthy V, Shukla J (2000) Intraseasonal and interannual variability of rainfall over India. *J Clim* 13:4366–4377. [https://doi.org/10.1175/1520-0442\(2000\)013%3c0001:IAIVOR%3e2.0.CO;2](https://doi.org/10.1175/1520-0442(2000)013%3c0001:IAIVOR%3e2.0.CO;2)
38. Kulkarni A, von Storch H (1995) Monte Carlo experiments on the effect of serial correlation on the Mann-Kendall test of trend. *Meteorol Z* 4:82–85
39. Kumar KK, Rajagopalan B, Hoerling M, Bates G, Cane M (2006) Unraveling the mystery of Indian monsoon failure during El Niño. *Science* 314:115–119
40. Liu W, Kogan F (1996) Monitoring regional drought using the vegetation condition index. *Int J Remote Sens* 17:2761–2782
41. Liu WT, Juárez RIN (2001) ENSO drought onset prediction in northeast Brazil using NDVI. *Int J Remote Sens* 22:3483–3501. <https://doi.org/10.1080/01431160010006430>
42. Lloyd-Huges B, Saunders MA (2002) A drought climatology for Europe. *Int J Climatol* 22:1571–1592
43. Loukas A, Vasilades L (2004) Probabilistic analysis of drought spatiotemporal characteristics in Thessaly region, Greece. *Nat Hazards Earth Syst Sci* 4:719–731
44. Mahajan DR, Dodamani BM (2015) Trend analysis of drought events over upper Krishna basin in Maharashtra. *Aquat Procedia* 4:1250–1257. <https://doi.org/10.1016/j.aqpro.2015.02.163>
45. Mallya G, Mishra V, Niyogi D, Tripathi S, Govindaraju RS (2016) Trends and variability of droughts over the Indian monsoon region. *Weather Clim Extrem*. <https://doi.org/10.1016/j.wace.2016.01.002>
46. Mallya G, Tripathi S, Govindaraju RS (2017) Detection of temporal changes in droughts over Indiana (under review)
47. Mallya G, Tripathi S, Govindaraju RS (2015) Probabilistic drought classification using gamma mixture models. *J Hydrol* 526:116–126
48. Mallya G, Tripathi S, Kirshner S, Govindaraju RS (2013) Probabilistic assessment of drought characteristics using hidden Markov model. *J Hydrol Eng* 18:834–845. [https://doi.org/10.1061/\(ASCE\)HE.1943-5584.0000699](https://doi.org/10.1061/(ASCE)HE.1943-5584.0000699)
49. Mann ME, Bradley RS, Huges MK (1999) Northern hemisphere temperatures during the past millennium: inferences, uncertainties, and limitations. *Geophys Res Lett* 26:759
50. McKee TB, Doesken NJ, Kleist J (1995) Drought monitoring with multiple time scales. In: Proceedings of the 9th conference on applied climatology. American meteorological society dallas, Boston, MA, pp 233–236
51. McKee TB, Doesken NJ, Kleist J (1993) The relationship of drought frequency and duration to time scales. In: Conference on applied climatology. American Meteorological Society, Anaheim, CA

52. Mishra AK, Desai VR (2006) Drought forecasting using feed-forward recursive neural network. *Ecol Model* 198:127–138. <https://doi.org/10.1016/j.ecolmodel.2006.04.017>
53. Mishra AK, Desai VR, Singh VP (2007) Drought forecasting using a hybrid stochastic and neural network model. *J Hydrol Eng* 12:626–638. [https://doi.org/10.1061/\(ASCE\)1084-0699\(2007\)12:6\(626\)](https://doi.org/10.1061/(ASCE)1084-0699(2007)12:6(626))
54. Mishra AK, Singh VP (2011) Drought modeling—a review. *J Hydrol* 403:157–175
55. Mishra AK, Singh VP (2010) A review of drought concepts. *J Hydrol* 391:202–216. <https://doi.org/10.1016/j.jhydrol.2010.07.012>
56. Mitra S, Srivastava P (2016) Spatiotemporal variability of meteorological droughts in south-eastern USA. *Nat Hazards*, 1–32. <https://doi.org/10.1007/s11069-016-2728-8>
57. Naresh Kumar M, Murthy CS, Sessa Sai MVR, Roy PS (2011) Spatiotemporal analysis of meteorological drought variability in the Indian region using standardized precipitation index. *Meteorol Appl* <https://doi.org/10.1002/met.277>
58. Niranjan Kumar K, Rajeevan M, Pai DS, Srivastava AK, Preethi B (2013) On the observed variability of monsoon droughts over India. *Weather Clim Extrem* 1:42–50. <https://doi.org/10.1016/j.wace.2013.07.006>
59. Niyogi D, Kishtawal C, Tripathi S, Govindaraju RS (2010) Observational evidence that agricultural intensification and land use change may be reducing the Indian summer monsoon rainfall. *Water Resour Res* 46, 17. <https://doi.org/10.1029/2008WR007082>
60. Palmer WC (1968) Keeping track of crop moisture conditions, nationwide: the new crop moisture index. *Weatherwise* 21:156–161. <https://doi.org/10.1080/00431672.1968.9932814>
61. Palmer WC (1965) Meteorological drought, Research Paper No. 45. US Weather Bureau, Washington DC
62. Parathasarathy B, Munot A, Kothawale D (1994) Droughts over homogeneous regions of India: 1871–1990. *Drought Network News* 1994–2001 67
63. Rajeevan M (2006) High resolution daily gridded rainfall data for the Indian region: analysis of break and active monsoon spells. *Curr Sci* 91:296
64. Rao G (2001) Household coping/survival strategies in drought-prone regions: a case study of Anantapur district. Andhra Pradesh India SPWD-Hyderabad Cent
65. Rayner NA, Parker DE, Horton EB, Folland CK, Alexander LV, Rowell DP, Kent EC, Kaplan A (2003) Global analyses of sea surface temperature, sea ice, and night marine air temperature since the late nineteenth century. *J Geophys Res* 108:29. <https://doi.org/10.1029/2002JD002670>
66. Richardson S, Green PJ (1997) On Bayesian analysis of mixtures with an unknown number of components (with discussion). *J R Stat Soc Ser B Stat Methodol* 59:731–792. <https://doi.org/10.1111/1467-9868.00095>
67. Rossi G, Cancelliere A (2003) At-site and regional drought identification by Redim model. In: Rossi G, Cancelliere A, Pereira LS, Oweis T, Shatanawi M, Zairi A (eds) *Tools for drought mitigation in mediterranean regions*, water science and technology library. Springer, Netherlands, pp 37–54
68. Russo S, Dosio A, Sterl A, Barbosa P, Vogt J (2013) Projection of occurrence of extreme dry-wet years and seasons in Europe with stationary and nonstationary standardized precipitation Indices. *J Geophys Res Atmos* 118:7628–7639. <https://doi.org/10.1002/jgrd.50571>
69. Ryu JH, Svoboda MD, Lenters JD, Tadesse T, Knutson CL (2010) Potential extents for ENSO-driven hydrologic drought forecasts in the United States. *Clim Change* 101:575–597. <https://doi.org/10.1007/s10584-009-9705-0>
70. Schwarz G (1978) Estimating the dimension of a model. *Ann Stat* 6:461–464
71. Shafer BA, Dezman LE (1982) Development of a Surface Water Supply Index (SWSI) to assess the severity of drought conditions in snowpack runoff areas
72. Shiau J-T, Feng S, Nadarajah S (2007) Assessment of hydrological droughts for the Yellow River, China, using copulas. *Hydrol Process* 21:2157–2163. <https://doi.org/10.1002/hyp.6400>
73. Shukla S, Wood AW (2008) Use of a standardized runoff index for characterizing hydrologic drought. *Geophys Res Lett* 35:7. <https://doi.org/10.1029/2007GL032487>

74. Solomon S, Qin D, Manning M, Marquis M, Averyt K, Tignor M, Miller HL Jr, Chen Z (2007) Climate change 2007: the physical science basis
75. Sprague LA (2005) Drought effects on water quality in the south platte river basin, Colorado1. JAWRA J Am Water Resour Assoc 41:11–24. <https://doi.org/10.1111/j.1752-1688.2005.tb03713.x>
76. Steinemann A (2003) Drought indicators and triggers: a stochastic approach to evaluation. Wiley Online Library
77. Türkeş M, Tatlı H (2009) Use of the standardized precipitation index (SPI) and a modified SPI for shaping the drought probabilities over Turkey. Int J Climatol 29:2270–2282. <https://doi.org/10.1002/joc.1862>
78. Varikoden H, Revadekar JV, Choudhary Y, Preethi B (2015) Droughts of Indian summer monsoon associated with El Niño and Non-El Niño years. Int J Climatol 35:1916–1925. <https://doi.org/10.1002/joc.4097>
79. Ventura V, Paciorek CJ, Risbey JS (2004) Controlling the proportion of falsely rejected hypotheses when conducting multiple tests with climatological data. J Clim 17:4343–4356. <https://doi.org/10.1175/3199.1>
80. Verdon-Kidd DC, Kiem AS (2010) Quantifying drought risk in a nonstationary climate. J Hydrometeorol 11:1019–1031. <https://doi.org/10.1175/2010JHM1215.1>
81. Wilhite DA, Glantz MH (1985) Understanding: the drought phenomenon: the role of definitions. Water Int 10:111–120. <https://doi.org/10.1080/02508068508686328>
82. Wiper M, Insua DR, Ruggeri F (2001) Mixtures of gamma distributions with applications. J Comput Graph Stat 10:440–454. <https://doi.org/10.1198/106186001317115054>
83. WMO (1975) “Drought and agriculture,” WMO Technical Note No. 138, Report of the CAgM Working Group on the Assessment of Drought, Geneva, Switzerland 127
84. Wu Z, Huang NE, Long SR, Peng C-K (2007) On the trend, detrending, and variability of nonlinear and nonstationary time series. Proc Natl Acad Sci 104:14889–14894
85. Yue S, Wang CY (2002) Applicability of prewhitening to eliminate the influence of serial correlation on the Mann-Kendall test. Water Resour Res 38:1068. <https://doi.org/10.1029/2001WR000861>
86. Zhang X, Obringer R, Wei C, Chen N, Niyogi D (2017) Droughts in India from 1981 to 2013 and implications to wheat production. Sci Rep 7:44552. <https://doi.org/10.1038/srep44552>

Urban Hydrology in a Changing World



James A. Griffiths and Shailesh Kumar Singh

1 Introduction

Across the globe, an increasing number of people are choosing to reside in cities rather than in rural areas (70% of the global population is expected to reside in cities by 2020) [30]. The resulting increase in population and land-cover change will increase the demand for water resources in such areas. In addition, climate change may result in an increased risk of both flood and drought frequency depending on the geographic location [43]. As combined impacts of urbanisation and climate change become evident, the need for accurate simulation of water demand, management and distribution will become critical. This chapter considers the different modelling approaches that can be used to represent the increased hydrological dynamics that will be found within urban areas. The role of sustainable urban water management in mitigating impacts of climate change and urbanisation is also considered.

2 Modelling Urban Hydrology

The hydrology of urban areas is very different from that of rural areas. Most obviously, urban areas exhibit higher percentages of impervious (or near impervious) areas. Runoff generation is also higher and faster in urban areas, as there is less natural storage to delay incident rainfall. There is also less vegetation compared to rural areas, so that whilst surface evaporation is comparable, there is less evapotranspiration and withdrawal of subsurface water. Urban areas also exhibit greater use of artificial subsurface drainage which may also combine domestic discharges with stormwater and subsurface seepage, resulting in an overall depletion of drainage water quality.

J. A. Griffiths (✉) · S. K. Singh
National Institute of Water and Atmospheric Research, 10 Kyle St, Christchurch,
New Zealand
e-mail: James.Griffiths@niwa.co.nz

© Springer Nature Switzerland AG 2019
S. K. Singh and C. T. Dhanya (eds.), *Hydrology in a Changing World*, Springer Water,
https://doi.org/10.1007/978-3-030-02197-9_3

The use of infrastructure responses to mitigate the impacts of urbanisation and climate change [13] makes the design stage use hydrological models crucial for developing infrastructure performance scenarios and comparisons. The choice of model should be made relative to the nature of the existing hydrological system and any expected future perturbation.

2.1 Network Representation

A key measure of the utility of any hydrological model is how robustly it can represent different surface and subsurface networks. This task is difficult because surface water networks in modern cities consist of both natural and man-made channels and pipelines. In addition to simulating surface water flows, sediments and pollutants, such models should also be able to provide information to help identify areas for habitat creation, recreation, and socio-cultural value.

Development of a realistic and representative city-scale hydrological model requires consideration of the surface and subsurface drainage networks. A consistent method for representation of existing and future network components is essential. Once a reliable model of the network topology is identified, operational models can populate the network with hydraulic equations to describe both hydraulic response and system control mechanisms [6]. A number of contemporary models utilise Geographic Information Systems (GIS) to capture the topology of urban networks. However, the extent to which such information reflects reality will depend on the level of detail required by the model (i.e. flow direction, intensity, variability and range) and the scale which the network is mapped.

Most GISs can also be used to provide a basic visual representation of water networks. Figure 1a shows an example of a standard representation of a surface water network for example. Features include a large river network represented by polygons, and a canal network represented by a polyline coverage. The database was compiled from satellite imagery using manual digitization. A semi-natural drainage network that surrounds (and feeds into) the urban network was determined from 30 m resolution ASTER GDEM data. The two networks were manually aligned, by identifying pour points at the interface between the canal and river network on the floodplain and the surrounding mountain stream network.

Figure 1b shows a width-weighted representation of the same network that uses channel width data to scale the canal system. The advantage of Fig. 1b is that channels that have more influence on the overall flow pattern within the network are more easily identifiable. For example, in Fig. 1b, the existence of a large, north–south, flood alleviation channel is more easily seen and can thus be better represented within numerical simulation models.

The ArcGIS (ESRI) ‘Geometric Network’ toolset allows mapping and representation of pipe and surface water networks, using nodes and vectors (referred to as junctions and edges). The connectivity of a network is based on ‘geometric coincidence’, so that it is possible to combine the topology and connectivity properties of a

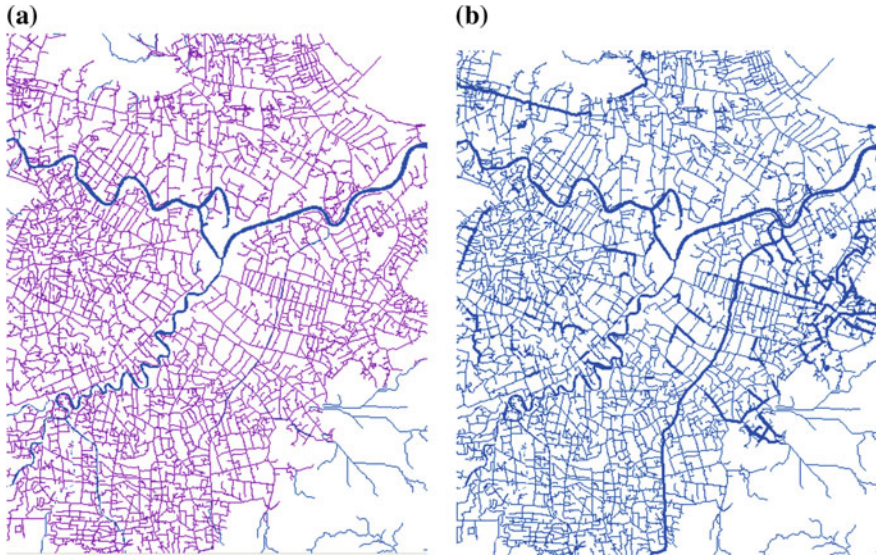


Fig. 1 **a** Standard network representation; and **b** width-weighted representation

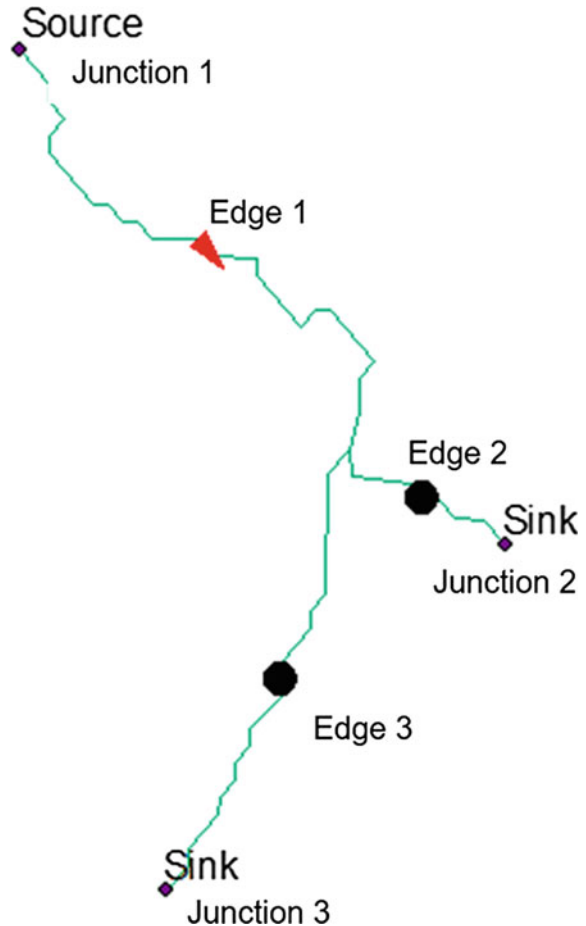
network with feature locations from other networks or point features. The framework allows drainage direction to be defined either as the direction in which the network was digitised, or by definition of ‘sink’ and ‘source’ point location data (nodes). Within a city network, sink nodes can be used to represent drainage outlets (such as floodgate or sluice gates), whilst source nodes can be used to represent inflows (such as tributaries from peri-urban areas).

Figure 2 illustrates a section of network consisting of three channel segments (Edges 1 to 3). In the illustration, a source node is linked to two sink nodes, and as a result water is adjudged to flow from the source node to the sink nodes. Table 1 illustrates the different flow directions that would be determined for different node-type combinations. It can be seen that only two combinations would result in a definitive flow direction in all three channels—other combinations will result in ‘null’ or unknown flow direction.

To obtain a more accurate representation of flow direction within a GIS, drainage direction can be defined by the direction of digitization (i.e. during the digitization process). However, this method would prove to be arduous on very large networks and would be unable to capture changes in flow direction caused by varying boundary conditions.

Figure 3a illustrates a new urban development in Ningbo, China. The observed water flow in the surrounding drainage network is largely controlled by pre-existing agricultural channels that drain this part of the city in a north-westerly direction towards the Yong River. Figure 3b indicates the location of GIS-digitised sink nodes that represent city floodgates. The flow direction in any channel, however, is

Fig. 2 Illustration of flow direction between Junction 1 (source) and two sink nodes (Junctions 2 and 3) indicating outflow becoming indeterminate (●) after the bifurcation point



determined as much by channel proximity to the floodgates as the location relative to other channels.

It can be seen from Fig. 4a that the western side of the area is characterised by newer linear-type larger channels, whilst the eastern side of the area retains the older irregular drainage pattern. As the area was relatively small, drainage direction could be defined manually using the direction of digitisation (Fig. 4b). Whilst the predominant direction of flow is from southeast to northwest, some drainage will still occur in the opposite direction because of the network configuration.

Development of GIS-based drainage maps such as those in Figs. 3 and 4 allows the analysis of total system storage, travel times, water transfer efficiencies assessment of the capacity of the system to manage high magnitude events (flood and drought),

Table 1 Possible combinations of flow directions within a tri-channel junction

Junction 1	Line 1	Junction 2	Line 2	Junction 3	Line 3
Sink	<	null	>	null	>
Source	>	null	<	null	<
Sink	<	Source	>	null	o
Source	>	Sink	o	Sink	o
Sink	<	Source	o	Source	o
null	<	Source	o	Source	o
null	>	Sink	o	Sink	o
Sink	o	Sink	o	Sink	o
Source	o	Source	o	Source	o
null	x	null	x	null	x

where **o** = unknown direction; **x** = no flow; **>** indicates flow towards junction; **<** indicates flow away from junction

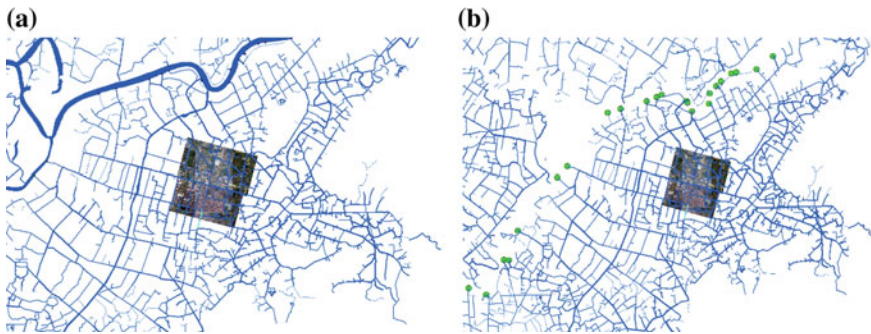


Fig. 3 **a** Location of Ningbo East City development area within canal network and relative to larger river system; and **b** location of sink points (floodgates)

and assessment options for diversion of water. A more dynamic characterization of flow and flow direction can only be achieved using independently developed, or bespoke, hydrological software.

2.2 Numerical Simulation Models

Most commercial hydrological models now incorporate the capture of surface or subsurface networks in their data preparation routines. Model performance generally improves with increased network representation, with the marked exception of some parsimonious modelling approaches (e.g. Coutu et al. [9], Griffiths et al. [15]). Table 2 lists some of the most widely used, commercial and open-source models. The models

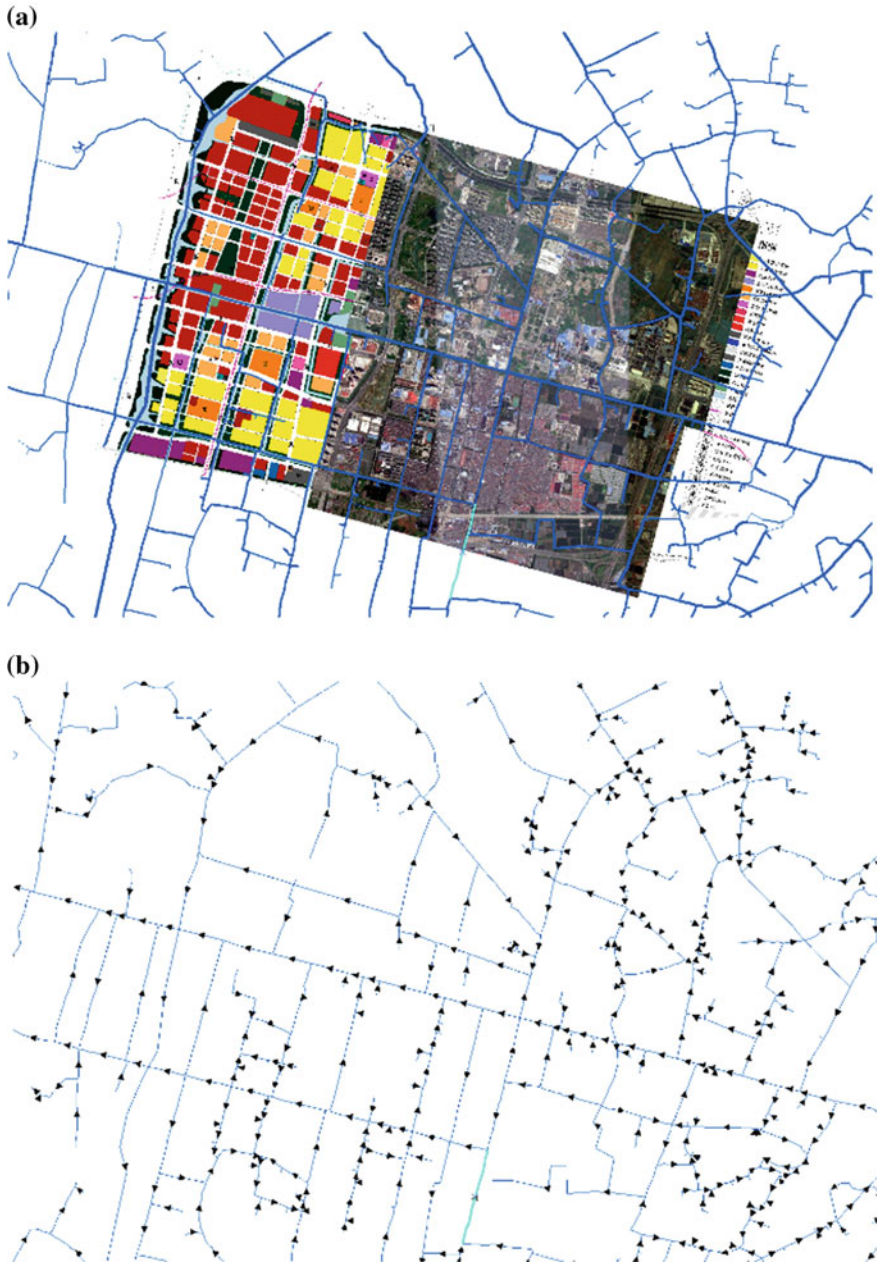


Fig. 4 a Detail of Ningbo East City development area within canal network. b Flow direction for (a) based on ArcGIS geometric network capability

are categorised by their function (hydrology, hydraulic and water quality). The most globally recognised and frequently utilised runoff models for urban areas include the rational method, SCS or curve number method (TR55), a range of models developed by the US Department of Agriculture (USDA) (TR-20; TR-55), and the US Army Corps of Engineers developed HEC-1 and HEC-HMS.

Many modelling platforms utilise the US Environmental Protection Agency's Surface Water Management Model (SWMM) for simulation of runoff, routing and network hydraulics (EPA SWMM; PCSWMM; InfoSWMM; xpSWMM). As a dynamic rainfall-routing model, it can be used for both event-based and continuous runoff simulation. SWMM also accounts for a range of hydrologic processes that produce runoff and will route both overland flow, pipe flows and channel flows. Larger modelling suites often used for urban water modelling include Infoworks, MIKE URBAN and the Soil Water Assessment Tool (SWAT).

Shrivastava [44] suggests that whilst all urban hydrological models can be described in terms of their spatial (lumped or distributed) and temporal (event-based or continuous) predictive capacity, no model currently exists that can meet all these needs. Currently, even models adjudged to be the most robust in the field have scope for improvement in terms of representation of runoff generation processes, ground-water interaction, integration of hydrological and ecological parameterisation, and calibration and validation of sub-catchment scale processes.

Joyce et al. [18] propose the use of a multi-scale modelling approach to gain a more robust assessment of drainage infrastructure and hydrological response. Whilst such an approach would require the use of a range of scale-dependent informatics to support hydrological modelling at different scales, it would be better able to account for locally scaled watershed response, to a larger range of climatic impacts.

2.3 Representing Climate Change

The International Climate Change Committee Report—Fifth Assessment Report (AR5) [2] indicates a worldwide increase in the frequency of extreme rainfall events as a result of global warming. Significant changes in annual rainfall totals and temperature variation are also expected [38]. Recent improvements in modelling capability and accuracy have led to improved assessment of climate-related hazards such as wildfire, drought, water security, flooding and water quality.

In spite of advances in our understanding of the implications of climate change for the design and operation of urban infrastructure, uncertainty related to interpretation of local-scale impacts remain. Spatial and temporal scales of interest for urban hydrology, for example, are most often described in metres or kilometres and minutes or hours, respectively [10, 41, 49]. Data from global climate models, therefore, require downscaling from regional climate models to higher spatial and temporal resolution climate change projections. A number of approaches can be used to interpret regional-scale climate models at the city-scale.

Table 2 Frequently used models in urban flood hydrology

Method/Model	Hydrologic model	Hydraulic model	Water quality model	Public domain	Link to further information
Rational				Yes	http://www.lmnoeng.com/Hydrology/rational.php
TR-55				Yes	http://www.epesc.org/reference/tr55.pdf
HEC-1	X			Yes	
HEC-HMS	X			Yes	http://www.hec.usace.army.mil/software/hec-hms/
WinTR-20	X			Yes	http://www.nrcs.usda.gov/wps/portal/3
WinTR-55	X			Yes	http://www.nrcs.usda.gov/
HydroCAD	X			No	http://www.hydrocad.net/
HEC-2		X		Yes	
WSPRO		X		Yes	http://ntl.bts.gov/lib/22000/22000/22020/wsproman
CulvertMaster		X		No	http://www.bentley.com/en-US/Products/CulvertMaster/
FlowMaster		X		No	http://www.bentley.com/en-US/Products/FlowMaster/
HY8		X			www.fhwa.dot.gov/engineering/hydraulics/software/hy8/
Hydro Toolbox		X			www.fhwa.dot.gov/engineering/hydraulics/software/
WinSLAMM			X	No	http://winslamm.com/
BASINS			X	Yes	http://water.epa.gov/scitech/datait/models/basins/
WASP			X	Yes	http://www.epa.gov/athens/wqqtsc/html/wasp.html
WMM			X		http://rougeriver.com/proddata/wmm.html
SHSAM			X	No	https://www.barr.com/services/269/

(continued)

Table 2 (continued)

Method/Model	Hydrologic model	Hydraulic model	Water quality model	Public domain	Link to further information
SMS			X		www.aquaveo.com/software/sms-riverine-modeling
HEC-RAS		X	X	Yes	http://www.hec.usace.army.mil/software/hec-ras/
PondPack	X	X		No	http://www.bentley.com/en-US/Products/PondPack/
MIKE 11	X	X			http://www.mikebydhi.com/Products/WaterResources/
CivilStorm	X	X		No	http://www.bentley.com/en-US/Products/CivilStorm/
MODRET	X	X			http://www.scisoftware.com/products/
Infoworks ICM	X	X	X	No	http://www.innovyze.com/products/infoworks_icm/
EPA SWMM	X	X	X	Yes	http://www.epa.gov/nrmrl/wswrd/wq/models/swmm/
PCSWMM	X	X	X	No	http://www.chiwater.com/Software/PCSWMM/
InfoSWMM	X	X	X	No	http://www.innovyze.com/products/infoswmm/
xpswmm	X	X	X	No	http://www.xpsolutions.com/software/xpswmm/
MIKE URBAN	X	X	X	No	http://www.mikebydhi.com/Products/Cities/
WinHSPF	X	X	X	Yes	http://www.aquaterra.com/resources/hspfsupport/
SWAT	X	X	X	Yes	http://swat.tamu.edu/
WARMF	X	X	X		http://www.epa.gov/athens/wwqts/html/warmf.html

Research into downscaling climate models for urban areas has developed over several decades, originally to account for lack of suitable precipitation data for drainage design [33]. The challenge of trying to represent the impact of global change on local hydrological systems has been discussed more fully by Arnbjerg-Nielsen [4] and Willems et al. [49]. Even recently, however, Arnbjerg-Nielsen et al. [3] concluded that describing precipitation patterns under changing climate for use in the design and operation of urban drainage infrastructure remains problematic. Olsson et al. (2016) suggest that climate impact assessment has been developed with a primary focus on applicability to a medium-sized rural basin. However, impact assessment is to increase the degree performed at scales smaller or larger than such basins. The co-optimisation of this aim with objectives of resilience, flexibility, robustness and rapid response will therefore become ever more important to safeguard habitable cities into the future.

The use of Global Circulation Model (GCM) data for urban hydrological modelling is hindered, however, by uncertainty within downscaling model estimates to spatial resolutions used by local-scale models. The extent of the uncertainty introduced will depend on the location being modelled, and the GCM data and downscaling methods used. Representation of potential changes to rainfall extremes is particularly difficult as they may not be represented in average annual changes predicted by the GCM. Similarly, precipitation extremes occur in durations less than 24 h meaning that interpreting future change requires temporal downscaling from climate change model.

3 Sustainable Approaches to Urban Water Management

Sustainable Urban Drainage Systems (SUDS) aim to reduce rates of stormwater runoff by limiting imperviousness and employing green technologies, while also promoting water capture and reuse [24]. The approach also provides a range of ecosystem service benefits, including water quality treatment, groundwater recharge and flood resilience [21, 26, 50]. Recent years have seen a marked increase in ‘Blue-Green’ approaches to urban water management [11, 25, 46], which has influenced the development of urban water network representation and subsequent mathematical modelling (e.g. Infoworks, SWMM, MIKE URBAN, XPS).

It can be argued that the development of urban hydrological models has facilitated the development of a more integrated approach to surface water management in cities. Indeed, SUDS and similar conceptual approaches [e.g. Water Sensitive Urban Design (WSUD) and Low Impact Development (LID)] are increasingly being adopted specifically to reduce the hydrological impacts of urbanisation. Typical measures that ideally can be represented within stormwater models include green roofs, bio-retention systems, permeable pavements, swales, infiltration ponds, etc. [24]. This is consistent with the needs of planners and developers who increasingly require reliable simulation of potential community and ecosystem service benefits, such as water quality treatment, groundwater recharge and flood resilience [21, 26, 50–52].

The concept of sustainable urban water management aims to reduce peak stormwater runoff in urban areas and improves the water quality of stormwater released to natural water courses. Additional environmental and community benefits of this approach are described by Wong [51] and Woods Ballard et al. [52]. Whilst there is growing evidence to support the effectiveness of SUDS, WSUD and LID [23, 34] and the efficiency of related infrastructure [1], its wide-scale adoption is not universal due to a lack of information about the long-term cost–benefits of such systems [36].

The identification of internationally accepted performance criteria or best practice guidelines will be critically important therefore to the long-term adoption of more sustainable approaches to surface water management. Such guidance already exists, including that by the Construction Industry Research and Information Association (CIRIA) in the UK [52], various state-level guidance documents by the Environmental Protection Agency in the USA (for example [39]) and national government Sponge City Construction Guidelines in China [7].

Most attempts to accurately measure the performance and overall impact on water quantity and quality of SUDS occur at the micro-scale and in the near-downstream area of the developed area. Golden and Hoghooghi [14] suggest that whilst such studies are useful, assessment of the overall impact of SUDS at the catchment scale should also be sought. Similarly, Trinh and Chui [47] highlight the fact that our current understanding of urban hydrological impacts is too focused on peak flow prediction or storm recession times, to the detriment of other hydrological aspects.

There is adequate evidence to support the effectiveness of this approach [23, 34] and the efficiency of related infrastructure [1], but its wide-scale adoption is still not standard beyond the site scale, and the reliance on traditional ‘grey’ infrastructure design continues. This is due to the convoluted nature of urban planning process [12] and the lack of a standardised approach to quantifying long-term cost–benefits of stormwater infrastructure [36].

3.1 Case Study—New Zealand

To assess the extent to which the SUDS approach may be adopted in the future, it is useful to look at the case of New Zealand where such measure has been used for over 10 years and is currently attracting increasing attention with respect to levels of service, legislation compliance and stakeholder expectation [22]. Recent flood and water quality incidents in the country have also pushed these issues further into the public spotlight (Christchurch flooding in 2014 and 2017; and Auckland flooding in 2017). Expected changes in climatic patterns across New Zealand also suggest that extreme events will become more common in future and should be considered in more detail in the planning and development of urban environments in the future. Whilst some regional and city councils have started to consider possible implications of climate change (e.g. [5]), there is still a need to describe replicable approaches to assess the impact of the most recent regional climate change projections

[29, 45]; consider available mitigation options; and thus recommend appropriate water management responses to reduce risk and improve resilience.

Several national and regional policy documents [22, 31, 32] already promote the use of WSUD as a way of combatting increased pressure on urban drainage systems and a way to improve the hydraulic and water quality characteristics of urban streams. Internationally, WSUD has also begun to gain traction as a mechanism for climate change adaptation [42], providing higher amenity value by ‘greening’ urban environments [8].

However, the wider uptake of WSUD in NZ is hindered by a range of barriers [29]. These include high capital cost, high maintenance requirements and inadequate assessments of long-term benefits [40], and uncertainty over costs relative to conventional infrastructure provision [16]. This information gap, along with a lack of clear national guidelines, represents a significant inertia against wider adoption [35, 48]. In this respect, there is much need for evidence to inform the wider adoption of WSUD in New Zealand cities where appropriate.

Commitment to mitigation measures requires capital expenditure and confidence that such measures will be effective under future conditions. Whilst there are examples of the use of cost–benefits analysis methods in urban water management and planning, the approach is still underutilised in New Zealand. For this purpose, reliable life cycle costing methods are needed to estimate the relative costs of WSUD compared to a conventional infrastructure approaches when adapting to projected climate change. Some work in this field has been conducted by Ira [17], which provides at least a foundation for urban developers and planners to develop new methods for evaluation of different climate change adaptation strategies.

The generation of location-specific flow estimates that account for the future climate change is needed to improve flood mapping in urban areas and to inform flood risk assessments for specified design events. Similarly, summary flow statistics can be used to better inform future of water supply, wastewater and transport infrastructure planning. Inter-disciplinary collaboration is needed to develop and apply new approaches that guide stormwater management to deliver more resilient and sustainable outcomes with greater cost-effectiveness. This in turn will aid wider environmental, social and cultural benefits that contribute to better urban livability within New Zealand.

4 Conclusion

It is generally held that urban areas have a lower capacity to adapt to climate change than natural environments, but that they can be managed to perform better [28]. Future challenges imposed by rapid urbanisation and climate change mean that urban planners and developers will need to consider more sustainable ways of managing water and related environmental services [20]. The development of cost-efficient and hi-tech water management models and monitoring systems will go some way to making this possible [19], but hydrologists should also take responsibility for

increasing implementation of such systems, and the continued development of related best practice.

In response to increasing urbanisation, many city governments around the world are legislating for stormwater infrastructure that integrates infiltration, storage and conveyance systems to achieve higher overall system performance, and ability to better meet multiple design objectives [37]. As suggested by Makropoulos [27], however, this strategy needs to be supported by a step change in conceptual representation and understanding of the technical and social components of the environmental systems concerned.

Hydrology will be increasingly important to the design and functioning of new urban development areas. Designing (or retrofitting) local urban drainage networks will continue to be challenging as larger surface water networks are managed at the city-scale. Indeed, only a modelling approach that considers plot-scale hydrology within the context of the dynamics of the larger drainage system will be useful in development and design of appropriate drainage systems.

While there is widespread capability in the engineering community to apply commercially available hydrological and hydraulic models for drainage design and flood studies, the process and results of flood modelling often lack transparency. Ideally, government agencies, engineers, developers and planners would refer to a common template that can be used to improve resilience of drainage designs to future risk. Such a template would improve on agency-specific guidance using common assessment methods to measure the benefits of water management investment strategies.

The use of GIS-based mapping and analysis techniques allows urban drainage networks to be topologically represented, so that information relating to upstream or downstream channel sections (such as the length between two points) can be determined relatively easily. However, such systems have limited ways to represent dynamic properties of networks (such as changes in flow direction). This means that for dual direction flow systems (such as tidally influenced networks), accurate representation of flow direction and magnitudes increasingly requires bespoke software.

Finally, climate change will continue to drive changes in urban drainage paradigms which will result in the implementation of more practical and sustainable drainage solutions. Indeed, the design and optimization of urban drainage infrastructure for climate change impacts will likely ensure our cities remain habitable well into the future.

References

1. Akhter MS, Hewa GA (2016) The use of PCSWMM for assessing the impacts of land use changes on hydrological responses and performance of WSUD in managing the impacts at Myponga catchment, South Australia. *Water* 8(11):511
2. Allen MR, Barros VR, Broome J, Cramer W, Christ R, Church JA, Clarke L, Dahe Q, Dasgupta P, Dubash NK, Edenhofer O (2014) IPCC fifth assessment synthesis report-climate change 2014 synthesis report

3. Arnbjerg-Nielsen K, Willems P, Olsson J, Beecham S, Pathirana A, Gregersen IB, Madsen H, Nguyen VT (2013) Impacts of climate change on rainfall extremes and urban drainage systems: a review. *Water Sci Technol* 68(1):16–28
4. Arnbjerg-Nielsen K (2008) Quantification of climate change impacts on extreme precipitation used for design of sewer systems. In: *Proceedings of the 11th international conference on urban drainage*, vol 31
5. Auckland Council (2014) *Natural hazard risk communication toolbox*. Auckland Council
6. Cembrano G, Quevedo J, Salamero M, Puig V, Figueras J, Martí J (2004) Optimal control of urban drainage systems. A case study. *Control Eng Pract* 12(1):1–9
7. Chan FKS, Griffiths JA, Higgitt D, Xu S, Zhu F, ang Y-T, Xu Y, Thorne CR (2018) “Sponge City” in China—A breakthrough of planning and flood risk management in the urban context. *Land Use Policy* 76:772–778
8. City of Copenhagen (2012) *Cloudburst Management Plan 2012*. http://en.klimatilpasning.dk/media/665626/cph_-_cloudburst_management_plan.pdf
9. Coutu S, Del Giudice D, Rossi L, Barry DA (2012) Parsimonious hydrological modeling of urban sewer and river catchments. *J Hydrol* 464:477–484
10. Einfalt T, Arnbjerg-Nielsen K, Golz C, Jensen NE, Quirnbach M, Vaes G, Vieux B (2004) Towards a roadmap for use of radar rainfall data in urban drainage. *J Hydrol* 299(3–4):186–202
11. Everett G, Lamond J, Lawson E (2015) *Green infrastructure and urban water management*. In: *Handbook on green infrastructure: planning, design and implementation*. Edward Elgar, Gloucester, pp 50–66
12. Furlong C, De Silva S, Guthrie L, Considine R (2016) Developing a water infrastructure planning framework for the complex modern planning environment. *Util Policy* 38:1–10
13. Gill SE, Handley JF, Ennos AR, Pauleit S (2007) Adapting cities for climate change: the role of the green infrastructure. *Built Environ* 33(1):115–133
14. Golden HE, Hoghooghi N (2018) Green Infrastructure and its catchment-scale effects: an emerging science. *WIREs. Water* 5:e1254. <https://doi.org/10.1002/wat2.1254>
15. Griffiths JA, Zhu FF, Chan FKS, Higgitt DL (2018) Modelling the impact of sea-level rise on urban flood probability in SE China. *Geosci Front*
16. Ira SJT (2011) *The development of a catchment scale life cycle costing method for stormwater management*. Cawthorne Institute, Report No. 2082
17. Ira SJT, Batstone CJ, Moores JP (2015) Does water sensitive design deliver beneficial net economic outcomes? In: *Asia Pacific stormwater conference*
18. Joyce J, Chang NB, Harji R, Ruppert T, Imen S (2017) Developing a multi-scale modeling system for resilience assessment of green-grey drainage infrastructures under climate change and sea level rise impact. *Environ Model Softw* 90:1–26
19. Kerkez B, Gruden C, Lewis M, Montestruque L, Quigley M, Wong B, Bedig A, Kertesz R, Braun T, Cadwalader O, Poresky A (2016) *Smarter stormwater systems*
20. Kılıç Ş (2017) A nearly net-zero exergy district as a model for smarter energy systems in the context of urban metabolism. *J Sustain Dev Energy Water Environ Syst* 5(1):101–126
21. Lamond J, Rose C, Booth C (2015) Evidence for improved urban flood resilience by sustainable drainage retrofit. *Proc ICE Urban Des Plan* 168(2):101–111. ISSN 1755-0793
22. *Land and Water Forum (LAWF)* (2015) *Fourth report of the land and water forum*
23. Lawson E, Thorne C, Wright N, Fenner R, Arthur S, Lamond J, Kilsby C, Mant J, Smith L, Ahilan S, Allen D (2015) *Evaluating the multiple benefits of a Blue-Green vision for urban surface water management*. In: *UDG autumn conference and exhibition 2015*. Leeds
24. Lewis M, James J, Shaver E, Blackbourn S, Leahy A, Seyb R, Simcock R, Wihongi P, Sides E, Coste C (2015) *Water sensitive design for stormwater*. Auckland Council Guideline Document GD2015/004. Prepared by Boffa Miskell for Auckland Council
25. Liao KH, Deng S, Tan PY (2017) *Blue-Green infrastructure: new frontier for sustainable urban stormwater management*. In: *Greening cities*. Springer, Singapore, pp 203–226
26. Loperfido J, Noe G, Taylor Jarnagin S, Hogan D (2014) Effects of distributed and centralized stormwater best management practices and land cover on urban stream hydrology at the catchment scale. *J Hydrol* 519:2584–2595

27. Makropoulos (2017) Thinking platforms for smarter urban water systems: fusing technical and socio-economic models and tools. In: Riddick AT, Kessler H, Giles JRA (eds) *Integrated environmental modelling to solve real world problems: methods, vision and challenges*, vol 408. Special Publications, Geological Society, London, pp 201–219
28. Miller JD, Hutchins M (2017) The impacts of urbanisation and climate change on urban flooding and urban water quality: a review of the evidence concerning the United Kingdom. *J Hydrol Reg Stud* 12:345–362
29. Ministry for the Environment (MFE) (2016) *Climate change projections for New Zealand: atmosphere projections based on simulations from the IPCC fifth assessment*. Ministry for the Environment, Wellington
30. NOAA (2016) *The coastal population explosion*. http://oceanservice.noaa.gov/websites/retiredsites/natdia_pdf/3hinrichsen.pdf
31. New Zealand Government Association (2014) *National policy statement on freshwater management*, National policy statement issued by notice in gazette on 4 July 2014
32. New Zealand Government Association (2015) *The thirty year national infrastructure plan*, New Zealand government
33. Niemczynowicz J, Sevruk B (1991) Urban rainfall and meteorology. *Atmos Res* 27(1–3):215
34. Ossa-Moreno J, Smith KM, Mijic A (2017) Economic analysis of wider benefits to facilitate SuDS uptake in London, UK. *Sustain Cities Soc* 28:411–419
35. O'Donnell EC, Lamond JE, Thorne CR (2017) Recognising barriers to implementation of Blue-Green Infrastructure: a newcastle case study. *Urban Water J* 1–11
36. O'Neill A, Gooding K, Wright A, Hoban A (2015) Water sensitive urban design on the line. In: *9th international water sensitive urban design (WSUD 2015)*, p 383
37. Porse EC (2013) Stormwater governance and future cities. *Water* 5(1):29–52
38. Reisinger A, Kitching RL, Chiew F, Hughes L, Newton PCD, Schuster S, Tait A, Whetton P (2014) *Australasia climate change 2014: impacts, adaptation and vulnerability*. Part B: regional aspects. In: Barros VR et al (eds) *Contribution of working group II to the fifth assessment report of the intergovernmental panel on climate change*. Cambridge University Press Cambridge, UK and New York, USA, pp 1371–1438
39. Rossman LA, Bernagros JT (2018) *National stormwater calculator user's guide—Version 1.2.0.1*. Office of Research and Development, USEPA, Ohio, USA
40. Roy AH, Wenger SJ, Fletcher TD, Walsh CJ, Ladson AR, Shuster WD, Thurston HW, Brown RR (2008) Impediments and solutions to sustainable, watershed-scale urban stormwater management: lessons from Australia and the United States. *Environ Manag* 42(2):344–359
41. Schilling W (1991) Rainfall data for urban hydrology: what do we need? *Atmos Res* 27(1–3):5–21
42. Semadeni-Davies A, Hernebring C, Svensson G, Gustafsson L-G (2008) The impacts of climate change and urbanisation on drainage in Helsingborg, Sweden: combined sewer system. *J Hydrol* 350:114–125
43. Seneviratne SI, Nicholls N, Easterling D (2012) Changes in climate extremes and their impacts on the natural physical environment. In: Field CB, Barros V, Stocker TF et al (eds) *Managing the risks of extreme events and disasters to advance climate change adaptation*. A special report of working groups I and II of the intergovernmental panel on climate change. Cambridge University Press, Cambridge, UK and New York, pp 109–230 (IPCC SREX Report)
44. Shrivastava P (2016) Urban water hydrological modelling. *Int J Latest Trends Eng Technol* 7:2
45. Stocker TF et al (2013) Technical summary. In: Stocker TF, Qin D, Plattner G-K, Tignor M, Allen SK, Boschung J, Nauels A, Xia Y, Bex V, Midgley PM (eds) *Climate change 2013: the physical science basis*. Contribution of working group I to the fifth assessment report of the intergovernmental panel on climate change. Cambridge University Press, Cambridge, United Kingdom and New York, USA
46. Thorne CR, Lawson EC, Ozawa C, Hamlin SL, Smith LA (2018) Overcoming uncertainty and barriers to adoption of Blue-Green Infrastructure for urban flood risk management. *J Flood Risk Manag* 11:S960–S972

47. Trinh DH, Chui TFM (2013) Assessing the hydrologic restoration of an urbanized area via an integrated distributed hydrological model. *Hydrol Earth Syst Sci* 17(12):4789–4801
48. White I, Howe J (2005) Unpacking the barriers to sustainable urban drainage use. *J Environ Plan Policy* 7(1):25–41
49. Willems P, Arnbjerg-Nielsen K, Olsson J, Nguyen VTV (2012) Climate change impact assessment on urban rainfall extremes and urban drainage: methods and shortcomings. *Atmos Res* 103:106–118
50. Winston R, Page J, Hunt W (2013) Catchment scale hydrologic and water quality impacts of residential stormwater street retrofits in Wilmington, North Carolina. In: *Green streets, highways, and development 2013*, pp 159-172. <https://doi.org/10.1061/9780784413197.014>
51. Wong (2006) An overview of water sensitive urban design practices in Australia. *Water Prac Technol* 1(1)
52. Woods Ballard B, Wilson S, Udale-Clarke H, Illman S, Scott T, Ashley R, Kellagher R (2015) *The SuDS manual*. CIRIA, London

Uncertainty in Calibration of Variable Infiltration Capacity Model



Ankita Pradhan and J. Indu

1 Introduction

Hydrological models are mathematical representations for understanding the hydrological processes such as, precipitation, evapotranspiration, infiltration, interception, snowmelt, surface flow, subsurface flow as well as the interaction between them in a simplified form. Hydrological modelling involves highly nonlinear processes, complex interactions and high spatial variability's at basin scale. The fundamental objective of hydrological modelling is to gain an understanding of the hydrological system in order to provide reliable information for managing water resources in a sustained manner. Over the history of model development, hydrological models have been adopted, modified and applied to solve a wide spectrum of hydrological problems [6, 28, 64]. Initiating from the mid of nineteenth century, the evolution of hydrological modelling is continuing with the development of understanding the physical processes, computational efforts and data retrieving facilities.

Coupled models of land surface and subsurface, which incorporate hydrologic components into Land Surface models (LSMs), may yield improvements in weather and short-term climate forecasting and flood/drought forecasting. LSMs have evolved from the original bucket model of Manabe et al. [48] which is the first generation of land surface models. The bucket model allows the water level in a soil moisture reservoir to increase during precipitation events and to decrease as the water evaporates. Here, the efficiency of evaporation varies with the water level in reservoir. As a result, rainy periods would lead to high evaporation rates and droughts would in turn lead to low rates. In the bucket model, runoff is non-existent until the precipitation reaches the maximum value, i.e. the field capacity. These resulted in limitations involving:

A. Pradhan · J. Indu (✉)

Department of Civil Engineering, Indian Institute of Technology, Bombay, India
e-mail: indusj@civil.iitb.ac.in

A. Pradhan

e-mail: pradhanankita60@gmail.com

© Springer Nature Switzerland AG 2019

S. K. Singh and C. T. Dhanya (eds.), *Hydrology in a Changing World*, Springer Water, https://doi.org/10.1007/978-3-030-02197-9_4

of the first-generation land surface models, i.e. the bucket model were: no explicit representation of vegetation, no heat conduction into soil and water holding capacity and the last being prescribed threshold for precipitation to runoff [48]. The Project for Intercomparison of Land surface Parameterisation Schemes (PILPS) showed that the bucket model was inadequate for diurnal to multi-annual scale surface hydrology representation.

The second-generation land surface models were introduced by Sellers et al. [53] and Dickinson et al. [21] in the mid-1980s with the Simple Biosphere Model (SiB) and Biosphere-atmosphere transfer scheme (BATS) model respectively. The major improvements of the second-generation land surface models were soil moisture and temperature in two layers [19], vegetation as a single-bulk layer, interaction of land surface with atmosphere, separate treatment of vegetation and soil (e.g. different albedo), explicit representation of visible (VIS) and Near Infrared (NIR) waveband (plants absorb most energy in VIS but reflect more in NIR), integration of satellite data (e.g. albedo), include the impact of vegetation and representation of evaporation from trees (stomatal conductance), inclusion of canopy interception of precipitation, runoff parameterization (varies according to models) and inclusion of multilayer snow schemes. The PILPS showed that the second-generation models outperformed the first-generation models.

The third-generation models incorporated include the physics of photosynthesis with a motive that plants and trees would open their stomata to maximize the carbon intake while minimizing water loss. The inclusion of physics of photosynthesis would be an accurate representation of realistic transpiration rates. The major improvements in the third-generation land surface models were physically based parameterization of stomatal conductance, inclusion of leaf photosynthesis, allocate carbon to simulate plant growth, inclusion of soil carbon and simulation of land surface in carbon cycle.

In these models, uniform soil moisture condition is assumed spanning over thousands of square kilometres. The processes that control movement of soil moisture and runoff production are three-dimensional in nature and are not controlled only in the vertical direction. For example, when rain falls in a saturated seepage face in a hill slope is spreading over a length of ten meters, water does not infiltrate the soil rather it runs off directly. The surface runoff over sub-saturated soil resulting from high precipitation intensities vary with space. On the other hand, rainwater falling on the top of the hill can infiltrate the soil. Thus, it becomes very difficult to separate these regimes explicitly only with a set of vertical layers. Hence, it becomes a necessity for a modeller to enforce parameterizations that can impart the sub-grid behaviour to average soil moisture contents in the different layers. The amount of precipitation that is converted to runoff can be found accurately by the spatial variation of soil moisture and not by averaging across a large area. These limitations in the third-generation models led to improve the land surface models with sub-grid variability that would produce realistic runoff rates. Liang et al. [43] came up with the Variable Infiltration Capacity (VIC) model to grip up with the problem. The model explicitly represents the spatial variation of infiltration capacity.

The VIC model was first stated by Stamm et al. [58] as an inclusion in Geophysical Fluid Dynamics Laboratory GCM. The authors wanted to characterize the land

surface hydrological processes and include it to global climate to determine its sensitivity. VIC model was initially designed to imitate the variation of moisture in soil within a grid. Initially the VIC model had one layer of soil with base flow consideration. The VIC model simulation was carried out in four different soil moisture scenarios. The first simulation was done with fixed global soil moisture of 15 cm which showed lower global average soil moisture. The second used a more realistic approach as they provided varying soil moisture capacity around the globe. The other two simulations were done considering global fixed soil moisture of 5 cm and 15 cm respectively. But the results were found to be unsatisfactory as it was found that evaporation over northern Eurasia and North America was unaffected by the soil moisture, due to the dry period drainage to base flow. Thus, realizing the need of more realistic hydrological model Liang et al. [43] improved the model by implementing two soil layers. They developed the model with a more realistic evaporation process in the form of three components of evapotranspiration: canopy evaporation, evaporation from bare soils and transpiration. In addition, the model was able to include the sub-grid spatial variability of land cover with their respective roots fraction. In spite of this, the two-layer VIC model was unable to imitate the evaporation as compared to the latent heat because of lower moisture in the upper soil layer in certain basin. Although such basins showed an appreciable simulation of total soil water content, soil moisture in the upper 0.5 m was found to be underestimated. This made the authors realize the need to improve the soil moisture transport capacity of the model. Hence, Liang et al. [42, 44] added 0.1 m top soil thus giving rise to a new three-layer VIC model. The specialities of the three-layer model were the variability of fractional coverage of vegetation and leaf area index at each time step. The authors found that root distribution was more sensitive to evapotranspiration and soil moisture rather than depth of soils.

Scientists were interested in coupling hydrological and atmospheric models through the use of Land Surface Parameterization schemes. But no research was carried out to analyse the reliability of LSP schemes. This made Lohmann et al. [46] to develop a horizontal routing model that could be coupled to land surface parameterisation schemes. They estimated the runoff by routing streams along a channel and then comparing it with measured stream flow data. The application of these routing models was done by Lohmann et al. [47] to predict the stream flow in Waser River Catchment of Germany. The routing model performed good in the prediction of daily, monthly and annual stream flow in the river catchment. The authors also highlighted the significance of infiltration parameter, soil thickness and base flow recession curve over runoff volume generated by the VIC model.

Abdulla and Lettenmaier [1] applied the VIC hydrological model to estimate the water balance of the Arkansa-Red River basin. The model derived stream flow and evapotranspiration were compared with observations from observed discharge and evapotranspiration derived from an atmospheric budget of the Arkansas-Red basin. [2, 3] framed a methodology for developing regional parameter estimation equations for the VIC hydrological model by using a set of 34 unregulated catchments distributed throughout the Arkansas-Red River basin of the south central U.S. Zhou et al. [73] assessed the VIC-3L hydrological model for the Baohe river basin to see

the importance of remote sensing data. They simulated the water fluxes using the VIC-3L model by taking land cover properties from the resource and environment database of China (REDC) and from the moderate resolution imaging spectroradiometer (MODIS) data and compared with the daily observed stream flow at the outlet of the river basin. Adam [4, 5] used the VIC hydrological model to understand the causes of stream flow changes in the Eurasian Arctic region in two studies. First, using a physically based reservoir model coupled to VIC model and second, by applying only VIC model. Liang et al. [41] investigated the impacts of spatially distributed precipitation and soil heterogeneity on modelling water fluxes at different spatial resolutions at the Blue water watershed in Oklahoma. The authors suggested that a critical spatial resolution for the VIC-3L model may exist for the study watershed. For spatial resolutions finer than the critical resolution, one does not necessarily obtain better model performance in terms of runoff, evapotranspiration, and soil moisture with increasing spatial resolution if the VIC-3L model parameters are calibrated at each special resolution. Guo et al. [31] explored the impacts of different precipitation data sources (radar and rain-gauge) on water budgets simulated by the VIC-3L land surface model over the watershed of the Illinois River at Watts, Oklahoma. Hurkmans et al. [35] investigated the effect of projected land use changes scenarios on river discharge in the Rhine basin which was expected to shift from a combined snowmelt-rainfall regime to a more rainfall-dominated regime because of the change of climate. Lakshmi and Wood [40] evaluated the variation of evaporation in time and space by simulating the fluxes using the VIC model for the King's Creek catchment in Manhattan. They found that the model computed fluxes match fairly well with the observed fluxes. Matheussen et al. [49] examined the effect of land cover change on stream flow in the Interior Columbia River basin using two land cover scenarios using the variable infiltration capacity hydrological model. The first land cover being the historical land covers vegetation and second as estimated from remote sensing data. Su and Xie [59] assessed the effects of climate change on runoff in entire China using the variable infiltration capacity surface parameterization scheme. The VIC land surface model contains physically conceptualized parameters that require calibration for optimal model performance. Troy et al. [63] framed an efficient calibration method for continental-scale land surface modelling. They examined the effect of model spatial and temporal resolutions on calibrated parameter sets to assess whether one could calibrate at coarser resolutions and apply these parameter sets to finer resolutions, thus reducing the computational time. Yuan et al. [71] applied the variable infiltration capacity land surface model to simulate stream flow using remote sensing data for the Hanjiang River basin in China. Slater et al. [56] compared the performance of five land surface models (Chameleon Surface Model (CHASM) Noah, Community Land Model (CLM), Variable Infiltration capacity Model (VIC), European Centre for Medium-Range Weather Forecasts (ECMWF)), in the simulation of hydrological processes across the terrestrial Arctic drainage system for the period 1980–2001. Hillard et al. [33] assessed the snowmelt dynamics with NASA scatterometer (NSCAT) data using the VIC hydrological model for the upper Mississippi River basin of the north central U.S. Gao et al. [29] focussed on generating observation operators for assimilating soil moisture into land surface models using

a number of satellite-model combinations. The authors employed a bivariate statistical approach based on copula distributions for representing the joint distribution between retrieved and modelled soil moisture, allowing for a quantitative estimation of the uncertainty in modelled soil moisture when merged with satellite retrieval. The remote sensing soil moisture products used is from Tropical Rainfall Measuring Mission (TRMM) Microwave Imager (TMI) and the NASA/Earth Observing System (EOS) Advanced Microwave Scanning Radiometer (AMSR-E). The soil moisture model predictions are from the VIC hydrological model; the 40-yr European Centre for Medium-Range Weather Forecasts (ECMWF) Re-Analysis (ERA-40); and the NCEP North American Regional Reanalysis (NARR). Huang et al. [34] framed a methodology for transferring model parameters for the VIC land surface scheme from data-rich areas to data-sparse areas. The authors came up with two essential steps for the successful transferring of model parameters. The first is to effectively classify the basic available data into clusters and the second is establishing nonlinear relationships between classified basic available data and the model parameters.

Some of the other hydrological models are Soil and Water Assessment Tool (SWAT) model, MIKE SHE model, TOPMODEL, Hydrologiska Byrans Vattenavdelning (HBV) model etc.

The SWAT model is a complex physically based model developed to quantify the impact of land management practices in large watersheds. The model is adequate in performing long-term simulations. The model uses a two-level disaggregation scheme; first dividing the entire Watershed into sub-watersheds and the second dividing the sub-watersheds into hydrologic response units (HRU), i.e. vegetation, land use and soil characteristics. The basic input into the model is the daily precipitation data, maximum and minimum air temperature, wind speed, relative air humidity and solar radiation. This model is capable enough to describe vegetation growth, water and sediment circulation and nutrients circulation. The MIKE SHE model is a physically based model taking into account different processes of hydrological cycle such as precipitation, evapotranspiration, interception, saturated and unsaturated groundwater flow, etc. The model is efficient enough to simulate surface and ground water movement and their interactions. It can also simulate sediment and nutrient transport and other water quality problems for large watersheds. TOPMODEL is a rainfall-runoff model that makes use of topographic information to relate it to runoff generation. The model can be used in single or multiple catchments using the catchment gridded elevation data. The model predicts the hydrological behaviour of the catchment. Catchment topography and soil transmissivity are the major factors considered by the model. The main aim of the model is to compute the water table depth and storage deficit at any location. The HBV model is a semi-distributed conceptual model. The model divides the entire catchment into sub-catchments, which are further divided into different vegetation and elevation zones. The model simulates on daily and monthly rainfall data, air temperature and evaporation.

In spite of the significant developments in hydrologic modelling, addressing the uncertainty associated with hydrological predictions remains a critical and challenging one. In order to address hydrological modelling uncertainty, one needs to understand, quantify and reduce the uncertainty involved in a systematic manner. It is now

being recognized that proper consideration of uncertainty in hydrologic predictions is essential for the purpose of both research and operational modelling [69]. The value of a hydrologic prediction to water resources and other relevant decision-making process is limited if reasonable estimates of the corresponding predictive uncertainty are not provided [30]. In general, hydrological modelling gets affected by three sources of uncertainties: (1) input uncertainty: like measurement errors in precipitation estimates, identifying proper land use/land cover, etc.; (2) model or structural uncertainty: originating from representation of hydrological processes in the models; (3) parametric uncertainty: model parameter approximations or calibration uncertainties.

Hydrological simulations depend critically on the input forcing datasets, specifically on precipitation [50, 62]. The input precipitation forcing regulates the amount of modelled precipitation that affects the simulation of runoff. The model results therefore rely heavily on the quality of these forcing as the uncertainty (measurement errors, etc.) in such data will propagate through all hydrological processes during simulations (Wagner and Gupta [7, 60, 69]. Some of the studies focus solely on forcing uncertainties rather than parametric and structural studies [9, 10, 12, 14–18, 24, 30, 36, 38, 39, 45, 52, 55, 57, 65–66]. In case of complex terrain forcing uncertainty is enhanced as meteorological variables exhibit high spatial variability [25, 26, 32].

Along with forcing datasets, many studies have focused their attention either on model structure [37, 51, 65, 70] or on calibration parameters [61]; Benett et al. [11]. Arsenault and Brissette [8] estimated the uncertainty due to parameter set selection using a hydrological model over several basins in Quebec. The authors found that parameter set selection can play an important role in model implementation and predicted flows. Poulin et al. [51] stated that for parameter uncertainty, a hydrological model can have many equivalent local optima within a realistic parameter space. Hence, parameter uncertainties involved in the model calibration process needs to be evaluated.

2 Description of VIC Model

Variable Infiltration Capacity (VIC) model [42, 44] is macro-scale hydrological model which has the capability to solve full water and energy balance within a grid cell. It was originally developed by Xu Liang at the University of Washington. The key characteristics of the VIC model are the sub-grid variations of vegetation, precipitation, elevation and multiple soil layer features. Some of the prominent features of VIC are variability of soil moisture storage capacity within a grid cell along with the sub-grid variations of land surface vegetation classes. VIC model also includes the flexibility to include the snow model, topography information in terms of elevation bands within a grid. The VIC model also includes a separate routing model developed by Lohmann et al. [46, 47] which simulates the stream flow based on a linear transfer function.

Figure 1 shows the schematic of the VIC model with a mosaic representation of vegetation coverage and three soil layers. The surface of a single grid cell is described

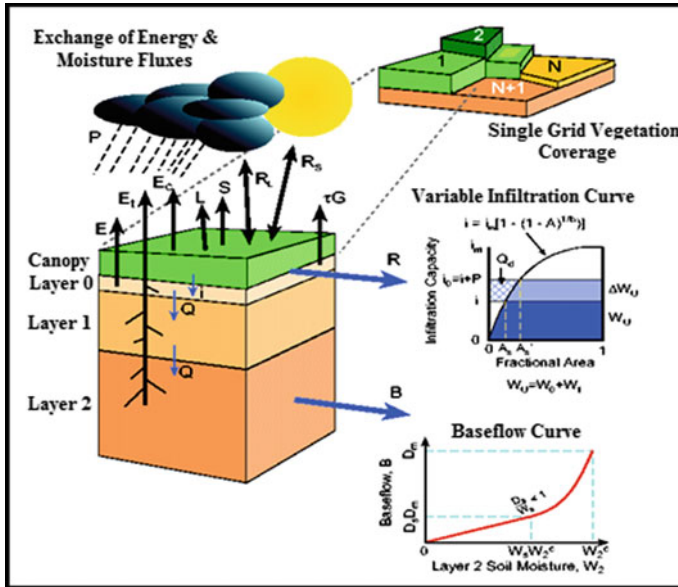


Fig. 1 Hydrologic process involved in VIC model (Adapted from: Gao et al. [29])

in 1 to N different vegetation tiles where N + 1 represents the bare soil. For each of the vegetation tile, the vegetation characteristics, such as leaf area index(LAI), albedo, minimum stomatal resistance, roughness length, architectural resistance and relative root fractions are assigned. The Penman–Monteith equation is used to calculate evapotranspiration where evapotranspiration transports moisture in upward direction. The total evapotranspiration is given by the sum of evaporation from canopy and bare soil tile which is further weighted by the coverage fraction for each surface cover class. The rainfall is intercepted by the canopy layer according to a biosphere–atmosphere transfer scheme (BATS) parameterization [20] as a function of LAI. The bottom layer responds to short-term rainfall only when the upper soil layers are saturated. The runoff from the bottom soil layer is described as per the drainage in Arno model [27]. The moisture from the roots can also be transported upward through evapotranspiration. For each of the land tile at each considered time step, the model calculates the infiltration, soil moisture distribution, surface runoff, subsurface runoff and drainage between soil layers. The summation of variables over each of the land tiles weighted by fractional coverage gives the total heat fluxes, i.e. (latent heat, sensible heat, ground heat), total surface and subsurface runoff.

2.1 Water Balance Mode

The water balance mode takes less computational time as compared to the energy balance model. One of the basic assumptions of this mode is air temperature is equal to the soil surface temperature. The water balance equation for each time step is

$$\frac{\partial S}{\partial t} = P - E - R, \quad (1.1)$$

where dS/dt , P , E and R are the change of water storage, precipitation, evapotranspiration and runoff, respectively. All units are in mm. Equation where vegetation is present in the canopy layer (interception) is

$$\frac{\partial W_i}{\partial t} = P - E_c - P_t, \quad (1.2)$$

where W_i is canopy intercepted water (mm), E_c is evaporation from canopy layer (mm), and P_t is through fall (mm).

2.1.1 Evapotranspiration

The three types of evaporation that the VIC model considers are: evaporation from the canopy layer (E_c , mm) of each vegetation tile, transpiration (E_t , mm) from each of the vegetation tiles and bare soil evaporation (E_l , mm) [43]. The total evapotranspiration over a grid cell is calculated as the sum of the above components, weighted by the respective surface cover area fractions.

$$E = \sum_{n=1}^N C_n \cdot (E_{c,n} + E_{t,n}) + C_{N+1} \cdot E_l, \quad (1.3)$$

where C_n is the vegetation fractional coverage for the n th vegetation tile, C_{N+1} is the bare soil fraction, and sum of all fractions has to be 1, i.e. $\sum_{n=1}^{N+1} C_n = 1$.

Canopy Evaporation

The maximum canopy evaporation (E_c^* , mm) from each vegetation tile is calculated using the following formulation:

$$E_c^* = \left(\frac{W_i}{W_{im}} \right)^{2/3} E_p \frac{r_w}{r_w + r_o}, \quad (1.4)$$

where W_{im} , r_o , r_w and E_p are the maximum amount of water the canopy can intercept (mm) (Dickinson [20]), the architectural resistance ($s \text{ m}^{-1}$), aerodynamic resistance ($s \text{ m}^{-1}$), the potential evapotranspiration (mm) given by the Penman–Monteith

equation respectively. The Penman–Monteith equation as given by Shuttleworth [54] is

$$\lambda_v E_p = \frac{\Delta(R_n - G) + \rho_a c_p (e_s - e_a)/r_a}{\Delta + \gamma}, \quad (1.5)$$

where λ_v , R_n , G , $(e_s - e_a)$, ρ_a , c_p , Δ , γ are the latent heat of evaporation (J kg^{-1}), the net radiation (W m^{-2}), the soil heat flux (W m^{-2}), the vapour pressure deficit of the air (Pa), the density of air at constant pressure (kg m^{-3}), the specific heat of the air ($\text{J kg}^{-1} \text{K}^{-1}$), the slope of the saturation vapour pressure temperature relationship (Pa K^{-1}), and the psychrometric constant (66 Pa K^{-1}) respectively.

Vegetation Transpiration

The vegetation transpiration (E^t , mm) is estimated using [13, 22, 23]:

$$E_t = \left(1 - \left(\frac{W_i}{W_{im}}\right)^{2/3}\right) E_p \frac{r_w}{r_w + r_o + r_c}, \quad (1.6)$$

where r_c is the canopy resistance given by:

$$r_c = \frac{r_{0c} g_T g_{vpd} g_{PAR} g_{sm}}{LAI} \quad (1.7)$$

where r_{0c} , g_T , g_{vpd} , g_{PAR} and g_{sm} are the minimum canopy resistance (s m^{-1}), the temperature factor, the vapour pressure deficit factor, photosynthetically active radiation flux (PAR) factor and soil moisture factor, respectively.

The sum of transpiration from all available soil layers in weightage to each layer roots fraction gives the total vegetation transpiration for a single vegetation tile.

Bare soil evaporation

The bare soil evaporation takes place only on the thin uppermost layer and evaporates at potential evaporation when the layer is saturated. In case the uppermost layer is not saturated the Arno method formulated by Franchini and Pacciani [27] is used to calculate the evaporation rate (E_1).

$$E_1 = E_p \left(\int_0^{A_s} dA + \int_{A_s}^1 \frac{i_0}{i_m (1 - (1 - A)^{1/b_i})} dA \right), \quad (1.8)$$

where i , i_0 , i_m are the infiltration capacity, infiltration capacity at a corresponding point and the maximum infiltration capacity respectively. Further, A , A_s , b_i , θ_s and Z represents fractional area of infiltration capacity being less than i , fractional area of saturated bare soil, infiltration shape parameter, soil porosity and depth of soil respectively. The infiltration capacity (i) as described by the Xianjiang model [72] that uses the spatial heterogeneous structure is expressed as

$$i = i_m(1 - (1 - A)^{1/b_i}) \quad \text{with} \quad i_m = (1 + b_i) \cdot \theta_S \cdot |z| \quad (1.9)$$

2.1.2 Soil Moisture and Runoff

The VIC model adopts the variable infiltration curve given by Zhao et al. [72] to consider the spatial heterogeneity in generation of runoff and the Arno model for the subsurface runoff formulation. The model assumes that the surface runoff is generated from the upper two soil layers by those areas for which precipitation added to soil moisture storage exceeds the storage capacity of the soil. The total runoff Q is the sum of direct runoff ($Q_{d,n}$, mm) and base flow ($Q_{b,n}$, mm) for each tile.

$$Q = \sum_{n=1}^{N+1} C_n \cdot (Q_{d,n} + Q_{b,n}) \quad (1.10)$$

The direct runoff Q_d , for the entire upper layer (layer 1 and 2) within each time step is given by Liang et al. [42, 44]

$$Q_d = \begin{cases} P - z_2 \cdot (\theta_S - \theta_2) + z_2 \cdot \theta_S \cdot (1 - \frac{i_0+P}{i_m})^{1+b_i}, & P + i_0 \leq i_m \\ P - z_2 \cdot (\theta_S - \theta_2), & P + i_0 \geq i_m \end{cases}, \quad (1.11)$$

where the terms are explained above. The base flow (subsurface runoff, Q_b) given by [27] which used the Arno model is

$$Q_b = \begin{cases} \frac{D_s D_m}{W_s \theta_S} \cdot \theta_3, & 0 \leq \theta_3 \leq W_s \theta_S \\ \frac{D_s D_m}{W_s \theta_S} \cdot \theta_3 + (D_m - \frac{D_s D_m}{W_s}) (\frac{\theta_3 - W_s \theta_S}{\theta_S - W_s \theta_S})^2, & \theta_3 \geq W_s \theta_S \end{cases}, \quad (1.12)$$

where D_m , D_s and W_s are the maximum subsurface flow (mm d^{-1}), fraction of D_m and the fraction of maximum soil moisture (soil porosity) θ_s . The base flow recession curve is linear below a threshold ($W_s \theta_s$) and nonlinear above the threshold.

2.2 VIC Routing Model

The VIC model simulates each grid cell independently with no horizontal flow among the grids. As VIC model simulates non-uniformly distributed runoff time series for each cell, a separate model is used to transport cell surface runoff and base flow to the outlet. Hence, the routing model used by the VIC model is adopted by Lohmann et al. [46, 47]. Figure 2 represents the schematic of the VIC routing model. The VIC routing model does not allow water to flow back into the grid cell from channel. To transport the surface runoff and base flow from each grid cell to the outlet of the cell

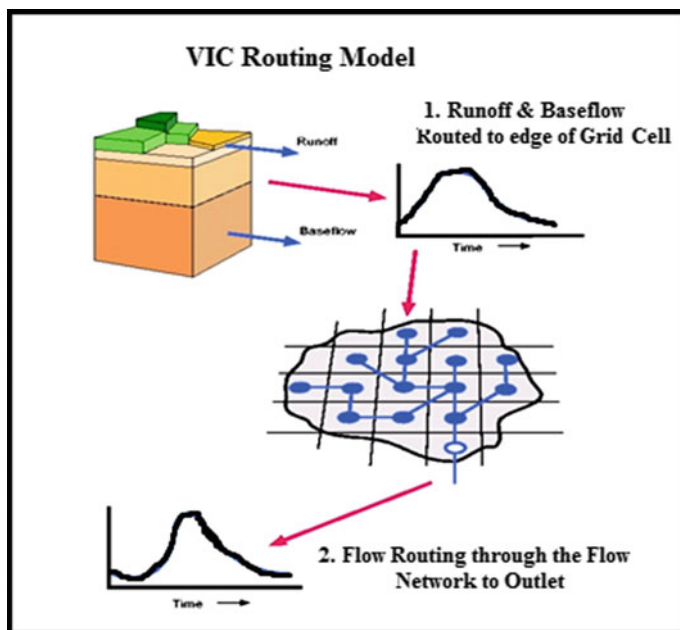


Fig. 2 VIC routing model (Adapted from: Gao et al. [29])

a triangular unit hydrograph is used and then routed to the river basin outlet. The basic principle of the routing scheme follows the linear transfer functions.

3 Case Study on Calibration of VIC Model

In this study, the uncertainties in VIC model are presented through a case study conducted over the Mahanadi basin, India (Fig. 3). The uncertainty associated with hydrological predictions needs to be addressed. An effort has been made to simulate the hydrological processes for the entire Mahanadi basin using the three-layer variable infiltration capacity model and estimate the parametric uncertainty or the uncertainty associated with calibration of the model.

The Mahanadi basin lies encompassed within geographical co-ordinates of $80^{\circ} 30'$ to $86^{\circ} 50'$ East longitudes and $19^{\circ} 20'$ – $23^{\circ} 35'$ North latitudes. The total catchment area of the basin is $1,41,600 \text{ km}^2$. Basin is bounded in the North by Central India hills, in the South and East by the Eastern Ghats and in the west by Maikala hill range. It is a typical basin considered from geographical and geological point of view covering major parts of Odisha, Chattisgarh, small portions of Madhya Pradesh and Jharkhand. The hydrological importance of the basin lies in the fact that it receives heavy to very heavy rainfall. The Mahanadi basin is subjected to frequent flooding

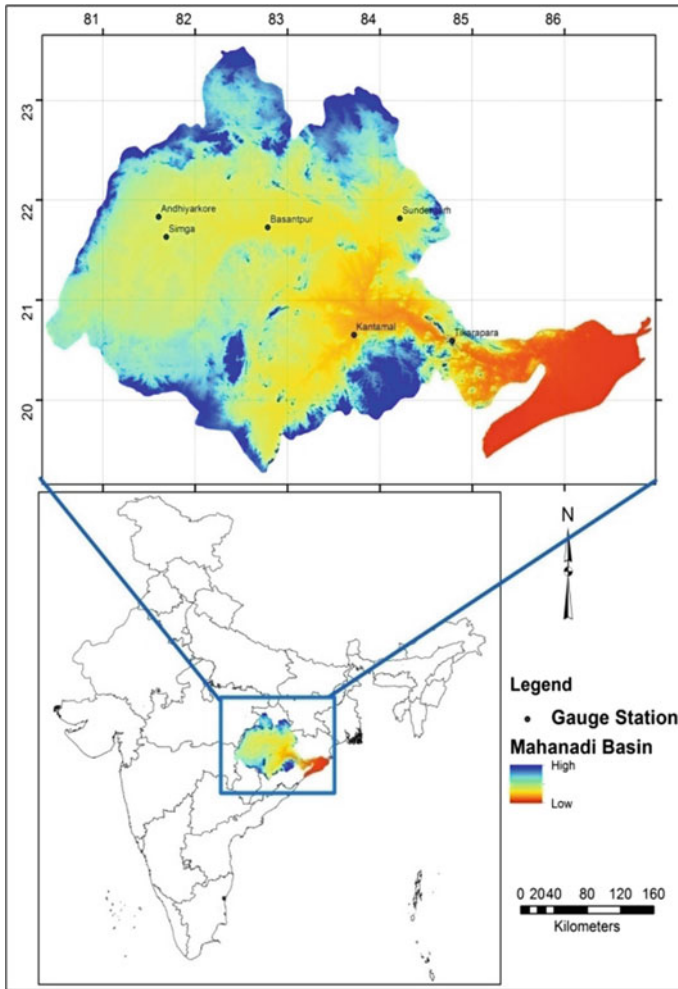


Fig. 3 Study area showing locations of Gauging stations

every year. Agriculture is the mainstay of basin’s economy and sustenance of the life of the people.

4 Datasets Used

Daily $0.25^\circ \times 0.25^\circ$ gridded rainfall dataset developed by Indian meteorological Department (IMD) was used to derive daily rainfall in millimetres over the Mahanadi basin. The IMD product uses gauge data from different stations from period 1951–till

date to estimate accumulated rainfall in the 24 h ending 0830 IST. The daily maximum temperature, minimum temperature and wind speed data is taken from the National Centres for Environmental Prediction(NCEP) and the National Centre for Atmospheric Research(NCAR) with a spatial resolution of $2.5^\circ \times 2.5^\circ$. To determine soil properties the FAO global soil map of world at scale 1:5000000 has been used. The global land use land cover map produced at 1 km spatial resolution using Advanced Very-High-Resolution Radiometer (AVHRR) data by University of Maryland is used in this study. The University Of Maryland Department Of Geography generated this global land cover classification collection in 1988. Imagery from the AVHRR satellites acquired between 1981 and 1994 were analysed to distinguish fourteen land cover classes. Observed hydro-meteorological data were collected for model calibration and validation of the results. These include the discharge data from Central Water Commission (CWC) for six stations, i.e. Kantamal, Sundergarh, Simga, Andhiyarkore, Bamnidhi and Tikarapara as shown in Fig. 3 for the period 2002–2011.

5 Results

The methodology for setting up the VIC model is shown in Fig. 4. All the input files have been created for the entire Mahanadi basin. Study period of 2003–2007 has been used for calibration with 2002 being the initialization period for the model. The model is validated for the period 2009–2011. The model is set to run at 0.5° resolution. Hence the basin gives total of 74 grid cells. A three soil layer VIC model is considered to run the model in water balance mode. All the input files as shown in Fig. 4 created for setting up the model.

Three hydrological stations of Mahanadi basin, i.e. Tikarapara, Kantamal and the Sundergarh gauging station has been selected for calibrating and validating the model (shown in Fig. 3) as continuous observed discharge data is available for these stations. Calibration of the VIC hydrological model is an iterative process involving the change of sensitive model parameters to obtain best possible match between the observed and simulated values. Six model parameters of the VIC-3L model need to be calibrated because as they cannot be determined well based on the soil information [71]. These six model parameters are the depths of the upper and lower soil layers (d_i , $i = 2,3$); the Variable Infiltration Capacity curve parameter(b_i) which defines the shape of the Variable Infiltration Capacity curve; and the three subsurface flow parameters (i.e. D_m , D_s and W_s , where D_m is the maximum velocity of base flow, D_s is the fraction of D_m and W_s is the fraction of maximum soil moisture

The general principle to VIC model calibration

1. Soil depth—[varies between 0.1 to 1.5 m] Thicker the depth of the soil layers, less is the runoff generated resulting in more soil moisture stored in the soil layers and increase the loss due to evapotranspiration.

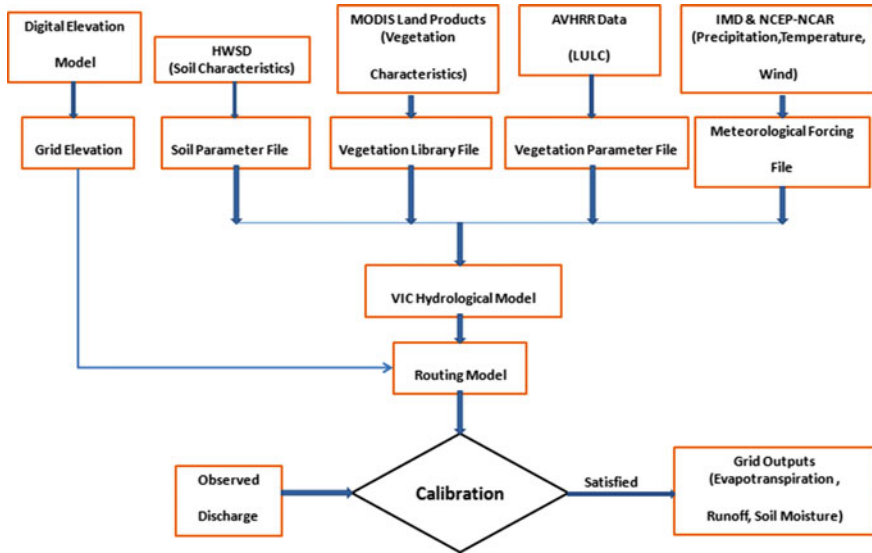


Fig. 4 Model inputs and VIC model methodology

2. b_i —[>0 to ~0.4] The variable infiltration capacity curve parameter represents the quantity of available infiltration capacity as a function of relative saturated grid cell area. Higher value of b_i will yield lower infiltration and higher surface runoff.
3. D_m —[0 to ~30] It is the maximum amount of baseflow that can occur from the lowest soil layer and depends on the hydraulic conductivity of the soil.
4. D_s —[>0 to 1] It represents the fraction of D_m where rapidly increasing nonlinear baseflow begins. A higher value of D_s will result in higher baseflow at lower water content in the lowest soil layer.
5. W_s —[>0 to ~0.4] It is the fraction of the maximum soil moisture of the lowest soil layer where the nonlinear baseflow occurs. A higher value of W_s will tend to raise the water content demanded for rapidly increasing nonlinear baseflow, which will tend to delay the runoff peaks.

The calibration of the above specified parameters is conducted through a trial-and-error procedure to have an acceptable match of model-predicted discharge with the observed discharge. Once the model is calibrated, the calibrated parameters are used to validate the model. Coefficient of determination (R^2) between the observed with respect to simulated stream flow for the gauging stations Tikarapara, Kantamal and Sundergarh for calibration and validation as shown in Fig. 5a, b and c are 0.73, 0.77, 0.67 and 0.68, 0.73, 0.61, respectively. The VIC model is primarily designed to evaluate long-term climate and land cover changes over the catchments. It does not take into effect human-induced activities such as effects of dams, reservoirs or any other structural intervention which may be a reason of disagreement between

observed and simulated discharge. The Mahanadi basin contains several storage reservoirs and diversion structures. When the flow is low, reservoirs store most of the river waters whereas during high flows reservoir throws out all waters once it is filled thus being a possible reason of overestimation during low flows and underestimation during high flows. The results of calibration and validation would have been better if there were no human induced activities present.

6 Open Questions

The VIC model has been widely used in a number of research areas such as water resource management, meteorology, environmental and atmospheric science, remote sensing, etc. It has played the role of a hydrological model as well as land surface model. The model has proved its efficiency by being well calibrated and applied to a number of large basins over the continental and global scale. The model also outperformed well relative to other land surface schemes in the PILPS project. In addition to the evaluation of stream flow, the model has also evaluated soil moisture, evapotranspiration and snow cover data across the globe. The VIC model has also been used to provide long-term data record of land surface fluxes and states when forced with high-quality meteorological forcing, the output of which can be used for a number of purpose such as water management, analysing and predicting drought and flood events, simulating hydrologic variables and snow simulations, etc.

Despite its number of well-proved applications the model is associated with a number of uncertainties which may be due to the deficiencies in forcing data, the model parameters or the model structure. The forcing uncertainty is enhanced due to the scarcity of data stations which seeks data estimation rather than being measured at the location, data prone to measurement errors or the high spatial variability of the forcing variable. This uncertainty propagates from the model input to the output; hence it needs to be quantified. Further, coming to parametric uncertainty the model performance is also affected by the choice of parameter set. Proper selection of parameters would lead to improvement in the model simulations.

Many studies have been done regarding quantification of uncertainty solely either due to forcing data, model parameter or the model structure. But the question remains “which out of all three is the most leading uncertainty factors?”. Multiple studies suggest different views stating either of the three being the most important factor. As, the ultimate goal of modelling is to produce the most accurate results it is needed to simulate the model with coexisting uncertainties in forcing errors, model parameters and model structure and to analyse how the model sensitivity changes with respect to all three sources of uncertainty.

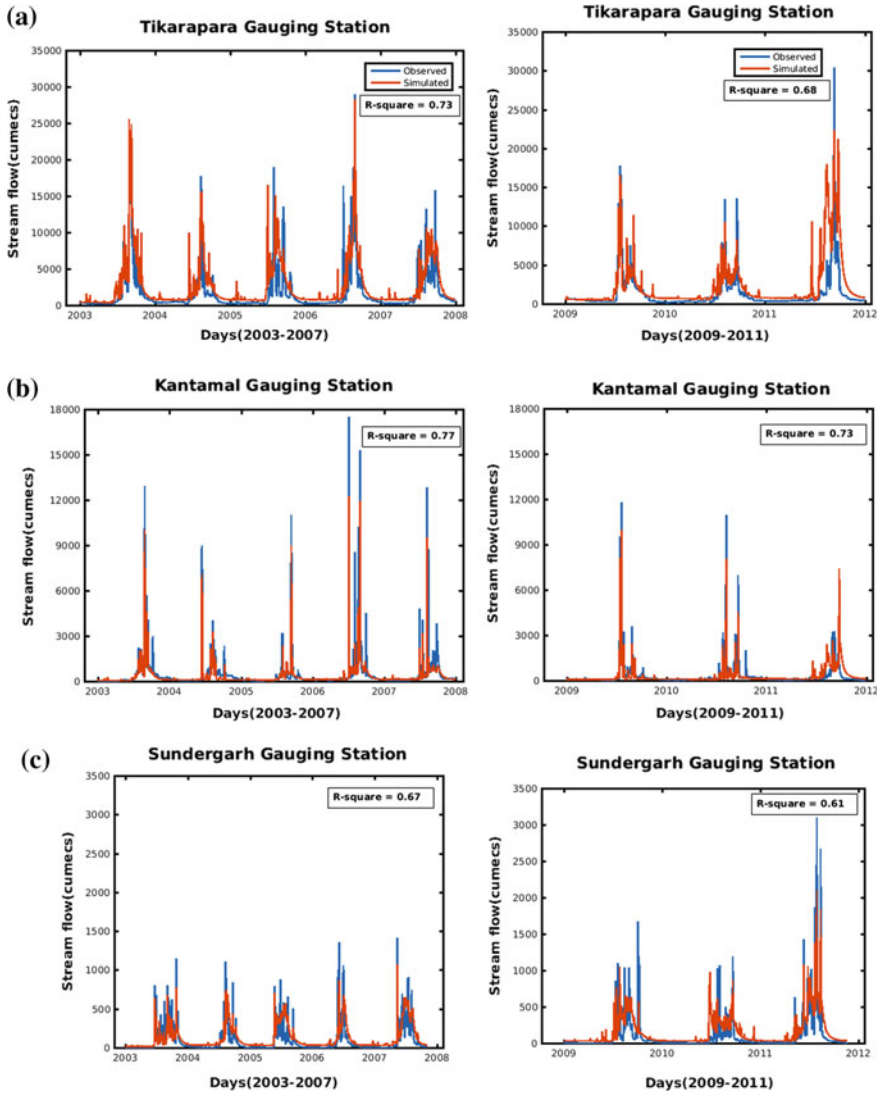


Fig. 5 a Comparison of Hydrograph at Tikarapara Gauging station: Calibration period and Validation period b Comparison of Hydrograph at Kantamal Gauging station: Calibration period and Validation period c Comparison of Hydrograph at Sundergarh Gauging station: Calibration period and Validation period

References

1. Abdulla FA (1996) Application of a macroscale hydrologic model to estimate the water balance of the Arkansas Red River basin. *J Geophys Res Atmos* 101(D3):7449–7459
2. Abdulla FA, Lettenmaier DP (1997a) Development of regional parameter estimation equations for a macroscale hydrologic model. *Journal of Hydrology* 197(1–4):230–257
3. Abdulla FA, Lettenmaier DP (1997b) Application of regional parameter estimation schemes to simulate the water balance of a large continental river. *Journal of Hydrology* 197(1–4):258–285
4. Adam JC (2007) Understanding the causes of streamflow changes in the Eurasian Arctic. University of Washington, pp 156
5. Adam JC et al (2007) Simulation of reservoir influences on annual and seasonal streamflow changes for the Lena, Yenisei, and Ob' rivers. *J Geophys Res Atmos* 112(D24)
6. Alley WM (1984) On the treatment of evapotranspiration, soil moisture accounting and aquifer recharge in monthly water balance models. *Water Resour Res* 20(8):1137–1149
7. Anderson, J., Chung, F., Anderson, M., Brekke, L., Easton, D., Ejeta, M., Peterson, R., and Snyder, R (2007): Progress on incorporating climate change into management of California's water resources. *Climatic Change*, 87, 91–108. <https://doi.org/10.1007/s10584-007-9353-1>
8. Arsenault R, Brissette FP (2014) Continuous streamflow prediction in ungauged basins: the effects of equifinality and parameter set selection on uncertainty in regionalization approaches. *Water Resour Res* 50:6135–6153. <https://doi.org/10.1002/2013WR014898>
9. Bastola S, Murphy C, Sweeney J (2011) The role of hydrological modelling uncertainties in climate change impact assessments of Irish river catchments. *Adv Water Resour* 34:562–576. <https://doi.org/10.1016/j.advwatres.2011.01.008>
10. Benke KK, Lowell KE, Hamilton AJ (2008) Parameter uncertainty, sensitivity analysis and prediction error in a waterbalance hydrological model. *Math Comput Model* 47:1134–1149. <https://doi.org/10.1016/j.mcm.2007.05.017>
11. Bennett KE, Werner AT, Schnorbus M (2012) Uncertainties in hydrologic and climate change impact analyses in headwater basins of British Columbia. *J Climate* 25:5711–5730. <https://doi.org/10.1175/jcli-d-11-00417.1>
12. Beven K, Binley A (1992) The future of distributed models: model calibration and uncertainty prediction. *Hydrol Process* 6:279–298. <https://doi.org/10.1002/hyp.3360060305>
13. Blondin C (1991) Parameterization of land-surface processes in numerical weather prediction. In: Schmugge TJ, Andre JC (eds) *Land surface evaporation: measurements and parameterization*. Springer, New York, pp 31–54
14. Butts MB, Payne JT, Kristensen M, Madsen H (2004) An evaluation of the impact of model structure on hydrological modelling uncertainty for streamflow simulation. *J Hydrol* 298:242–266. <https://doi.org/10.1016/j.jhydrol.2004.03.042>
15. Clark MP, Slater AG., Rupp DE, Woods RA, Vrugt JA, Gupta HV, Wagener T, Hay LE (2008) Framework for Understanding Structural Errors (FUSE): a modular framework to diagnose differences between hydrological models. *Water Resour Res* 44, W00B02. <https://doi.org/10.1029/2007wr006735>
16. Clark MP, Kavetski D, Fenicia F (2011b) Pursuing the method of multiple working hypotheses for hydrological modeling. *Water Resour Res* 47:W09301. <https://doi.org/10.1029/2010wr009827>
17. Clark MP, Nijssen B, Lundquist JD, Kavetski D, Rupp DE, Woods RA, Freer JE, Gutmann ED, Wood AW, Brekke LD, Arnold JR, Gochis DJ, Rasmussen RM (2015a) A unified approach for process-based hydrologic modeling: 1. Modeling concept. *Water Resour Res* 51:2498–2514. <https://doi.org/10.1002/2015wr017198>
18. Clark MP, Nijssen B, Lundquist JD, Kavetski D, Rupp DE, Woods RA, Freer JE, Gutmann ED, Wood AW, Gochis DJ, Rasmussen RM, Tarboton DG, Mahat, V, Flerchinger GN, Marks DG (2015b) A unified approach for process-based hydrologic modeling: 2. Model implementation and case studies. *Water Resour Res* 51:2515–2542. <https://doi.org/10.1002/2015wr017200>
19. Deardorff JW (1978) Efficient prediction of ground surface-temperature and moisture, with inclusion of a layer of vegetation. *J Geophys Res Ocean Atmos* 83(NC4):1889–1903

20. Dickinson RE (1984) Modeling evapotranspiration for three-dimensional global climate models. In: Hansen JE, Takahashi T (eds) *Climate processes and Climate Sensitivity (Monograph Series)*. Washington, D.C., pp 58–72
21. Dickinson RE, Henderson-Sellers A, Kennedy PJ, Wilson MF (1986) Biosphere-atmosphere transfer scheme (BATS) for the NCAR community climate model. NCAR Tech. Note TN-275 + STR
22. Ducoudre NI et al (1993a) SECHIBA, a new set of parameterizations of the hydrologic exchanges at the land-atmosphere interface within the LMD atmospheric general circulation model. *J Clim* 6(2):248–273
23. Ducoudre NI et al (1993b) SECHIBA, a new set of parameterizations of the hydrologic exchanges at the land atmosphere interface within the LMD atmospheric general-circulation model. *J Clim* 6(2):248–273
24. Essery R, Morin S, Lejeune Y, Ménard CB (2013) A comparison of 1701 snow models using observations from an alpine site. *Adv Water Resour* 55:131–148. <https://doi.org/10.1016/j.advwatres.2012.07.013>
25. Feld SI, Cristea NC, Lundquist JD (2013) Representing atmospheric moisture content along mountain slopes: examination using distributed sensors in the Sierra Nevada, California. *Water Resour Res* 49:4424–4441. <https://doi.org/10.1002/wrcr.20318>
26. Flint AL, Childs SW (1987) Calculation of solar radiation in mountainous terrain. *Agr Forest Meteorol* 40:233–249. [https://doi.org/10.1016/0168-1923\(87\)90061-X](https://doi.org/10.1016/0168-1923(87)90061-X)
27. Franchini M, Pacciani M (1991) Comparative-analysis of several conceptual rainfall runoff models. *J Hydrol* 122(1–4):161–219
28. Gabos A, Gasparri L (1983) Monthly runoff model for regional planning. *Water Int* 8:42–45
29. Gao H, Tang Q, Shi X, Zhu C, Bohn TJ, Su F, Sheffield J, Pan M, Lettenmaier DP, Wood EF (2010) Water budget record from variable infiltration capacity (VIC) model. In: *Algorithm theoretical basis document for terrestrial water cycle data records*
30. Georgakakos KP et al (2004) Towards the characterization of streamflow simulation uncertainty through multimodal ensembles. *J Hydrol* 298:222–241. <https://doi.org/10.1016/j.jhydrol.2004.03.037>
31. Guo JZ, Liang Xu, Leung LR (2004) Impacts of different precipitation data sources on water budgets. *J Hydrol* 298(1–4):311–334
32. Herrero J, Polo MJ (2012) Parameterization of atmospheric longwave emissivity in a mountainous site for all sky conditions. *Hydrol Earth Syst Sci* 16:3139–3147. <https://doi.org/10.5194/hess-16-3139-2012>
33. Hillard U, Sridhar V, Lettenmaier DP, McDonald KC (2003) Assessing snowmelt dynamics with NASA scatterometer (NSCAT) data and a hydrologic process model. *Remote Sens Environ* 86(1):52–69
34. Huang M, Liang X, Liang Y (2003) A transferability study of model parameters for the variable infiltration capacity land surface scheme. *J Geophys Res Atmos* 108(D22)
35. Hurkmans R, Moel H, Aerts JCJH, Troch PA (2008) Water balance versus land surface model in the simulation of Rhine river discharges. *Water Resour Res* 44(1)
36. Jackson C, Xia Y, Sen MK, Stoffa PL (2003) Optimal parameter and uncertainty estimation of a land surface model: A case study using data from Cabauw, Netherlands. *J Geophys Res* 108:4583. <https://doi.org/10.1029/2002JD002991>
37. Jiang T, Chen YD, Xu C, Chen X, Chen X, Singh VP (2007) Comparison of hydrological impacts of climate change simulated by six hydrological models in the Dongjiang Basin, South China. *J Hydrol* 336:316–333. <https://doi.org/10.1016/j.jhydrol.2007.01.010>
38. Kelleher C, Wagener T, McGlynn B (2015) Model-based analysis of the influence of catchment properties on hydrologic partitioning across five mountain headwater subcatchments. *Water Resour Res* 51:1–28. <https://doi.org/10.1002/2014WR016147>
39. Kuczera G, Parent E (1998) Monte Carlo assessment of parameter uncertainty in conceptual catchment models: the Metropolis algorithm. *J Hydrol* 211:69–85. [https://doi.org/10.1016/S0022-1694\(98\)00198-X](https://doi.org/10.1016/S0022-1694(98)00198-X)

40. Lakshmi V, Wood EF (1998) Diurnal cycles of evaporation using a two-layer hydrological model. *J Hydrol* 204(1–4):37–51
41. Liang X et al (2004) Assessment of the effects of spatial resolutions on daily water flux simulations. *J Hydrol* 298(1–4):287–310
42. Liang X, Lettenmaier DP, Wood EF (1996) One-dimensional statistical dynamic representation of subgrid spatial variability of precipitation in the two-layer variable infiltration capacity model. *J Geophys Res* 101(D16):21403–21422
43. Liang X, Lettenmaier DP, Wood EF, Burges SJ (1994) A Simple hydrologically Based Model of Land Surface Water and Energy Fluxes for GSMs. *J Geophys Res* 99(D7):14415–14428
44. Liang X, Wood EF, Lettenmaier DP (1996) Surface soil moisture parameterization of the VIC-2L model: evaluation and modifications. *Global Planet Change* 13:195–206
45. Liu Y, Gupta HV (2007) Uncertainty in hydrologic modeling: toward an integrated data assimilation framework. *Water Resour Res* 43:W07401. <https://doi.org/10.1029/2006WR005756>
46. Lohmann D, Nolte-Holube R, Raschke E (1996) A large-scale horizontal routing model to be coupled to land surface parametrization schemes. *Tellus* 48(A):708–721
47. Lohmann D, Raschke E, Nijssen B, Lettenmaier DP (1998) Regional scale hydrology: I. Formulation of the VIC-2L model coupled to a routing model. *Hydrol Sci J* 43(1):131–141
48. Manabe S (1969) Climate and the ocean circulation: I. The atmospheric circulation and the hydrology of the earth's surface. *Month Weather Rev* 97(11):739–774
49. Matheussen B, Kirshbaum RL, Goodman IA, Donnel GM (2000) Effects of land cover change on streamflow in the interior Columbia River Basin (USA and Canada). *Hydrol, Process*
50. Mote PW, Hamlet AF, Clark MP, Lettenmaier DP (2005) Declining mountain snowpack in western North America. *B Am Meteorol Soc* 86:39–49. <https://doi.org/10.1175/bams-86-1-39>
51. Poulin A, Brissette F, Leconte R, Arsenault R, Malo JS (2011) Uncertainty of hydrological modelling in climate change impact studies in a Canadian, snow-dominated river basin. *J Hydrol* 409:626–636. <https://doi.org/10.1016/j.jhydrol.2011.08.057>
52. Refsgaard JC, van der Sluijs JP, Brown J, van der Keur P (2006) A framework for dealing with uncertainty due to model structure error. *Adv Water Resour* 29:1586–1597. <https://doi.org/10.1016/j.advwatres.2005.11.013>
53. Sellers PJ, Mintz Y (1986) A Simple Biosphere Model (SiB) for use within generation circulation models. *J Atmos. Sci*
54. Shuttleworth WJ (1993) Evaporation. In: Maidment DR (ed) *Handbook of hydrology*. McGraw-Hill, Inc., New York, pp 4.1–4.53
55. Slater AG, Schlosser CA, Desborough CE, Pitman AJ, Henderson-Sellers A, Robock A, Vinnikov KY, Entin J, Mitchell K, Chen F, Boone A, Etchevers P, Habets F, Noilhan J, Braden H, Cox PM, de Rosnay P, Dickinson RE, Yang Z-L, Dai Y-J, Zeng Q, Duan Q, Koren V, Schaake S, Gedney N, Gusev YM, Nasonova ON, Kim J, Kowalczyk EA, Shmakin AB, Smirnova TG, Verseghy D, Wetzel P, Xue Y (2001) The representation of snow in land surface schemes: results from PILPS 2(d). *J Hydrometeorol* 2:7–25. doi:10.1175/1525-7541(2001)002<0007:TROSIL>2.0.CO;2
56. Slater AG et al (2007) A multimodel simulation of pan-Arctic hydrology, *J Geophys Res Biogeo*, 112(G4)
57. Smith PJ, Beven KJ, Tawn JA (2008) Detection of structural inadequacy in process-based hydrological models: a particle-filtering approach. *Water Resour Res* 44:W01410. <https://doi.org/10.1029/2006WR005205>
58. Stamm JF et al (1994) Sensitivity of a GCM simulation of global climate to the representation of land-surface hydrology. *J Clim* 7(8):1218–1239
59. Su FG, Xie ZH (2003) A model for assessing effects of climate change on runoff in China. *Prog Nat Sci* 13(9):701–707
60. Tapiador FJ, Turk FJ, Petersen W, Hou AY, García-Ortega E, Machado LAT, Angelis CF, Salio P, Kidd C, Huffman GJ, de Castro M (2012) Global precipitation measurement: Methods, datasets and applications. *Atmos Res* 104–105:70–97. <https://doi.org/10.1016/j.atmosres.2011.10.021>
61. Teutschbein C, Wetterhall F, Seibert J (2011) Evaluation of different downscaling techniques for hydrological climate-change impact studies at the catchment scale. *Clim Dynam* 37:2087–2105. <https://doi.org/10.1007/s00382-010-0979-8>

62. Tobin C, Nicotina L, Parlange MB, Berne A, Rinaldo A (2011) Improved interpolation of meteorological forcings for hydrologic applications in a Swiss Alpine region. *J Hydrol* 401:77–89. <https://doi.org/10.1016/j.jhydrol.2011.02.010>
63. Troy TJ et al (2008) An efficient calibration method for continental-scale land surface modeling. *Water Resour Res* 44(9):13
64. Vandewiele GL, Xu, C-Y, Win NL (1992) Methodology and comparative study of monthly water balance models in Belgium, China and Burma
65. Velazquez JA, Schmid J, Ricard S, Muerth MJ, Gauvin St-Denis B, Minville M, Chaumont D, Caya D, Ludwig R, Turcotte R (2013) An ensemble approach to assess hydrological models' contribution to uncertainties in the analysis of climate change impact on water resources. *Hydrol Earth Syst Sci* 17:565–578. <https://doi.org/10.5194/hess-17-565-2013>
66. Vrugt JA, Diks CGH, Gupta HV, Bouten W, Verstraten JM (2005) Improved treatment of uncertainty in hydrologic modeling: combining the strengths of global optimization and data assimilation. *Water Resour Res* 41:W01017. <https://doi.org/10.1029/2004WR003059>
67. Vrugt JA, Gupta HV, Bastidas LA, Bouten W, Sorooshian S (2003a) Effective and efficient algorithm for multiobjective optimization of hydrologic models. *Water Resour Res* 39:1214. <https://doi.org/10.1029/2002wr001746>
68. Vrugt JA, Gupta HV, Bouten W, Sorooshian S (2003b) A shuffled complex evolution metropolis algorithm for optimization and uncertainty assessment of hydrologic model parameters. *Water Resour Res* 39:1201. <https://doi.org/10.1029/2002wr001642>
69. Wagener T, Gupta HV (2005) Model identification for hydrological forecasting under uncertainty. *Stoch Environ Res Risk A* 19:378–387. <https://doi.org/10.1007/s00477-005-0006-5>
70. Wilby RL, Harris I (2006) A framework for assessing uncertainties in climate change impacts: low-flow scenarios for the River Thames, UK. *Water Resour Res* 42:W02419. <https://doi.org/10.1029/2005WR004065>
71. Yuan F et al (2004) An application of the VIC-3L land surface model and remote sensing data in simulating streamflow for the Hanjiang River basin. *Can J Remote Sens* 30(5):680–690
72. Zhao R-J et al (1980) The Xinanjiang model. In: *Hydrological forecasting proceedings Oxford symposium, IASH 129*, pp 351–356
73. Zhou S et al (2004) An assessment of the VIC-3L hydrological model for the Yangtze River basin based on remote sensing: a case study of the Baohe River basin. *Can J Remote Sens* 30(5):840–853

Predictability of Hydrological Systems Using the Wavelet Transformation: Application to Drought Prediction



Rajib Maity and Mayank Suman

1 Introduction

Hydrological processes are complex and associated with multiple hydroclimatic factors. As a consequence, the hydrologic time series are continuously evolving over time and exhibit nonstationary nature [1, 2]. Generally, the hydrologic time series is presented in the time domain and this representation is useful when the temporal changes in different statistical properties are attempted. However, this representation is not adequate in some cases as it hides important information about frequency content of the time series and its temporal evolution (if any). Information on constituting frequency of a time series may be extracted using mathematical transforms like Fourier Transform, Wavelet Transform, etc.

Fourier Transform (FT) is a mathematical tool that is used to separate frequency component of time series. The basis function used in the FT is circular functions (sine and cosine functions). FT is based on the fact that any continuous periodic time series can be constructed by using adequate number of appropriate sine or cosine waves. FT transforms a time series from the time–amplitude domain to frequency–amplitude domain. FT has been used in hydrology by many investigators. For instance, FT was used by Kirchner et al. [3] for studying contaminant transport in catchment. Şen [4] studied the FT of periodic-stochastic hydrologic sequences in general.

The outcome of FT can point out the frequencies of sine or cosine waves in the given time series, however, it cannot provide the information about the temporal evolution of amplitude of these frequencies. Rather, it provides the mean amplitude or power of the different frequencies present in the time series. This drawback can

R. Maity (✉)

Department of Civil Engineering, Indian Institute of Technology, Kharagpur, India
e-mail: rajib@civil.iitkgp.ac.in; rajibmaity@gmail.com

M. Suman

School of Water Resources, Indian Institute of Technology, Kharagpur, India
e-mail: mayanksuman@protonmail.com

© Springer Nature Switzerland AG 2019

S. K. Singh and C. T. Dhanya (eds.), *Hydrology in a Changing World*, Springer Water,
https://doi.org/10.1007/978-3-030-02197-9_5

109

be partially overcome by using short-term Fourier transform (also called Windowed Fourier Transform), in which the transformation instead of operating on the whole of time series at once operates on some selected length of the time series called a window. However, this approach can only be applied when one is confident about window size. If the window size changes too often for a time series, this methodology does not yield satisfactory results. Hence, the FT is best suited for stationary time series.

The Wavelet Transform (WT) is another mathematical tool extensively used for analysis of time series in hydrology. Unlike FT, WT helps in getting temporal information about different frequencies in the time series also, which may prove useful while analyzing nonstationary time series. WT is being widely used for hydrological time series prediction [5–7]. Smith et al. [8] used WT for streamflow prediction. Özger et al. [9] and Maity et al. [10] utilized WT for drought forecasting and its evolution. Labat et al. [11] modeled the rainfall–runoff relation using WT. These studies highlight the appropriateness and effectiveness of WT based methodologies to model relationship between hydrological series.

This chapter aims at exploring the potential of wavelet transform for prediction of hydrological systems. In this regard, the mathematical framework of wavelet transform and multi-resolution analysis using wavelet functions are discussed in the subsequent sections. An example problem of predicting drought using multi-resolution wavelet is also provided for showing the effectiveness of wavelet transform for hydrologic prediction.

2 Wavelet Function

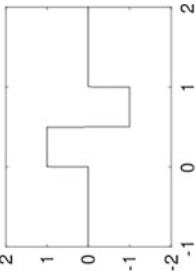
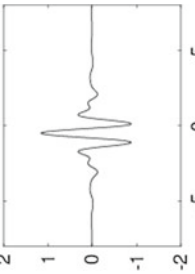
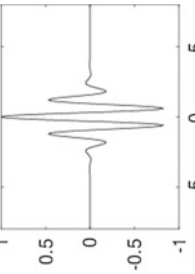
Wavelet is a finite disturbance of zero mean amplitude. Wavelet function has unit energy and its integration over the real number line is zero. Details of a few well-known wavelet functions like Haar, Morlet, etc., are shown in Table 1. Wavelet functions are localized in both time and frequency space. Many different wavelet functions can be derived from one wavelet function by shifting it temporally and/or scaling, without changing any functional form [12]. The original wavelet function is called mother wavelet and all the derived wavelet functions are called daughter wavelets.

For a mother wavelet function $\Psi(t)$, the daughter wavelet functions (denoted by $\Psi_{a,b}(t)$) can be obtained as

$$\Psi_{a,b}(t) = \frac{1}{\sqrt{a}} \Psi\left(\frac{t-b}{a}\right) \quad (1)$$

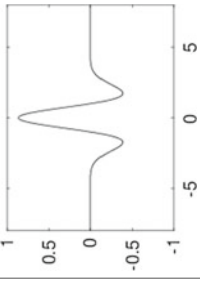
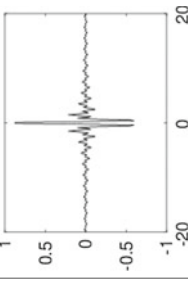
where a , b and t are scaling parameter, shifting parameter, and time step, respectively. The scaling parameter helps in varying the frequency of mother wavelet as it is inversely related to wave frequency and the shifting parameter helps in shifting the mother wavelet with respect to time. Scaling as a mathematical operation

Table 1 Details of some mother wavelets

Name	Mother wavelet function	Graphical representation
Haar or Daubechies 1	$\psi(t) = \begin{cases} 1 & 0 \leq t \leq 0.5 \\ -1 & 0.5 \leq t \leq 1 \\ 0 & \text{otherwise} \end{cases}$	
Meyer	<p>In frequency domain</p> $\psi(\omega) = \begin{cases} \frac{1}{\sqrt{2\pi}} \sin\left(\frac{\pi}{2} \nu \left(\frac{3 \omega }{2\pi} - 1\right)\right) e^{i\omega t/2} & \text{if } \frac{2\pi}{3} < \omega < \frac{4\omega}{3} \\ \frac{1}{\sqrt{2\pi}} \sin\left(\frac{\pi}{2} \nu \left(\frac{3 \omega }{2\pi} - 1\right)\right) e^{i\omega t/2} & \text{if } \frac{4\pi}{3} < \omega < \frac{8\omega}{3} \\ 0 & \text{otherwise} \end{cases}$ <p>where, $\nu(x) = \begin{cases} 0 & x \leq 0 \\ x & 0 < x < 1 \\ 1 & x \geq 1 \end{cases}$</p>	
Morlet	$\psi(t) = c_\sigma \pi^{(-1/4)} e^{(-1/2)t^2} (e^{i\sigma t} - k_\sigma)$ <p>where, $k_\sigma = e^{-1/2\sigma^2}$ and $c_\sigma = (1 + e^{-\sigma^2} - 2e^{-3/4\sigma^2})^{-1/2}$</p>	

(continued)

Table 1 (continued)

Name	Mother wavelet function	Graphical representation
Ricker or Mexican Hat	$\psi(t) = \frac{2}{\sqrt{3\sigma\pi^{1/4}}} \left(1 - \left(\frac{t}{\sigma}\right)^2\right) e^{-\frac{t^2}{2\sigma^2}}$	
Complex Shannon 1-1	$\psi(t) = \sqrt{F_b} \text{sinc}(F_b x) e^{(2i\pi F_c x)}$ <p>The wavelet is named as $F_b - F_c$ For Figure $F_b = F_c = 1$</p>	

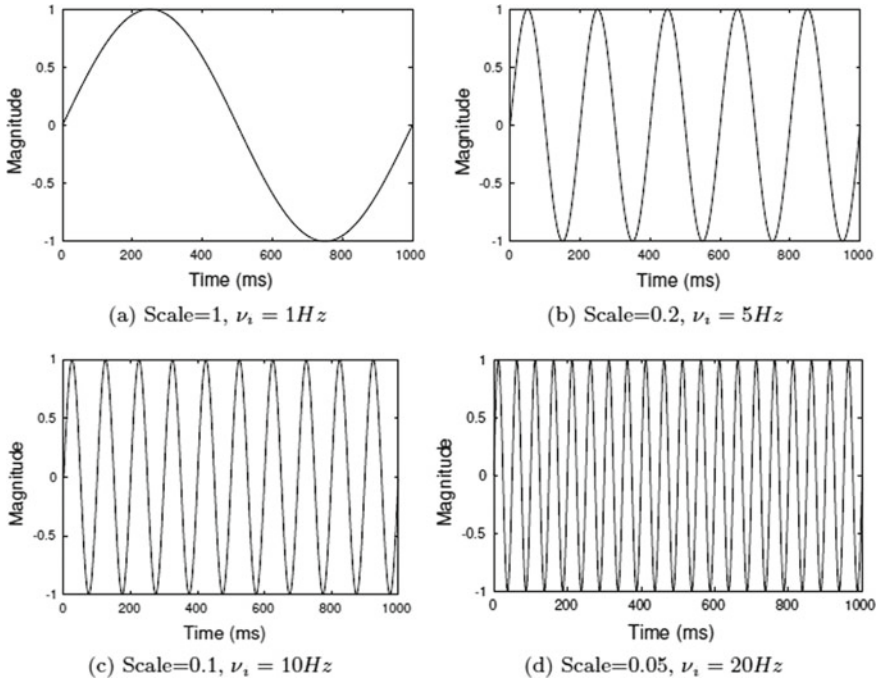


Fig. 1 Different scale/frequencies of unit amplitude sign wave (ν_i represents frequency)

either dilates or compresses a wavelet function, i.e., larger scales correspond to the dilated (or stretched out) daughter wavelet function (compared to mother wavelet) and smaller scales correspond to the compressed daughter wavelet function. For instance, in Fig. 1, different scales of sine wave with unit amplitude are shown. It can be observed from Fig. 1 a and d that decrease in scale leads to contraction in signal and *vice versa*.

The importance of shifting and scaling operation on mother wavelet for wavelet transform is discussed in Sect. 3. It should be further noticed that, with the increase in scaling parameter, the frequency of the derived daughter wavelet decreases. Hence, with finite scaling factor the mother wavelet and all daughter wavelet cannot cover lower frequency range (in that case, scaling factor can become too high as scaling factor is inversely proportional to frequency). Another function called scaling function or Father wavelet function (denoted by $\phi(t)$) is used for covering the whole frequency range of the time series during discrete wavelet transform (discussed later). Father wavelet functions, like mother wavelet functions, are of finite duration and act as low-pass filter. In the next section, Haar wavelet is dealt in greater depth.

Haar Wavelet

Haar wavelet, proposed by Alfréd Haar in 1909, is a square-shaped wavelet, which is also the first member of the Daubechies class of wavelets and regarded as daubechies I

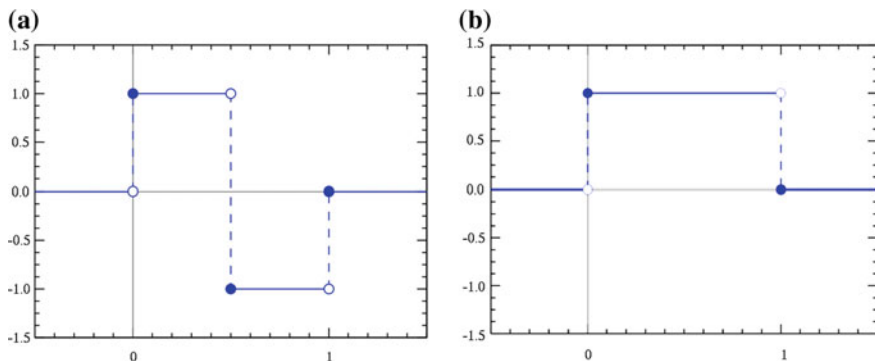


Fig. 2 Haar Wavelet function **a** Mother Wavelet **b** Scaling function

or db1. As per Maheswaran and Khosa [13], this wavelet function has better time localization capability, so, it is useful for short-term predictions. Haar wavelet (Fig. 2a) is defined as

$$H(t) = \begin{cases} 1 & 0 \leq t < 0.5 \\ -1 & 0.5 \leq t < 1 \\ 0 & \text{otherwise} \end{cases} \quad (2)$$

The scaling function for Haar wavelet (Fig. 2b) is given by:

$$S(t) = \begin{cases} 1 & 0 \leq t < 1 \\ 0 & \text{otherwise} \end{cases} \quad (3)$$

Haar wavelet and scaling functions are having the following properties:

- (i) The Haar wavelet and its scaling function can be expressed as linear combination of scaling function of different scales.

$$S(t) = S(2t) + S(2t - 1) \quad (4)$$

$$H(t) = S(2t) - S(2t - 1) \quad (5)$$

- (ii) Any continuous real function on $[0, 1]$ can be approximated by linear combinations of dyadic Haar wavelet with different scales and shifts $(1, H(t + b_1), H(2t + b_2), H(4t + b_3), \dots, H(2^n t + b_n), \dots)$.
- (iii) Similarly, any continuous real function with compact support can be approximated by a linear combination of scale functions with different scales and shifts $(S(t + b_1), S(2t + b_2), S(4t + b_3), \dots, S(2^n t + b_n), \dots)$.

3 Wavelet Transform

Wavelet transform aims to provide the state of different frequency/frequency band in the time series with time. For this purpose, the WT uses a family of daughter wavelets (Eq. 1) for transformation. Both the operations of shifting and scaling used during the derivation of different daughter wavelets have their significance with respect to wavelet transform. Shifting of wavelet function helps in capturing the state of different frequencies along the time. Scaling operation on the other hand changes the frequency of the mother wavelet function (Eq. 1). The scaling parameter is similar to the scale used in maps, i.e., high scale (thus low frequency) corresponds to non-detailed global view (of the time series), and low scale (high frequency) corresponds to detailed view. Scaling is required to capture the information regarding different frequency ranges in the time series as per the uncertainty principle of signal analysis which states

$$\Delta t \Delta \omega \geq \frac{1}{2} \quad (6)$$

where Δt represents time step and $\Delta \omega$ represents resolution in angular frequency ($\omega = 2\pi\nu$, where ν is wave frequency). Hence, the larger is time resolution chosen for the analysis, the smaller will be frequency resolution analyzed or *vice versa*. Hence, to analyze the time series at different frequency resolutions, the scaling of mother wavelet is required.

In a nutshell, WT transforms the time series into its constituents or components based on shifting and dilation or scaling of the mother wavelet $\Psi(t)$. During WT, the time series is convoluted with mother wavelet of different scales and shifts to obtain the wavelet components. It should be noted that despite having finite length, scaling and shifting of mother wavelet enable it to catch most of intermittent disturbances of different durations. By using daughter wavelet of higher scale, WT extracts the slow moving changes or global information in time series and by using daughter wavelet of lower scale, WT extracts the detailed information about local disturbances. This enables the wavelet transform to provide the time and frequency information or time–frequency representation of the time series, unlike, Fourier Transform. Fourier Transform loses the time information during transformation because it uses sinusoidal wave, a function with infinite support as basis function.

Based on the selection of scaling and shifting parameters and mode of application of wavelet transform, the wavelet transform can be of different types. Three of the most widely used wavelet transforms are as follows:

- Continuous Wavelet Transform (CWT)
- Discrete Wavelet Transform (DWT)
- Stationary Wavelet Transform (SWT)

These transforms are discussed in the following subsections.

3.1 Continuous Wavelet Transform (CWT)

If shifting and scaling factors are considered to be continuous over real number line while applying wavelet transform, the WT is called continuous wavelet transform (CWT). The CWT is computed by changing the scale of the analysis window, shifting the window in time, multiplying by the time series, and integrating over all times. In CWT, the transform is mathematically expressed as

$$W_f(a, b) = \frac{1}{\sqrt{C_\psi}} \int X(t) \Psi_{a,b}^*(t) dt \quad (7)$$

where $\Psi^*(t)$ denotes complex conjugate of $\Psi(t)$, $C_\psi = 2\pi \int |\hat{\Psi}(\omega)|^2 / \omega d\omega$ and $\hat{\Psi}(\omega)$ denotes the Fourier transform of $\Psi(t)$ given by

$$\hat{\Psi}(\omega) = \frac{1}{\sqrt{2\pi}} \int e^{i\omega t} \Psi(t) dt \quad (8)$$

If the mother wavelet ($\Psi(t)$) is orthogonal, then the inverse of wavelet transformation is given by

$$X(t) = \frac{1}{\sqrt{C_\psi}} \iint \frac{W_f(a, b) \Psi_{(a,b)}(t)}{a^2} da db \quad (9)$$

3.2 Discrete Wavelet Transform (DWT)

Discrete class of wavelets is formed when shifting and scaling parameters are considered discrete instead of continuous variables while applying wavelet transform. If the discrete wavelet is sampled over dyadic space-time grid, the resulting wavelets are called dyadic discrete wavelet [14]. The dyadic daughter wavelets are denoted by

$$\Psi_{j,b}(t) = \frac{1}{\sqrt{2^j}} \Psi\left(\frac{t}{2^j} - b\right) \quad (10)$$

The wavelet transform is given by

$$W_f(a, b) = \frac{1}{\sqrt{C_\psi}} \sum X(t) \Psi_{a,b}^*(t) \quad (11)$$

where $\Psi^*(t)$ denotes complex conjugate. C_ψ is as defined before. Discrete wavelet component is down-sampled or subband coded according to Nyquist–Shannon theorem [15]. The Nyquist–Shannon sampling theorem is a fundamental connection

between continuous and discrete representation of time series or signal. This theorem is applicable to any signal having finite range of frequencies or in other words, signal having zero Fourier transform coefficient outside some finite range of frequencies. According to this theorem, if any signal is sampled two times, first with a sampling rate of N_1 at scale a_1 , second at a sampling rate of N_2 at scale a_2 , then the information contained in these two sampling procedures is equivalent, given

$$N_2 = \frac{a_1}{a_2} N_1 \tag{12}$$

As the frequency range of wavelet components (generated by Eq. 11) is decreased by half, hence, the components can therefore be subsampled by 2, by discarding every alternate sample or sample falling at even places from the beginning. As a result, each of the components has half the length that original time series or signal had. Hence, DWT halves the time resolution but doubles the frequency resolution. Since, the frequency band of the time series now spans only half the previous frequency band; it effectively reduces the uncertainty in the frequency by half. This procedure is also known as subband coding (or down-sampling). Subband coding, however, results in wavelet coefficients depending on their location. As a result, a small change in input signal causes large changes in wavelet coefficients. This is termed as translation-invariance of DWT and is considered a major drawback which limits its application in signal analysis [16].

It should be noted that a discrete mother wavelet acts as a band-pass filter and scaling it for each level (for dyadic space) effectively halves its bandwidth. This creates the problem that in order to cover the entire spectrum (till the frequency limiting to zero), an infinite number of scaling is required. Hence, to cover the complete spectrum another function associated with the mother wavelet, Father Wavelet is used. Further, dyadic wavelet functions are orthogonal so the inverse of wavelet transform is given by

$$X(t) = \frac{1}{\sqrt{C_\psi}} \sum_{j, k \in \mathbb{Z}} X(t) \psi_{a,b}(t) \tag{13}$$

Alternatively, DWT can also be carried out by using a pair of filters—a high-pass and a low-pass filter. In DWT, the component obtained after convolution of signal with low-pass filter followed by dyadic down-sampling is called approximate component and one obtained by using high-pass filter and dyadic down-sampling is called detailed component. Low-pass filter is derived from scaling function and high-pass filter is derived from mother wavelet function. The DWT filters for Haar mother wavelet (discussed in Sect. 2) are given by

$$h_{r,c} = \begin{cases} 1/\sqrt{2} & c \in \{r, (r + 1) \bmod n\} \\ 0 & \text{otherwise} \end{cases} \tag{14}$$

$$g_{r,c} = \begin{cases} (-1)^{r-c}/\sqrt{2} & c \in \{r, (r+1) \bmod n\} \\ 0 & \text{otherwise} \end{cases} \quad (15)$$

where $h_{r,c}$ and $g_{r,c}$ are the elements of matrix H and G respectively, r and c represent the row and column of filter matrix. H and G are low-pass and high-pass filter matrix, respectively. Here, “mod” represents a module function. $k \bmod n = n$ if $k = n$, otherwise $k \bmod n =$ remainder of k divided by n . On closer observation, the low-pass filter is 2 term moving average operation and the high-pass filter is first-order differencing operation normalized with a factor of $1/\sqrt{2}$. When the time series is multiplied with these filters followed by dyadic down-sampling (ignoring every other value), two components are obtained. The component obtained after multiplication with high-pass filter is called detailed DWT component (denoted by d) and component obtained after multiplication with low-pass filter is termed approximate DWT component (denote by a).

3.3 Stationary Wavelet Transform (SWT)

Stationary Wavelet Transform (SWT) is specially designed to avoid the translation-invariance of DWT. SWT components are not down-sampled (as per Nyquist–Shannon sampling theorem) and the filter coefficients are up-sampled by a factor of $2^{(j-1)}$ in the j th level of algorithm. Hence, the SWT unlike DWT does not change the time resolution at any stage. But lack of subband coding results in redundancies in components as SWT components have twice the number of elements needed as per Nyquist–Shannon Theorem. However, SWT reduces the complexity of signal analysis as both input signal and its components have equal length. For obtaining Haar SWT components, time series can be multiplied with the filters given by Eqs. 14 and 15 without dyadic down-sampling.

4 Multi-resolution Analysis

Multi-Resolution Analysis (MRA) provides the detailed and approximate components at even lower levels by using low-pass filter component (approximate component) from higher level as input to wavelet transform at each subsequent level. Each application of WT reduces the frequency band of component into half and it helps in getting slow and fast dynamic component at different levels, which may enhance the accuracy of prediction. The MRA is named on the basis of the wavelet transform algorithm being used repeatedly, like Multi-Resolution Discrete Wavelet Transform (MRDWT) or Multi-Resolution Stationary Wavelet Transform (MRSWT). Irrespective of wavelet transformation used, after application of MRA a time series $X(t)$ is represented as

$$X(t) = \sum_k a_{0,k} \varphi_{0,k}(t) + \sum_{j=0}^{\infty} \sum_k d_{j,k} \Psi_{j,k}(t) \quad (16)$$

where $\varphi_{0,k}(t)$ and $\Psi_{j,k}(t)$ represent scaling function and mother wavelet function, respectively. The subscript pair j and k represent scale and shift parameters of mother wavelet or scaling function. The approximate component ($a_{0,k}$) and detailed component ($d_{j,k}$) are expressed as

$$a_{0,k} = \sum X(t) \varphi_{0,k}(t - k) \quad (17)$$

$$d_{j,k} = \sum X(t) 2^{-j} \Psi_{j,k}(2^{-j}t - k) \quad (18)$$

If maximum level of decomposition is L , $a_{0,k}$ series is also represented as a_L . Similarly, $d_{j,k}$ series are also represented as d_j , where $j \in 1, 2, \dots, L$. In form of filters, the components a_L and d_j are expressed as

$$a_L = G_L G_{L-1} \dots G_1 X \quad (19)$$

$$d_j = H_j G_{j-1} G_{j-2} \dots G_1 X = H_j a_{j-1} \text{ for } j \in \{1, 2, \dots, L\} \quad (20)$$

The low- and high-pass filters for Haar mother wavelet at any level l are given by

$$h_{l,r,c} = \begin{cases} 1/\sqrt{2} & c \in \{r, (r + 2^{(l-1)}) \bmod n\} \\ 0 & \text{otherwise.} \end{cases} \quad (21)$$

$$g_{l,r,c} = \begin{cases} (-1)^{r-c}/\sqrt{2} & c \in \{r, (r + 2^{(l-1)}) \bmod n\} \\ 0 & \text{otherwise.} \end{cases} \quad (22)$$

where $h_{l,r,c} \in H_l$, $g_{l,r,c} \in G_l$, H_l and G_l are low-pass and high-pass filter at level l . r and c represent row and column, respectively. It should be noted that for $l = 1$ the above equations are same as Eqs. 14 and 15.

5 Illustrative Example on Drought Prediction

Drought is a hydrological extreme of prolonged water deficit. It is slow initiating but long lasting phenomenon leading to huge economic losses. As per the American Meteorological Society [17], droughts are of four types, namely meteorological, agricultural, hydrological, and socioeconomic. The deficit in precipitation, soil moisture, and stream flow/reservoir storage leads to meteorological, agricultural, and hydrological drought, respectively. This illustrative example is on the drought prediction over one small and another medium size watersheds from central part of India. The

methodology and the results are mostly borrowed from Maity et al. [10] and Suman and Maity [18].

Since the hydrologic cycle is a continuous transport of water, the occurrence of meteorological drought is expected to propagate to other types of droughts [19]. Hence, it can be hypothesized that prolonged period of meteorological drought along with high evaporation loss may lead to soil moisture deficit, resulting in agricultural drought. Further, in the same way, intense agricultural drought may turn into hydrological drought given the long duration. This precedence or temporal consequences of different types of drought are easy to speculate, but it is difficult to model as a number of factors (of climatological, topographical and geographical characteristics) affect this precedence order. If basin size is relatively large, the lag in transition of drought is also expected [20]. Study of temporal transition of drought also has added advantage—the measurement of precipitation is more accurate and economical compared to measurement of soil moisture and streamflow (which may require specialized structure and may not be economical for large streams/catchment), hence, with the information of temporal transition of different types of drought, the drought prediction will be economical. Further, it may also lead to better drought preparedness and thus better mitigation strategy for the community. The following subsection briefly discusses the methodology of study followed by subsection for details of study area and results.

5.1 Methodology

Overall methodology is broadly divided into two modules—(i) Drought characterization using drought indices and generation of its time series. Further, the study of lagged correlation between the drought indices to check whether there is any delayed response of one drought index exists on the other, (ii) Formulation of different models considering the lagged information of predictor drought index, based on MRSWT components of drought indices. As stated above, the selected wavelet function is Haar wavelet, as this wavelet function is having better time localization capability, which renders it good for short lead period prediction. Further, the most potential model structure/type is selected for prediction. It should be noted that selected model structure may differ for different basins. The methodological overview is shown in Fig. 3. Details of these modules are presented in the following subsections.

5.1.1 Drought Characterization Through Standardized Indices

For drought characterization, many different drought indices are available in the literature like Palmer Drought Severity Index (PDSI), Keetch–Byram drought index (KBDI), Standardized Precipitation Index (SPI), etc. However, no single drought index is considered universal, rather, their suitability depends on its application for a particular problem [21]. For analyzing the interrelation of different kinds of drought

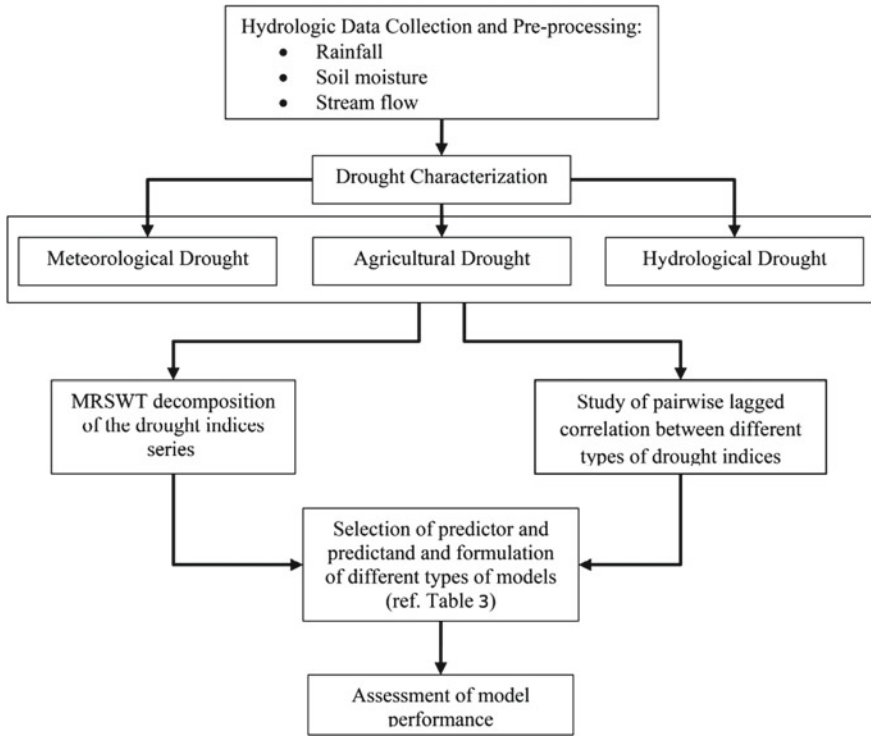


Fig. 3 Methodological overview (Source Maity et al. [10])

such as meteorological, agricultural, and hydrological droughts, a mathematical consistent drought index is needed for each of this drought type. Keeping this in mind, Standardized Precipitation Index (SPI), Standardized Soil Moisture Index (SSMI), and Standardized Stream Flow Index (SSFI) are used for characterization of meteorological, agricultural, and hydrological droughts, respectively. SPI, SSMI, and SSFI are calculated using monthly precipitation, soil moisture, and streamflow (at basin outlet), respectively. The concept of these drought indices is statistically similar to each other. SPI was first developed by McKee et al. [22] for the Fort Collins, Colorado river basin in the USA. SPI can be defined as standard normal variate of precipitation with respect to the standard deviation of precipitation for a given location and time period calculated from the historical precipitation data. SSMI and SSFI have similar conceptualization.

The computation of all the above mentioned indices (at a particular averaging timescale, say 3-monthly) can be outlined in the following common steps:

- (i) Time series of concerned variable is either accumulated or moving averaged for the desired averaging temporal scale.

- (ii) A suitable Probability Density Function (pdf) is fitted (Gamma distribution in this example) and corresponding Cumulative Distribution Function (CDF) is obtained.
- (iii) Using the fitted CDF, reduced variate of the concerned variable is computed.
- (iv) The reduced variate is transformed to a standard normal variate (mean = 0 and standard deviation = 1) to obtain the desired standardized index.

All these indices can have both positive and negative values, positive value showing a surplus and negative value showing a deficit. Prolonged and severe period of deficit may indicate a drought.

Depending on the characteristics of the study basin, sometime lag may be expected before effect of predecessor drought situation is observed over a successor one. The time lag may also originate due to nature of variable being studied. On the basis of expected precedence order, different predictor and predictant drought index relationships are considered. For instance, SPI is taken as predictor for SSMI and SSFI; SSMI is considered a predictor for SSFI. To quantify the time lag in drought propagation, lagged correlations between different predictand–predictor drought indices are studied. The lag with highest correlation is considered as the measure of delay in response that predictor drought series has on the predictand drought series.

5.1.2 Modeling of Drought Indices Interrelation

The drought indices are decomposed into components using MRSWT up to level 2. The mathematical details of MRSWT are presented in Sect. 4. By using MRSWT, the prediction of drought indices leads to the problem of predicting the slow and fast dynamic components separately. This approach may be advantageous, as prediction of slow dynamic or approximate component can be done with more confidence because variations are expected to be smaller and less abrupt compared to fast dynamic or detailed signal component. Prediction of the fast dynamic component is challenging as the model has to learn the fast dynamic and reduce noise simultaneously. The challenge can be solved by overfit/underfit tradeoff. Learning fast dynamic can lead to under fitting but learning to predict noise cause over fitting [23]. The decomposition through MRSWT results in three components (d_1 , d_2 , and a_2) for each of the drought indices.

The modeling of interrelation between the drought indices components may facilitate the prediction of successor drought from the state of predecessor one. Many approaches such as traditional (Multiple Linear Regression (MLR), Auto-Regressive Integrated Moving Average model with exogenous inputs (ARIMAX)) or even soft computing approaches (Artificial Neural Network (ANN)) can be used for modeling. In this example, models are formulated in two versions (keeping input and output variables same)—one using feed-forward ANN with single hidden layer and other using MLR. Models are formulated on the assumption that a dependent drought index or its components are affected by all the decomposed components of the independent drought index simultaneously with some delay. The information about the

delay in response is given due consideration in formulation of models. It should also be noted that minimum lead period also depends upon the level of decomposition being used to avoid the use of future information during the prediction. Since the maximum level for MRSWT is 2, minimum lead period for prediction is 2^2 , i.e., 4.

5.1.3 Model Validation Scheme

All the proposed models, except those based on ANN approach, are tested using two different validation schemes—I and II. Details of these schemes can be found in Maity et al. [10] and also briefly explained hereafter. ANN-based models are validated with scheme I only. Details of these schemes are discussed below. These validation schemes are also illustrated in Fig. 4.

- (i) Scheme I—Fixed Development and Testing Period: In this scheme, the whole data set is divided into development period and testing period. These periods remain stationary in one model calibration–prediction run. The parameters of the model are estimated during the development period. Complete testing period data set is predicted in the next model run. Hence, in this validation scheme, a model runs only two times, one for calibration in development period and other for prediction of testing data set.
- (ii) Scheme II—Moving Window Approach: In this scheme, testing period data length is same as that of development period, but these data periods are moving over the time series from one iteration to another. The model is first developed with the development period data set and for prediction, the window is shifted by one time step and the data from this new time step is considered in the testing period pool. Hence, though there is overlap between the development and testing period datasets, only one time step of the time series is considered as predicted in each iteration. For the next iteration, both development and testing periods are shifted by one time step and the process is continued until the prediction of whole remaining time series is complete. This scheme is useful to update the model parameters to capture any slow moving changes in the time series, particularly in the context of climate change.

5.1.4 Model Performance Evaluation

Performances of different models are assessed based on four statistical measures, namely correlation coefficient (r), Refined Index of Agreement (D_r) and unbiased Root Mean Square Error ($uRMSE$). Expressions for r can be found elsewhere [24]. The expression of D_r is given by [25]

$$D_r = \begin{cases} 1 - D_{r_frac} & \text{for } D_{r_frac} \leq 1 \\ \frac{1}{D_{r_frac}-1} & \text{for } D_{r_frac} > 1 \end{cases} \tag{23a}$$

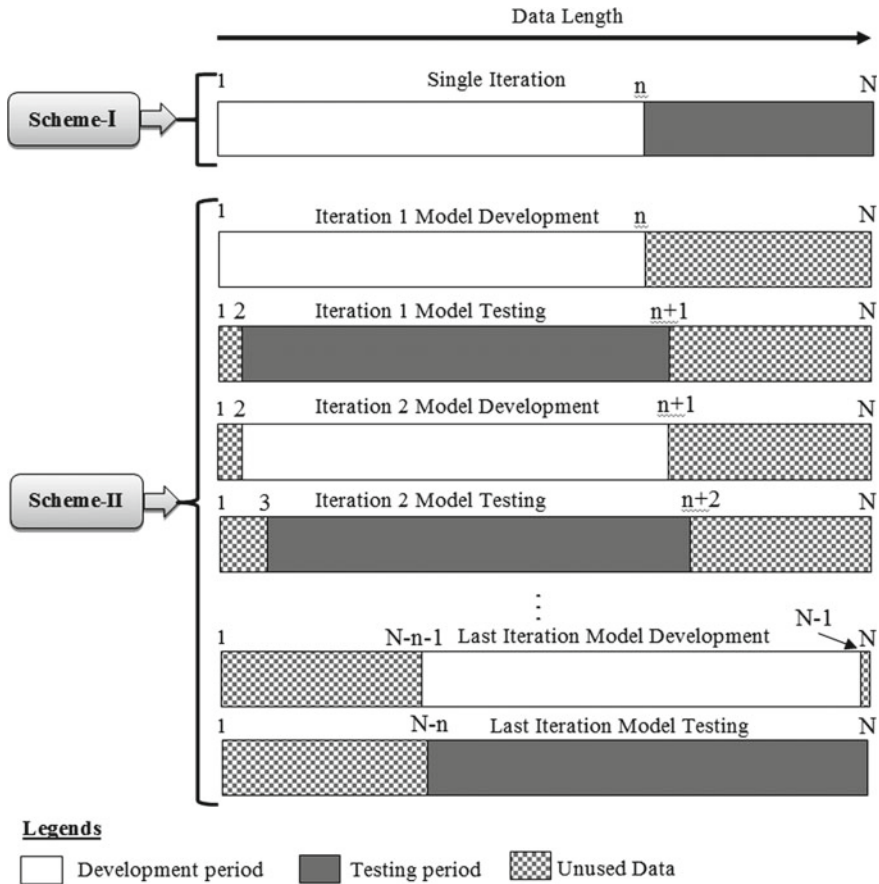


Fig. 4 Schematic diagram of two types of validation schemes [10]. In Scheme II, at any model testing iteration only the last value is recorded for performance assessment though the testing period overlaps the model development period of the same iteration

where D_{r_frac} is intermediate calculation step which is calculated as

$$D_{r_frac} = \frac{\sum_{i=1}^n |Y_i - X_i|}{2 \sum_{i=1}^n |X_i - \bar{X}|} \tag{23b}$$

where X_i and Y_i are the i^{th} observed and predicted values, \bar{X} is the mean of the observed values and n is the total number of observations.

The $uRMSE$ is the RMSE calculated between the deviations of observed and predicted values from their respective means. It is expressed as

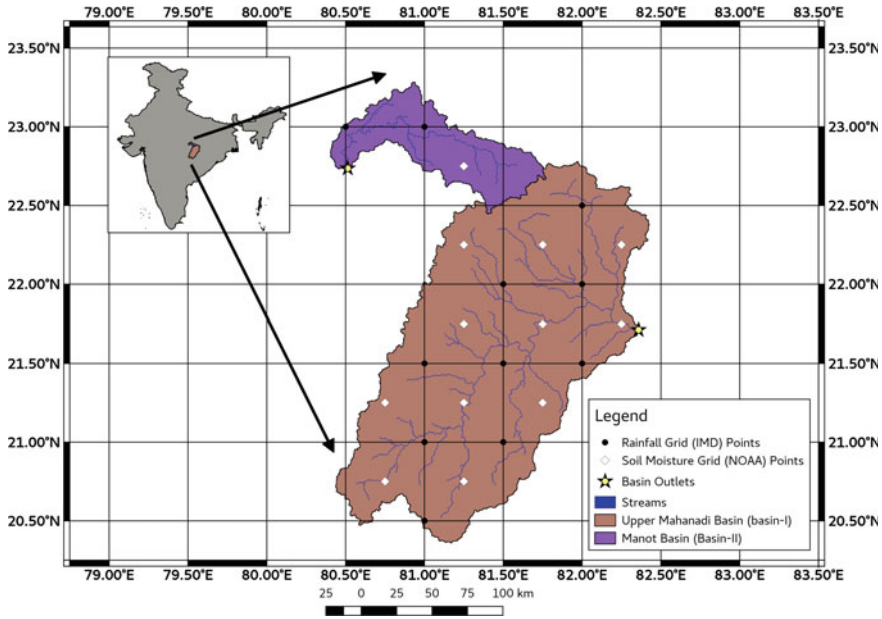


Fig. 5 Study basins—Upper Mahanadi Basin (Basin-I) and Upper Narmada Basin (Basin-II)

$$uRMSE = \sqrt{\frac{\sum_{i=1}^n \{(X_i - \bar{X}) - (Y_i - \bar{Y})\}^2}{n}} \tag{24}$$

where X_i, Y_i, \bar{X} and n are as defined before, \bar{Y} is the mean of the predicted values. The lower the value of uRMSE, the better the model performance. The uRMSE removes the mean bias between observed and predicted time series (unlike RMSE). Hence, uRMSE is better model performance measure (compared to RMSE) in the presence of mean bias [26].

5.2 Study Areas

Two different basins are selected—upper Mahanadi basin up to Jondra (henceforth, basin-I) and upper Narmada basin up to Manot (henceforth, basin-II). Basin-I is mostly located in the state of Chhattisgarh in India as shown in Fig. 5. The area of the basin is 29645 km² and it is approximately bounded by 20° N to 23° N latitude and 80.5° E to 82.5° E longitude. Basin-II is located in state of Madhya Pradesh in India as shown in Fig. 5. It has an area of 4667 km² and it is approximately bounded by 22.5° N to 23.5° N latitude and 80° E to 82° E longitude.

Daily rainfall data and monthly soil moisture data for the study basins are obtained for the period of 1971 to 2005 from the India Meteorological Department (IMD) [27] and Climate Prediction Center (CPC) of the National Oceanic and Atmospheric Administration (NOAA) [28], respectively. These data are available at a spatial resolution of 0.5° latitude \times 0.5° longitude and the data are taken from grid point lying within the respective study basin as shown in Fig. 5. Daily rainfall data at each grid point is converted to monthly rainfall depth by accumulating it over the month. Daily stream flow data at the outlet of the basins (Jondhra station for Basin-I and Manot station for Basin-II) are procured from the Water Resources Information System [29] in India. For basin-I streamflow record of June, 1979 to December, 2005 is available, so the study period for basin-I is considered as January 1980 to December 2005. However, for basin-II the streamflow record for June, 1978 to December, 2005 is available, hence, the study period is taken as January, 1979 to December, 2005 for this basin. The daily stream flow data is converted to monthly data.

5.3 Results and Discussions

Taking monthly rainfall depth, soil moisture time series, and stream flow series as input SPI, SSMI, and SSFI, respectively, for different basins are calculated using a mixed distribution—Gamma distribution for nonzero values with probability mass at zero. For monthly rainfall depth, accumulation over averaging timescale was done during SPI calculation but for all other variables moving average is calculated during index calculation. Notations of SPI-1, SSMI-1, and SSFI-1 are used for 1-month timescale. Similarly, SPI-3, SSMI-3, and SSFI-3 are used for 3-month timescale. SPI-3, SSMI-3, and SSFI-3 time series are shown in Fig. 6. From Fig. 6, it can be inferred that indices does not possess seasonality.

For studying the interrelation and propagation of different types of droughts, possible predecessor–successor or predictor–predictand pairs are selected. SPI is taken as predictor for SSMI and SSFI; SSMI is considered a predictor for SSFI. The relationships are deemed valid regardless of selected averaging period and basin. As stated earlier, January, 1980 to December, 2005 is chosen as study period for basin-I, so all drought index series are having 312 data points. First 160 data points are considered for the initial scrutiny and model development. For basin-II, the study period is selected as January, 1979 to December, 2005. Being a small basin, the response of one variable over the other is expected to be fast and more dynamic, hence, a longer development length of 204 is selected. It should be further noted that 10% of the data length after development length is used for validation in case of ANN-based models. The rest of the data are used for model testing. For initial scrutiny, the pairwise correlation coefficients (r) and the refined index of agreement (D_r) between the indices are computed according to their predictand–predictor relationship and the results are tabulated in Table 2. From Table 2, the correlation coefficient and refined index of agreement are higher for 3-month timescale indices. It is due to higher average period used to calculate the indices, which lead to more smoothing. The coefficient of

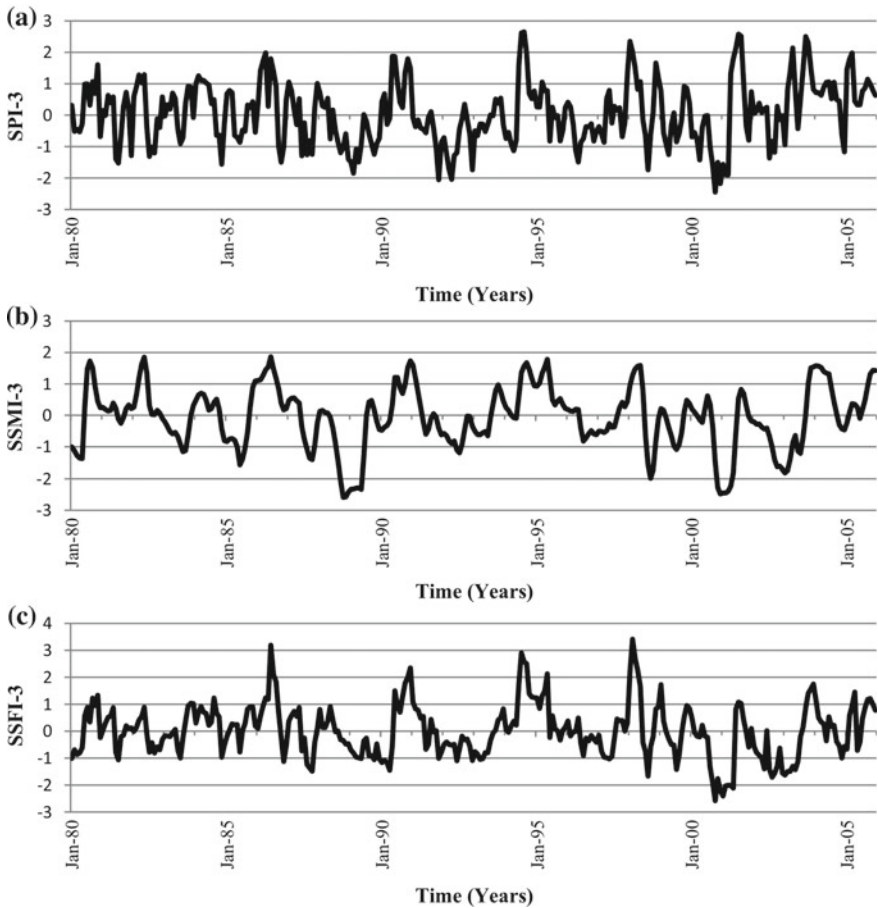


Fig. 6 Time series of **a** SPI-3 **b** SSMI-3 **c** SSFI-3 (January, 1980–December, 2005) for basin-I

correlation is found significant for all the cases, reaffirming the hypothesis that SSFI should be affected by both SPI and SSMI. Direct runoff due to precipitation events in catchment may affect the streamflow immediately, whereas the soil moisture is expected to affect streamflow by delayed subsurface flow. This suggests to incorporate the combination of different predictors (say, SPI and SSMI) with suitable lag to achieve possible better performance in predicting target drought index (say SSFI). It should also be noted that so far the lagged information is not considered from any of the predictor. The values in Table 2 are used as a reference for comparing the performance of different models as mentioned in the methodology. Any model that can exhibit better performance compared to these values can be considered as efficient and improvement over these reference values can be quantified.

The lagged correlation between all possible predictor–predictant drought index pairs is then calculated for both basins. The results for basin-I are shown in Fig. 7. It

Table 2 Correlation coefficients (r) and the refined index of agreement (D_r) for different drought indices pairs during development period

Basin	Averaging period (in months)	Performance statistics	Predictand drought index	Predictor drought index	
				SPI	SSMI
Basin-I	1	r	SSMI	0.401	1.000
			SSFI	0.588	0.607
		D_r	SSMI	0.436	1.000
			SSFI	0.516	0.502
	3	r	SSMI	0.590	1.000
			SSFI	0.682	0.661
		D_r	SSMI	0.543	1.000
			SSFI	0.585	0.564
Basin-II	1	r	SSMI	0.303	1.000
			SSFI	0.613	0.517
		D_r	SSMI	0.433	1.000
			SSFI	0.541	0.496
	3	r	SSMI	0.494	1.000
			SSFI	0.618	0.479
		D_r	SSMI	0.502	1.000
			SSFI	0.564	0.447

is noticed that the correlation coefficient between SSMI-3 and SPI-3 with lag 1 is the highest. This result suggests that SSMI has higher memory and changes slowly as compared to SPI. Thus, utilization of lagged values from predictor time series may enhance the prediction performance. In case of SSFI-3 and SSMI-3 as well as SSFI-3 and SPI-3, the correlation coefficient is highest without any lag. These observations suggest that SSFI is affected by both SPI and SSMI; utilization of values from these two predictors combined should enhance the prediction performance. In all predictor–predictant pairs, the value of correlation coefficients decreases gradually with the further increase in lag. For basin-II, the correlation coefficient for zero lag is found to be the highest for all predictand–predictor relationships. The correlation coefficient is found to decrease gradually with increase in lag. However, the lag considered in modeling of interrelation of drought indices should be either equal or greater than the averaging period and minimum lead period requirement as discussed in Sect. 5.1.2. To reiterate, minimum required lead period for prediction is 4, since MRSWT with level 2 is used. In case of drought indices calculated using 3-month accumulation, SPI-3 with lag 4 and/or 5 may be considered while predicting SSMI-3. Similarly, for SSFI-3, SPI-3 with lag 4, 5 and SSMI-3 with lag 4 may be important.

Five different models as shown in Table 3 are framed. Models 1 and 2 are used for predicting SSMI and models 3 to 5 are used for predicting the SSFI. During the

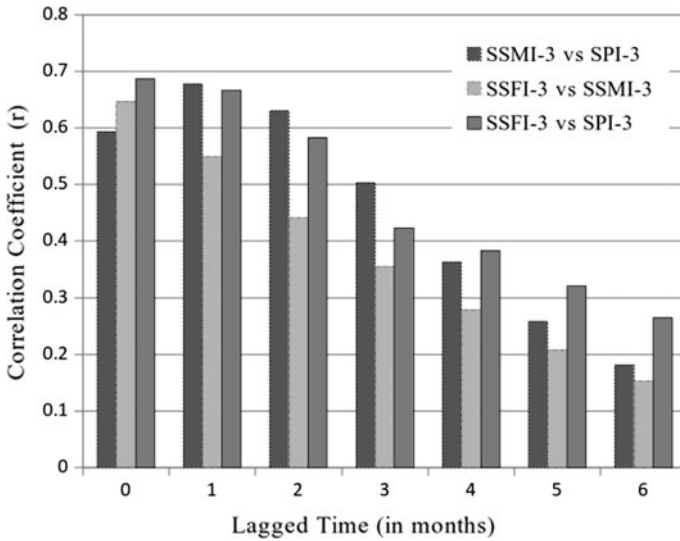


Fig. 7 Pairwise linear correspondence between SPI, SSMI and SSFI with lags during model development period in basin-I. Lags are applicable for the second index as shown in the legends for different pairs

application of models, the predictor drought time series is first decomposed into its components using MRSWT up to level 2. For instance, the components of SPI-3 for basin-I are shown in Fig. 8. The model performances during the development period and testing period are tabulated in Tables 4, 5 and 6, respectively. It should be noted that for ANN-based model, each model is trained 200 times and best trained model is selected for prediction.

During development period, the model performance is found to improve (Table 4a and 4b) as compared to Table 2. The improvement in performance is more apparent in case of higher averaging period. For instance, in case of basin-I corresponding to 1 month averaging period, the coefficient of correlation for MLR version of model 2 during development period is 0.831 between observed and predicted SSMI-1 (Table 4a) which is higher than the coefficient of correlation 0.401 between observed SSMI-1 and SPI-1 (Table 2). Though it is apparent that model 2 (for SSMI) and 5 (for SSFI) are best among other alternatives, it should be noted that the previous values of SSMI and SSFI are used in model 2 and 5, respectively. On the other hand, model 1 uses only information of SPI (with lags) and model 4 uses only SPI and SSMI (with lags), not the previous values of predictant series. Thus, the merit of model 1 (in case of SSMI) and model 4 (in case of SSFI) should be duly credited.

It is also noticed from the Table 4b that ANN versions of models are performing better than MLR version in most of the cases during model development period. However, the difference in performance between MLR and ANN is found to decrease when the averaging period is higher, i.e., 3. For example, in basin-I, the correlation

Table 3 Details of different types of models (No. 1 to 5). The function f is either of multiple linear regression or feed-forward ANN function with single hidden layer and the function g represents wavelet reconstruction function. Subscripts a_2 , d_2 and d_1 represent the decomposed components of the respective drought index series at level 2. $T_1 = 2^D$, where D is the level of decomposition, hence, $T_1 = 2^2 = 4$ and $T_{n+1} = T_n + 1$ for $n = 1, 2, \dots$

Model no.	Model description
1	$SSMI(t) = f \left(\begin{array}{l} SPI_{a_2}(t - T_1), SPI_{d_2}(t - T_1), SPI_{d_1}(t - T_1), \\ SPI_{a_2}(t - T_2), SPI_{d_2}(t - T_2), SPI_{d_1}(t - T_2) \end{array} \right)$
2	$SSMI(t) = f \left(\begin{array}{l} SPI_{a_2}(t - T_1), SPI_{d_2}(t - T_1), SPI_{d_1}(t - T_1), \\ SPI_{a_2}(t - T_2), SPI_{d_2}(t - T_2), SPI_{d_1}(t - T_2), \\ SSMI_{a_2}(t - T_1), SSMI_{d_2}(t - T_1), SSMI_{d_1}(t - T_1) \end{array} \right)$
3	$SSFI(t) = f \left(\begin{array}{l} SPI_{a_2}(t - T_1), SPI_{d_2}(t - T_1), SPI_{d_1}(t - T_1), \\ SPI_{a_2}(t - T_2), SPI_{d_2}(t - T_2), SPI_{d_1}(t - T_2) \end{array} \right)$
4	$SSFI(t) = f \left(\begin{array}{l} SPI_{a_2}(t - T_1), SPI_{d_2}(t - T_1), SPI_{d_1}(t - T_1), \\ SPI_{a_2}(t - T_2), SPI_{d_2}(t - T_2), SPI_{d_1}(t - T_2), \\ SSMI_{a_2}(t - T_1), SSMI_{d_2}(t - T_1), SSMI_{d_1}(t - T_1) \end{array} \right)$
5	$SSFI(t) = f \left(\begin{array}{l} SPI_{a_2}(t - T_1), SPI_{d_2}(t - T_1), SPI_{d_1}(t - T_1), \\ SPI_{a_2}(t - T_2), SPI_{d_2}(t - T_2), SPI_{d_1}(t - T_2), \\ SSMI_{a_2}(t - T_1), SSMI_{d_2}(t - T_1), SSMI_{d_1}(t - T_1), \\ SSFI_{a_2}(t - T_1), SSFI_{d_2}(t - T_1), SSFI_{d_1}(t - T_1) \end{array} \right)$

coefficient between observed and predicted SSMI-1 for MLR version and ANN version of model 2 are 0.831 and 0.873 respectively but for SSMI-3 it is 0.941 and 0.962 respectively. The performance of models predicting SSFI is, in general, inferior compared to model predicting SSMI. The decrease in performance may be due to combined effect of higher memory of soil moisture and the fact that many factors that affect streamflow, like evapo-transpiration, air temperature, etc., are not considered while predicting the SSFI.

Model performance during testing period is shown in Tables 5 and 6. As mentioned earlier, two different validation schemes are followed for MLR version of models. For MLR versions of model predicting SSMI, it is noticed that the model performance is either better or comparable with validation scheme I as compared to validation scheme II. Similarly, for MLR models predicting SSFI, model performance is either better or comparable with validation scheme II as compared to validation scheme I in case of basin-I, however, the opposite behavior is observed in case of basin-II. This observation suggests that in basin-I streamflow perhaps has time-varying correspondence or dynamic relationship with other drought indices, i.e., its relationship with other variable has changed with time, so validation scheme II, which is more compe-

Table 4 Performance of model no. 1 to 5 during development period

(a) using MLR							
Basin	Averaging period (in months)	Performance measures	Model no.				
			1	2	3	4	5
Basin-I	1	r	0.657	0.831	0.581	0.589	0.607
		D_r	0.612	0.733	0.620	0.620	0.626
		uRMSE	0.730	0.538	0.660	0.655	0.644
	3	r	0.748	0.941	0.736	0.743	0.792
		D_r	0.666	0.837	0.687	0.690	0.719
		uRMSE	0.632	0.322	0.559	0.552	0.503
Basin-II	1	r	0.447	0.815	0.434	0.438	0.513
		D_r	0.564	0.733	0.570	0.571	0.693
		uRMSE	0.785	0.508	0.816	0.814	0.778
	3	r	0.558	0.935	0.672	0.674	0.767
		D_r	0.584	0.831	0.651	0.653	0.715
		uRMSE	0.725	0.309	0.694	0.692	0.601
(b) using ANN							
Basin-I	1	r	0.681	0.873	0.563	0.428	0.567
		D_r	0.629	0.758	0.599	0.570	0.420
		uRMSE	0.710	0.472	0.675	0.735	0.869
	3	r	0.579	0.962	0.619	0.818	0.888
		D_r	0.550	0.867	0.612	0.725	0.783
		uRMSE	0.779	0.261	0.669	0.476	0.383
Basin-II	1	r	0.446	0.789	0.374	0.387	0.278
		D_r	0.543	0.696	0.438	0.502	0.408
		uRMSE	0.803	0.540	0.840	0.865	1.138
	3	r	0.517	0.941	0.657	0.781	0.807
		D_r	0.557	0.837	0.645	0.723	0.709
		uRMSE	0.755	0.297	0.709	0.589	0.555

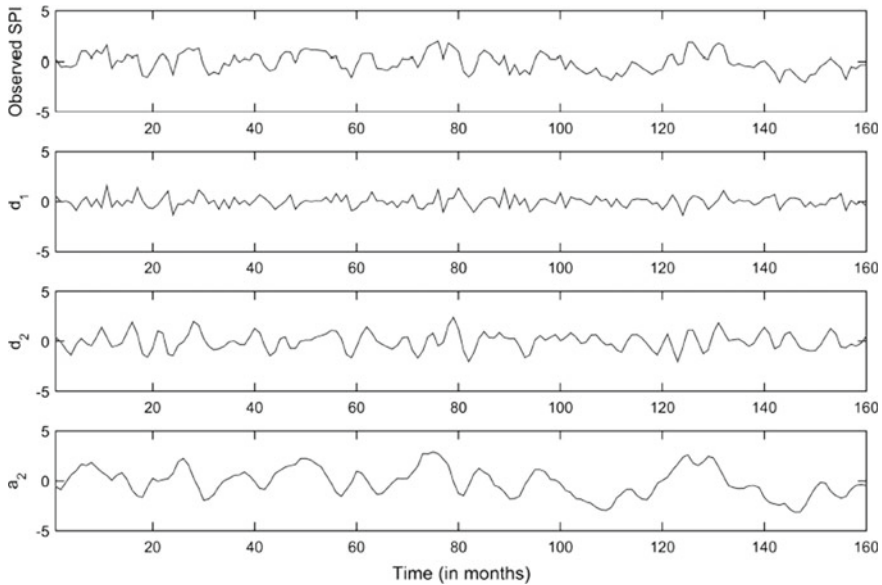


Fig. 8 Observed SPI-3 and its decomposed components up to level 2 for basin-I, i.e., a_2 , d_2 and d_1 , using Haar MRSWT. Figure shows the first 160 data points of decomposed series, i.e., development period for models. Such decomposed series for SSMI-3 and SSFI-3 are also obtained (not shown) for both basins

tent in modeling these dynamic relationships, produces better results. For example, with the validation scheme I and for predicting SSFI-3, the model 5 performance measures (r , D_r and uRMSE) are 0.792, 0.693, and 0.698, respectively, whereas the same with validation scheme II are 0.801, 0.712, and 0.682, respectively. Thus, the validation scheme II may be considered as more suitable where the correspondence between predictor and predictant may get modified over time due to the various reasons, including changing basin characteristics, climate regime, etc.

Interestingly, during testing, models using MLR version are found to perform comparable to ANN version in most of cases. This observation suggests that decomposed wavelet coefficient has linear relationship, so ANN version could not add much to the performance achieved by MLR version. Moreover, as stated earlier the per-

Table 5 Performance for model no. 1 to 5 during model testing period using MLR with both validation schemes I and II

Basin	Averaging period (in months)	Validation scheme	Performance measures	Model no.				
				1	2	3	4	5
Basin-I	1	I	r	0.671	0.871	0.446	0.427	0.550
			D_r	0.628	0.761	0.544	0.538	0.580
			uRMSE	0.766	0.507	1.018	1.031	0.949
		II	r	0.652	0.862	0.496	0.571	0.642
			D_r	0.621	0.754	0.566	0.594	0.627
			uRMSE	0.782	0.522	0.990	0.934	0.873
	3	I	r	0.720	0.954	0.636	0.625	0.792
			D_r	0.634	0.850	0.611	0.607	0.693
			uRMSE	0.709	0.304	0.879	0.889	0.698
		II	r	0.709	0.947	0.646	0.711	0.801
			D_r	0.633	0.843	0.630	0.659	0.712
			uRMSE	0.716	0.324	0.869	0.801	0.682
Basin-II	1	I	r	0.652	0.841	0.465	0.491	0.560
			D_r	0.592	0.748	0.556	0.557	0.589
			uRMSE	0.954	0.641	0.987	0.973	0.922
		II	r	0.651	0.837	0.391	0.388	0.497
			D_r	0.623	0.750	0.545	0.535	0.566
			uRMSE	0.914	0.645	1.023	1.030	0.969
	3	I	r	0.735	0.935	0.735	0.749	0.791
			D_r	0.629	0.836	0.618	0.623	0.683
			uRMSE	0.863	0.415	0.744	0.727	0.666
		II	r	0.728	0.934	0.700	0.691	0.763
			D_r	0.658	0.836	0.646	0.638	0.677
			uRMSE	0.828	0.420	0.779	0.783	0.700

formance of model predicting SSFI is inferior to model predicting SSMI in testing period too. The scatter plots for SSMI-3 and SSFI-3 modeled by MLR version of model 1 to 5 for validation scheme II are shown in Fig. 9.

The models are checked for sensitivity for mother wavelet selection and development data length. Mother wavelet sensitivity analysis on MLR version of the model was carried out using 160 development period data and with three mother wavelets namely Haar, Biorthogonal 1.1, and Reverse Biorthogonal 1.1. The model perfor-

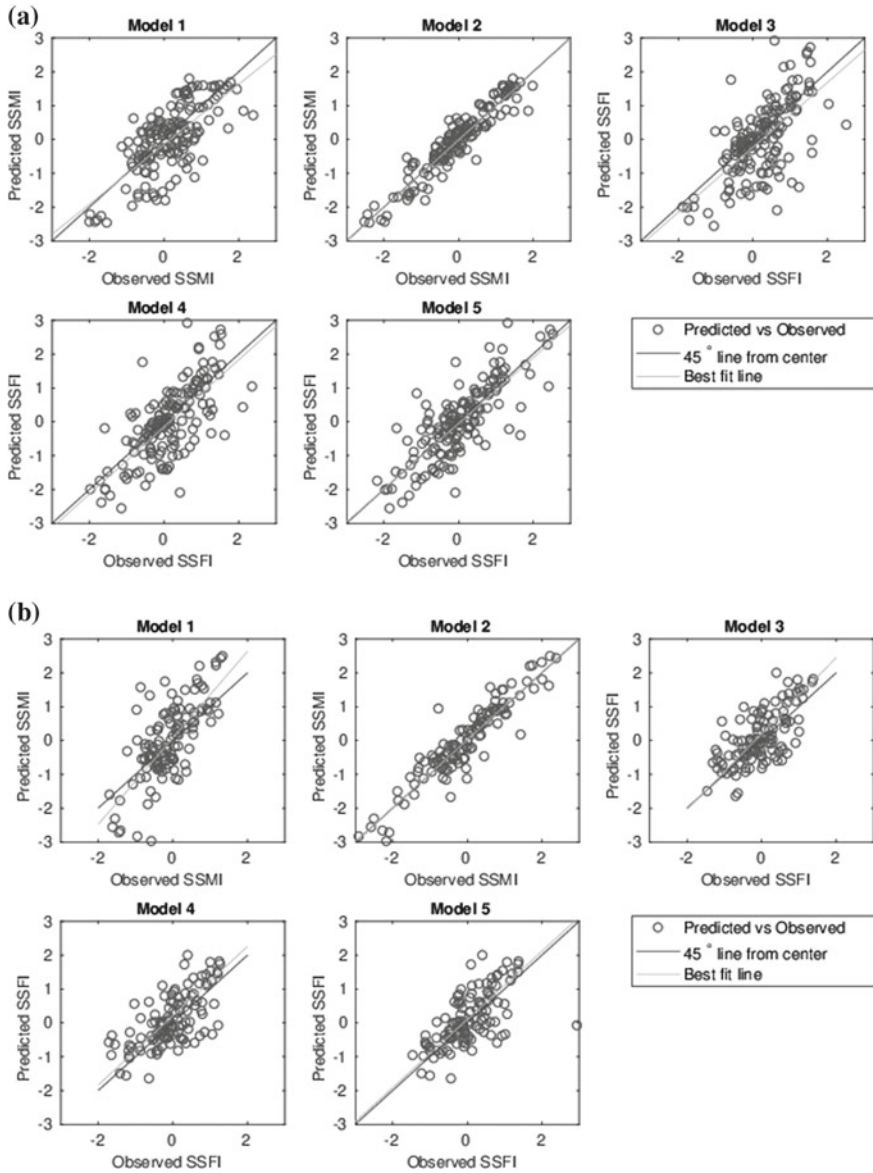


Fig. 9 Scatter plot between observed and predicted SSMI-3 and SSFI-3 by MLR version of models 1 to 5 during the testing period with validation scheme II for **a** Basin-I and **b** Basin-II

Table 6 Performance for model no. 1 to 5 during model testing period using ANN (only for validation scheme I)

Basin	Averaging period (in months)	Performance measures	Model no.				
			1	2	3	4	5
Basin-I	1	r	0.619	0.817	0.504	0.423	0.523
		D_r	0.592	0.712	0.533	0.544	0.517
		uRMSE	0.827	0.596	0.990	1.038	1.100
	3	r	0.638	0.884	0.596	0.566	0.698
		D_r	0.538	0.778	0.592	0.515	0.617
		uRMSE	0.789	0.473	0.939	1.059	0.822
Basin-II	1	r	0.620	0.796	0.426	0.420	0.262
		D_r	0.588	0.704	0.512	0.516	0.344
		uRMSE	0.929	0.719	1.014	1.020	1.309
	3	r	0.653	0.933	0.754	0.600	0.389
		D_r	0.616	0.829	0.587	0.513	0.546
		uRMSE	0.913	0.425	0.727	0.927	1.019

mances are found to be mostly insensitive to mother wavelet. Development period data length sensitivity is carried out on the MLR version of the models for development period data length ranging from 16 to 192. Model performance depends on the development data length, but its variation is very less beyond the length of 140 data points.

6 Summary and Concluding Remarks

Nonstationary nature of hydrologic variables, owing to various reasons including climatic change, poses a mathematical challenge to its predictability. In this chapter, the potential of wavelet transform is investigated in this regard. Initially, a brief introduction to various wavelets is presented followed by mathematical background of three mostly used wavelet transform. Next, mathematical details of MRSWT are provided which is used in an illustrative problem on drought prediction using the concept of temporal translation of one type of drought to another type.

In the illustrative example, one small and another medium size watersheds were considered from central part of India. For modeling the propagation of one drought type to another, the drought indices series are first transformed to their MRSWT components and their interrelationship is modeled using either ANN- or MLR-based models. Two different types of validation schemes (I and II) are used. Validation scheme I assumes that the model development period and testing period do not

change, hence, the underlying relationship between drought components is considered to be the same during development and testing periods. On the other hand, in validation scheme II, the relationship is assumed to evolve with time and such evolution is modeled by shifting the window for development and testing period by one month on each application of the model. Thus, the validation scheme II is more suitable in cases where the relationship between the decomposed components of drought indices time series is expected to be dynamic. On the other hand, validation scheme I assumes the relationship to be static.

The prediction of drought indices at component level is better as compared to when they are analyzed without decomposition. Hence, MRSWT is effective tools for decomposing the hydrological time series and the models developed utilizing the decomposed components usually have better prediction performance. For most of the cases, MLR-based models are found to perform comparable to their ANN counterparts. This observation suggests that decomposed wavelet coefficient has linear relationship, another benefit of MRSWT decomposition in our case (though it is not guaranteed). While considering three different mother wavelets namely Haar, Biorthogonal 1.1, and Reverse Biorthogonal 1.1, the model performances are found to be mostly insensitive to the choice of mother wavelet. Further, model performance depends on the development data length, but its variation dies down beyond the data length of 140. However, moving window approach of validation scheme (validation scheme II) is found to be more competent in modeling the dynamic/time-varying association between different drought indices as compared to the scheme with fixed development and testing period.

The methodological framework based on MRSWT is general in nature can be applied to other similar problems of hydrologic prediction. However, as in case of many statistical models, the methodology heavily depends on the length of the available historical data to capture the temporal evolution properly.

References

1. Milly PCD, Betancourt J, Falkenmark M, Hirsch RM, Kundzewicz ZW, Lettenmaier DP, Stouffer RJ (2008) Stationarity is dead: whither water management? *Science* 319(5863):573–574
2. Pichuka S, Maity R (2018) Development of a time-varying downscaling model considering non-stationarity using a Bayesian approach. *Int J Climatol* 38(7):3157–3176
3. Kirchner JW, Feng X, Neal C (2000) Fractal stream chemistry and its implications for contaminant transport in catchments. *Nature* 403(6769):524
4. Şen Z (1980) Adaptive fourier analysis of periodic-stochastic hydrologic sequences. *J Hydrol* 46(3–4):239–249
5. Pan F, Smerdon J, Stieglitz M, Webster P (2005) A wavelet approach to reconstructing near-surface temperature time series from observations of subsurface temperatures at several meters depth. In: AGU fall meeting abstracts
6. Westra S, Sharma A (2006) Dominant modes of interannual variability in australian rainfall analyzed using wavelets. *J Geophys Res Atmos* 111(D5)
7. Karthikeyan L, Kumar DN (2013) Predictability of nonstationary time series using wavelet and emd based arma models. *J Hydrol* 502:103–119

8. Smith LC, Turcotte DL, Isacks BL (1998) Stream flow characterization and feature detection using a discrete wavelet transform. *Hydrol Process* 12(2):233–249
9. Özger M, Mishra AK, Singh VP (2012) Long lead time drought forecasting using a wavelet and fuzzy logic combination model: a case study in texas. *J Hydrometeorol* 13(1):284–297
10. Maity R, Suman M, Verma NK (2016) Drought prediction using a wavelet based approach to model the temporal consequences of different types of droughts. *J Hydrol* 539:417–428
11. Labat D, Ababou R, Mangin A (2000) Rainfall–runoff relations for karstic springs. Part ii: continuous wavelet and discrete orthogonal multiresolution analyses. *J Hydrol* 238(3–4):149–178
12. Daubechies I (1988) Orthonormal bases of compactly supported wavelets. *Commun Pure Appl Math* 41(7):909–996
13. Maheswaran R, Khosa R (2012) Comparative study of different wavelets for hydrologic forecasting. *Comput Geosci* 46:284–295
14. Cao L, Hong Y, Fang H, He G (1995) Predicting chaotic time series with wavelet networks. *Physica D* 85(1–2):225–238
15. Shannon CE (1949) Communication in the presence of noise. *Proc IRE* 37(1):10–21
16. Bradley AP (2003) Shift-invariance in the discrete wavelet transform. In: *Proceedings of VIIIth digital image computing: techniques and applications*. Sydney 2003
17. American Meteorological Society (1997) Policy statement: meteorological drought. *Bull Amer Meteor Soc* 78:847–849
18. Suman M, Maity R (2016) Foreseeing the agricultural and hydrological drought knowing the ongoing meteorological scenarios through wavelet analysis. In: *Proceedings of the international conference on hydraulics, water resources, coastal & environmental engineering (HYDRO 2016 International)*, December 8–10, 2016 at CWPRS, Pune.
19. Maybank J et al (1995) Drought as a natural disaster. *Atmos Ocean* 33(2):195–222
20. Peters E, Torfs PJFF, van Lanen HAJ, Bier G (2003) Propagation of drought through groundwater—a new approach using linear reservoir theory. *Hydrol Process* 17(15):3023–3040. <https://doi.org/10.1002/hyp.1274>
21. Keyantash J, Dracup JA (2002) The quantification of drought: an evaluation of drought indices. *Bull Am Meteor Soc* 83(8):1167–1180
22. McKee TB, Doesken NJ, Kleist J others (1993) The relationship of drought frequency and duration to time scales. In: *Proceedings of the 8th conference on applied climatology* 17:179–183
23. Soltani S (2002) On the use of the wavelet decomposition for time series prediction. *Neuro-computing* 48(1–4):267–277
24. Krause P, Boyle D, Bäse F (2005) Comparison of different efficiency criteria for hydrological model assessment. *Adv Geosci* 5:89–97
25. Willmott CJ, Robeson SM, Matsuura K (2012) A refined index of model performance. *Int J Climatol* 32(13):2088–2094
26. Entekhabi D, Reichle RH, Koster RD, Crow WT (2010) Performance metrics for soil moisture retrievals and application requirements. *J Hydrometeorol* 11(3):832–840
27. ajeevan M., Bhate J (2009) A high resolution daily gridded rainfall dataset (1971–2005) for mesoscale meteorological studies. *Curr Sci*, 558–562
28. Fan Y, van den Dool H (2004) Climate prediction center global monthly soil moisture data set at 0.5 resolution for 1948 to present. *J Geophys Res Atmos* 109(D10)
29. India WRIS version 4 (2014) Non classified hydro observation data. <http://india-wris.nrsc.gov.in/HydroObservationStationApp.html>

Land–Atmosphere Interactions in Indian Monsoon at Sub-seasonal to Seasonal Scale



Amey Pathak and Subimal Ghosh

1 Introduction

The Indian Summer Monsoon Rainfall (ISMR) is a seasonal phenomenon that determines the fate of seasonal water availability across various sectors in the Indian subcontinent. Although the summer monsoon rainfall is generally perceived as a regular annual meteorological event, the variability associated in its evolution, persistence, and withdrawal emphasizes on its complex and uncertain nature. The monsoon system in the Indian subcontinent typically persists between the June and September month, and it exhibits a large amount of rainfall variability at various timescales ranging from daily to multi-decadal. The critical importance of understanding the monsoon variability can be sensed by looking at the trail of the monsoon research in the past few decades. A quantum of monsoon research is mostly aligned toward understanding the variability aspect of monsoon rainfall with an objective to have a better prediction insight of its cause and evolution. The variability component of summer monsoon rainfall is governed by the interplay of several atmospheric and geophysical phenomena such as the interaction between the large-scale processes over the tropical oceans, Eurasia, and the local-scale processes within the subcontinental land.

The role of tropical disturbances, especially over the Pacific Ocean and Indian Ocean [31] that are generally visible in wide range of time-varying physical mechanisms such as El Niño Southern Oscillations (ENSO), the Madden Julian Oscillations (MJO), the Indian Ocean Dipole (IOD), etc., are well documented in the

A. Pathak (✉)

Agricultural and Food Engineering Department, Indian Institute of Technology Kharagpur, Kharagpur 721302, West Bengal, India

e-mail: amey@agfe.iitkgp.ac.in; pathak.amey1@gmail.com

S. Ghosh

Interdisciplinary Program in Climate Studies and Department of Civil Engineering, Indian Institute of Technology Bombay, Mumbai 400076, Maharashtra, India

e-mail: subimal@civil.iitb.ac.in; subimal.ghosh@gmail.com

© Springer Nature Switzerland AG 2019

S. K. Singh and C. T. Dhanya (eds.), *Hydrology in a Changing World*, Springer Water, https://doi.org/10.1007/978-3-030-02197-9_6

139

literature. However, there exists very limited understanding of how the temperature anomalies (through evaporation–precipitation feedback) over the land surface can influence the precipitation over the Indian subcontinent. Here, in the present chapter, we emphasize the role of land surface feedback through evaporation in the seasonal and sub-seasonal variability of summer monsoon rainfall in the Indian subcontinent.

2 Importance Land Surface Feedback in ISMR

The precipitation during summer monsoon season in the Indian subcontinent is a response of a coupled ocean–land–atmosphere interactions that are reflected in terms of large-scale atmospheric circulations. Although the air–sea interactions during the monsoon season play a bigger role in the instigation of the temporal variability, the role of land surface cannot be ignored.

The land–atmosphere interactions result in a mass, momentum, and energy exchanges [7, 19, 20, 25] between the earth’s surface and the overlying atmosphere. These interactions can regulate the characteristics of the regional climate through various feedbacks (independent as well as overlapping). Hence, a proper understanding of the land–atmosphere interactions is necessary.

In order to study these interactions, we will have to understand the role of different hydrological variables in the precipitation process. The hydrological variables that mainly influences rainfall are the evaporation, the soil moisture, and the snow cover. The role of these three hydrological variables (soil moisture, snow cover, and evapotranspiration) in the ISMR is briefly discussed here.

2.1 *Soil Moisture–Precipitation Feedback*

Soil moisture prior to precipitation event can also influence the strength of the precipitation. A positive anomalous antecedent soil moisture condition can favor the precipitation [11] by altering the surface energy budget (i.e., by increasing the moist static energy near the surface). This is known as soil moisture–precipitation feedback which can either be negative (soil wetness suppresses the rainfall) or positive (soil wetness enhances the rainfall) in nature. Koster et al. [15] identified different regions (including central India) across the globe where the soil moisture anomaly has a substantial impact on precipitation during the northern hemisphere summer season. Moreover, Asharaf et al. [1] also found a dominant negative feedback mechanism over the Western and Northern India region, in response to wet initial soil conditions. Additionally, they also found a positive response to dry condition over the eastern region. Therefore, the seasonal predictability of monsoon can be improved by correctly prescribing the soil moisture anomalies and modeling the response of initialized soil moisture in the ISMR.

2.2 *Snow Cover–Precipitation Feedback*

The terrestrial snow cover influences the precipitation in four ways—(i) it controls the surface albedo (snow cover has high albedo), (ii) it insulates the heat between land and atmosphere, (iii) by heat sink effect due to snow melting, and (iv) as a climate memory by providing the soil moisture due to melting of snow [36]. Few studies have suggested that snow melting can have a negative impact on the ISMR [8, 35, 37]. Robock et al. [29] examined the interannual variability in monsoon rainfall due to the impact of land surface conditions over Eurasia and Indian summer monsoon rainfall using observations of snow cover and other hydrometeorological variables. The anomalous snow cover depth over western Eurasia is negatively linked with the summer monsoon precipitation over the Indian subcontinent [16, 32]. Furthermore, Peings and Douville [24] suggested that the relationship between the Indian summer monsoon and Eurasian snow cover is not direct and stationary, but through the ENSO condition.

2.3 *Evapotranspiration–Precipitation Feedback*

The earth surface through evapotranspiration provides water vapor to the atmosphere, which in turn may influence the characteristics of regional precipitation [5, 14, 34]. The atmospheric column of water vapor in any region is composed of two components—(i) “internal” component (i.e., water vapor evaporated within the same region) and (ii) the advective component (which is evaporated from another region and advected to the present region). The contribution of the locally evaporated water vapor (internal component) to the precipitation in the same region is known as “Precipitation Recycling” [9, 10], and the precipitation generated from the internal component is known as recycled precipitation. The recycling is quantified by recycling ratio “ R ”, which is a ratio of recycled precipitation to the total precipitation.

During the ISMR, the evapotranspiration increases as monsoon progresses and reaches its maximum during the end phase of the summer monsoon. The increased evapotranspiration during the monsoon activates the land surface feedback mechanism and significantly contributes to the recycled precipitation [21]. The oceanic moisture (advective component) has a main role in monsoon initiation but the moisture supplied from the local evapotranspiration enhances the subsequent precipitation through recycling. It is observed that the precipitation recycling has a strong contribution to the seasonal precipitation especially in central India, Ganges Plain, and northeast India during the August and September. In addition to that, Pathak et al. [21] also proposed that the precipitation recycling may have an important role in delaying the monsoon withdrawal over northeast India.

In this section, we have seen that the various land surface feedbacks, such as snow precipitation feedback, evapotranspiration–precipitation feedback, and soil moisture–precipitation feedback, are strongly associated with the Indian summer

monsoon. However, in this chapter, our main objective is to discuss the role of evapotranspiration–precipitation feedback in the Indian monsoon.

The evapotranspiration–precipitation feedback as described by Pathak et al. [21] suggests the potential role of evapotranspiration within the subcontinent to the ISMR; however, a recycling estimate alone cannot describe the complete moisture transport process, especially the origin and advection of moisture across different regions. Therefore, in order to have a detailed understanding on how moisture originated within the subcontinent induces variability in the ISMR, we need to identify key moisture sources and study the moisture transport and relative contributions of terrestrial moisture sources to the ISMR variability. In the next section, we shall discuss the identification of major terrestrial moisture sources within the subcontinent and quantification of their impact on the ISMR variability at seasonal and sub-seasonal scale.

3 Identification of Major Terrestrial Moisture Sources

In the past, studies involving quantification of moisture transport to the rainfall have been dealt with in a variety of ways, such as numerical tracer experiments, physical analysis using the isotopes, and analytical models. A detailed discussion of various methods, their assumptions, and limitation can be found in Budyko [3], Lettau et al. [17], Brubaker et al. [2], Eltahir and Bras [9, 10], Burde and Zangvil [4], and Dominguez et al. [6]. In the present chapter, we restrict ourselves to use dynamic recycling model (a physics-based Lagrangian moisture tracking approach) of Dominguez et al. [6] and Martinez and Dominguez [18]. The readers are advised to go through these articles for an in-depth understanding and comparison of the model physics.

DRM developed by Dominguez et al. [6] is based on conservation of atmospheric water vapor. The local recycling ratio “ R ” at any grid point (x, y, t_f) is calculated by following a trajectory of moisture weighted wind backward in time and estimating a ratio “ ε/w ” (evapotranspiration/precipitable water) for each of the time steps.

$$R(x, y, t_f) = 1 - \exp \left[- \int_0^{\tau} \frac{\varepsilon(\chi, \xi, \tau')}{\omega(\chi, \xi, \tau')} \partial \tau' \right] \quad (1)$$

Here, it is important to note that as the model runs are backward in time, the integration starts from the time of precipitation ($t_f = \tau$) to the time when it first enters the boundary of the region (at time = 0).

The model proposed by Martinez and Dominguez [18] is an extension of their previous model [6] with the ability to accommodate the effect of different moisture source regions. Figure 1 shows the schematic representation of the trajectory (starting at point “ a ” and ending at point “ f ”) of moisture weighted wind that accumulates evaporated water vapor from five different regions, i.e., the Ganga Basin (GB), South-Central India (SCI), South Peninsular India (SPI), Western Ghats (WG), and Western

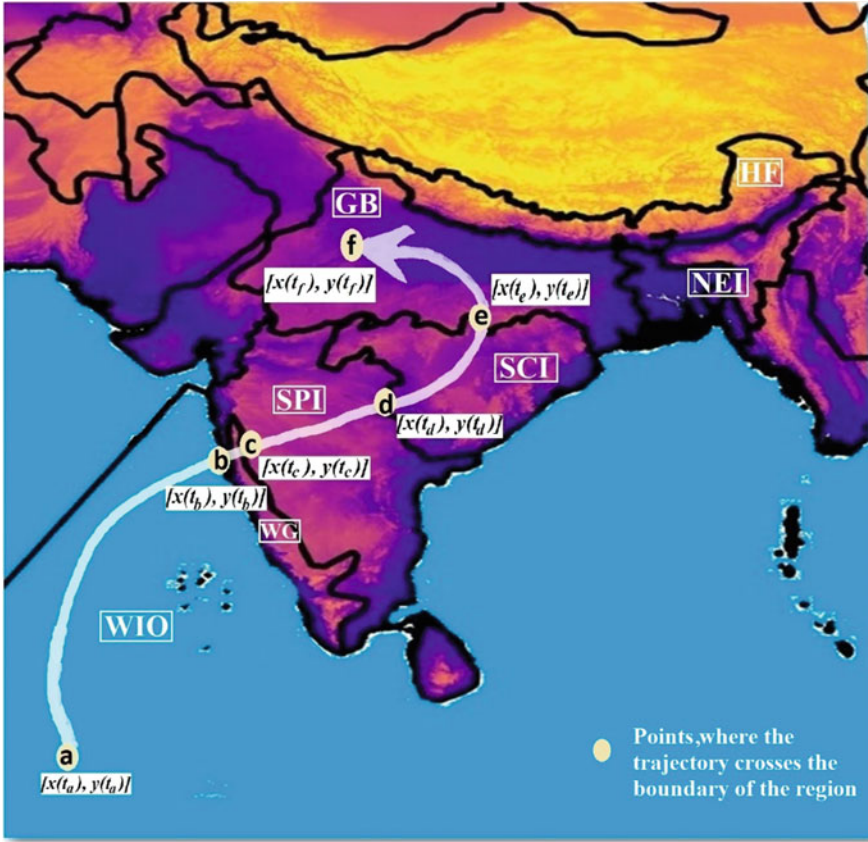


Fig. 1 Schematic representation of the moisture trajectory (in white color). Here, the region boundaries are similar to that of Pathak et al. [22]

Indian Ocean (*WIO*), respectively, prior to precipitation over sink location (x, y, t_f) in *GB*.

The fraction of precipitation originated from any two adjoining regions altogether, for example, from the regions *GB* and *SCI*, can be obtained by calculating the ratio (“ ε/ω ”) along the path of the trajectory segment $f-d$. The fraction of atmospheric moisture present in the trajectory between the points $[x(t_f), y(t_f)]$ and the $[x(t_d), y(t_d)]$, resulting from evaporation in *GB* and *SCI*, is given by

$$R(x, y, t_f) = 1 - \exp \left[- \int_{t_d}^{t_f} \frac{\varepsilon(\chi, \xi, \tau')}{\omega(\chi, \xi, \tau')} \partial \tau' \right] = R_{GB}(x, y, t_f) + \alpha_{GB}(x, y, t_f) * R_{SCI}(x, y, t_f) \quad (2)$$

where

$$R_{GB}(x, y, t_f) = 1 - \exp \left[- \int_{t_e}^{t_f} \frac{\epsilon(\chi, \xi, \tau')}{\omega(\chi, \xi, \tau')} \partial \tau' \right], \quad (3)$$

$$R_{SCI}(x, y, t_f) = 1 - \exp \left[- \int_{t_d}^{t_e} \frac{\epsilon(\chi, \xi, \tau')}{\omega(\chi, \xi, \tau')} \partial \tau' \right], \quad (4)$$

$$\alpha_{GB}(x, y, t_f) = 1 - R_{GB}(x, y, t_f). \quad (5)$$

Here, α_{GB} represents the fraction of moisture produced in *SCI* of the trajectory that is not lost (via precipitation) in the intermediate part of the trajectory: that is, *GB*. Therefore, the total contribution at sink (x, y, t_f) , from all the four regions (traversed by the trajectory segments $S_1: f-e$, $S_2: e-d$, $S_3: d-c$, and $S_4: c-b$ in Fig. 1) within the Indian subcontinent, and along the trajectory of the moisture weighted winds, is grouped as

$$\alpha_{Ind_sub}(x, y, t_f) = \sum_{S_i \in Ind_sub} \left(\prod_{j=1}^{S_i-1} \alpha_j(x, y, t_f) \right) * R_{S_i}(x, y, t_f). \quad (6)$$

4 Role of Terrestrial Moisture Sources in the Seasonal Precipitation

The seasonal mean [June, July, August, and September (JJAS)] of the fraction of moisture originating from different terrestrial sources that contribute to the ISMR is presented here. Among the subcontinental terrestrial regions, GB (Ganga Basin), and SCI (South-Central India) are the main sources of atmospheric moisture (Fig. 2). A high amount of moisture contribution from GB can be interpreted as recycling within the GB, which is probably associated with the evapotranspiration from the large-scale agricultural land use. In addition to high recycling, the evaporated water from the GB also provides atmospheric moisture for the precipitation over Northeast India (NEI) and Himalayan Forest (HF).

The SCI, which has a relatively higher density of forest cover and high atmospheric moisture from high evapotranspiration, provides water vapor to central India, East India, and south-central India. Although the recycling is in a range of 5–10%, the contribution from south-central India to ISMR is relatively lesser (~5%) than the contributions from the GB (~15%). The significant amount of recycling is observed in NEI region; however, its effect is mainly concentrated within the same region. Similarly, the regions such as SPI and HF do not contribute significantly toward the all India monsoon rainfall.

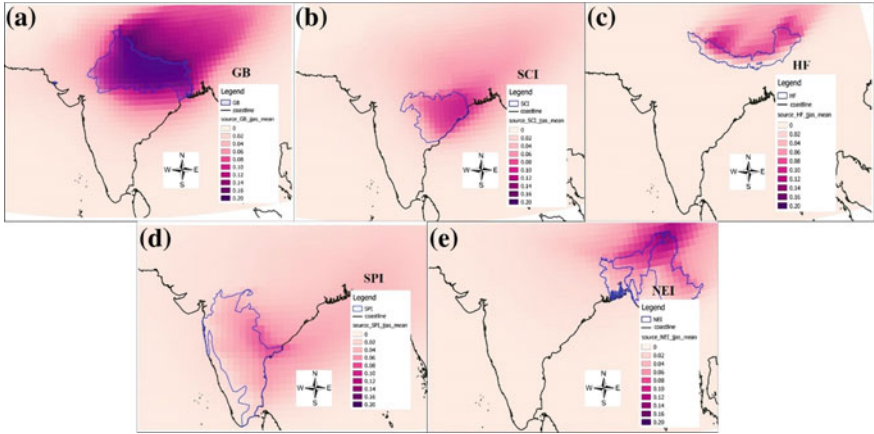


Fig. 2 Mean fraction of JJAS moisture originated from subcontinental land regions (Reproduced from: Pathak A., Ghosh S., Martinez J.A., Dominguez F., and P. Kumar, 2017a: Role of Oceanic and Land Moisture Sources and Transport in the Seasonal and Interannual variability of Summer Monsoon in India, *Journal of Climate*, 30, 1839–1859, under the copyright of ©American Meteorological Society)

Here, it is important to note that these contributions are only from the terrestrial sources those are within the Indian subcontinent, and the contribution of oceanic sources is not included in this chapter. Readers are advised to see Pathak et al. [22] to have a detailed discussion on the role of moisture transport from different oceanic sources to the ISMR.

4.1 Role of Terrestrial Moisture Sources in Interannual Variability of ISMR

Among all the scales of temporal variations, the interannual variation of ISMR has a significant impact on seasonal water availability in the Indian subcontinent. Even with the standard deviation, only about 10% of its mean, the impacts are extremely large and, therefore severely affects the Gross Domestic Product (GDP) of India [13]. Skillful predictions of seasonal variability are still a challenge for climate models. The variability in the rainfall during strong and weak years is linked with the transport of atmospheric moisture from different oceanic and terrestrial evaporative sources. Figure 3 shows the percentage of atmospheric moisture originated from subcontinental evaporative sources (GB, SCI, SPI, and NEI) that contribute to the precipitation over the core monsoon zone during the JJAS. The contribution from almost all the terrestrial evaporative sources increases as the monsoon season progresses, and there exists a large amount of daily as well as year-to-year variability in atmospheric moisture transport from different terrestrial evaporative sources to

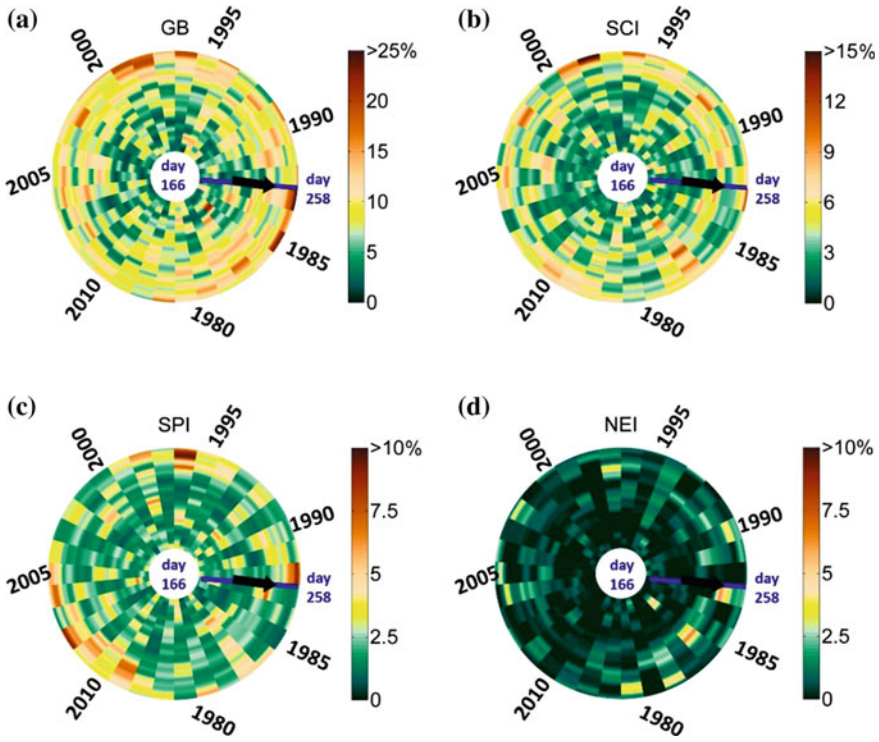


Fig. 3 Percentage of JJAS moisture originated from different subcontinental land regions resulting into precipitation over core monsoon zone

the core monsoon zone. Therefore, we need to separately analyze the atmospheric moisture transport from different terrestrial sources during the strong monsoon and weak monsoon years.

The precipitation over the core monsoon zone is a well-known measure of the strength of ISMR over the Indian subcontinent. Therefore, we can use standardized precipitation anomaly over the core monsoon zone (as shown in Rajeevan et al. [26] and in Fig. 5c) as an indicator to quantify the strength of the rainfall across different years. Pathak et al. [22] analyzed the atmospheric moisture transport from different evaporative sources during a strong monsoon and a weak monsoon year.

Figure 4 shows the contributions from major evaporative sources during strong and weak monsoon years. Generally, precipitation over the core monsoon zone is dominated by the oceanic sources, when compared with the subcontinental terrestrial sources. However, their contributions during strong and weak monsoon years (Fig. 4a, b) are different. During strong years, oceanic sources, as well as terrestrial sources, contribute significantly to the total precipitation, with very high oceanic contributions at the start and high terrestrial contributions during the end of the monsoon. The high evapotranspiration from the terrestrial sources in addition to the good contributions

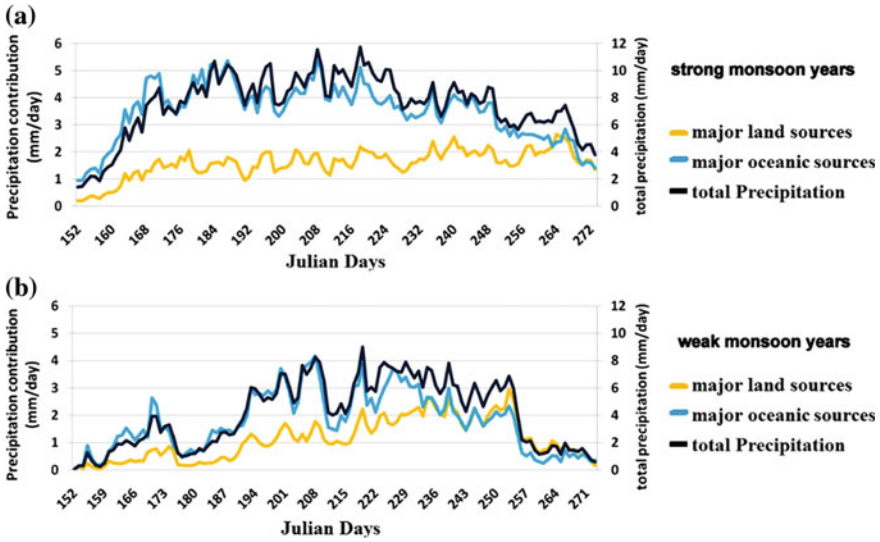


Fig. 4 Moisture originating from different sources during strong (a) and weak (b) monsoon rainfall years (Reproduced from: Pathak A., Ghosh S., Martinez J.A., Dominguez F., and P. Kumar, 2017a: Role of Oceanic and Land Moisture Sources and Transport in the Seasonal and Interannual variability of Summer Monsoon in India, *Journal of Climate*, 30, 1839–1859, under the copyright of ©American Meteorological Society)

from oceanic sources collectively sustains the monsoon and results in an increased monsoon spell duration (Fig. 4a).

Contrary to that, during weak monsoon years, a weaker atmospheric moisture transport from the ocean results in low rainfall in the initial phase of the monsoon. The delayed onset and low rainfall during the initial phase of monsoon results in early weakening of evapotranspiration–precipitation feedback due to low availability of soil moisture over the subcontinent land, and hence, it ultimately results in shorter spell length compared to the strong monsoon years. Furthermore, it is observed that the prolonged and increased moisture supply from the oceanic sources and the GB during the initial and final phases of the monsoon period, respectively, results in a net strong seasonal rainfall [22].

4.2 Role of Terrestrial Moisture Sources in Sub-seasonal Variability of ISMR

In the previous section, we have seen that a strong land surface feedback due to high evapotranspiration–precipitation leads to a prolonged and strong monsoon season. The seasonal variability of the summer monsoon rainfall is strongly linked with the sub-seasonal variability, and most of the agricultural activities are dependent on the

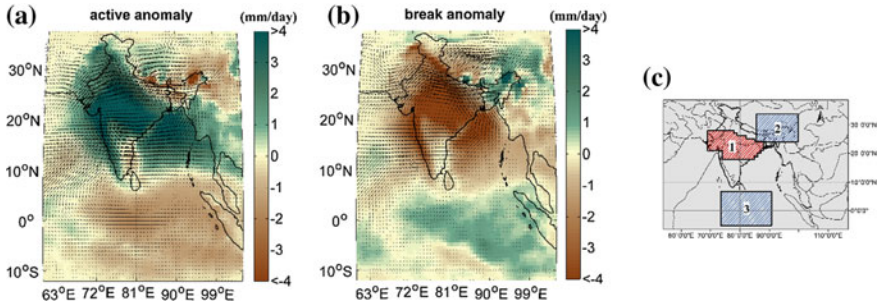


Fig. 5 Precipitation anomaly during **a** active and **b** break period of Indian summer monsoon (Adapted from [23], under **Creative Commons Attribution 4.0 License**)

good spells of rainfall within the monsoon season. Hence, for reliable modeling and prediction of ISMR, an understanding of the causes and impact of variability at the sub-seasonal scale is of utmost importance. Therefore, in this section, we will discuss, how the intraseasonal variability of the ISMR is linked with the terrestrial moisture transport?

The sub-seasonal variability of ISMR is generally characterized in the form of periods of active (increased rainfall) and periods of break (less or cessation of rainfall activity), over the core monsoon region. The active and break period can be identified using criteria proposed by Rajeevan et al. [26] which is based on standardized rainfall anomaly over the core monsoon zone. Active periods are the periods (in days) during which standardized rainfall anomaly is greater than ± 1.0 for at least 3 consecutive days. Similarly, break periods are the periods (in days) during which standardized rainfall anomaly is less than -1.0 for at least 3 consecutive days.

A monsoon trough [27] that builds up over the core monsoon zone (Fig. 5c) results in excess precipitable water and rainfall over the core monsoon zone during the active period (Fig. 5a). In contrast to that, during a break period, this low-pressure system migrates to the Himalayan foothills [28, 33], resulting in excess rainfall over *region2* (Fig. 5c) and low rainfall over the core monsoon zone (Fig. 5b).

If we look closely at Fig. 5a, b, we can see that there are two kinds of asymmetrical pattern between *region1*, *region2*, and *region3* (Fig. 5c); a north–south contrast in precipitation anomaly between the *region1* and *region3* (Fig. 5a, b) and an east–west fluctuating pattern between the *region1* and *region2* (Fig. 5a, b). The north–south contrast is associated with the sub-seasonal fluctuations of Tropical Convergence Zone (TCZ) [12, 30], between the core monsoon zone “*region1*” and the tropical Indian Ocean “*region3*”. A northward (southward) shift of TCZ results in high (low) rainfall over the core monsoon zone during the active (Break) period. Pathak et al. [23] observed that the atmospheric moisture transport from the oceanic sources is strongly linked with this north–south anomalous pattern of precipitation between *region1* and *region3*. It is important to note that the north–south fluctuating pattern of precipitation anomaly has been widely discussed in the literature and often viewed as the predominant mode of intraseasonal variability, but the east–west variability has

not received much attention. Here, we investigate this interesting feature of ISMR variability with the help of moisture transport from different evaporative sources during active and break periods.

Figure 6 shows the anomaly of the moisture contributions from major terrestrial sources (GB and SCI) during active and break period. This closely resembles an anomalous east–west asymmetric pattern of precipitation between the *region1* and *region2* in Fig. 5a, b. Therefore, the east–west rainfall asymmetry during active and break periods (Fig. 5a, b) is strongly linked with the anomalous contribution from the terrestrial moisture sources to the core monsoon zone and to northeast India. Furthermore, the monsoon breaks are generally associated with a northward shift of monsoon trough to the Himalayan foothills and northeast India (Fig. 5.4b in Pathak et al. [23]) and a southward protruding mid-latitude trough [28, 33]. This condition results in an establishment of a strong subtropical westerlies circulation by replacing the monsoonal easterlies. A strong northwesterly current during the breaks results in an advection of terrestrial moisture from the GB to northeast India (Fig. 6b), whereas, in case of active periods, the southwesterly jet becomes prominent. A relatively higher amount of recycling within the GB is observed during active periods (Fig. 6a) than during the monsoon breaks.

5 Conclusions

In this chapter, we analyzed the atmospheric moisture transport from different terrestrial evaporative sources to the Indian subcontinent during the summer monsoon rainfall. The major terrestrial sources that significantly influence the monsoon rainfall variability within the Indian subcontinent are Ganga basin (GB) and South-Central India (SCI). The overall strength of the monsoon rainfall is strongly governed by the amount of oceanic moisture transport during the initial phase of the monsoon and high terrestrial contributions, especially from GB during the withdrawal phase of the monsoon at the end of September. During the strong monsoon years, a strong evapotranspiration–precipitation feedback leads to a prolonged and sustained monsoon season, whereas during the weak monsoon years, the contributions from the terrestrial sources do not last long and it results in a shorter span of the monsoon season.

The sub-seasonal variability of ISMR in the form of active and break periods is also strongly associated with the fluctuations of Tropical Convergence Zone (TCZ) and resulting anomalous atmospheric moisture transport from different oceanic and terrestrial evaporative sources. The terrestrial sources such as GB and SCI under the influence of the large-scale westerlies significantly contribute to the east–west asymmetry in rainfall anomaly between the core monsoon zone and northeast India. The north–south asymmetry, between the core monsoon zone and the tropical Indian Ocean, however, is mostly governed by the oceanic moisture transport.

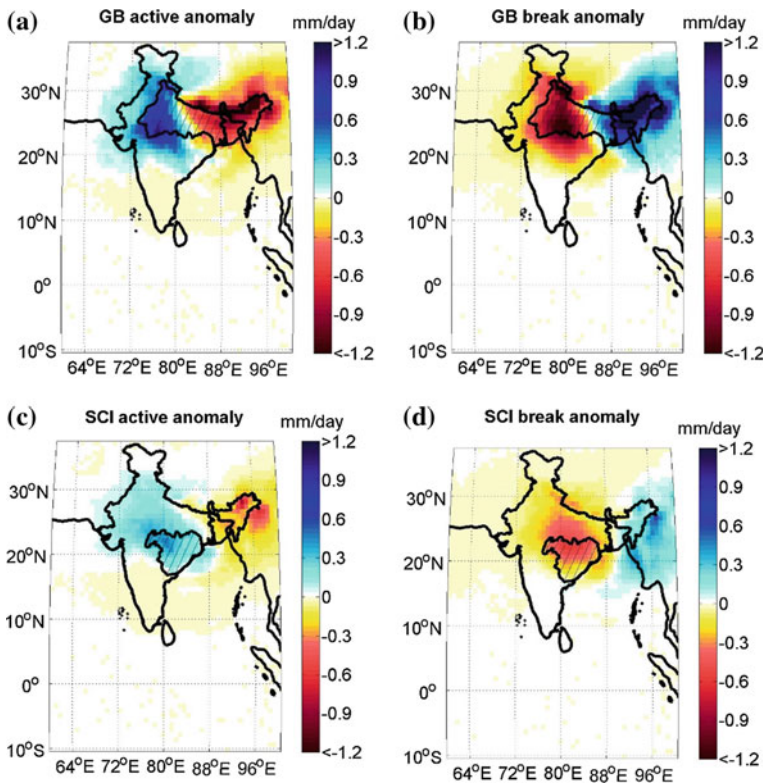


Fig. 6 Anomaly of the moisture contributions from major terrestrial sources (*GB* and *SCI*) during active and break period (Adapted from [23], under **Creative Commons Attribution 4.0 License**)

In this chapter, we have seen that the terrestrial moisture through evapotranspiration–precipitation feedback has an important role in the seasonal and sub-seasonal variability of ISMR. Here, it is also important to note that the land surface processes and their interactions with the atmosphere are complex in nature. Therefore, a considerable amount of uncertainty is associated with the reanalysis data of land surface evapotranspiration and the computed amount of recycled precipitation. Hence, by improving the land surface processes in the model and by including the more realistic dataset, we can achieve the goal of accurate prediction of the seasonal and sub-seasonal variability of ISMR.

References

1. Asharaf S, Dobler A, Ahrens B (2011) Soil moisture initialization effects in the Indian monsoon system. *Adv Sci Res* 6:161–165
2. Brubaker KL, Entekhabi D, Eagleson PS (1993) Estimation of continental precipitation recycling. *J Climate* 6:1077–1089
3. Budyko MI (1974) *Climate and life*. Academic Press, p 508
4. Burde GI, Zangvil A (2001) The estimation of regional precipitation recycling. Part I: review of recycling models. *J Climate* 14:497–2508
5. Dirmeyer PA, Shukla J (1993) Observational and modeling studies of the influence of soil moisture anomalies on the atmospheric circulation. In: Shukla J (ed) *Predictions of interannual climate variations*. NATO Series I, vol. 6. Springer–Verlag, pp 1–23
6. Dominguez F, Kumar P, Liang X, Ting M (2006) Impact of atmospheric moisture storage on precipitation recycling. *J Climate* 19:1513–1530
7. Dominguez F, Kumar P (2008) Precipitation recycling variability and ecoclimatological stability—a study using NARR data. Part I: central US plains ecoregion. *J Climate* 21:5165–5186
8. Douville H, Royer JF (1996) Sensitivity of the Asian summer monsoon to an anomalous Eurasian snow cover with in the Meteo-France GCM. *Clim Dyn* 12:449–466
9. Eltahir EAB, Bras RL (1994) Precipitation recycling in the Amazon basin. *Q J R Meteorol Soc* 120:861–880
10. Eltahir EAB, Bras RL (1996) Precipitation recycling. *Rev Geophys* 34:367–378
11. Eltahir EAB (1998) A soil moisture–rainfall feedback mechanism: theory and observations. *Water Resour Res* 34(4):765–776. <https://doi.org/10.1029/97wr03499>, <http://dx.doi.org/10.1029/46897WR03499>
12. Gadgil S (2003) The Indian monsoon and its variability. *Annu Rev Earth Planet Sci* 31:429–467. <https://doi.org/10.1146/annurev.earth.31.100901.141251>
13. Gadgil S, Vinayachandran PN, Francis PA (2003) Droughts of the Indian summer monsoon: role of clouds over the Indian Ocean. *Curr Sci* 85:1713–1719
14. Higgins W, Gochis D (2007) Synthesis of results from the North American Monsoon Experiment (NAME) process study. *J Climate* 20:1601–1607
15. Koster RD, Dirmeyer PA, Guo ZC, Bonan G, Chan E, Cox P, Gordon CT, Kanae S, Kowalczyk E, Lawrence D, Liu P, Lu CH, Malyshev S, McAvaney B, Mitchell K, Mocko D, Oki T, Oleson K, Pitman A, Sud YC, Taylor CM, Verseghy D, Vasic R, Xue YK, Yamada T (2004) Regions of strong coupling between soil moisture and precipitation. *Science* 305:1138–1140
16. Kripalani RH, Kulkarni A, Sabade SS (2001) El Niño–Southern Oscillation, Eurasian Snow Cover and the Indian monsoon rainfall. *Proc Ind Natl Sci Acad* 67A:361–368
17. Lettau H, Lettau K, Molion LCB (1979) Amazonia’s hydrologic cycle and the role of atmospheric recycling in assessing deforestation effects. *Mon Wea Rev* 107:227–238
18. Martinez JA, Dominguez F (2014) Sources of atmospheric moisture for the La Plata River Basin. *J Clim* 27:6737–6753. <https://doi.org/10.1175/JCLI-D-14-00022.1>
19. McPherson RA (2007) A review of vegetation–atmosphere interactions and their influences on mesoscale phenomena. *Prog Phys Geogr* 31:261–285. <https://doi.org/10.1177/0309133307079055>
20. Osborne TM, Lawrence DM, Slingo JM, Challinor AJ, Wheeler TR (2004) Influence of vegetation on the local climate and hydrology in the tropics: sensitivity to soil parameters. *Clim Dyn* 23:45–61. <https://doi.org/10.1007/s00382-004-0421-1>
21. Pathak A, Ghosh S, Kumar P (2014) Precipitation recycling in the Indian subcontinent during summer monsoon. *J Hydrometeorol* 15:2050–2066. <https://doi.org/10.1175/JHM-D-13-0172.1>
22. Pathak A, Ghosh S, Martinez JA, Dominguez F, Kumar P (2017) Role of oceanic and land moisture sources and transport in the seasonal and inter–annual variability of summer monsoon in India. *J Clim* 30:1839–1859

23. Pathak A, Ghosh S, Murtugudde R, Kumar P (2017b) Role of Oceanic and Terrestrial Atmospheric Moisture Sources in Intra-seasonal variability of Indian summer monsoon rainfall. *Sci Rep* 7. Nature Publishing Group. Article number: 12729. <https://doi.org/10.1038/s41598-017-13115-7>
24. Peings Y, Douville H (2010) Influence of the Eurasian snow cover on the Indian summer monsoon variability in observed climatologies and CMIP3 simulations. *Clim Dyn* 34:643–660. <https://doi.org/10.1007/s00382-009-0565-0>
25. Pielke RA, Avissar R, Raupach M, Dolman AJ, Zeng X, Denning AS (1998) Interaction between the atmosphere and terrestrial ecosystems: influence on weather and climate. *Glob Chang Biol* 4:461–475. <http://www.climatesci.org/publications/pdf/R-192.pdf>
26. Rajeevan M, Gadgil S, Bhate J (2010) Active and break spells of Indian summer monsoon. *J Earth Syst Sci* 119(3):229–247
27. Ramamurthy K (1969) monsoon of India: Some aspects of breaks in the Indian south west monsoon during July and August. *Forecasting Manual, Part IV, India Meteorological Department*
28. Ramaswamy C (1962) Breaks in the Indian summer monsoon as a phenomenon of interaction between the easterly and the sub-tropical westerly jet streams. *Tellus XIV*:337–349. <https://doi.org/10.3402/tellusa.v14i3.9560>
29. Robock A, Mu M, Vinnikov K, Robinson D (2003) Land surface conditions over Eurasia and Indian summer monsoon rainfall. *J Geophys Res* 108. ISSN 0148-0227. <https://doi.org/10.1029/2002jd002286>
30. Sikka DR, Gadgil S (1980) On the maximum cloud zone and the ITCZ over Indian, longitudes during the southwest monsoon. *Mon Weather Rev* 108:1840–1853. [https://doi.org/10.1175/1520-0493\(1980\)108<1840:otmcza>2.0.co;2](https://doi.org/10.1175/1520-0493(1980)108<1840:otmcza>2.0.co;2)
31. Sreejith OP, Panickal S, Pai S, Rajeevan M (2015) An Indian Ocean precursor for Indian summer monsoon rainfall variability. *Geophys Res Lett* 42:9345–9354. <https://doi.org/10.1002/2015GL065950>
32. Turner A, Slingo J (2011) Using idealized snow forcing to test teleconnections with the Indian summer monsoon in the Hadley centre GCM. *Clim Dyn*, 1–19. <https://doi.org/10.1007/s00382-010-0805-3>
33. Vellore, RK, Krishnan R, Pendharkar J, Choudhury AD, Sabin TP (2014) On the anomalous precipitation enhancement over the Himalayan foothills during monsoon breaks. *Clim Dyn*, 1–23. <https://doi.org/10.1007/s00382-013-2024-1>
34. Watts C, Scott R, Garatuza-Payan J, Rodriguez JC, Prueger JH, Kustas WP, Douglas M (2007) Changes in vegetation condition and surface fluxes during NAME 2004. *J Clim* 17:3892–3906
35. Yang S, Lau KM, Yoo SH, Kinter JL, Miyakoda K, Ho CH (2004) Upstream subtropical signals preceding the Asian summer monsoon circulation. *J Clim* 17:4213–4229
36. Yasunari T (2007) Role of land-atmosphere interaction on Asian monsoon climate. *J Meteor Soc Jpn* 85B:55–75
37. Yasunari T (1991) The monsoon year—a new concept of the climatic year in the tropics. *Bull Am Meteor Soc* 72:1131–1138

Assessment of Climate Change Impacts on IDF Curves in Qatar Using Ensemble Climate Modeling Approach



Abdullah Al Mamoon, Ataur Rahman and Niels E. Joergensen

1 Introduction

Understanding the climate change impact on hydrological conditions is considered to be a major challenge in the context of management of stormwater and infrastructure planning. According to the climate projections of the Intergovernmental Panel on Climate Change (IPCC), for the Arabian Peninsula, the future average annual rainfall may decrease, and the frequency and intensity of extreme rainfall events are likely to increase [19]. This study, in particular, focuses on the assessment of the impacts of climate change on extreme rainfall in Qatar.

Climate change is a major future risk affecting multiple sectors in the Gulf countries including Qatar [31]. Studies on rainfall in Qatar showed evidence of a greater spatial and temporal variability [27]. The 5th phase of Coupled Model Inter-comparison Project (CMIP5) model results show that Qatar is at the high end of precipitation sensitivity to changes in average mean temperature [20].

There have been few studies on the application of CMIP5 models to extreme rainfalls. For example, Kawazoe and William [21] analyzed the ability of CMIP5 models to produce heavy daily precipitation events in an upper Mississippi region. The study focused on the winter season during 1980–1999. By comparing the climate model output with observations, the study supports the use of CMIP5 models to assess the changes in heavy rainfall events in future climate scenarios. In another study, Chadwick et al. [7] investigated the spatial pattern of precipitation change

A. A. Mamoon
Ministry of Municipality and Environment, Doha, Qatar

A. A. Mamoon · A. Rahman (✉)
School of Computing, Engineering and Mathematics, University of Western
Sydney, Sydney, NSW, Australia
e-mail: a.rahman@westernsydney.edu.au

N. E. Joergensen
COWI A/S, Doha, Qatar

in fourteen CMIP5 models for the scenario RCP 8.5 (Representative Concentration Pathways) between the historical 1971–2000 and 2071–2100. The study covers the tropical region between 30°N and 30°S which includes Qatar. The rate-of-change around Qatar is found to have the lowest magnitude in the studied tropical region.

For climate impact assessment regarding design rainfall estimation, the availability of high-quality long precipitation time series with high temporal and spatial resolution is essential [13]. A possible source of obtaining this data is through downscaling of data from a Global Climate Model (GCM) [10]. Typically, climate data simulated by GCMs have a horizontal resolution between approximately 150 and 300 km. Downscaling of information from GCMs to a finer spatial resolution is therefore used to assess the impacts of climate change at regional and local scales [14].

Numerous GCMs and statistical downscaling methods have been applied to climate change impact studies, but none clearly recommended the most appropriate one for a particular application. Choice of GCMs is therefore considered extremely important in projecting impact of climate change [5]. Because multi-model ensembles contain information from all participating models [33], it is generally believed that multi-model ensembles are superior to single GCM [9].

Climate model projections are associated with uncertainties from various sources. The most common sources of uncertainties include the GCMs used, climate downscaling techniques, emission scenarios, model structure, and parameters [8, 25, 32, 35, 40]. For example, Mandal et al. [24] investigated different sources of uncertainty in the assessment of the climate change impacts on total monthly precipitation in the Campbell River basin, British Columbia, Canada. The results show that the selection of a downscaling method for Campbell River basin provides the largest degree of uncertainty when compared to the choice of GCM and/or emission scenario.

Extreme design rainfalls in the form of IDF curves are used as an essential tool for the purpose of urban drainage system planning [15]. Worldwide, studies have been carried out assessing the impact of future climate on IDF curves. For example, Singh et al. [37] assessed the impact of IDF curves for Roorkee, India using observed and an ensemble of GCMs. Analysis of the IDF curves indicated an increase in precipitation intensities for all the RCP scenarios. Increase in the intensities of extreme storms also observed by Zhu [42] in various climatic regions across the USA with strong regional variations. Abiodun et al. [1] observed an increase in the intensity and frequency of grid-point extreme rainfall events over three cities in Africa.

Afroz et al. [2] investigated climate change impact on Probable Maximum Precipitation (PMP) in Chenar Rahdar River basin, southern Iran. Two GCMs (HadCM3 and CGCM3) used under A2 emission scenario. Comparison of the future to the base extreme rainfalls and PMP showed an increase of up to 18.2% and 27.3%, respectively, by the two models. A study by Akbari et al. [3] on the impact of climate change on IDF curves over the same Chenar Rahdar River basin indicated a decrease in short duration rainfall (1- and 3-h) and increase in long duration rainfall (6-, 9-, and 12-h) intensities.

Xu et al. [40] modeled possible impacts of climate change on regional extreme precipitation (indicated by 24-h design rainfall depth) at seven rainfall stations in the Qiantang River basin, East China. The final results indicated that 24-h design rainfall depth would increase in the majority of the stations under the three GCMs and emission scenarios. On the other hand, IDF curves developed by Herath et al. [14] for future periods taking future climate change into account for Perth in Australia found decreasing rainfall depth for the 2020s, 2050s, and 2080s. Sun et al. [36] adopted nonstationary frequency analysis to predict extreme rainfall over the globe under a warming climate condition and found that daily extreme precipitation is likely to increase in future in the high latitude regions of the Northern Hemisphere. Sarhadi and Soulis [34] found that stationarity assumptions underestimate the IDF curves in the Great Lakes area of North America.

In a recent study, the climate change scenarios in Qatar were analyzed using two models (NCAR-CCSM and CSIRO-MK3.5) from the third phase of the Coupled Model Inter-comparison Project (CMIP3), available for AR4 [26]. The results indicated an increase of 68–76% for the 100-year rainfall depth from the current (2000–2029) to future scenario (2070–2099).

From the above studies, it appears that the impact of global warming on design rainfall varies with geographic location and it is not possible to draw any general conclusion across the globe from a particular study [6]. Hence, region-specific studies are needed to assess the impacts of climate change on design rainfall for a specific region. This is the main motivation behind this study, which focuses on the use of the state-of-the-art CMIP5 models to assess the impacts of climate change on design rainfall in Qatar till 2100. Qatar is investing significantly in infrastructure with long service lives such as large stormwater systems. These structures are required to be resilient under influence of climate change expected to occur within their design lives. The main objective of this study is to provide an estimation of the change in IDF curves under the influence of climate change up to the year 2100.

2 Study Area and Rainfall Data Selection

Qatar is located off the eastern coast of Saudi Arabia, in the Arabian Gulf. Extreme rainfall intensities vary significantly over Qatar with higher intensity in the north compared to the south. The multi-model average of CMIP5 models also exhibits high seasonal variability of precipitation around Qatar at the end of twenty-first century.

A total of 32 stations with daily data from Qatar and the surrounding countries were initially selected in this study. The data period ranges from 1972 to 2015. In addition to Qatar data, the daily rainfall data from the neighboring Gulf countries including Bahrain, UAE, and KSA were also included in the analysis. The majority of data collected measured as daily (24-h) rainfall. The additional short duration rainfall data have also been used to derive rainfall distributions for short duration rainfall. Extensive quality control of collected rainfall data was carried out using

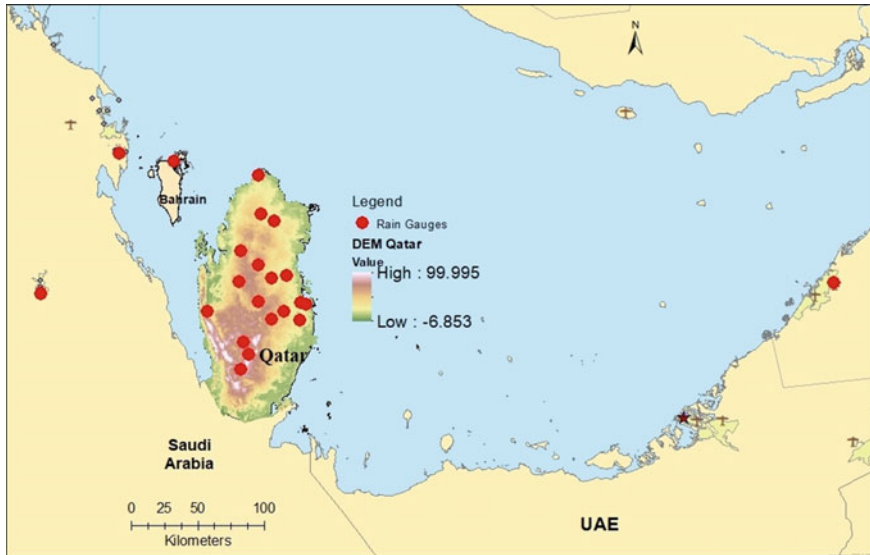


Fig. 1 Location of selected 23 stations

several techniques that included application of double mass curve analysis, tests for record consistency between nearby gauges and discordance measurement tests. Rain gauges with fewer than 15 years of observations were excluded. After applying the above criteria, only 23 stations were retained for the analysis. The locations of selected rain gauges are shown in Fig. 1.

3 Current Climate IDF Curves

The IDF curves for current climate in Qatar have been developed using similar approach adopted by the previous studies, i.e., L moments-based index frequency approach [26, 28]. This study incorporates additional rainfall data from the years 2012–2015 and includes additional short duration rainfall data from Qatar and three neighboring countries as described in Sect. 2. The additional short duration rainfall data have also been used to derive better sub-daily rain depth ratios. The site L-moments are used to form homogeneous regions using H-statistics [16]. A total of seven regions are tested with various combinations of stations. A homogeneous region consisting of 23 stations is selected, providing an Annual Maximum Series (AMS) with 1014 data points. The preferred homogeneous region is comprised of 19 Qatari stations, one Bahraini station, two KSA stations, and one UAE station (total 23 stations). Based on Z-statistics, the analysis indicated Pearson Type III (PE3) as the preferred three-parameter statistical distribution. Additionally, upper and lower bounds for 68%- and 95% confidence intervals of the regional curve were

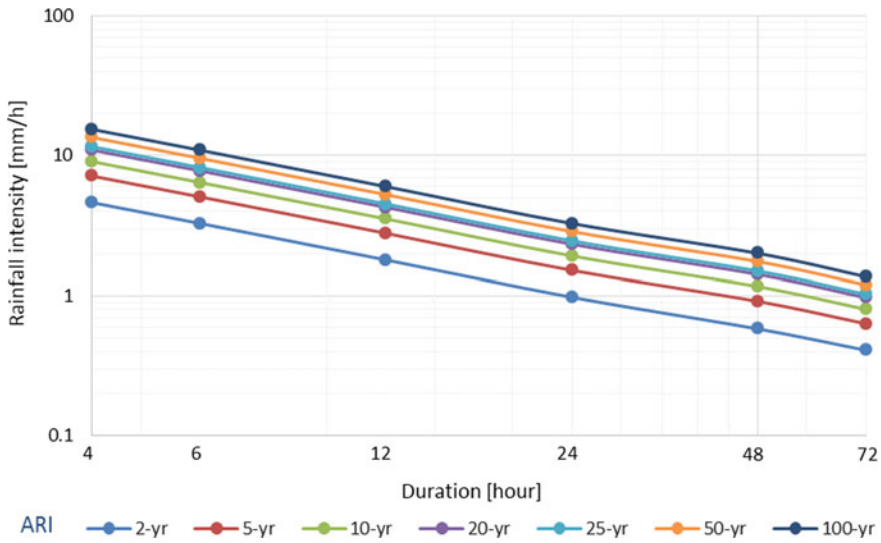


Fig. 2 Current climate IDF curves (Doha Old Airport)

determined applying the procedure recommended by Hoskings and Wallis [16]. The current climate IDF curve for Doha Old Airport is shown in Fig. 2.

4 Methodology for Development of Future IDF Curves

4.1 Selection of Models and Scenarios

The future climate conditions are established based on the Fifth Assessment Report (AR5) [20]. AR5 is based on CMIP5; with more than 50 models developed by 24 modeling groups around the world, the CMIP5 is the state-of-the-art multi-model dataset with generally higher spatial resolution. Compared with the IPCC AR4, the GCM simulations in AR5 include a more diverse set of model types [23].

The CMIP5 models represent a significant improvement over CMIP3 models used in the earlier study in Qatar [26], especially for simulation of global surface temperature, large-scale precipitation, climate variability, and extreme events [20]. For precipitation specifically, it is found that the spatial pattern correlation between modeled and observed annual mean has increased from 0.77 for CMIP3 models to 0.82 for CMIP5 models [12]. With these improvements, the current study is expected to capture a wider and more accurate range of variability in terms of design rainfall under climate change [29].

The CMIP5 models include two types of simulations: (i) near-term simulations (10- to 30-year time horizon) and (ii) long-term simulations (century timescale, up to

the year 2100 and beyond). The scenarios for the long-term simulations are of interest for this study, as they are designed for comparison with observations or providing projection.

There are 61 models from 22 modeling centers worldwide. Each model has been run with several scenarios, and in total there are 609 scenarios available for selection. Special conditions have been applied for the selection of appropriate models and model scenarios for this study, which include the following:

- The grid cell size of the model should not exceed $300 \text{ km} \times 300 \text{ km}$; and
- The simulation output should have daily precipitation with continuous simulation covering the period from 2010 to 2100.

As a result of the above conditions, 16 models with 49 scenarios are found suitable for this study. Simulation data were downloaded from Earth System Grid Federation (ESGF) and World Data Center for Climate Hamburg (WDCC) homepage.

AR5 models use a new set of greenhouse gas concentration (not emissions) trajectories called Representative Concentration Pathways (RCPs) [30]. There are four RCPs in CMIP5 model, with the high emission scenario designated as RCP 8.5. In addition to RCPs, scenarios of piControl, esmRCP85, and esmControl from model INM-CM4 are also found to have the required projection period for this study. The global models for performing the CMIP5 scenarios include Atmosphere-ocean Climate Models (AOGCM), Earth System Models of Intermediate Complexity (EMIC), and Earth System Models (ESM) [39].

4.2 *Rate-of-Change Estimation Using Multi-model Ensemble*

For each selected CMIP5 model scenario, only the output from the cell covering Doha is used. To assess the rate-of-change, data from two periods are employed to represent the current and future projections. Data refer to average daily annual maximum precipitation from the cell covering Doha of each model.

Three periods have been used for analysis:

- **P1:** 2010–2039, represents the rainfall under current climate conditions;
- **P2:** 2040–2069, represents the intermediate period; and
- **P3:** 2070–2100, represents the rainfall under future climate conditions at the end of the twenty-first century.

The model assumptions are as follows:

- The selected scenarios are equally possible and unbiased.
- Trends within each of the simulated periods P1, P2, and P2 are ignored.
- Each P2 model is a realization of a future condition, but with different emission scenarios and different parameterizations. The same assumption applies to P3.
- The regional data from P1 are fitted with the PE3 distribution. This assumption is based on the regional frequency analysis (described in Sect. 3), in which the PE3 was the selected distribution for the homogeneous regions consisting of 23 sites.

- The regional data from P2 and P3 are assumed to share the same type of distribution as data from P1, namely, the PE3. It should be noted that other distributions like generalized extreme value could have been adopted; however, PE3 was selected in this study as it was found to be the best-fit regional distribution based on the historical data.
- The Monte Carlo sample data drawn from the PE3 distribution will still fit with a PE3 distribution, but with variable moments.
- The rate-of-change for a cell is the same as the rate-of-change for a point rainfall.
- The models are not specifically calibrated for a single location, but the rate-of-change will be correctly reflected by the model for a certain location. However, model results of the current period (P1) deviating significantly from observed data are discarded from the analysis.
- It is assumed that 10000 Monte Carlo sample sets are statistically sufficient to capture the expected variation in the rate-of-change.

4.3 Model Screening

To analyze the local impact of climate change, appropriate climate scenarios are selected (by screening) as presented below to capture the present-day climate of the study area. It should be noted that bias correction could have been applied instead of model screening; however, in this study model screening was adopted as the preferred methodology.

4.3.1 Screening I

Screening I is based on the assumption that the data from climate models during period P1 represent the current condition in Doha. The regional frequency analysis (Sect. 3) identified 23 stations for the homogeneous region for Qatar. These 23 stations are taken as regional observations representing the “true” status of current conditions, and the AMS of the regional observations (daily data) and the P1 data for model screening. It should be noted that the P1 and P2 data in screening I have been divided by areal reduction factor (ARF) to convert point rainfall to areal rainfall.

Figure 3 shows the scatter plot of the mean and standard deviation of both the regional observations (Blue Square) and the climate model results, P1 data (pink point). The blue ellipse is the best-fit ellipse to regional observations using least squares approach. The P1 data (pink point) within this ellipse have high similarity with the regional observations in terms of mean and standard deviation of AMS. There are 27 sets of P1 data (pink point) located outside the blue ellipse, and these models have larger discrepancy with the regional observations. However, considering that the regional observation (1962–2015) and the P1 data (2010–2039) cover different periods, it is reasonable that the P1 data are showing certain deviation from the regional observation. Therefore, the best-fit ellipse is increased by four on major

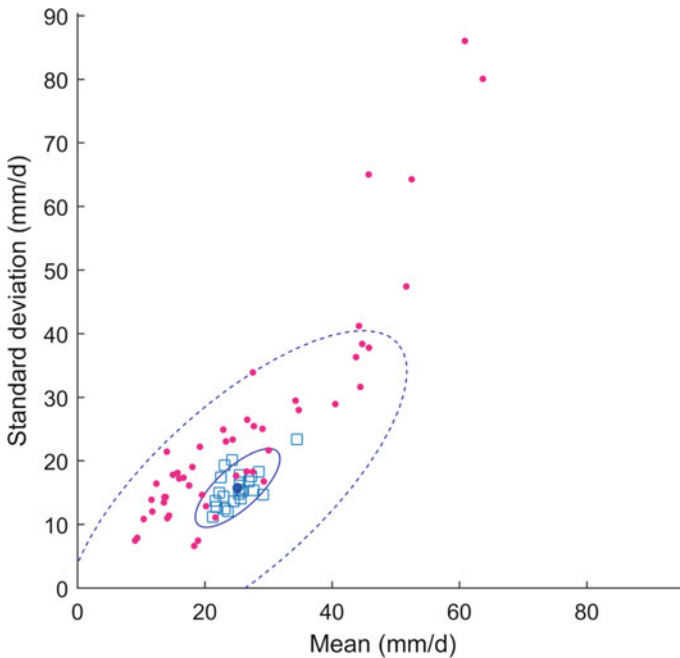


Fig. 3 Mean and standard deviation of AMS data from 23 stations of regional observations and 49 sets of P1 data (pink point). The inner blue ellipse is the best-fit ellipse of the regional observations, while the major and minor axes of the outer ellipse are four times of the inner one

and minor axes to create the “critical ellipse,” shown as the blue dashed line ellipse in Fig. 3, and P1 data within this ellipse are considered to resemble the regional observations in terms of mean and standard deviation of AMS. The models outside the critical ellipse are not directly rejected; instead, the P1 data are subject to bootstrap analysis and the mean and standard deviation of AMS of bootstrap samples are compared with the regional observations.

Each set of P1 data covers 2010–2039, which are 10957 days of data (including data with rain depth equal to 0). Bootstrapping is applied to these 10957 days of data and partitioned in years to derive the AMS. This procedure is repeated 1000 times, generating 1000 sets of AMS for each set of P1 data. The result indicates that the major portions of the bootstrap samples are within the critical ellipse. There are five models with both original P1 data and 90% of the bootstrap samples located outside the critical ellipse (CCSM4_RCP26, CCSM4_RCP45, CCSM4_RCP60, CCSM4_RCP26, and EC-EARTH_RCP26). These models are rejected due to limited similarity with the regional observations in terms of the mean and standard deviation of AMS.

Besides the mean and standard deviation, the discordancy measure [17] is also used for model screening. For each model, the discordancy statistic is the measure of the discordancy between the P1 data of this model and the regional observations. For regions with 15 sites or more, Hosking and Wallis [17] suggested the critical

discordancy value to be 3, and sites with discordancy higher than 3 are regarded as discordant. However, considering the source of difference of the regional observation and P1 data, together with their data range difference, the critical discordancy value is increased by 2, which means model scenarios with discordancy statistic greater than 6 are taken as discordant from the regional observation, and they are MPI-ESM-LR_RCP26, MPI-ESM-LR_RCP45, MPI-ESM-LR_RCP85, and MPI-ESM-MR_RCP45.

4.3.2 Screening II

There are 40 model scenarios remaining after screening I. Screening II is based on the assumption that distribution of AMS from P1, P2, and P3 data follows a PE3 distribution. The goodness of fit is evaluated by the Kolmogorov–Smirnov test (KS test) using AMS data. The critical value for sample size 30 (2010–2039, 2040–2069, 2070–2099), with significance level of 5%, is 0.2417 for the hypothesized distribution (PE3), and if the computed KS statistic is higher than 0.2417, the hypothesis is rejected. The results of the KS test show that the rejected fitting is P1 data of ACCESS1-3_RCP85, and CESM1-BGC_RCP45, CMCC-CM_RCP45, and EC-EARTH_RCP85 of P2 data, and these four model scenarios are therefore excluded.

4.4 Multi-model Ensemble

Instead of relying on the outcomes of a single model, there is an increasing use of ensembles of a large number of models for assessing the impact of future climate. The multi-model ensemble has been shown to be more efficient in improving the accuracy and consistency of the predictions than a single climate model [22, 38].

There are in total 39 model scenarios for applying multi-model ensemble, and the adopted procedure of deriving rate-of-change is presented below.

(a) Drawing sample by Monte Carlo simulation

For each model scenario ($m_1, m_2, m_3 \dots m_n$), draw 10,000 Monte Carlo samples from its fitted PE3 distribution. A single set of Monte Carlo sample is

$$\begin{aligned}
 (d1_{p1,i,k}, d2_{p1,i,k}, d3_{p1,i,k} \dots d30_{p1,i,k}) &= \text{Random}(D_{P1,i}) \\
 (d1_{p2,i,k}, d2_{p2,i,k}, d3_{p2,i,k} \dots d30_{p2,i,k}) &= \text{Random}(D_{P2,i}) \\
 (d1_{p3,i,k}, d2_{p3,i,k}, d3_{p3,i,k} \dots d30_{p3,i,k}) &= \text{Random}(D_{P3,i})
 \end{aligned}
 \tag{1}$$

The sample size is consistent with the original data size, which has 30 data in each set. ($d1_{p1,i,k}, d2_{p1,i,k}, d3_{p1,i,k} \dots d30_{p1,i,k}$) are samples drawn from the fitted distribution ($D_{P1,i}$) of AMS of the P1 data of model scenario m_i , while ($d1_{p2,i,k}, d2_{p2,i,k}, d3_{p2,i,k} \dots d30_{p2,i,k}$) are samples drawn from the fit-

ted distribution ($D_{P2,i}$) of AMS of the P2 data of model scenario m_i , and ($d1_{p3,i,k}, d2_{p3,i,k}, d3_{p3,i,k} \dots d30_{p3,i,k}$) are samples drawn from the fitted distribution ($D_{P3,i}$) of AMS of the P3 data of model scenario m_i . Here, i denotes the i th model scenario, and k denotes the k th Monte Carlo sample. To avoid highly correlated samples, the 10000 samples' Pearson Correlation coefficient is controlled to be within -0.9 and 0.9 .

(b) Drawing quantile values from samples

Each Monte Carlo sample is also fitted with a PE3 distribution, from which the quantile values Q for certain typical design return periods are computed. The design return periods are 1, 2, 5, 10, 20, 25, 50, 100, 500, 1000, and 10000 years, and the corresponding quantiles are noted as

$$\begin{aligned} Q_{p1, i, k(T), T = 1, 2, 5, 10, 20, 25, 50, 100, 500, 1000, 10000} \\ Q_{p2, i, k(T), T = 1, 2, 5, 10, 20, 25, 50, 100, 500, 1000, 10000} \\ Q_{p3, i, k(T), T = 1, 2, 5, 10, 20, 25, 50, 100, 500, 1000, 10000} \end{aligned}$$

where $p1$ denotes the sample corresponds to P1 data, $p2$ denotes the sample corresponds to P2 data, and $p3$ denotes the sample corresponds to P3 data. i denotes the i th model scenario, and k denotes the k th Monte Carlo sample.

The overall methodology adopted in this study is summarized in Fig. 4.

5 Results and Discussions

5.1 Summary of Screened Scenarios

Screening I and screening II rejected ten model scenarios, which are ACCESS1-3_RCP85, CCSM4_RCP26, CCSM4_RCP45, CCSM4_RCP60, CCSM4_RCP26, EC-EARTH_RCP26, MPI-ESM-LR_RCP26, MPI-ESM-LR_RCP45, MPI-ESM-LR_RCP85, and MPI-ESM-MR_RCP45.

There are in total 609 scenarios of CMIP5 models. Seventy-seven scenarios could not be used due to usage restrictions of the models. A major part of the scenarios (483) are not suitable for this study due to the specific requirement on model discretization and data range as discussed in Sect. 4. As a result, 49 scenarios were used for screening.

Screening I excluded three RCP26 scenarios, three RCP45 scenarios, one RCP60, and two RCP85 scenarios. Screening II excluded two RCP45 and two RCP85 scenarios. As a result, there are 36 scenarios suitable for applying the multi-model ensemble. They include 11 RCP45 scenarios, 12 RCP85 scenarios, 6 RCP26 scenarios, 4 RCP60 scenarios, 1 piControl scenario, 1 esmRCP85 scenario, and 1 esmControl scenario.

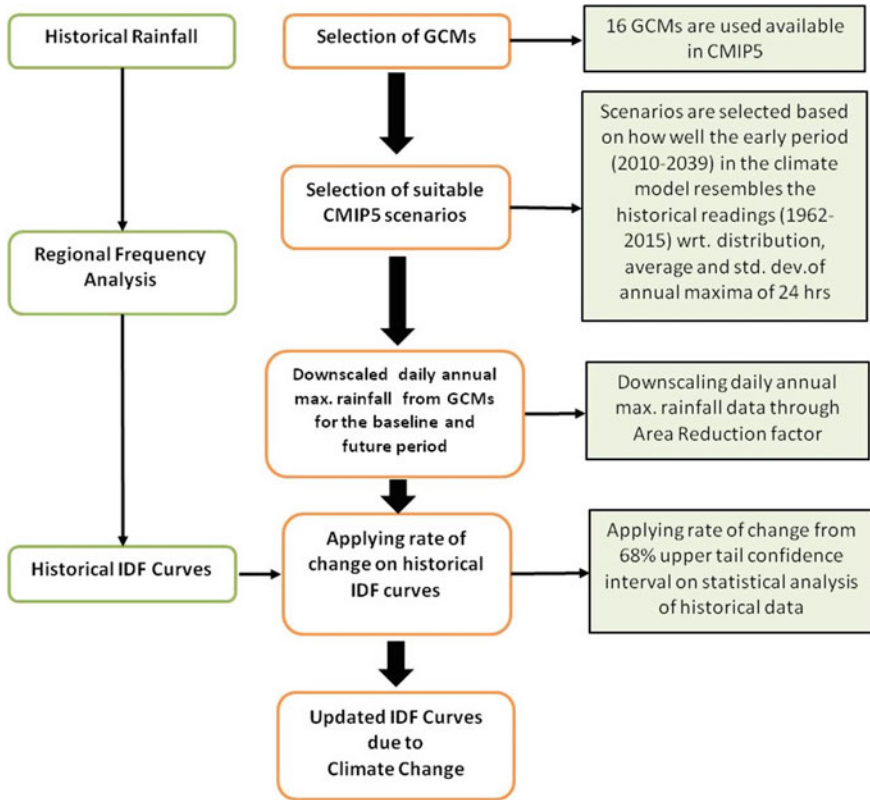


Fig. 4 Schematic of the adopted procedure

5.2 Computation of Rate-of-Change

The rate-of-change is used to represent the relation between rainfall event of P2 (or P3) and that of P1. It is computed as

$$\begin{aligned}
 R_{p1-p2,i,k}(T) &= Q_{p2,k,i}(T) / Q_{p1,k,i}(T) - 1 \\
 R_{p1-p3,i,k}(T) &= Q_{p3,k,i}(T) / Q_{p1,k,i}(T) - 1
 \end{aligned}
 \tag{2}$$

With 36 model scenarios and 10000 Monte Carlo samples from each model scenario, the size of ensemble is $36 \times 10000 = 360000$ (360,000 for P1 data and 360,000 for P2 data, respectively). The medians, 68%, 90%, and 95% uncertainty range of the 360000 sets of $R_{p1-p3,i,k}(T)$ are used to represent the uncertainty range of rainfall event variation at the end of twenty-first century, as illustrated in Fig. 5. In general, the median of the 360000 ensembles illustrates a slightly decreasing tendency with increasing design Average Recurrence Interval (ARI), which means the short ARI

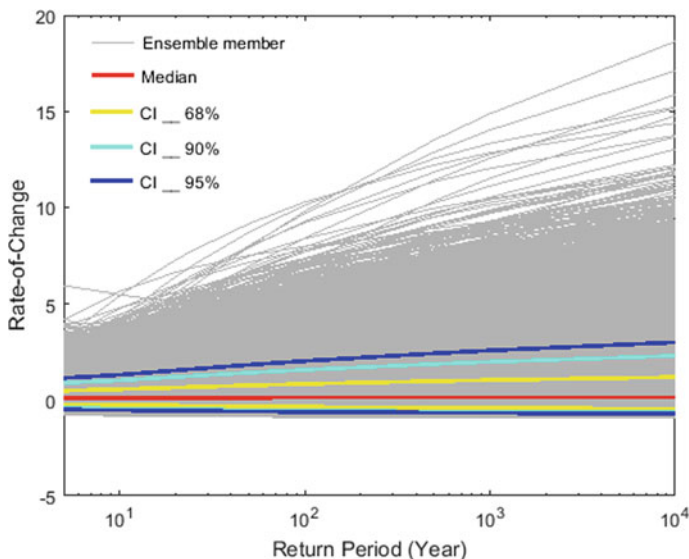


Fig. 5 The 360,000 sets of $R_{p1-p3,i,k}(T)$ together with their median, the 68, 90, and 95% uncertainty ranges

rainfall will experience a higher magnitude of variation at the end of twenty-first century than the long ARI rainfall.

The rate-of-changes found in this study are compared with similar studies carried out in other countries. For example, the changes of seasonal precipitation extremes in UK by 2070–2100 were evaluated by Fowler and Ekström [11] applying multi-model ensemble on 13 regional climate models under SRES A2 emission scenario. For daily extreme rainfall of 5-year event, the study suggested 10–30% increases in spring, autumn, and winter rainfalls by 2010–2070. Projections are similar for the 25-year event, with larger uncertainty. The median rate-of-change of our study is around 13% for 5-year event and 12% for 25-year event, which is at the lower end of the rate-of-change found in the UK.

Similar climate studies, based on results from 40 CMIP 5 models, reported by the Department of the Environment, [4] provide a range of projections for major climatic parameters including rainfall. The median projections for a 20-year rainfall event at the end of the century are predicted to increase by 10–15% for RCP 4.5 and 20–25% for RCP 8.5.

The rate-of-changes predicted for Denmark are in the same range as the values in Australia with median values for a short duration 1-h rainfall under climate change year 2100 vary from 10 to 20%, while the 84-percentile (upper part of the 68% confidence intervals) vary from 20 to 50% depending on the return period (IDA) [18]. The worst projections predict more than a 100% increase in extreme rainfall between 200 and 280%. The standard rate-of-change adopted in Denmark is approximately 66% of the 84-percentile value (for 1-h and 100-year ARI).

A study from Antalya, Turkey, a location considerable closer to Qatar, conducted by Yilmaz [41] predicted an increase in the median value of 11% for a 10-year event, 20% for 20-year event, and 37% for 100-year event using a single climate model (Reg3CM3). The results indicated more significant changes in the median value compared to the current study.

Transforming IDF Curves to future conditions

Transition between current baseline meteorological conditions and future meteorological conditions is expressed by a climate change factor expressed as [41]/ [18]

$$CF(T, d, t + \Delta t) = \frac{I_{Fut}}{I_{Cur}} = \frac{I_{Fut}(T, d, t + \Delta t)}{I_{Cur}(T, d, t + \Delta t)} = 1 + R_{t,t+\Delta t}(T, d) \tag{3}$$

where

- I_{Fut} = Future rainfall intensity [mm/hr]
- I_{Cur} = Current rainfall intensity [mm/hr]
- $R_{t,t+\Delta t}$ = Rate-of-change from t to t + Δt
- CF = Climate Change Factor
- T = Average Recurrence Interval [years]
- d = Duration of rainfall [minutes]
- t = The current [year]
- Δt = The number of years into the future from current date [year]

The future IDF relations are found through conversion of the current to future rainfall design criteria expressed as

$$I_{Fut}(T, d, t + \Delta t) = I_{Cur}(T, d, t)CF(T, t + \Delta t) \tag{4}$$

Several aspects must be considered while choosing rate-of-change for updating IDF for the future scenario in Qatar, such as the design horizon, the replacement cost, the interest rate, the sensitivity of the infrastructure, and the cost of waiting until more information becomes available. There is a 50% chance the median value will be exceeded; hence, the median value would be an unsafe choice. Considering the Danish standard, it has been chosen to use approximately 66% of the 84-percentile value equivalent to the upper 68% confidence interval and apply this value for all ARIs in Qatar. The computed and proposed rate-of-change values for Qatar for the different ARIs, are shown in Table 1. The results indicate an increase of up to 50% for the 100-year rainfall event from current to the intermediate scenario (2040–2069). The rate-of-change for the far future (2070–2100) is at similar level as the intermediate period.

Future IDF curves for the year 2100 have been developed by applying the developed climate change factor as indicated by Eq. 4. As an example, the IDF curve for the year 2100 for Doha old airport is shown in Fig. 6.

Table 1 Proposed rate-of-change (66% of the climate change factor based on 84-percentile) for design rainfall in Qatar due to climate change

ARI (year)	Proposed rate-of-change (2040–2069)	Proposed rate-of-change (2070–2100)
2	30%	30%
5	30%	30%
10	30%	30%
20	40%	30%
25	40%	30%
50	40%	40%
100	50%	50%

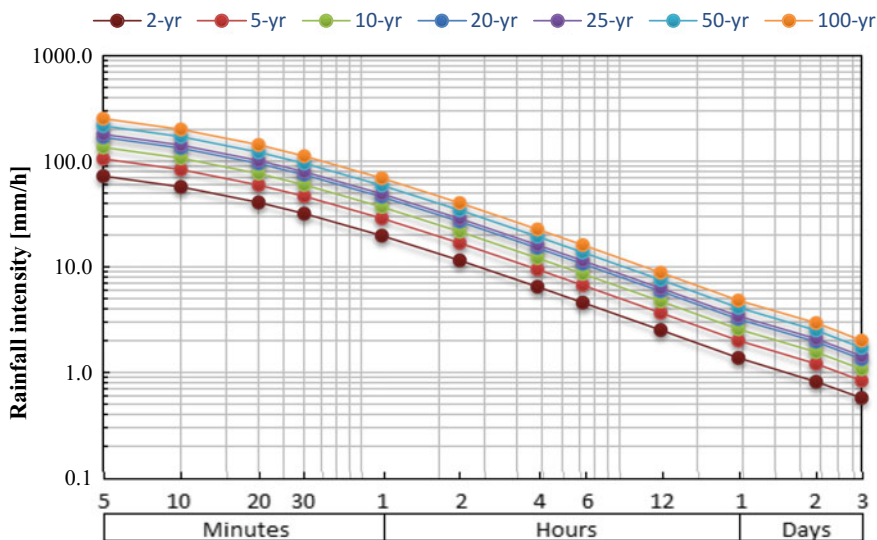


Fig. 6 Future IDF curves (year 2100) for Doha Old Airport under climate change (applied rate-of-change value for climate change 30% for 2–10 years, 40% 20 years to 50 years ARIs, and 50% beyond for 100-year ARI)

6 Conclusions

The study evaluates climate change impacts based on IPCC’s most recent climate models used in AR5. In order to reduce the uncertainty, this study uses ensemble approach that includes new generation of CMIP5 models with generally higher spatial resolution.

In this study, the relationship between current (2010–2039), intermediate future (2040–2069), and the far future (2070–2100) IDF curves are examined. A total of

61 Global Circulation Models (GCMs) with 609 emission scenarios are considered. Samples are drawn from the selected multi-model ensemble to provide projections of the rate-of-change between current and future IDFs as predicted by the selected climate models and individual scenarios. A bootstrap analysis of the current period (2010–2039) is carried out and compared with historical data. The climate models are rejected if the deviations between the bootstrapped data and the historical measured data show notable deviation.

Both the median and the upper 68% confidence interval of the rate-of-change from the climate change analysis show increased rainfall from present to the future. Only the lower 68% confidence intervals show decreased rainfall. The upper 68% confidence interval from the climate change analysis is used to predict the future design rainfall.

The result shows that the rate-of-change of intermediate period (2040–2069) is at similar level as the far future (2070–2099). There is a slightly larger increase for rainfall of short and intermediate ARIs (<100 years) and lower magnitude increases for extreme rainfall (>100-year ARIs) at far future, considering the median values. However, the confidence intervals widen with increase in the ARI; accordingly, the typical rate-of-changes increase with increasing ARI taking safety into account.

The rate-of-change due to climate change obtained from this study is compared with similar studies in Australia, Denmark, and Turkey. Considering the Danish standards, it is recommended to use rate-of-change for Qatar based on approximately 66% of the 84-percentile value equivalent to the upper 68% confidence interval. This provides a reasonable degree of safety for design of infrastructure with long design horizon in Qatar.

The future IDF curves to account for climate change have been developed by applying the recommended rate-change-values to the IDF curves developed for the present condition. The climate change factor is introduced given as $(1 + \text{rate-of-change})$. The climate factor is multiplied on current IDF intensities to derive the future IDF curves. The adopted methodology can be applied to other Gulf and similar countries.

Acknowledgements The authors would like to acknowledge the Ministry of Municipality and Environment, Qatar for providing the data used in this study.

References

1. Abiodun BJ, Adegoke J, Abatan, A (2016) Potential impacts of climate change on extreme rainfall events over three coastal cities in Africa. Geophysical research abstracts, vol 18, EGU2016-12373, 2016. EGU General Assembly
2. Afrooz AH, Akbari H, Rakhshandehroo GR, Pourtouserkani A (2015) Climate change impact on probable maximum precipitation in Chenar Rahdar River Basin. Watershed Management 2015, ASCE
3. Akbari H, Rakhshandehroo GR, Pourtouserkani A, Afrooz AH (2015) Climate change impact on intensity-duration-frequency curves in Chenar-Rahdar River Basin. Watershed Management 2015, ASCE

4. Australian Government (2015) Department of the environment, bureau of meteorology, natural resource management, Technical Report, CCIA Projections, Chapter 7
5. Camici S, Brocca L, Melone F, Moramarco T (2014) Impact of climate change on flood frequency using different climate models and downscaling approaches. *J Hydrol Eng* 19(8):04014002
6. Carlier E, El Khattabi J (2016) Impact of global warming on Intensity-Duration-Frequency (IDF) relationship of precipitation: a case study of Toronto, Canada. *Open J Mod Hydrol* 6:1–7. <https://doi.org/10.4236/ojmh.2016.61001>
7. Chadwick R, Boutle I, Martin G (2012) Spatial patterns of precipitation change in CMIP5: why the rich do not get richer in the tropics. *J Clim* 26(11):3803–3822
8. Chen J et al (2011) Overall uncertainty study of the hydrological impacts of climate change for a Canadian watershed. *Water Resour Res* 47(12)
9. Duan QY, Phillips TJ (2010) Bayesian estimation of local signal and noise in multimodel simulations of climate change. *J Geophys Res* 115(D18)
10. Easterling DR, Evans JL, Groisman PYa, Karl TR, Kunkel KE, Ambenje P (1999) Observed variability and trends in extreme climate events: a brief review. *Bull Am Meteorol Soc* 417–425
11. Fowler HJ, Ekstrom M (2009) Multi-model ensemble estimates of climate change impacts on UK seasonal precipitation extremes. *Int J Climatol* 29(3):385–416
12. Flato et al (2013) Evaluation of climate models. In: *Climate Change 2013: the physical science basis. Contribution of working group I to the fifth assessment report of the intergovernmental panel on climate change*. Cambridge University Press, Cambridge, United Kingdom and New York, USA
13. Haberlandt U, Belli A, Bárdossy A (2015) Statistical downscaling of precipitation using a stochastic rainfall model conditioned on circulation patterns—an evaluation of assumptions. *Int J Climatol* 35:417–432
14. Herath SM, Sarukkalgige PR, Va VT (2016) Nguyen (2016) A spatial temporal downscaling approach to development of IDF relations for Perth airport region in the context of climate change. *Hydrol Sci J* 61(11):2061–2070
15. Holesovsky J, Fusek M, Blachut V, Michálek J (2016) Comparison of precipitation extremes estimation using parametric and nonparametric methods. *Hydrol Sci J*. <https://doi.org/10.1080/02626667.2015.1111517>
16. Hosking JRM, Wallis JR (1997) *Regional frequency analysis: an approach based on L-moments*. Cambridge University Press
17. Hosking JRM, Wallis JR (2005) *Regional frequency analysis: an approach based on L-moments*. Cambridge University Press
18. IDA, Spildevandskomiteen (2014) Ida Bülow Gregersen, DTU, Henrik Madsen, DHI, Jens Jørgen Linde, Krüger, and Karsten Arnbjerg-Nielsen, DTU, Skrift 30
19. IPCC (2007) *Climate change 2007: the physical science basis. Contribution of working group I to the fourth assessment report of the intergovernmental panel on climate change*. Cambridge University Press, Cambridge, UK, p 996
20. IPCC (2013) *Climate change 2013: the physical science basis. Contribution of working group I to the fifth assessment report of the intergovernmental panel on climate change*. Cambridge University Press, Cambridge, United Kingdom and New York, NY, USA, p 1535
21. Kawazoe S, Gutowski WJ (2013) Regional, very heavy daily precipitation in NARCCAP simulations. *J Hydrometeorol* 14(4):1212–1227
22. Koutroulis et al (2013) Impact of climate change on water resources status: a case study for Crete Island, Greece. *J Hydrol* 479:146–158
23. Liu JP, Song MR, Horton RM, Hu YY (2013) Reducing spread in climate model projections of a September ice-free arctic. *Proc Natl Acad Sci USA* 110:12571–12576
24. Mandal S, Breach PA, Simonovic SP (2016) Uncertainty in precipitation projection under changing climate conditions: a regional case study. *Am J Clim Chang* 5:116–132
25. Mamoon AA, Rahman A (2014) Uncertainty in design rainfall estimation: a review. *J Hydrol Environ Res* 2(1)

26. Mamoon AA, Joergensen NE, Rahman A, Qasem H (2016) Design rainfall in Qatar: sensitivity to climate change scenarios. *Nat Hazards* 81(3):1797–1810
27. Mamoon AA, Rahman A (2017) Rainfall in Qatar: is it changing? *Nat Hazards* 85:453–470
28. Mamoon AA, Joergensen NE, Rahman A, Qasem H (2014) Derivation of new design rainfall in Qatar using L-moments based index frequency approach. *Int J Sustain Built Environ* 3:111–118
29. Miao et al (2014) Assessment of CMIP5 climate models and projected temperature changes over Northern Eurasia. *Environ Res Lett* 9:055007 (12 pp)
30. Moss et al (2010) The next generation of scenarios for climate change research and assessment. *Nature* 463:747–756
31. Ministry of Municipality and Urban Planning (2014) Qatar National Development Framework 2032
32. Osborne T, Rose G, Wheeler T (2013) Variation in the global-scale impacts of climate change on crop productivity due to climate model uncertainty and adaptation. *Agric For Meteorol* 170:183–194
33. Pincus R, Batstone CP, Hofmann RJP, Taylor KE, Glecker PJ (2008) Evaluating the present-day simulation of clouds, precipitation, and radiation in climate models. *J Geophys Res* 113(D1427)
34. Sarhadi A, Soulis ED (2017) Time-varying extreme rainfall intensity-duration-frequency curves in a changing climate. *Geophys Res Lett* 44(5):2454–2463
35. Sellami H, Benabdallah S, Jeunesse IL, Vanclooster M (2016) Climate models and hydrological parameter uncertainties in climate change impacts on monthly runoff and daily flow duration curve of a Mediterranean catchment. *Hydrol Sci J* 61(8):1415–1429
36. Sun Q, Miao C, Qiao Y, Duan Q (2017) The nonstationary impact of local temperature changes and ENSO on extreme precipitation at the global scale. *Clim Dyn* 49:4281–4292
37. Singh R, Arya DS, Taxak AK, Vojinovic Z (2016) Potential impact of climate change on rainfall intensity-duration-frequency curves in Roorkee. *Water Resour Manag, India*. <https://doi.org/10.1007/s11269-016-1441-4>
38. Tebaldi C, Knutti R (2007) The use of the multi-model ensemble in probabilistic climate projections. *Philos Trans R Soc A Math Phys Eng Sci* 365(1857):2053–2075
39. Taylor K, Stouffer RJ, Meehl GA (2011) An overview of CMIP5 and the experiment design. *Bull Am Meteorol Soc* 93:485–498
40. Xu YP, Zhang X, Tian Y (2012) Impact of climate change on 24-h design rainfall depth estimation in Qiantang River Basin, East China. *Hydrol Process* 26:4067–4077
41. Yilmaz AG (2017) Climate change effects and extreme rainfall non-stationarity. *Proc Inst Civ Eng Water Manag* 170(2):57–65
42. Zhu J (2013) Impact of climate change on extreme rainfall across the United States. *J Hydrol Eng* 18(10):1301–1309

River Water Temperature Modelling Under Climate Change Using Support Vector Regression



Shaik Rehana

1 Introduction

A model is a simplified system, which can be used to represent the complex real-life system and can be used as a substitute for a real system under specific conditions [17]. Generally, such models are based on the formalized concepts of the real system. A surface water quality modelling was developed as a tool for the better understanding of the mechanisms and interactions between anthropogenic residual inputs and resulting water quality [7]. In the context of global climate change under anthropogenic greenhouse warming, the sensitivity of water quality will be more intensified under changes in hydro-meteorological variables. The self-purification capacity of the river in response to the pollutants and climate depends on various hydro-meteorological variables and water quality parameters. One such water quality variable, which gets most influenced by climate change and human interventions is River Water Temperature (RWT). The reasons for the alterations in RWT are generally due to human activities and anthropogenic heat sources include water withdrawals and additions, changes in channels, dam operation, alterations in riparian cover, industrial cooling water, outfalls from a sewage treatment plant, net exchange from groundwater temperature and downstream of a thermal plant. The RWT is of particular significance as (i) the discharge of excess heat from industries and municipal effluents can affect the aquatic ecosystem, (ii) temperature influences all biological and chemical reactions, and (iii) temperature variations affect the density of water and hence the transport of water [35]. It is also a vital physical property of rivers, directly affecting water quality in terms of reaction rates and dissolved oxygen (DO) levels. Increase in RWT results in the decrease of DO levels which leads to anaerobic conditions in aquatic systems, thereby affecting marine life in terms of availability of food, reproduction and migration. Besides, the river water temperature is a prominent variable in the

S. Rehana (✉)

Lab for Spatial Informatics, International Institute of Information Technology,
Gachibowli, Hyderabad 500032, India

e-mail: rehana.s@iiit.ac.in

© Springer Nature Switzerland AG 2019

S. K. Singh and C. T. Dhanya (eds.), *Hydrology in a Changing World*, Springer Water,
https://doi.org/10.1007/978-3-030-02197-9_8

context of climate change as it is a function of climatic variables such as air temperature, humidity, solar radiation and wind speed. Reliable prediction and assessment of RWT sensitivity under climate change have become the main issue for many environmental applications, hydrology and ecology. To this end, numerous methods have been developed in the recent years by several authors for the estimation of river water temperature as a basic mathematical model to represent the complex system of hydro-meteorological and climate data along with water quality parameters.

Some of the river water temperature models generally used are heat advection-dispersion transport equations [30, 41], which incorporates the net heat transfer processes at surface of water by using thermal equilibrium concepts [4, 5, 11, 19, 26]. Stochastic RWT models separate the RWT time series into long-term annual component (annual cycle) and short-term components [6]. Few RWT models were based on the mathematical representation of the underlying physics of heat exchange between the river and the surrounding environment [20, 32, 30]. To incorporate the watershed hydrology from climatic changes on RWT, the physically based hydrologic and stand-alone stream temperature models have been effectively used to simulate RWT (e.g. Soil Water Assessment Tool (SWAT), [2, 13]; BasinTEMP, [1]; QUAL2K, [8]). Although a mechanistic temperature model could give very accurate results, it requires large amounts of detailed data and also computationally intensive. These typically require numerous input data including stream geometry, hydro-meteorology, vegetation cover and land use, along with in-depth knowledge of the field. Furthermore, these models sometimes have complex practical implementation issues, when it is the large spatial domain of interest.

To this end, the regression-based models become well accepted in the research community under the limitation of complex meteorological and hydrological river data availability. Traditionally, river water temperature has been related to air temperature as a surrogate for net heat exchange and as an approximation to equilibrium temperature (e.g. [31]). A linear regression model relating air and water temperatures are generally most adopted model to predict the RWTs (e.g. [5, 23, 25]). These models usually predict river water temperature at weekly, monthly and annual time steps, relying mainly on the relatively high correlation between air and water temperature at those timescales. Due to the computational feasibility and ease of implementation, linear regression models have been used to obtain the relation between air and water temperature (e.g. [12, 23, 24, 25, 33]). Neumann et al. [23], developed a linear regression method to model daily maximum stream temperature in terms of maximum air temperature for the Truckee River in California and Nevada. In linear regression models, the AT and RWT are considered as the independent and dependent variables respectively and these models are claimed to work more accurately at weekly to monthly scale rather than daily scale [5]. Webb et al. [40] noted that flow is another important variable that should be considered in water temperature prediction models, and air and water temperatures are more strongly correlated when flows are below median levels. Several authors related river water temperature with both streamflow and air temperatures with the linear regression models (e.g. [21, 25]). Streamflow has an inverse relationship with the water temperature, due to the fact that as sufficient amount of streamflow is available, then the effect of river water temperature will

decrease. The streamflow will be of more interest in the RWT prediction models, particularly in snowmelt-fed rivers and rivers impacted by hydropower production [36]. Generally, such regression-based models are applied by training or calibrating the model for a subset of historical data and then validate or test with the historical data which may be independent of historical data used in the training or calibration. The trained and tested models can be used for future prediction of RWT. Such linear models facilitate to study the sensitivity of the RWT to the changes in AT under changed conditions of climate [21, 25, 27, 28, 38]. Rehana and Mujumdar [25], used a linear regression model with daily data for understanding the sensitivity of RWT for the changes in AT of 1 to 2 °C and 10 to 20% reduction in the streamflows for Tunga-Bhadra river India. Further, Rehana et al. [27] revealed that the sensitivity of RWT will be for about 2.76 °C under various air temperature and discharge changes when compared with the observed conditions at mean annual scale for the Missouri River at Nebraska City, Nebraska, USA.

Morrill et al. [21] used both linear and nonlinear models in 43 river and stream sites in 13 countries and indicated that the air/water temperature relationship is better fitted with non-linear regression. Linear Regression is less appropriate if the assumption of linear relationship cannot be verified. Also, these models are sensitive to outliers and can suffer from the problems of overfitting. i.e., regression begins to model the random error (noise) in the data, rather than just the relationship between the variables. Further, linear regressions become unsuitable for modelling the RWT extremes, for example, at highest (due to increased evaporative cooling) and lowest temperatures (due to freezing). Mohseni et al. [18] developed a four-parameter non-linear regression model at a weekly time step, which is widely accepted in the research community (e.g. [28, 38]). Van Vliet et al. [38] improved the non-linear regression model developed by Mohseni et al. [18] with the inclusion of streamflow and applied at daily time scale.

Apart from regression-based models, another set of data-driven models which became promising due to the advancement of machine learning models in the RWT estimation are based on Artificial Neural Networks, Support Vector Machines (SVM), Boosted Regression Trees (BRS), specifically for data scarce regions. There is a recent advancement towards the use of Artificial Neural Networks (ANN) in river water quality prediction (e.g. [14, 29]). Modelling of RWT using ANN has gained much attention in the literature (e.g. [9, 29]) due to its ability to capture and represent complex non-linear relationships. DeWeber and Wagner [10] applied ANN for estimating daily mean RWT of the individual stream reaches throughout the range of Brook Trout *Salvelinus Fontinalis* in the eastern U.S with different groups of predictor variables including climate, landform and land cover attributes. Temizyurek and Dadaser-Celik [34], used ANN to study the effect of meteorological parameters on RWT at Kızılırmak River in Turkey. However, Support vector regression (SVR), which is based on structural risk minimization to avoid overfitting [37] has been adopted over ANN in several research studies due to the uniqueness and globalization of the solution [39]. In this context, there are limited studies for testing the predictability of RWT with SVR in the literature. To this end, the present work adopted well-accepted machine learning algorithm, such as Support Vector

Machine (SVR) to analyze the predictability performance of river water temperature. The present study used SVR model to compare the predictability performance with a linear regression model. A Multiple Linear Regression Model (MLRM) with air temperature and streamflow as predictors and daily RWT as predictand variable was compared with the predictability of SVR model. The proposed machine learning algorithm of SVR is applied with air temperature and streamflow as predictors to estimate the RWT at Shimoga river water quality checkpoint along Tunga-Bhadra, a tributary of Krishna river, India. For understanding the possible variability in RWT under climate change, a statistical downscaling model based on Canonical Correlation Analysis (CCA) has been adopted. The future RWT projections were analyzed using the trained and tested MLRM and SVR models with the downscaled projections of air temperature and streamflow.

2 Data and Methods

Tungabhadra River is one of the highly polluted rivers in India after Yamuna River due to the rapid growth of urban industries located along the river such as effluents from paper, pulp, rayon and steel industries such as Mysore paper mill and Harihar poly fibre. Tunga River, of length 147 km and Bhadra River, about 178 km long originates in the Western Ghats, and join at Kudli, which is about 14.5 km from Shimoga city, to form the Tungabhadra River (Fig. 1). The river location considered for the quantification of RWT is Shimoga along the Tunga River. The river location receives the waste load from Shimoga city municipal effluent. The daily streamflow and river water temperature data from 1988 to 2005 recorded at Shimoga station was obtained from Central Water Commission (CWC), Karnataka, India.

To study the impact of climate change on RWT, the downscaled streamflow and air temperatures were obtained by considering the large-scale climate predictor variables as air temperature, mean sea level pressure, specific humidity, U-wind, V-wind and geopotential height based on earlier studies [26]. The selected predictor variables for the period of January 1948 to December 2005 for six (National Center for Environmental Prediction/National Center for Atmospheric Research) NCEP/NCAR grid points were extracted for the given region of 10–20°N to 70–80°E with a spatial resolution of $2.5^\circ \times 2.5^\circ$. The daily streamflow and air temperature data and predictor set for the period of 10 years (1988–1998) were used for training the downscaling model with CCA and the data from 1999 to 2005 was used for testing. The future climate variables were obtained from the simulations of the Beijing Climate Center (BCC-CSM1-1) model output prepared from CMIP5 (Coupled Model Inter-comparison Project 5), by the Beijing Climate Center, China Meteorological Administration. The BCC-CSM1-1 model was selected based on the availability of CMIP5 projections of predictor variables to demonstrate the modelling of RWT using SVR and to analyze the future projections. The IPCC AR5 models implemented set of scenarios, called Representative Concentration Pathways (RCPs) in which radiative forcing due to anthropogenic factors reaches 2.6 (RCP 2.6), 4.5 (RCP 4.5) and 8.5 (RCP

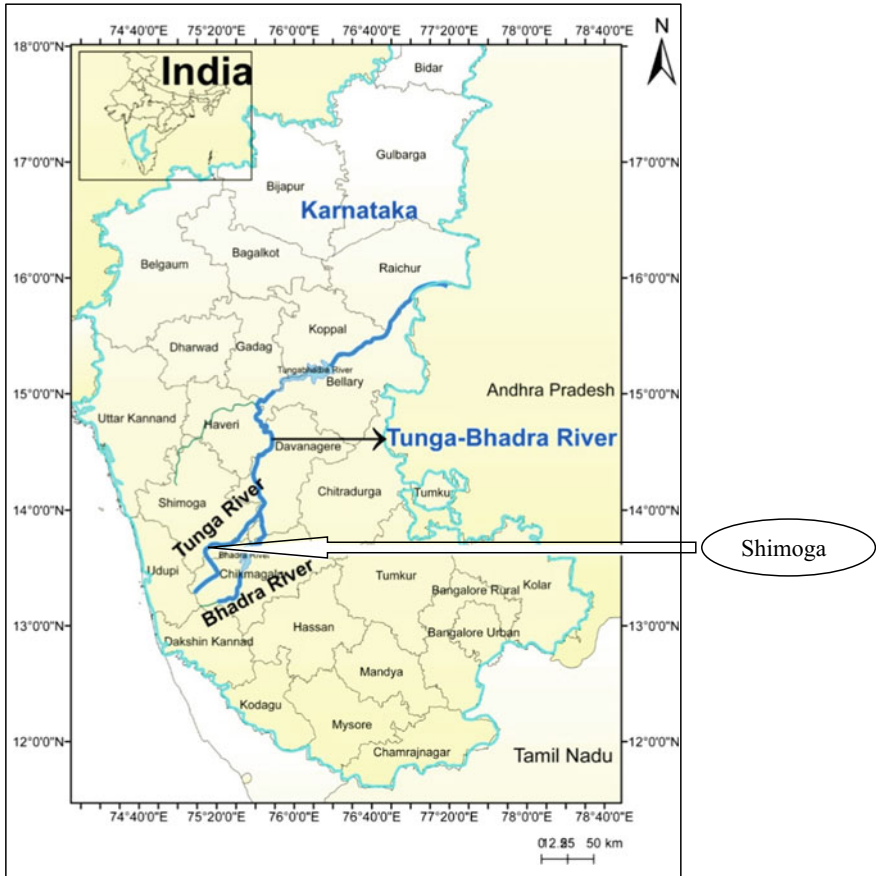


Fig. 1 Location map of Tunga-Bhadra River and Shimoga station, India

8.5) Wm^{-2} by 2100, were selected for studying the possible RWT changes under climate change. The RCP 8.5, was considered as a possible scenario for the present study, which represents high concentration mitigation pathway which continues to rise throughout the 21st century. The daily GCM simulations for historical and future scenarios from CMIP5, RCP8.5 were obtained from World Data Center for Climate (<http://cera-www.dkrz.de/maintenance.html>).

3 Multiple Linear Regression Model (MLRM)

A MLRM is developed at daily scale to predict the RWT for Tunga-Bhadra River with air temperature and streamflow as predictor variables. The MLRM developed based on the training is given in the following equation:

$$T_w = a + bT_{air} + cQ \quad (1)$$

where T_w is the daily river water temperature in °C, T_{air} is the daily air temperature in °C, Q is the daily discharge in m^3/s , and a , b , c are the parameters estimated based on the training the MLRM.

4 Support Vector Regression (SVR)

The Support Vector Machine (SVM) is a kernel function learning machine, which follows the structural risk principle [37]. When the training data of $\{(x_1, y_1), \dots, (x_n, y_n)\}$ with n patterns, a function $f(x)$ will be identified with the consideration of the deviation from the actually observed target variables y_i for all the training data [16]. The input variables, X will be mapped into a higher dimensional feature space using a non-linear mapping function Φ .

$$f(x; w) = \langle W, \Phi(x) \rangle + b \quad (2)$$

where \langle, \rangle denotes the inner product, and W and b are the regression coefficients, which can be estimated by minimizing the error between $f(x)$ and the observed values of y . SVR uses the ϵ -insensitive error to measure the error between $f(x)$ and the observed values of y .

$$|f(x; w) - y|_{\epsilon} = \begin{cases} 0 & \text{if } |f(x; w) - y| < \epsilon \\ |f(x; w) - y| - \epsilon, & \text{otherwise,} \end{cases} \quad (3)$$

Using the training data of (x_i, y_i) , the values of w and b are estimated by minimizing the objective function:

$$F = \frac{C}{N} \sum_{i=1}^n |f(x_i, w) - y_i|_{\epsilon} + \frac{1}{2} \|w\|^2 \quad (4)$$

where C and ϵ are the hyper-parameters. The minimization of the objective function, F , uses Lagrange multiplier method, and the final regression equation with kernel function $K(X, X')$ can be in the form:

$$f(X) = \sum_i K(X, X_i) + b \quad (5)$$

The well-known kernel functions are Linear, Polynomial, Radial Basis Function (RBF), Sigmoidal. The present study tried the Linear and Gaussian and RBF kernels and the Gaussian kernel function has been identified as suitable one in terms of the performance measures for the RWT modelling.

5 Evaluation Criteria of Model Performance

The model performance of MLRM was tested based on the Nash-Sutcliffe coefficient (NSC) [22] (Eq. 6), to show the efficiency of the model fit. The quality of the MLRM is analyzed using Root Mean Square Error (RMSE) [15] (Eq. 7).

$$NSC = \frac{\sum_{i=1}^n (T_{W_{Sim}} - T_{W_{Obs}})^2}{\sum_{i=1}^n (T_{W_{Obs}} - T_{W_{Obs,Avg}})^2} \quad (6)$$

$$RMSE = \sqrt{\frac{\sum_{i=1}^n (T_{W_{Sim}} - T_{W_{Obs}})^2}{n}} \quad (7)$$

where $T_{W_{Sim}}$ is the simulated daily river water temperature at time step i in $^{\circ}\text{C}$; $T_{W_{Obs}}$ is the observed daily river water temperature at time step i in $^{\circ}\text{C}$; $T_{W_{Obs,Avg}}$ is the average daily river water temperature at time step i in $^{\circ}\text{C}$; n is the number of data pairs in comparison.

6 Statistical Downscaling Model

A statistical downscaling model can be adopted to predict the changes in daily streamflow and air temperature projections based on General Circulation Models (GCMs) outputs. GCMs are climate models designed to simulate time series of climate variables globally, accounting for the greenhouse gases in the atmosphere for current and future scenarios. Downscaling models are the statistical techniques, which are used to bridge the spatial and temporal resolution gaps between the GCMs and impact assessment studies. Generally, these methods involve deriving empirical relationships that relate the large-scale simulations of climate variables (referred as the predictors) provided by a GCM to regional scale hydrologic variables (referred as the predictands). A multivariable statistical downscaling model based on Canonical Correlation Analysis (CCA) was used in the present study, which relates the atmospheric climate variables and downscalable variables (e.g. streamflow and air temperatures) linearly. The downscaling model involves, data pre-processing of standardization and normalization to remove the systematic bias in the climate model simulations, data reduction methodology of Principal Component Analysis (PCA) on the large-scale climate variables of predictors [26]. The preprocessed predictors and

predictands (streamflow and air temperatures) were given as input to CCA model, which converts them into canonical variables (Eqs. 1 and 2). Canonical regression equations will be developed for both streamflow and air temperatures separately with the NCEP/NCAR reanalysis data sets (X) and observed data (Y) of period

$$U_m = a^T X, q = 1, \dots, \min(N, M) \quad (8)$$

$$V_m = b^T Y, q = 1, \dots, \min(N, M) \quad (9)$$

where U_m and V_m are called predictor and predictand canonical variables respectively, $a = [a_1, a_2, \dots, a_N]^T$ and $b = [b_1, b_2, \dots, b_N]^T$ are canonical loadings or weights. The canonical correlation, ρ_{c_q} , between predictors canonical variable, U_q and predictand canonical variable, V_q is maximum. The canonical coefficients of the predictor and predictand variables estimated based on the training period from 1988 to 1998 and tested for the period from 1999 to 2005 was used for the future projections of streamflow and air temperatures with GCM projected climate variable.

7 Results and Discussion

The statistical downscaling model based on CCA was used to predict the changes in daily streamflow and air temperature projections from BCC-CSM 1-1 GCM for the period from 2006 to 2099. Figure 2 shows the observed, simulated with NCEP data and simulated with GCM data for streamflow and air temperature for the training period of 1988 to 1998. The performance of the statistical downscaling model was tested with the Root Mean Square Error (RMSE) and Nash-Sutcliffe coefficients. The performance of the downscaling model in terms of N-S coefficients as 0.73 and 0.21 for the training and testing periods respectively for streamflow, whereas, for air temperature as 1.00 and 0.56 for the training and testing periods respectively. The RMSE values for the training and testing periods for streamflow were obtained as 403.61 and 419.77 respectively, whereas, for air temperature, the RMSE values were obtained as 3.41 and 3.92 for the training and testing periods, respectively.

Overall, a significant decrease in daily streamflow values and increase in air temperatures were observed for Tunga river at station Shimoga for current and projected scenarios [26]. The historical and projected streamflow and air temperatures were used with MLRM and SVR to study the impact of RWT under climate change. The present study compared the MLRM and SVR models to predict the RWT at daily scale along Tunga-Bhadra River. For both the models, the training period is considered as 1989 to 1999 and the testing period as 2000 to 2005. The trained and tested models of the MLRM and SVR with good agreement over the performance measures were used for the future prediction of RWT. The Fig. 3 shows the observed, simulated daily RWT with MLRM and SVR for (a) training and (b) testing period of 1989 to 1999 and 2000 to 2005 respectively. The performance of MLRM in pre-

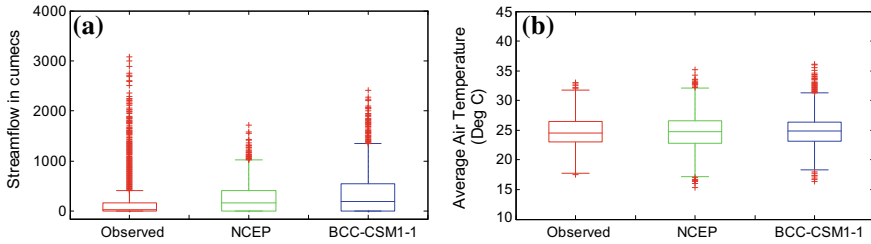


Fig. 2 Observed and simulated from NCEP and GCM (BCC-CSM1-1) data sets for the training period of 1988 to 1998 for **a** streamflow and **b** air temperatures

dicting the RWT in terms RMSE for training and testing periods were obtained as 1.19 and 1.85 respectively, whereas, the N-S numbers for training and testing were obtained as 0.79 and 0.53 respectively. The predictability of RWT has been improved by applying the SVR model with RMSE for training and testing periods as 0.95 and 1.69 respectively. The N-S numbers in the prediction of RWT for training and testing periods were obtained as 0.87 and 0.61 respectively with SVR. Overall, the performance of the MLRM and SVR in the prediction of daily RWT were satisfactory in terms of RMSE and N-S numbers, with more accuracy towards the SVR model. The trained and tested MLRM and SVR models were used to predict the RWT for future scenarios with the projections obtained from CCA downscaling model.

Table 1 shows the annual mean of RWT at Shimoga, along Tunga-Bhadra river for the historical period of 2000–2005 and for the future time periods of 2020–2040, 2041–2060, 2061–2080, 2081–2100 for MLRM and SVR models. Figure 4 shows the observed and projected annual RWT for the future time periods of with MLRM and SVR models. From Table 1 and Fig. 4, it is evident that the RWT projections based on regression model have been identified as more pronounced compared to SVR model. However, the present study revealed that there will be a significant impact on climate change on RWT with pronounced increases at annual scales. Tunga-Bhadra river has been suffered in terms of river water quality with the decrease of streamflow of about 3.1% at Shimoga for the historical periods [25] and 21% of reduction for the period of 2070–2100 MIROC 3.2 GCM along the Tungabhadra River [26]. Furthermore, the air temperature is also projected to increase about 1.66 °C for the period from 2070 to 2100 according to MIROC 3.2 GCM along the Tunga-Bhadra River [26] and therefore a significant increase in the RWT extremes [28] leading to deterioration of water quality.

8 Conclusions and Future Directions

Modelling river water quality under climate change is prominent to understand the projected risk of low water quality and possible adaptation and management policies to be implemented. Such impact assessment models need to be integrated with cli-

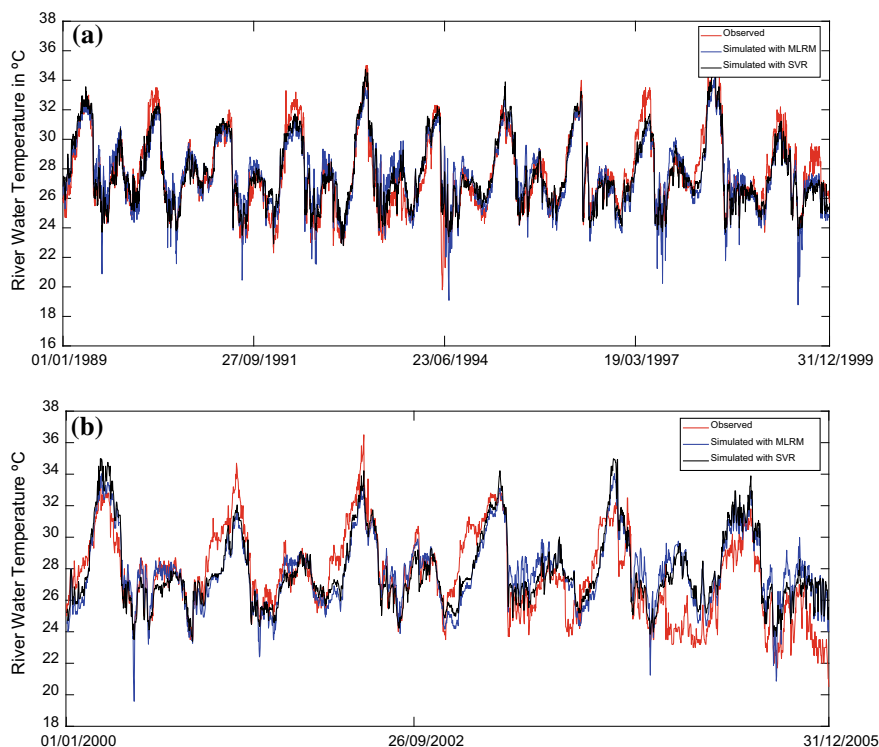


Fig. 3 Observed and simulated river water temperature for **a** training **b** testing periods for Tung-Bhadra River at Shimoga, Karnataka, India

Table 1 The annual mean of RWT for the observed and future time periods for MLRM and SVR

Time period	MLRM	SVR
Historical (2000–2005)	27.87	27.87
2020–2040	25.91	25.85
2041–2060	27.23	26.69
2061–2080	28.66	27.45
2081–2100	29.99	28.09

mate change projections models. The present study integrated the RWT prediction models with a statistical downscaling model to analyze the climate change impacts on temperatures of rivers. A multiple linear regression model and support vector regression models were developed to predict the daily RWT under climate change along Shimoga Tunga-Bhadra river, India. The SVR model has identified as the best prediction performance compared to linear regression models. The SVR model fitted the daily RWT with a N-S number of 0.87 and 0.61, whereas the MLRM fitted the RWT with N-S numbers as 0.79 and 0.53 respectively for training and testing peri-

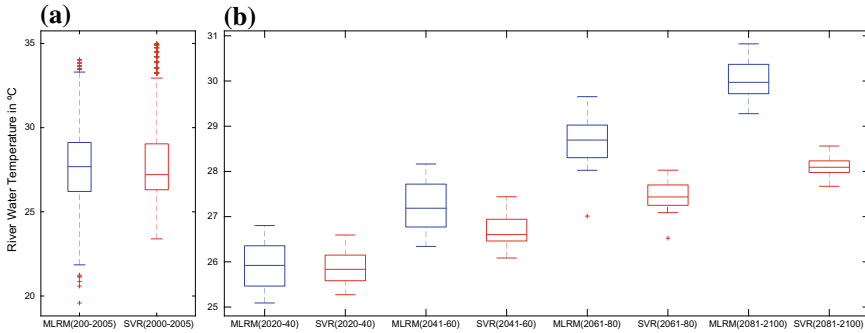


Fig. 4 Annual river water temperature for **a** observed period of 2000–2005 **b** future projections for period of 2020–2040, 2041–2060, 2061–2080 and 2081–2100 with MLRM and SVR models for Shimoga station, Tunga-Bhadra river, India

ods. The fitted models of SVR and MLRM based on historical data were used with the downscaled projections of streamflow and air temperatures from CCA down-scaling model. The RWT projections based on MLRM model has been identified as more pronounced compared to SVR model. The annual RWT increase for the river from near future time period of 2020–2040 to 2081–2100 is estimated as 3.99 and 2.24 °C for MLRM and SVR respectively. The more intensified changes in RWT was predicted based on a linear regression model compared to the advanced machine learning algorithm of SVR. Therefore, the present study suggests the use of both the data-driven models for the possible application to study the RWT under climate change. Although such data-driven models are not accurate to predict the changes in RWT due to the non-stationarity relationship between air and RWT over time, the simplicity of applicability for predicting future RWT motivates to adapt in the management policies. Further, the data-driven models will not provide a physical justification, and projections made on such models are always subjected to uncertainties [3] as the models are validated within the range of measured values [36]. Therefore, knowing the limitations and strengths of each of the existing models, the RWT prediction tools can be applied for the effective assessment of river water quality for various spatial and temporal scales of the case studies varying from global to local/regional scales.

References

1. Allen D, Dietrich WE, Baker PF, Ligon F, Orr B (2007) Development of a mechanistically-based, basin-scale stream temperature model: applications to cumulative effects modeling. In: Standiford RB, et al (eds) Proceedings of the redwood region forest science symposium: What does the future hold? Forest Service, US department of agriculture, Albany, California, pp 11–24

2. Arnold JG, Srinivasan R, Muttiah RS, Williams JR (1998) Large area hydrologic modeling and assessment part I: model development. *J Am Water Resour Assoc* 34(1):73–89
3. Benyahya L, Caissie D, St-Hilaire A, Ouarda TB, Bobe B (2007) A review of statistical water temperature models. *Can Water Resour J* 32:179–192
4. Bogan T, Mohseni O, Stefan HG (2003) Stream temperature-equilibrium temperature relationship. *Water Resour Res* 39(9):1245. <https://doi.org/10.1029/2003WR002034>
5. Caissie D (2006) The thermal regime of rivers: a review. *Freshw Biol* 51:1389–1406
6. Caissie D, El-Jabi N, St-Hilaire A (1998) Stochastic modeling of water temperatures in a small stream using air to water relations. *Can J Civil Eng* 25:250–260
7. Chapra SC (1997) *Surface water quality modelling*. McGraw Hill Kogakusha Ltd., New York
8. Chapra SC, Pelletier GJ, Tao H (2006) *QUAL2 K: a modeling framework for simulating river and stream water quality, version 2.04: documentation and users manual*. Civil and environmental engineering department, Tufts University, Medford, MA
9. Chenard J-F, Caissie D (2008) Stream temperature modelling using artificial neural networks: application on catamaran brook, new Brunswick, Canada. *Hydrol Process* 22(17):3361–3372
10. DeWeber JT, Wagner TA (2014) Regional neural network ensemble for predicting mean daily river water temperature. *J Hydrol* 517:187–200. <https://doi.org/10.1016/j.jhydrol.2014.05.035>
11. Edinger JE, Duttweiler DW, Geyer JC (1968) The response of water temperatures to meteorological conditions. *Water Resour Res* 4(5):1137–1143
12. Erickson TR, Stefan HG (2000) Linear air/water temperature correlations for streams during open water periods. *J Hydrol* 5(3):317–321
13. Ficklin DL, Luo Y, Stewart IT, Maurer EP (2012) Development and application of a hydroclimatological stream temperature model within the soil and water assessment tool. *Water Resour Res* 48:W01511. <https://doi.org/10.1029/2011WR011256>
14. Hsu K-l, Gupta HV, Sorooshian S (1998) *Streamflow forecasting using artificial neural networks*. In: *Water resources engineering '98*, ASCE, pp 967–972
15. Janssen PHM, Heuberger PSC (1995) Calibration of process oriented models. *Ecol Modell* 83(1–2):55–66
16. Lima AR, Cannon AJ, Hsieh WW (2012) Downscaling temperature and precipitation using support vector regression with evolutionary strategy. In: *WCCI 2012 IEEE World congress on computational intelligence*, Brisbane, Australia
17. McCuen RH, Synder WM (1986) *Hydrologic modeling: statistical methods and applications*. Prentice-Hall, Englewood Cliffs, N.J. ISBN 0134481194
18. Mohseni O, Stefan HG, Erickson TR (1998) A nonlinear regression model for weekly stream temperatures. *Water Resour Res* 34:2685–2692
19. Mohseni O, Stefan H (1999) Stream temperature/air temperature relationship: a physical interpretation. *J Hydrol* 218(3):128–141
20. Morin G, Couillard D (1990) Predicting river temperatures with a hydrological model. *Encycl Fluid Mech Surf Groundw Flow Phenom* 10:171–209
21. Morrill JC, Bales RC, Conklin MH (2005) Estimating stream temperature from air temperature: implications for future water quality. *J Environ Eng* 131(1):139–146
22. Nash JE, Sutcliffe JV (1970) River flow forecasting through conceptual models, part 1: a discussion of principles. *J Hydrol* 10(3):282–290
23. Neumann DW, Rajagopalan B, Zagona EA (2003) Regression model for daily maximum stream temperature. *J Environ Eng* 129(7):667–674
24. Pilgrim JM, Fang X, Stefan HG (1998) Stream temperature correlations with air temperatures in Minnesota: implications for climate warming. *J Am Water Resour Assoc (JAWRA)* 34(5):1109–1121
25. Rehana S, Mujumdar PP (2011) River water quality response under hypothetical climate change scenarios in Tunga-Bhadra river, India. *Hydrol Process* 25(22):3373–3386
26. Rehana S, Mujumdar PP (2012) Climate change induced risk in water quality control problems. *J Hydrol* 444:63–77

27. Rehana S, Munoz-Arriola F, Rico DA, Bartelt-Hunt SL (2017) Modeling water temperature's sensitivity to atmospheric warming and river flow. In: Sobti RC, Arora NK, Kothari R (eds) *Environmental biotechnology: for sustainable future*. Springer. ISBN 978-981-10-7284-0. <http://www.springer.com/la/book/9789811072833>
28. Rehana S, Dhanya CT (2018) Modeling of extreme risk in river water quality under climate change. *J Water Clim Chang*. <https://doi.org/10.2166/wcc.2018.024> (Pub: International Water Association)
29. Sahoo G, Schladow S, Reuter J (2009) Forecasting stream water temperature using regression analysis, artificial neural network, and chaotic non-linear dynamic models. *J Hydrol* 378(3):325–342
30. Sinokrot BA, Stefan HG (1993) Stream temperature dynamics: measurements and modeling. *Water Resour Res* 29(7):2299–2312
31. Smith K (1972) River water temperatures-an environmental review. *Scott Geogr Mag* 88(3):211–220
32. St-Hilaire A, Morin G, El-Jabi N, Caissie D (2000) Water temperature modelling in a small forested stream: implication of forest canopy and soil temperature. *Can J Civ Eng* 27(6):1095–1108
33. Stefan HG, Preud'homme EB (1993) Stream temperature estimation from air temperature. *J Am Water Resour Assoc (JAWRA)* 29(1):27–45
34. Temizyurek M, Dadaser-Celik F (2018) Modelling the effects of meteorological parameters on water temperature using artificial neural networks. *Water Sci Technol* 77(6):1724–1733
35. Thomann RV, Mueller JA (1987) *Principles of surface water quality modelling and control*. Harper Collins Publishers, New York
36. Toffolon M, Piccolroaz S (2015) A hybrid model for river water temperature as a function of air temperature and discharge. *Environ Res Lett* 10:114011
37. Vapnik V, Golowich S, Smola AJ (1997) Support vector method for function approximation, regression estimation, and signal processing. In: *Advances in neural information processing systems*. MIT Press, Cambridge, MA, pp 281–287
38. van Vliet MTH, Ludwig F, Zwolsman JGG, Weedon GP, Kabat P (2011) Global river temperatures and sensitivity to atmospheric warming and changes in river flow. *Water Resour Res* 47:W02544. <https://doi.org/10.1029/2010WR009198>
39. Wang WC, Xu DM, Chau KW, Chen S (2013) Improved annual rainfall-runoff forecasting using PSO-SVM model based on EEMD. *J Hydroinf* 15(4):1377–1390
40. Webb B, Clack P, Walling D (2003) Water air temperature relationships in a Devon river system and the role of flow. *Hydrol Process* 17(15):3069–3084
41. Yearsley JR (2009) A semi-lagrangian water temperature model for advection dominated river systems. *Water Resour Res* 45(12)

Assessing the Impact of Climate Change on Water Resources: The Challenge Posed by a Multitude of Options



Riddhi Singh and Basudev Biswal

1 Introduction

The rise of global mean temperature due to anthropogenic emissions of greenhouse gases, a phenomenon known as global warming, is widely recognized by climate scientists [3, 82]. However, it is not clear how global warming will impact water resources around the world. Although according to Clausius–Clapeyron relationship, global mean precipitation should increase due to global warming, climate models predict a highly uneven picture of precipitation changes spatially. In some parts of the world, mean annual precipitation is likely to increase, whereas in other parts, it may decrease. The uncertainty in precipitation estimates is pronounced in regions such as the Indian subcontinent, which receive precipitation mainly due to summer monsoon [38, 64, 63, 70]. Even if the mean annual precipitation remains unchanged in a region, the temporal distribution of precipitation may change significantly. For instance, in most parts of India, mean annual precipitation is within the historically observed ranges but extreme precipitation events are on the rise—heavy rainfall events are becoming more frequent, whereas moderate ones are becoming fewer [64].

From a water resources manager's point of view, the main concern is whether climate change will impact water resources of a region negatively and currently used management strategies will fail. Many studies suggest that a changing climate coupled with other anthropogenic alterations may adversely affect water resources in several parts the world, thus exposing the population in those regions to increased risks of hydrologic disasters [36, 37, 40]. According to one estimate, nearly two-thirds of the global population, about a half of whom live in India and China, are

R. Singh (✉) · B. Biswal
Department of Civil Engineering, Indian Institute of Technology Bombay,
Powai, Mumbai 400076, India
e-mail: riddhi@civil.iitb.ac.in

B. Biswal
Interdisciplinary Program in Climate Studies, Indian Institute of Technology Bombay,
Powai, Mumbai 400076, India

© Springer Nature Switzerland AG 2019
S. K. Singh and C. T. Dhanya (eds.), *Hydrology in a Changing World*, Springer Water,
https://doi.org/10.1007/978-3-030-02197-9_9

currently living under severe water scarcity for at least 1 month in a year [50]. Moreover, due to the expected rise of extreme rainfall events in a changing climate, a significant percentage of the global population may be at risk of experiencing catastrophic flooding [5]. An additional challenge faced by many countries, particularly the developing ones, is increasingly uneven distribution of population due to the migration of people from rural areas to urban areas, which requires transportation of water from faraway places to cities [86]. It has also been argued that the water crisis caused by climate change may lead to large-scale political conflicts [35, 45, 84]. In view of the imminent challenges posed by climate change, it is important for hydrologists and water resources managers to carefully study climate change impact on freshwater resources which are already under stress in many parts of the world due to population growth, lifestyle changes, industrialization, and agricultural intensification [14, 33, 59].

Many efforts have already been made to estimate the possible impacts of a changing climate on water resources. A wide variety of methods have been developed and continue to be explored [91]. Generally, approaches involve the use of general circulation models (GCMs), also called global climate models. By simulating how possible changes in future greenhouse gas forcings will affect the global climate, GCMs project possible changes in two main hydro-climatic variables: precipitation and temperature. These projections are then used to drive hydrologic models at various spatial scales and translate the impact of changing climate on water resources. However, with the proliferation of methods, there is also a growing confusion as to the best way to approach the issue of impact assessment. One of the most challenging issues is the high uncertainty in GCM-projected precipitation in many parts of the globe [55]. Apart from this, the choice of suitable techniques to post process coarse-resolution GCM data to match the scale of predictions required in local decision-making, choice of hydrologic models, evaluation metrics, etc., may present quite a dilemma to a modeler.

Climate change impact assessment studies require realistic projections of future precipitation and temperature from climate models, but often are unable to obtain them. It is also important for us to develop an adequate understanding of how hydrological systems respond to climate change as the selected hydrological models may not predict hydrological variables well [10, 78, 85]. Although there are several methods and models one can find in the hydrologic literature, there is no standard guideline on how to perform climate change impact assessment. The main aim of this chapter is to highlight the dilemma a hydrologic modeler may encounter while attempting to study the impact of climate change on water resources of a region. In Sect. 2, we discuss the various approaches that are currently available to assess the impact of changing climate on water resources. We discuss the relative advantages and disadvantages of different approaches. Section 3 focuses on uncertainties that emerge from the choice of hydrological models and discusses the philosophical bases behind the model selection. The section also highlights the issues related to the evaluation of models. We close the chapter with a discussion on some recent developments and highlights of future research areas on this subject.

2 Assessment of Climate Change Impact on Water Resources: An Overview of the Existing Methods

2.1 *Climate Change and the Global Hydrologic Cycle*

The hydrological cycle, which determines the distribution of fresh water across the globe, is driven by energy gradients induced by differential heating of Earth from the Sun. Therefore, at a global scale, the hydrological cycle is intimately linked with the large-scale atmospheric circulation patterns. Oceans also affect the hydrological cycle considerably due to their influence on atmospheric availability of moisture and their heat absorption properties, among other functions. Thus, the hydrological cycle is an essential component of the general circulation of moisture and energy on the Earth. This is true not only at a global scale, but also at continental, regional, and local scales. For example, hydrologic partitioning at small scales is primarily governed by available water and energy from the atmosphere [7]. Concurrently, the topography, moisture state of soil, and vegetative cover on the land surface feedbacks to the local atmospheric circulation. This tight, two-way linkage between climate and water cycle at varying spatial scales indicates that any change in climate will cause changes in the spatiotemporal distribution of freshwater resources across the globe.

Today, the scientific community agrees that anthropogenic emission of carbon dioxide and other greenhouse gases have led to an increase in global mean temperature and consequent changes in large-scale circulation patterns of the atmosphere [55]. A generally warmer atmosphere can hold more water, as expected from the Clausius–Clapeyron relationship. So, on an average, the hydrological cycle is expected to intensify, i.e., both evaporation and precipitation fluxes will increase [30, 42]. The Clausius–Clapeyron relationship projects that for each degree rise in global mean temperature, there will be nearly 7% increase in global mean precipitation. However, variations from this estimate have been observed when analyzing historically observed data [30]. The variation is due to local factors such as vegetation, topography, humidity conditions, etc. Thus, it is generally not possible to directly estimate the impact of increases in greenhouse gas concentrations on changes in precipitation and thereafter streamflow at regional (decision-relevant) scales. However, some attempts have been made to directly link large-scale indicators of atmospheric circulation (such as sea surface temperatures) to streamflow [20].

The effects of increasing concentrations of greenhouse gases on the long-term evolution of the atmosphere are studied via general circulation models (GCMs) that simulate the global climate. While some effects of anthropogenic emissions of carbon dioxide on the global climate are strongly debated, other impacts are more certain. For example, GCMs typically show large uncertainties in projections of precipitation in many parts of the world [55, 57]. However, there is a strong agreement between GCMs that temperatures will rise across the globe [55]. The coupling between hydrologic partitioning and atmospheric conditions manifests itself in the model structure of GCMs that includes mechanisms for hydrologic partitioning, and even hydrologic routing in advanced versions [47, 49, 89]. Simply put, each GCM has a hydrologic

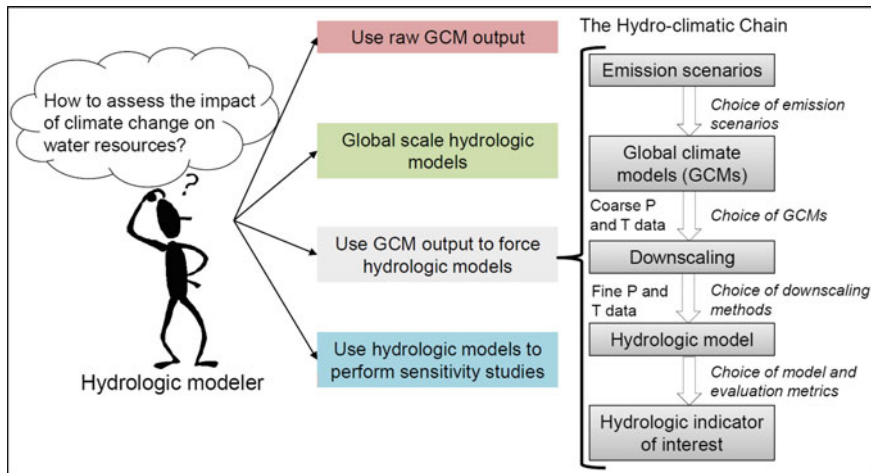


Fig. 1 Various choices that a modeler faces when assessing the impact of climate change on water resources. P: precipitation, T: temperature

model built into it. In an ideal scenario, GCMs should be able to model the Earth system in detail including the feedback between the hydrologic fluxes and atmospheric circulation at various scales. Thus, the output from a climate model should also provide an accurate estimation of hydrologic variables such as soil moisture states and runoff. But, GCMs tend to focus more on atmospheric and oceanic processes. They divide the atmosphere into several vertical layers and simulate processes at time steps for few minutes. On the other hand, the parametrization of land surface processes in GCMs is considered quite rudimentary though improvements have been made over different generations of GCMs. Thus, many alternative methods have been used to overcome this scale mismatch between GCMs outputs and decision-relevant hydrologic variables. We discuss these methods (Fig. 1).

2.1.1 GCM-Projected Runoffs

As discussed before, global as well as regional climate models (RCMs) simulate runoff as a secondary variable. They provide grid-scale runoff outputs on a global scale. The grid size is determined by the spatial resolution of the GCM or RCM. The time series of these runoff fields can be studied to assess the impact of changing greenhouse gas concentrations on freshwater availability. However, we generally do not use direct runoff outputs from GCMs or RCMs for assessing the future availability of water resources at regional scales. One of the main drawbacks of raw GCM runoff fields is their coarse resolution. Decision-makers are interested in output variable statistics at a much finer resolution [68, 91]. Another issue is that the land surface and hydrologic processes in GCMs are oversimplified and do not consider the role

of detailed topography, land cover, or soil types. Finally, there are several GCMs available to users, and it is known that different GCMs may or may not agree on the nature of precipitation change in many parts of the world. This creates a large uncertainty in projected raw runoff outputs derived from the GCMs. These issues are in-part addressed by using RCMs, which can be run at a finer resolution as compared to GCMs using the boundary conditions from the parent GCM. However, RCMs inherit the biases from the parent GCMs via their boundary conditions and are computationally very expensive [39].

2.1.2 Global or Continental Water Balance Models

Global to continental scale water balance models can be run by using forcing of temperature and precipitation available as GCM output. These models can be run at a finer resolution (0.25° – 0.5°) as compared to GCMs and can also include a more detailed representation of hydrologic processes. These models were borne out of the need to develop calibration-free hydrologic models that could be coupled with climate models to simulate the global hydrologic cycle. Any hydrologic model needs parameterization for runoff generation and flow routing processes. To avoid computationally expensive automatic calibration, the parameters of such macroscale models are derived for each grid cell directly from global datasets for soil texture, vegetation, etc. Even after estimating some parameters directly from global datasets, each macroscale model required some level of tuning for the remaining parameters. In most instances, manual calibration was carried out for such parameters by the model developers. Examples include the water balance model (WBM by Vörösmarty et al. [82, 83]), macroPDM [4], and the variable infiltration capacity model (VIC by Wood et al. [89]).

The development of such global scale water balance models ushered in a new era of global scale runoff projections. These models made it feasible to visualize changes in runoff globally, enabling translation of global scale GCM outputs to global water availability. Despite their advantages, these models are also beset with the same challenges as any other hydrologic model. The quality of parameterization of these models will depend directly on the quality of the input data, and the streamflow data against which they were manually tuned. The uncertainty in their projections is generally more in ungauged regions, where there is no way to assess model performance. Therefore, the challenge in regionalization of model parameters that afflicts predictions in ungauged basins also afflicts the outputs of macroscale hydrologic models. These issues are further elaborated in Sect. 3.

2.1.3 Using GCM Outputs to Drive Hydrologic Models

This is by far the most commonly used method to assess the impact of climate change on water resources. The approach involves using raw or post-processed GCM-projected climate to drive a hydrological model. To account for the scale mismatch

between the raw GCM outputs and input requirements for regional hydrologic models, GCM outputs are often downscaled using a variety of statistical or dynamic methods [34]. The downscaled precipitation and temperature data are then used as an input to a hydrologic model. The hydrologic model is typically parameterized using past climate and streamflow information. There are two main ways in which GCM data is used to project future runoff. These are listed below:

- i. **Downscaling GCM output:** This approach uses the downscaled time series of hydro-climatic variables to simulate streamflow and other hydrologic variables for both the historical and future time periods. Then, the relative change in the relevant indicator of interest, say mean annual runoff, is estimated by using the historical and future estimates from each GCM and downscaling approach [82, 87]. This method focuses on the projected relative changes from the downscaled GCM output and not on the absolute projections of the indicator. It is well known that GCMs can carry a significant bias in their projected climate even after downscaling. By focusing the analysis on relative changes, studies attempt to eliminate this lack of performance of the downscaled product on the historically observed climate. The underlying assumption here is that the biases observed in a GCM–downscaling combination remain the same as we move to a new climate.
- ii. **Change factor approach:** This approach is motivated from the fact that even after downscaling, a GCM product may not reproduce the observed historical climate of a catchment very well. Alternatively, easily accessible downscaled GCM data may not be available for the region of interest. It is also possible that the process of downscaling introduces synthetic patterns in the climate data, distorting the information regarding expected changes in climate. Finally, it is not necessary that statistical relationships developed using historical data will hold true under a changing climate, thus questioning the reliability of statistical downscaling techniques under nonstationary climatic conditions. In such cases, a modeler can choose to use the information about projected relative changes in climate from the raw GCM outputs and apply it to the historically observed climate time series. Thus, instead of forcing the hydrologic model with downscaled GCM climate, the modeler uses synthetically generated climates by combining the information from historically observed time series and raw GCM outputs. This approach is termed as the change factor approach [27]. However, this approach required the development of methods that can be used to alter the time series of historically observed temperature or precipitation. For example, a modeler can decide to estimate only the changes in long-term precipitation and temperature from the raw GCM output and apply it to the historically observed time series. Alternatively, more sophisticated techniques such as quantile mapping can be used. This choice adds an additional source of uncertainty to the projections thus derived.

In general, the use of GCM outputs, with or without downscaling, to force hydrologic models has gained popularity in water-related climate change impact assessments due to several reasons. First, most decision-making related to water resources is done at a regional or catchment scale. For example, dam operators will be inter-

ested to know whether the inflows to the reservoir may change significantly under possible climatic changes. In most cases, they have already established various kinds of hydrologic models to manage such water-related decision-making under the historical climate. It is prudent for them to utilize the knowledge developed through previous modeling exercises to understand how a system may behave under a changing climate [60]. Therefore, a method that can utilize existing hydrologic models to project future changes would be preferred. Second, alternatives such as using direct GCM-projected runoff or macroscale water balance models do not provide the necessary information at a fine spatial or temporal resolution. Such global scale outputs may be useful to understand changes in the global hydrological cycle broadly but are not so helpful in local to regional decision-making related to water. This is partly due to large uncertainties in projections of future runoff arising from GCM-projected runoff fields, or due to large uncertainties inherent in regionalized model parameters in global scale models [91]. Finally, this approach allows hydrologist to utilize a variety of hydrologic models, ranging from conceptual to semi-distributed to fully distributed, to assess the impact of climate change on a range of hydrologic variables of interest (see Sect. 3 for details).

2.1.4 Sensitivity-Based Approaches

All the approaches discussed, until now require climate model outputs to understand possible changes in a hydrologic indicator of interest. As discussed before, many times, climate model outputs are beset with large uncertainties or are heavily biased when compared against observed historical climate. These uncertainties or biases will be reflected in the future assessments of hydrologic indicators. Sensitivity-based approaches attempt to understand the response of a hydrologic system to changing climate, independent of possible changes in future climate. They provide a quantification of changes in hydrologic indicators as a function of synthetic changes in climate. These synthetic changes are applied to historically observed time series of climate data. The simplest approach is the delta change method that creates alternative climates by adding or subtracting constants from the time series of precipitation and temperature. For example, the delta change approach can be used to generate precipitation time series with long-term means varying from -50 to 50% of the historically observed mean annual precipitation. Together, the combination of precipitation and temperature change thus generated constitutes a suite of scenarios. More sophisticated techniques involve the use of weather generators [69]. The modeler can thus explore likely changes in hydrologic variables such as mean annual runoff across many possible climate change scenarios by using different hydrologic models [53, 66]. Alternatively, existing database of streamflow, climate, and other catchment characteristics can be used to identify relationships between streamflow and climate variables [80]. These relationships developed across many catchments can also be used to understand how streamflow might change in the future [73].

2.2 *Uncertainty Quantification*

Given the vast array of choices available to modelers, it is natural that assessments of climate change impact on water resources have gradually moved toward development of various methods of uncertainty quantification. Typically, uncertainty quantification methods do not explore all possible approaches as discussed in Sects. 2.1.1–2.1.4. Rather, they focus on quantification of uncertainty once a broader approach is decided upon based on the requirements of the impact assessment exercise. Numerous studies quantify the uncertainty in impacts of climate change and/or attribute it to various sources such as choice of climate models, downscaling methods, hydrologic models, etc. An exhaustive treatment of different types of uncertainties and their quantification is beyond the scope of this chapter.

The most commonly used uncertainty quantification methods are ensemble-based methods [67] and probabilistic approaches [88]. Ensemble-based approaches use several GCMs, downscaling approaches, and hydrologic models to generate an ensemble of future streamflow. The uncertainty in streamflow projections can then be quantified using various summary statistics such as the interquartile range as estimated from the projected ensemble. Probabilistic approaches assign weights to different GCMs or downscaling methods in proportion to their ability to reproduce the historical climate. When projecting future streamflow, the same weights are used to assign probability to various projections [88]. There are also studies that attempt to attribute the total uncertainty in the projection of a hydrologic indicator to various sources using a variety of statistical or simulation-based techniques [44]. In general, most studies indicate that GCMs are the major source of uncertainty in the future runoff. However, the choice of hydrologic model may also be an important source of uncertainty when the focus is on indicators such as lean season flows [79]. Such conclusions are typically dependent on the choice of study area, GCMs, etc., and cannot be generalized unless further studies are carried out across many catchments.

2.3 *Decision-Relevant Hydrologic Indicators*

As changing climate alters the global hydrologic cycle, all major hydrologic fluxes are liable to change. A decision maker may be interested in one or more hydrologic fluxes depending upon the application. For example, dam operators will be concerned about how inflows to the dam may change in the future. In this case, both the magnitude and timing of inflows will impact the operation of dams. Similarly, the design of any water-related infrastructure such as pipe or sewer networks will require estimation of design flows, which in turn requires estimation of streamflow volumes at prescribed return periods. Similarly, water managers may be interested in possible yields that can be obtained by construction of reservoirs to deal with water scarcity. In this case, only seasonal or annual surface water availability may be of interest. Reservoir designs will also need to account for possible changes in sediment yields in the

future, which in turn depend partly on the inflows. Farmers may be interested in both the availability of surface runoff as well as soil moisture and groundwater. Similarly, environmental requirements will also depend on maintaining soil moisture as well as instream flows. Among these various hydrologic fluxes, streamflow has been the focus of numerous assessments [2, 6, 7, 27, 44, 67, 82, 87], while recent efforts have also focused on changes in soil moisture states [65].

Since both the timing and magnitude of streamflow are required for most applications, simulating a time series of future streamflow has been the most common approach to study the impact of climate change on water resources. Once a time series of streamflow is derived for a given future climate, possible changes in mean annual runoff, or indicators of hydrologic extremes can be studied. Examples of hydrologic indicators that can be derived from streamflow time series, apart from mean annual runoff, include frequency of floods or droughts, duration of droughts, flow duration curves, etc. In addition, some application may require an understanding of how surface and groundwater resources may be jointly affected by a changing climate [31, 56]. In such cases, models that can simulate both surface hydrology, as well as groundwater related processes such as recharge and baseflow formation, are used. Long-term means of hydrologic variables are generally used to assess changes in water availability of a region [72]. Note that the finer the time scale at which an indicator is required, the greater the uncertainty related to its projection. These issues are further discussed in Sect. 3.2.

3 Hydrological Models and Evaluation Criteria

As we discussed in the previous section, hydrological models play a crucial role in climate change impact assessment on water resources. If we had an ideal hydrological model, we would be able to predict hydrological fluxes and variables with a high degree of accuracy. However, processes responsible for the transformation of rainfall into streamflow and evapotranspiration are extremely complex and often unobservable. Thus, hydrologic modeling is bound to involve subjectivity [9, 12, 21]. The structure of a hydrological model primarily depends on the modeler's perception about key hydrological processes [13]. Not surprisingly, numerous models have been proposed for hydrological modeling in the past [13, 26, 71, 75]. Someone who is new to hydrological modeling may, therefore, wonder if it is possible to find the most suitable model for a climate change impact assessment study. The main purpose of this section is to elucidate the subjectivities involved in hydrological modeling and model development. This will help a reader in making a more informed decision when choosing a hydrologic model to assess the impact of climate change on water resources.

3.1 *Hydrological Models: Which One to Choose?*

First and foremost, a hydrological model's structure largely depends on the philosophical viewpoint of the modeler. Every model is designed keeping in mind several objectives. In the context of climate change impact assessment, we classify hydrological models into the following three groups: (i) pure data-based models, (ii) models based on established physical principles, and (iii) conceptual models.

Pure data-based models are black-box-type models that use only observed hydrological fluxes to make predictions. In other words, they predict hydrological variables without even attempting to understand the underlying hydrological processes. These models seem to rely on two key assumptions. First, hydrological processes are far too complex to be incorporated in a model in a meaningful manner. Second, hydrological data from a river basin contain enough information to model the behavior of the basin. Examples of pure data-based models include multiple linear regression (MLR) based models [28], variations of autoregressive–moving-average (ARMA) models [90], and artificial neural network (ANN) models [52]. They are widely used mainly because they take relatively less time for set up. However, they are often considered to be not very reliable because of their inability to explain hydrological processes, and, therefore, their use in climate change impact assessment is limited.

In contrast to the pure data-based modeling approaches, there are approaches that solve established fluid flow equations (Saint-Venant's and Richard's equation, etc.) for modeling hydrological fluxes and variables. These models are often called distributed hydrological models, as they typically solve fluid flow equations at sub-grid scale [13]. A catchment is divided into small sub-grids or pixels, and fluid flow equations are applied separately to each sub-grid. Sub-grid-scale model outputs are then upscaled to predict hydrological fluxes at a desired scale such as that of a catchment. The main motivation behind the development of such models is the notion that true hydrological modeling can be performed only by applying fundamental equations of fluid flow [1, 19, 62]. Although this approach seems rigorous, there are several shortcomings, in particular, with respect to its implementation. The assumptions behind any fluid flow equation are rarely satisfied at sub-grid scale. In fact, it is almost impossible to find a scale at which common fluid flow equations can be meaningfully applied, because natural catchments are far too heterogeneous for a distributed hydrological model [11, 46]. Sub-grid-scale discretization forces distributed models to employ a large number of free parameters, whose values are generally determined through calibration. Although the original idea was that the parameters of a sub-grid will be directly determined from catchment properties, such an exercise is not possible at a fine spatial scale. A modeler thus ends up setting some parameters as constant across an entire grid, while others are allowed to vary spatially. In addition to the issue of defining model parameters at a fine spatial scale, it is practically impossible to obtain all relevant field data for distributed hydrological models, particularly for subsurface domains [13]. Finally, as distributed models solve partial differential equations for each sub-grid, their runtime is quite high because of which they cannot be applied to large catchments. Due to the above reasons, the

applicability of distributed hydrological models is limited to a small number of experimental catchments. Nevertheless, many hydrologists emphasize the need to have distributed models, arguing that we need to properly consider hydrological processes for many scientific and practical problems, e.g., transport of contaminants [76] and ecohydrological modeling [77]. Overall, there is no clear advantage of a distributed hydrologic model over other model types in the context of climate change impact assessment.

The third group of models tries to find a middle ground between the above two groups. Such models are generally called conceptual hydrological models. They account for dominant hydrological processes at catchment scale, and attempt to optimally utilize information contained in observational datasets. Conceptual models are generally preferred for climate change impact studies because of their simplicity and effectiveness. One can find numerous conceptual models in the hydrological literature [8, 13, 15, 16, 41]. Each model describes hydrological processes in a unique way, although there are many commonalities among various conceptual models. For example, both probability distributed model (PDM, [51]) and variable infiltration capacity model (VIC, [48]) employ the concept of partial area flow generation for rainfall–runoff modeling. Some studies divide a large catchment into various sub-catchments, employing conceptual hydrological models for each sub-catchment. By using a routing model, they predict streamflow for the large catchment. Such models are classified as semi-distributed hydrological models [13]. Different conceptual hydrological models have different complexity levels—some conceptual models are very simple containing less than five parameters, whereas others can be more complex containing more than a dozen or so parameters. Model complexity implies both number of free parameters the model requires to simulate hydrologic fluxes as well as the volume of data required for model calibration and prediction. Conceptual models are most preferred for climate change impact assessment for their low computational expense as climate change impact studies often require running the models for various GCMs and downscaling combinations.

3.2 What is to be Predicted?

As discussed on Sect. 2.3, the model structure as well as model complexity may depend on the purpose of a climate change assessment exercise. If the purpose is to predict say some statistical properties of future streamflow, the required hydrological model will generally be far less complex compared to models required for simulating continuous time series of streamflow. A common example is the prediction of flow duration curves (FDCs) which is performed for many water resources related management projects. Flow duration curve for a basin can be constructed either by using the past discharge observations or by using stochastic soil-water-balance models [17, 29].

The choice of temporal and spatial scales can also play a key role in the selection of a hydrological model. For instance, a model developed for simulating hydrologic

fluxes at an annual timescale, by design, cannot be applied to simulate hydrological fluxes at a daily timescale. Why do we have different models for different scales? The scientific rationale is that hydrological process complexity decreases with scale. Rainfall–runoff relationship at an hourly timescale is generally much more complex compared to that at an annual timescale. In other words, it is easier to develop hydrological models to predict for annual or decadal timescales. A notable example in this regard is the Budyko model, which is an allied term for many hydrological models that employ the concept of energy and water limits to perform modeling at large timescales employing none to one free parameter [7, 72]. On the other hand, models developed for simulation at smaller temporal and spatial scales generally employ greater number of free parameters and demand more detailed datasets for calibration [13]. However, many attempts have been made by hydrologists, particularly by conceptual modelers, to reduce model complexity. Some studies have suggested that the optimum number of parameters required for rainfall–runoff modeling at daily time steps ranges between 3 and 5 [43]. Recent studies have shown that modeling at small timescales may be possible even without employing a single free parameter [15].

3.3 The Issue of Prediction in Ungauged Basins

As discussed above, most models available for simulating hydrological fluxes and variables need observed discharge data for calibration. Calibration is the process of adjusting model parameters until the simulated streamflow comes reasonably close to observed streamflow. Once a model is calibrated using historical hydrological data, it can be applied for predicting hydrological fluxes and variables for any climate change scenario. However, we cannot calibrate a model for a river basin if we do not have discharge data, i.e., if the basin is ungauged. This problem is commonly faced when we attempt to predict hydrological fluxes for smaller catchments. The general solution to the problem of ungauged basins is to transfer hydrological model parameters from gauged basins, which is called regionalization [8, 54, 61]. In some cases, while attempting to predict the statistical properties of streamflow, regionalization methods are used to directly transfer relevant hydrologic information from gauged basins to ungauged basins [58]. Again, the challenge in front of a hydrologic modeler is the identification of a suitable regionalization method because one can come across numerous regionalization methods, none of which having a clear advantage over others in every region.

3.4 How do We Evaluate a Model's Prediction?

Let us consider a model trying to predict a certain static property (x) of a system. We can easily compare the modeled $x(x_m)$ with the observed $x(x_0)$. Now, consider x to be varying with time, and the model predicts x_t for every time step. We thus have a

series of modeled $x_{m,t}$ values, which needs to be compared with the corresponding observed $x_{o,t}$ values. The model's prediction may be acceptable for some time steps but may not be acceptable for some others. How do we evaluate the model in this case? Essentially, we need to have an aggregate performance index that gives a quantitative overview of the model's performance. Such an indicator is very useful for evaluating hydrological models since hydrological systems are dynamic in nature. The commonly used lumped indices for hydrological model evaluation are coefficient of determination (R^2), Nash–Sutcliffe efficiency (NSE), bias, and mean squared error (MSE). However, the adoption of an aggregate metric does not eliminate the subjectivity of model evaluation completely as different metrics may give different pictures of a model's performance, focusing on performance in different parts of the hydrograph.

Thus, a modeler may face dilemma not only while choosing a model but also while choosing a metric for model evaluation. Several researchers have attempted to overcome the problem of model evaluation by employing multi-objective frameworks with which one can objectively compare modeled values with observed values considering multiple objectives at a time [32]. However, multi-objective frameworks cannot fully resolve the issue of model evaluation as the problem is because a model's performance cannot be fully quantified with the help of lumped performance metrics, no matter how many of them are being used. As an alternative route, one may combine performance in multiple lumped metrics with the model ability to explain certain hydrological processes, say by subjectively evaluating how well the model captures catchment-scale storage–discharge relationship [16]. Another way to ensure the applicability of a model for impact assessment is to test its performance for all indicators that will be used to assess the impact. For example, if an impact assessment exercise focuses on changes in flood frequency, it will be useful to test the model's ability to historically observed flood frequency, in addition to performing well in metrics such as NSE.

3.5 Final Remarks on the Model Selection Dilemma

Due to several options available for climate change impact assessment, one should make effort to select the most suitable modeling framework for a particular climate change impact assessment study. However, model selection is generally based on two main factors: data availability and expertise. As we discussed earlier in this section, different models use different datasets for calibration and prediction purposes. Therefore, a model may not be found suitable for a certain level of data availability. Nevertheless, for any given data availability situation, a modeler may come across several suitable modeling frameworks, and he/she may not have adequate expertise to set up and test all the models in order to identify the most suitable model for the impact assessment study. In general, a hydrological model is chosen for climate change impact assessment mainly because of the modeler's familiarity with

the model. This problem is confounded by the fact that there is no clear guideline in the hydrological literature on why and when a model should be chosen or discarded.

Nevertheless, many efforts have been made in the past to facilitate proper use of hydrological models. Many modelers provide model source code freely. For example, VIC model code is available at the University of Washington's website. Some modelers have gone so far as to freely provide model code along with sophisticated graphical user interfaces, e.g., SWAT model with ArcGIS-based user interface is available at the website of Texas A&M University. Many modelers have made efforts recently to develop frameworks to objectively compare different models [16, 22]. While these developments have advanced our understanding of hydrological systems remarkably and enabled multi-model comparison exercises, it is up to the modeler to objectively compare different models and decide when a model's use is appropriate. Model codes are not generally accessible for a majority of hydrological models, thus limiting the ability of a modeler to explore model structures that may be suitable for a particular climate change impact assessment study. Furthermore, as we learned in Sect. 3.4, a modeler needs to be careful while evaluating a model as different evaluation metrics may give different views of a model's performance in a catchment. To minimize the subjectivity involved in the model evaluation, a modeler should use state-of-the-art multi-objective model evaluation frameworks. Furthermore, adequate attention needs to be given to check if a model accurately depicts hydrological processes that transform rainfall into streamflow by carefully analyzing the model state variables and outputs.

4 Closing Remarks

The previous sections have outlined the vast array of choices that a decision maker faces when planning for water management under a changing climate. It is evident that a multitude of approaches exists, each with its own merit and shortcomings. Often, studies that utilize downscaled GCM outputs to drive hydrologic models have been found lacking in terms of their ability to support decision-making. This is mainly due to large uncertainties inherent in the projections of the hydrologic variables [67]. Recently, novel approaches have been suggested to overcome the challenge of large uncertainties in projections. These approaches are termed "bottom-up" or "decision-scaling" approaches as opposed to the "top-down" approach commonly employed in climate change impact assessment [18, 23, 59]. Bottom-up approaches begin by eliciting information from decision-makers regarding relevant hydrologic indicators and associated limits of performance (Fig. 2). Instead of providing an ensemble of streamflow time series by using a "top-down" approach, they employ a bottom-up modeling framework that assesses the limits of climate change within which the system maintains acceptable performance. Bottom-up approaches can answer questions such as: what degree of climate change will cause the current reservoir operation strategies to become suboptimal in the future? Such approaches, therefore, allow decision-makers to understand how to improve system's resilience to changing

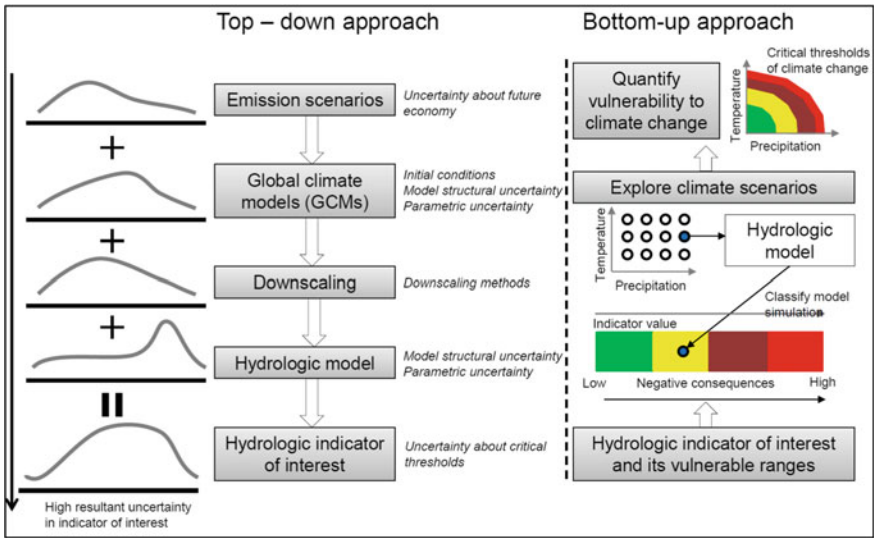


Fig. 2 Comparing “top-down” and “bottom-up” approaches when assessing the impact of climate change on water resources

climate. They are also advantageous as they can integrate readily available climate projections from GCMs into the analysis to shed light on the possibility of witnessing drastic system failures in the future.

Another suite of approaches that are gaining traction is those that focus on *story-lines* that detail the possible trajectories a system may take when undergoing climate change. Instead of relying on GCM outputs and various downscaling techniques, plausible trajectories of relevant hydro-climatic indicators such as precipitation are constructed by expert elicitation [25]. These trajectories are based on the physical understanding of mechanisms affecting precipitation by a group of experts. Their opinions can be collected via individual interviews or by group discussions. Expert elicitation may be advantageous over direct use of downscaled GCM outputs in cases where uncertainties regarding future climate are large but detailed information on the historical climate of the region exists. In a way, this approach is akin to constructing representative concentration pathways (RCPs) that detail how carbon dioxide emissions will change over the century. RCPs represent various trajectories in which the socioeconomic system may evolve and are based primarily on expert judgements as opposed to detailed modeling of the human system [81]. Trajectories based on story-lines are advantageous over probabilistic or large ensemble-based projections as they enable clarity of communication to the decision maker. Furthermore, probabilistic forecasts may convey a false sense of confidence in the estimated projections, particularly when only a limited number of GCMs or downscaling methods have been explored [24].

We conclude this chapter by mentioning a few areas of research that will benefit the study of climate change impact on water resources. First, changing climate may alter a catchment's land cover and subsequently soil properties. This alteration of catchment characteristics is generally neglected in hydrologic models used in climate change impact studies. Most of the studies calibrate the hydrologic model on past streamflow and climate, and expect the parameterization to work under very different future climates. This approach may introduce significant biases in future projections of runoff and methods are needed to address this issue [73]. Second, climate change is only one of the drivers of environmental change in catchments today. Human-induced land cover changes and other impacts such as excessive groundwater withdrawals or construction of reservoirs perhaps have an equivalent or greater effect on the hydrologic cycle. Understanding the impact of climate change on water resources in isolation of these other drivers of change may be a good academic exercise, but for all practical purposes, will likely lead to suboptimal adaptation strategies. Joint assessment of the impact of environmental change, including climatic and land use changes, are needed. Finally, it is now understood that the natural system is closely interlinked with the human system and understanding both systems within a unified framework will greatly advance our understanding of the consequences of various water management strategies [74]. Recent studies in socio-hydrology have begun to disentangle these complex interactions but further research is needed across a variety of study areas to build region-specific adaptation strategies.

References

1. Abbott MB, Bathurst JC, Cunge JA, O'Connell PE, Rasmussen J (1986) An introduction to the European hydrological system—Systeme Hydrologique Europeen, "SHE", 1: history and philosophy of a physically-based, distributed modelling system. *J Hydrol* 87(1–2):45–59
2. Andersson L, Samuelsson P, Kjellstro`ME (2011) Assessment of climate change impact on water resources in the Pungwe river basin. *Tellus A Dyn Meteorol Ocean* 63(1):138–157
3. Arnell NW (1999) Climate change and global water resources. *Glob Environ Chang* 9:S31–S49
4. Arnell NW (1999) A simple water balance model for the simulation of streamflow over a large geographic domain. *J Hydrol* 217(3–4):314–335
5. Arnell NW, Gosling SN (2016) The impacts of climate change on river flood risk at the global scale. *Clim Change* 134(3):387–401
6. Arnell NW, Hudson DA, Jones RG (2003) Climate change scenarios from a regional climate model: estimating change in runoff in Southern Africa. *J Geophys Res Atmos* 108(D16)
7. Arora VK (2002) The use of the aridity index to assess climate change effect on annual runoff. *J Hydrol* 265(1–4):164–177
8. Beck HE, van Dijk AI, de Roo A, Miralles DG, McVicar TR, Schellekens J, Bruijnzeel LA (2016) Global-scale regionalization of hydrologic model parameters. *Water Resour Res* 52(5):3599–3622
9. Benke KK, Lowell KE, Hamilton AJ (2008) Parameter uncertainty, sensitivity analysis and prediction error in a water-balance hydrological model. *Math Comput Model* 47(11–12):1134–1149
10. Berghuijs WR, Woods RA, Hrachowitz M (2014) A precipitation shift from snow towards rain leads to a decrease in streamflow. *Nat Clim Chang* 4(7):583

11. Beven K (2001) How far can we go in distributed hydrological modelling? *Hydrol Earth Syst Sci Discuss* 5(1):1–12
12. Beven K, Binley A (1992) The future of distributed models: model calibration and uncertainty prediction. *Hydrol Process* 6(3):279–298
13. Beven KJ (2011) *Rainfall-runoff modelling: the primer*. Wiley
14. Biggs EM, Bruce E, Boruff B, Duncan JM, Horsley J, Pauli N, McNeill K, Neef A, Van Ogtrop F, Curnow J, Haworth B (2015) Sustainable development and the water–energy–food nexus: a perspective on livelihoods. *Environ Sci Policy* 54:389–397
15. Biswal B (2016) Dynamic hydrologic modeling using the zero-parameter Budyko model with instantaneous dryness index. *Geophys Res Lett* 43(18):9696–9703
16. Biswal B, Singh R (2017) Incorporating channel network information in hydrologic response modelling: development of a model and inter-model comparison. *Adv Water Resour* 100:168–182
17. Botter G, Porporato A, Rodriguez-Iturbe I, Rinaldo A (2009) Nonlinear storage-discharge relations and catchment streamflow regimes. *Water Resour Res* 45(10)
18. Brown C, Ghile Y, Lavery M, Li K (2012) Decision scaling: linking bottom-up vulnerability analysis with climate projections in the water sector. *Water Resour Res* 48(9)
19. Camporese M, Paniconi C, Putti M, Orlandini S (2010) Surface-subsurface flow modeling with path-based runoff routing, boundary condition-based coupling, and assimilation of multisource observation data. *Water Resour Res* 46(2)
20. Chu H, Wei J, Li J, Li T (2018) Investigation of the relationship between runoff and atmospheric oscillations, sea surface temperature, and local-scale climate variables in the Yellow River headwaters region. *Hydrol Process* 32(10):1434–1448
21. Clark MP, Nijssen B, Lundquist JD, Kavetski D, Rupp DE, Woods RA, Freer JE, Gutmann ED, Wood AW, Brekke LD, Arnold JR (2015) A unified approach for process-based hydrologic modeling: 1. Modeling concept. *Water Resour Res* 51(4):2498–2514
22. Clark MP, Slater AG, Rupp DE, Woods RA, Vrugt JA, Gupta HV, Wagener T, Hay LE (2008) Framework for understanding structural errors (FUSE): a modular framework to diagnose differences between hydrological models. *Water Resour Res* 44(12)
23. Deshmukh A, Singh R (2016) Physio-climatic controls on vulnerability of watersheds to climate and land use change across the US. *Water Resour Res* 52(11):8775–8793
24. Dessai S, Hulme M (2004) Does climate adaptation policy need probabilities? *Clim Policy* 4(2):107–128
25. Dessai S, Bhawe A, Birch CE, Conway D, Garcia-Carreras L, Gosling JP, Mittal N, Stainforth DA (2018) Building narratives to characterise uncertainty in regional climate change through expert elicitation. *Environ Res Lett*
26. Devia GK, Ganasri BP, Dwarakish GS (2015) A review on hydrological models. *Aquat Procedia* 4:1001–1007
27. Diaz-Nieto J, Wilby RL (2005) A comparison of statistical downscaling and climate change factor methods: impacts on low flows in the River Thames, United Kingdom. *Clim Change* 69(2–3):245–268
28. Diskin MH (1970) Definition and uses of the linear regression model. *Water Resour Res* 6(6):1668–1673
29. Doulatyari B, Betterle A, Basso S, Biswal B, Schirmer M, Botter G (2015) Predicting streamflow distributions and flow duration curves from landscape and climate. *Adv Water Resour* 83:285–298
30. Durack PJ, Wijffels SE, Matear RJ (2012) Ocean salinities reveal strong global water cycle intensification during 1950 to 2000. *Science* 336(6080):455–458
31. Eckhardt K, Ulbrich U (2003) Potential impacts of climate change on groundwater recharge and streamflow in a central European low mountain range. *J Hydrol* 284(1–4):244–252
32. Efstratiadis A, Koutsoyiannis D (2010) One decade of multi-objective calibration approaches in hydrological modelling: a review. *Hydrol Sci J–J Des Sci Hydrol* 55(1):58–78
33. Evans S, Zanni A, Ford A, Dawson R, Barr S, Walsh C, Tight M, Köhler J, Harwatt H, Batty M, Hall J (2017) A blueprint for the integrated assessment of climate change in cities. In: *Green citynomics*. Routledge, pp 46–66

34. Fowler HJ, Blenkinsop S, Tebaldi C (2007) Linking climate change modelling to impacts studies: recent advances in downscaling techniques for hydrological modelling. *Int J Climatol* 27(12):1547–1578
35. Gleick PH (2014) Water, drought, climate change, and conflict in Syria. *Weather Clim Soc* 6(3):331–340
36. Gosain AK, Rao S, Arora A (2011) Climate change impact assessment of water resources of India. *Curr Sci*, 356–371
37. Gosain AK, Rao S, Basuray D (2006) Climate change impact assessment on hydrology of Indian river basins. *Curr Sci*, 346–353
38. Goswami BN, Venugopal V, Sengupta D, Madhusoodanan MS, Xavier PK (2006) Increasing trend of extreme rain events over India in a warming environment. *Science* 314(5804):1442–1445
39. Graham LP, Hagemann S, Jaun S, Beniston M (2007) On interpreting hydrological change from regional climate models. *Clim Change* 81(1):97–122
40. Haddeland I, Heinke J, Biemans H, Eisner S, Flörke M, Hanasaki N, Konzmann M, Ludwig F, Masaki Y, Schewe J, Stacke T (2014) Global water resources affected by human interventions and climate change. *Proc Natl Acad Sci* 111(9):3251–3256
41. Hengade N, Eldho TI (2016) Assessment of LULC and climate change on the hydrology of ashti catchment, India using VIC model. *J Earth Syst Sci* 125(8):1623–1634
42. Huntington TG (2006) Evidence for intensification of the global water cycle: review and synthesis. *J Hydrol* 319(1):83–95
43. Jakeman AJ, Hornberger GM (1993) How much complexity is warranted in a rainfall-runoff model? *Water Resour Res* 29(8):2637–2649
44. Kay AL, Davies HN, Bell VA, Jones RG (2009) Comparison of uncertainty sources for climate change impacts: flood frequency in England. *Clim Change* 92(1–2):41–63
45. Kelley CP, Mohtadi S, Cane MA, Seager R, Kushnir Y (2015) Climate change in the fertile crescent and implications of the recent Syrian drought. *Proc Natl Acad Sci*, 201421533
46. Klemeš V (1983) Conceptualization and scale in hydrology. *J Hydrol* 65(1–3):1–23
47. Liang X, Lettenmaier DP, Wood EF, Burges SJ (1994) A simple hydrologically based model of land surface water and energy fluxes for general circulation models. *J Geophys Res Atmos* 99(D7):14415–14428
48. Lohmann D, Raschke E, Nijssen B, Lettenmaier DP (1998) Regional scale hydrology: I. Formulation of the VIC-2L model coupled to a routing model. *Hydrol Sci J* 43(1):131–141
49. Manabe S, Smagorinsky J, Strickler RF (1965) Simulated climatology of a general circulation model with a hydrologic cycle. *Mon Weather Rev* 93(12):769–798
50. Mekonnen MM, Hoekstra AY (2016) Four billion people facing severe water scarcity. *Sci Adv* 2(2):e1500323
51. Moore RJ (2007) The PDM rainfall-runoff model. *Hydrol Earth Syst Sci Discuss* 11(1):483–499
52. Nayak PC, Sudheer KP, Rangan DM, Ramasastri KS (2004) A neuro-fuzzy computing technique for modeling hydrological time series. *J Hydrol* 291(1–2):52–66
53. Nĕmec J, Schaake J (1982) Sensitivity of water resource systems to climate variation. *Hydrol Sci J* 27(3):327–343
54. Oudin L, Andréassian V, Perrin C, Michel C, Le Moine N (2008) Spatial proximity, physical similarity, regression and ungauged catchments: a comparison of regionalization approaches based on 913 French catchments. *Water Resour Res* 44(3)
55. Pachauri RK, Allen MR, Barros VR, Broome J, Cramer W, Christ R, Church JA, Clarke L, Dahe Q, Dasgupta P, Dubash NK (2014) Climate change 2014: synthesis report. Contribution of working groups I, II and III to the fifth assessment report of the intergovernmental panel on climate change. IPCC, p 151
56. Panagoulia D, Dimou G (1996) Sensitivities of groundwater-streamflow interaction to global climate change. *Hydrol Sci J* 41(5):781–796
57. Parry M, Parry ML, Canziani O, Palutikof J, Van der Linden P, Hanson C (eds) (2007) Climate change 2007-impacts, adaptation and vulnerability: working group II contribution to the fourth assessment report of the IPCC (Vol. 4). Cambridge University Press

58. Patil S, Stieglitz M (2011) Hydrologic similarity among catchments under variable flow conditions. *Hydrol Earth Syst Sci* 15(3):989–997
59. Poff NL, Brown CM, Grantham TE, Matthews JH, Palmer MA, Spence CM, Wilby RL, Haasnoot M, Mendoza GF, Dominique KC, Baeza A (2016) Sustainable water management under future uncertainty with eco-engineering decision scaling. *Nat Clim Chang* 6(1):25
60. Raje D, Mujumdar PP (2010) Reservoir performance under uncertainty in hydrologic impacts of climate change. *Adv Water Resour* 33(3):312–326
61. Razavi T, Coulibaly P (2012) Streamflow prediction in ungauged basins: review of regionalization methods. *J Hydrol Eng* 18(8):958–975
62. Refsgaard JC (1997) Parameterisation, calibration and validation of distributed hydrological models. *J Hydrol* 198(1–4):69–97
63. Roxy MK, Ritika K, Terray P, Murtugudde R, Ashok K, Goswami BN (2015) Drying of Indian subcontinent by rapid Indian Ocean warming and a weakening land-sea thermal gradient. *Nat Commun* 6:7423
64. Roxy MK, Ghosh S, Pathak A, Athulya R, Mujumdar M, Murtugudde R, Terray P, Rajeevan M (2017) A threefold rise in widespread extreme rain events over central India. *Nat Commun* 8(1):708
65. Samaniego L, Thober S, Kumar R, Wanders N, Rakovec O, Pan M, Zink M, Sheffield J, Wood EF, Marx A (2018) Anthropogenic warming exacerbates European soil moisture droughts. *Nat Clim Chang* 8(5):421
66. Sankarasubramanian A, Vogel RM, Limbrunner JF (2001) Climate elasticity of streamflow in the United States. *Water Resour Res* 37(6):1771–1781
67. Schewe J, Heinke J, Gerten D, Haddeland I, Arnell NW, Clark DB, Dankers R, Eisner S, Fekete BM, Colón-González FJ, Gosling SN (2014) Multimodel assessment of water scarcity under climate change. *Proc Natl Acad Sci* 111(9):3245–3250
68. Schulze RE (1997) Impacts of global climate change in a hydrologically vulnerable region: challenges to South African hydrologists. *Prog Phys Geogr* 21(1):113–136
69. Semenov MA, Barrow EM (1997) Use of a stochastic weather generator in the development of climate change scenarios. *Clim Change* 35(4):397–414
70. Sharmila S, Joseph S, Sahai AK, Abhilash S, Chattopadhyay R (2015) Future projection of Indian summer monsoon variability under climate change scenario: an assessment from CMIP5 climate models. *Glob Planet Chang* 124:62–78
71. Singh VP (2018) Hydrologic modeling: progress and future directions. *Geosci Lett* 5(1):15
72. Singh R, Kumar R (2015) Vulnerability of water availability in India due to climate change: a bottom-up probabilistic budyko analysis. *Geophys Res Lett* 42(22):9799–9807
73. Singh R, Wagener T, Werkhoven KV, Mann ME, Crane R (2011) A trading-space-for-time approach to probabilistic continuous streamflow predictions in a changing climate—accounting for changing watershed behavior. *Hydrol Earth Syst Sci* 15(11):3591–3603
74. Sivapalan M, Savenije HH, Blöschl G (2012) Socio-hydrology: a new science of people and water. *Hydrol Process* 26(8):1270–1276
75. Sood A, Smakhtin V (2015) Global hydrological models: a review. *Hydrol Sci J* 60(4):549–565
76. Stryker J, Wemple B, Bomblies A (2017) Modeling sediment mobilization using a distributed hydrological model coupled with a bank stability model. *Water Resour Res* 53(3):2051–2073
77. Tai X, Mackay DS, Sperry JS, Brooks P, Anderegg WR, Flanagan LB, Rood SB, Hopkinson C (2018) Distributed plant hydraulic and hydrological modeling to understand the susceptibility of riparian woodland trees to drought-induced mortality. *Water Resour Res*
78. Thirel G, Andréassian V, Perrin C (2015) On the need to test hydrological models under changing conditions. *Hydrol Sci J*
79. Velázquez JA, Schmid J, Ricard S, Muerth MJ, Gauvin St-Denis B, Minville M, Chaumont D, Caya D, Ludwig R, Turcotte R (2013) An ensemble approach to assess hydrological models' contribution to uncertainties in the analysis of climate change impact on water resources. *Hydrol Earth Syst Sci* 17(2):565–578
80. Vogel RM, Wilson I, Daly C (1999) Regional regression models of annual streamflow for the United States. *J Irrig Drain Eng* 125(3):148–157

81. Van Vuuren DP, Edmonds J, Kainuma M, Riahi K, Thomson A, Hibbard K, Hurtt GC, Kram T, Krey V, Lamarque JF, Masui T (2011) The representative concentration pathways: an overview. *Clim Change* 109(1–2):5
82. Vörösmarty CJ, Green P, Salisbury J, Lammers RB (2000) Global water resources: vulnerability from climate change and population growth. *Science* 289(5477):284–288
83. Vörösmarty CJ, Moore B, Grace AL, Gildea MP, Melillo JM, Peterson BJ, Rastetter EB, Steudler PA (1989) Continental scale models of water balance and fluvial transport: an application to South America. *Glob Biogeochem Cycles* 3(3):241–265
84. Weinthal E, Zawahri N, Sowers J (2015) Securitizing water, climate, and migration in Israel, Jordan, and Syria. *Int Environ Agreem Polit Law Econ* 15(3):293–307
85. Westra S, Thyer M, Leonard M, Kavetski D, Lambert M (2014) A strategy for diagnosing and interpreting hydrological model nonstationarity. *Water Resour Res* 50(6):5090–5113
86. Whitehead PG, Barbour E, Futter MN, Sarkar S, Rodda H, Caesar J, Butterfield D, Jin L, Sinha R, Nicholls R, Salehin M. 2015. Impacts of climate change and socio-economic scenarios on flow and water quality of the Ganges, Brahmaputra and Meghna (GBM) river systems: low flow and flood statistics. *Environ Sci Process Impacts* 17(6):1057–1069
87. Wilby RL, Whitehead PG, Wade AJ, Butterfield D, Davis RJ, Watts G (2006) Integrated modelling of climate change impacts on water resources and quality in a lowland catchment: River Kennet, UK. *J Hydrol* 330(1–2):204–220
88. Wilby RL, Harris I (2006) A framework for assessing uncertainties in climate change impacts: low-flow scenarios for the River Thames, UK. *Water Resour Res* 42(2)
89. Wood EF, Lettenmaier DP, Zartarian VG (1992) A land-surface hydrology parameterization with subgrid variability for general circulation models. *J Geophys Res Atmos* 97(D3):2717–2728
90. Wu CL, Chau KW, Li YS (2009) Predicting monthly streamflow using data-driven models coupled with data-preprocessing techniques. *Water Resour Res* 45(8)
91. Xu CY, Widén E, Halldin S (2005) Modelling hydrological consequences of climate change—progress and challenges. *Adv Atmos Sci* 22(6):789–797

Streamflow Connectivity in a Large-Scale River Basin



Koren Fang, Bellie Sivakumar, Fitsum M. Woldemeskel
and Vinayakam Jothiprakash

1 Introduction

Large-scale river basins play a vital role in the survival, sustainability, and socio-economic development of many regions around the world. On one hand, the sheer enormity of such basins is certainly a positive, as it helps support various demands and activities associated with our water, environmental, and ecologic systems. On the other hand, it is the same enormity of such basins that also makes their planning and management a tremendous challenge. For instance, in large-scale river basins, undertaking short-term emergency measures (especially to deal with floods) as well as devising long-term management strategies (especially to deal with droughts) almost always poses enormous challenges. Adequate understanding of the functions of large-scale river basins is, therefore, essential for their proper planning and management. Streamflow is, arguably, the central component in this regard.

Streamflow arises as a result of complex and nonlinear interactions between climate inputs (external factors) and landscape characteristics (internal factors) at a wide range of spatial and temporal scales. As a result, streamflow dynamic behavior changes as a function of both space and time. One of the keys to understand the dynamics of streamflow in a river basin is to understand the “connections” that generally exist between the various points (or parts) of the basin. Such connections can, at times, be somewhat simplified in small and medium-scale basins, due to, in

K. Fang · B. Sivakumar (✉) · F. M. Woldemeskel
UNSW Water Research Centre, School of Civil and Environmental Engineering,
The University of New South Wales, Sydney, Sydney, NSW 2052, Australia
e-mail: s.bellie@unsw.edu.au

B. Sivakumar · V. Jothiprakash
Department of Civil Engineering, Indian Institute of Technology Bombay, Powai, Mumbai
400076, Maharashtra, India

B. Sivakumar
State Key Laboratory of Hydrosience and Engineering, Tsinghua University,
Beijing 100084, China

© Springer Nature Switzerland AG 2019
S. K. Singh and C. T. Dhanya (eds.), *Hydrology in a Changing World*, Springer Water,
https://doi.org/10.1007/978-3-030-02197-9_10

general, the limited variability in climatic conditions across the basin, limited heterogeneity in the catchment medium, and short concentration time. In large-scale river basins, however, the connections are enormously complex, due to, in general, the significant variability in climatic conditions across the basin, significant heterogeneity in the catchment medium, and long concentration time. It is these enormously complex connections in large-scale river basins and our inability to accurately identify/represent them make streamflow modeling in such basins extremely challenging.

There exist a number of concepts and methods for studying the connections associated with streamflow, including those based on time, distance, correlation, variability, scale, patterns, and many others. Such concepts and methods have been extensively applied to study the dynamics of streamflow processes around the world [5, 19, 23, 26, 30, 33, 34, 41, 43]. A compilation of the applications of several major data-based approaches for studying patterns and connections in hydrologic systems can be found in Sivakumar and Berndtsson [36]. In the past two decades, in particular, some key developments made in the field of complex systems science have enhanced the study of connections in numerous natural and socioeconomic systems. Among such developments, the concepts of *complex networks* seem very appealing [2, 10, 14, 45], for their ability to represent various types of connections encountered in large, complex, and dynamically evolving systems, such as large-scale river systems. Studies on the applications of complex networks concepts have been gaining considerable attention in many different fields, including in hydrology [3, 9, 21, 24, 25, 27, 38, 42, 48]. Comprehensive accounts of complex networks concepts and their applications are available in Estrada [10]; see also Sivakumar et al. [39] for details of their applications in hydrology in particular.

Applications of the concepts of complex networks for studying connections in river systems have recently started to emerge [4, 7, 8, 15, 16, 29, 28, 32, 37, 40, 46, 47], and their potential to help formulate a generic theory for hydrology has also been discussed [35]. However, such studies have essentially been limited to small rivers/regions and/or small number of monitoring stations (at most, a few hundreds). As a result, they do not offer strong evidence on the appropriateness and effectiveness of the concepts for large-scale river systems, since such systems generally cover a broad range of hydroclimatic, topographic, geomorphologic, soil, land use, and many other characteristics and present enormous complexities in connections. To adequately test the concepts of complex networks for river systems in general, especially toward developing a generic framework for modeling/management, it is imperative to consider very large river basins that provide very stringent system conditions (i.e., test bed) and analyze data from a large number of monitoring stations (say, at least one thousand).

To our knowledge, the study by Fang et al. [13] has been the only study that has, thus far, applied the concepts of complex networks to a large-scale river basin. Fang et al. [13] focused on catchment classification in the Mississippi River basin. The Mississippi River is one of the world's major river systems in size, habitat diversity, and biological productivity. Of the world's rivers, the Mississippi River ranks fourth in length, fourth in watershed area, and fifth in average discharge. With a river length stretching over 3,770 km, basin area covering 4.76 million km², and

possessing a wide range of hydroclimatic, topographic, geomorphologic, soil, land use, and other properties, the Mississippi River basin meets many of the stringent conditions for studying connections in river systems. In their study on catchment classification, Fang et al. [13] employed six community structure methods to classify 1663 catchments (streamflow stations) across the Mississippi River basin. These 1663 gaging stations were considered to cover as much data as possible from across the basin. The results revealed that only a few communities combine to represent a majority of the catchments, with the 10 largest communities (roughly 4% of the total number of communities) representing almost two-thirds of the catchments. Fang et al. [13] also reported that community formation was influenced not only by geographic proximity but also by the organization of the river network.

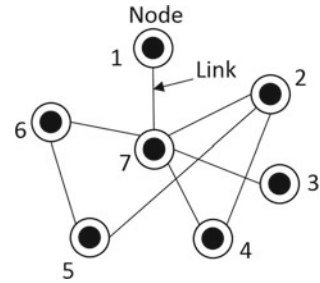
Following on the study by Fang et al. [13], the present study employs the concepts of complex networks to study the spatial connections in streamflow in the Mississippi River basin. The same 1663 stations considered by Fang et al. [13] are also analyzed in the present study. The connections in streamflow data between these stations are examined by employing three basic and important network-based methods: clustering coefficient, degree distribution, and shortest path length. The sensitivity of these methods to streamflow correlation threshold is also investigated.

The rest of this chapter is organized as follows. Section 2 describes the concept of network and the three methods used in this study. Section 3 presents the details of the Mississippi River basin and streamflow data considered in this study. Section 4 presents the results and discussion. Section 5 draws some conclusions from this study.

2 Network Methods

A network (or a graph) is a set of points called nodes (or vertices) joined together by a set of connections called links (or edges), as shown in Fig. 1. Mathematically, a network can be represented as $G = \{P, E\}$, where P is a set of N nodes (P_1, P_2, \dots, P_N) and E is a set of n links. In a network, the existence/nonexistence of links is identified based on a measure that represents the strength of the link, such as correlation. For instance, node pairs that have strengths exceeding a certain threshold value T may be assigned links.

There are various measures to study the properties of networks, including centrality, clustering, adjacency, distance, community structure, bipartivity, fragments (or subgraphs), communicability, and global invariants, among others; see, for example, Estrada [10] for details. Such measures not only identify/quantify different properties of networks, but also often offer cross-verification, and possible confirmation, of results. For some measures, there are also different definitions, sub-measures, and

Fig. 1 Concept of a network

corresponding methods. In what follows, a brief description of clustering coefficient, degree distribution, and average shortest path length is provided, as these measures are used in this study for analysis of streamflow data.

2.1 Clustering Coefficient

One of the most fundamental properties of networks is their tendency to cluster. The concept of clustering has its origin in sociology [44]. In the context of complex networks, however, it was first used by Watts and Strogatz [45]. The tendency of a network to cluster is quantified by the clustering coefficient. Let us consider first a selected node i in the network, having k_i links which connect it to k_i other nodes. If the neighbors of the original node i were part of a cluster, there would be $k_i(k_i - 1)/2$ links between them. The clustering coefficient of node i is then given by the ratio between the number E_i of links that actually exist between these k_i nodes and the total number $k_i(k_i - 1)/2$, i.e.,

$$C_i = \frac{2E_i}{k_i(k_i - 1)} \quad (1)$$

The procedure is repeated for each and every node of the network. The average of the clustering coefficients C_i of all the individual nodes is the clustering coefficient of the whole network C . An example of the clustering coefficient calculation is presented in Sivakumar and Woldemeskel [37].

The clustering coefficient of the individual nodes and of the entire network can be used to obtain important information about the type of network, grouping (or classification) of nodes, and identification of dominant nodes (e.g., super nodes), among others. For instance, a high clustering coefficient (close to 1.0) indicates a regular network, while a very low clustering coefficient (close to zero), with $C = p$, indicates a random network. For a small-world network or a scale-free network, the clustering coefficient is generally smaller than that of the regular network but also considerably larger than that of a comparable random network (i.e., having the same number of nodes and links). It should be noted that both small-world networks and scale-

free networks are certain forms of random networks, but are different from classical random networks. For instance, small-world networks are both stable (unlike classical random networks) and efficient (like classical random networks); scale-free networks exhibit power-law behavior in degree distribution (unlike classical random networks that exhibit Poisson degree distribution—see below).

2.2 Degree Distribution

In a network, different nodes may have different number of links. The number of links (k) of a node is called as *node degree*. The degree is an important characteristic of a node, as it allows derivation of many measurements for the network. The spread in the node degrees is characterized by a distribution function $p(k)$, which expresses the fraction of nodes in a network with degree k . This distribution is called *degree distribution*. The degree distribution is often a reliable indicator of the type of network. In a random graph, since the links are placed randomly, the majority of nodes have approximately the same degree, and close to the average degree \bar{k} of the network. Therefore, the degree distribution of a completely random graph is a Poisson distribution with a peak at $P(k)$, and is given by:

$$p(k) = \frac{e^{-\bar{k}} \bar{k}^k}{k!} \quad (2)$$

Similarly, depending upon the properties of networks, degree distribution can be Gaussian:

$$p(k) = \frac{1}{\sqrt{2\pi}\sigma_k} e^{-\left(\frac{(k-\bar{k})^2}{2\sigma_k^2}\right)} \quad (3)$$

exponential:

$$p(k) \sim e^{-k/\bar{k}} \quad (4)$$

power-law or scale-free:

$$p(k) \sim k^{-\gamma} \quad (5)$$

or other.

2.3 Shortest Path Length

The shortest path length is considered as one of the most robust measures of network topology, along with clustering coefficient and degree distribution. In a network, the shortest path length of a node pair i and j is the number of links on the shortest path connecting the node pair. If the node pair is unconnected, then the value of the shortest path length is set to infinity. The average shortest path length (L) of a network with N nodes is the average over all nodes of the shortest path between every combination of node pairs, and is given by:

$$L = \frac{1}{N(N-1)} \sum d_{ij} \quad (6)$$

where d_{ij} is the distance between pair i and j .

This definition for average shortest path length, however, diverges if there are unconnected nodes in the network, since the distance between such nodes is set to infinity [6]. Consideration of only the connected node pairs avoids this divergence problem, but such also introduces a distortion for networks with many unconnected pairs of nodes. The consequence of this is a small value of the average path length, which is expected only for networks with a high number of connections.

A closely-related measurement is the global efficiency (E), proposed by Latora and Marchiori [22]:

$$E = \frac{1}{N(N-1)} \sum \frac{1}{d_{ij}} \quad (7)$$

where the sum takes all pairs of nodes into account. The global efficiency quantifies the efficiency of the network in sending information between nodes, with the assumption that the efficiency for sending information between two nodes i and j is proportional to the reciprocal of their distance. The reciprocal of the global efficiency is the harmonic mean of the geodesic distances (see Eq. 6), given by:

$$h = \frac{1}{E} \quad (8)$$

The fact that the harmonic mean eliminates the divergence problem otherwise encountered in the average shortest path length makes it a more appropriate measurement for networks with more than one connected component.

The average shortest path length offers important information about the type of network. For instance, regular networks, with their high clustering (i.e., stable), have long average path lengths (i.e. inefficient). Random networks, while unstable (i.e., low clustering), have short average path lengths (i.e., efficient). Small-world networks have short path lengths and are both stable and efficient (the latter due to high clustering).

3 Study Area and Data

In the present study, the Mississippi River basin is considered as a representative basin to investigate the utility and effectiveness of the concepts of complex networks for studying spatial connections in large-scale river basins. The Mississippi River is one of the world's major river systems in size, habitat diversity, and biological productivity. Of the world's rivers, the Mississippi River ranks fourth in length, fourth in watershed area, and fifth in average discharge. It is the longest river and has the largest drainage area in North America, originating at Lake Itasca in northern Minnesota in the United States and flowing for about 3,770 km through the midcontinental United States, the Gulf of Mexico Coastal Plain, and its subtropical Louisiana Delta (see Fig. 2). The entire river basin measures about 4.76 million km², of which about 3.22 million km² is in the continental United States. The main stem, together with its tributaries, extends over 31 states in the continental United States and two Canadian Provinces; see Alexander et al. [1] for further details. The United States is separated into 21 hydrologic unit regions based on the drainage areas of major rivers or the combined drainage areas of a series of rivers [31]. Of the 18 hydrologic regions which make up the conterminous United States (see Kiang et al. [20]), six of them are in the Mississippi River basin: the Missouri River region, the Upper Mississippi River region, the Ohio River region, the Tennessee River region, the Arkansas-White-Red River region, and the Lower Mississippi River region.

For the present study, daily streamflow data from a network of as many as 1663 gaging stations within the Mississippi River Basin are analyzed. Figure 3 shows the locations of these 1663 stations, with the different colors indicating the hydrologic region the stations belong to. Only the stations within the United States are considered. The data are obtained from the US Geological Survey National Water Information System website; see <http://nwis.waterdata.usgs.gov/nwis> for details. The stations are chosen in such a way that they have continuous streamflow records for at least a 5-year common period. The data considered here span from October 2008 to September 2013, and are daily values. A large number of these stations are likely to have streamflow influences due to human activities; indeed, only 257 of these stations are classified as "reference quality stations" [11, 12]. However, none of these stations are excluded from the present analysis, and all 1663 stations are considered.

The 1663 streamflow stations and their observed streamflow data show enormous variations in their characteristics, with several orders of magnitudes of differences in their properties. For example: (1) basin drainage area ranges from 0.70 to 2,964,240 km²; (2) station elevation ranges from -0.24 to 3,167 m; (3) mean flow ranges from 0.0374 to 20,100 m³s⁻¹; and (4) maximum flow ranges from 0.21 to 65,400 m³s⁻¹. Therefore, the 1663 stations collectively possess a great level of complexity in catchment characteristics and streamflow properties, thus making the Mississippi River basin one of the best test cases for studying connections in a river system.



Fig. 2 The Mississippi River basin (adapted from [1])

4 Results and Discussion

The clustering coefficient, degree distribution, and average shortest path length methods are employed to study the connections in streamflow in the Mississippi River basin. The streamflow network consists of 1663 nodes, corresponding to the 1663 streamflow monitoring stations considered. Each node consists of a time series of daily streamflow values observed over the period October 2008–September 2013. With this, the links in the network are identified by looking at the correlations between the different nodes. More specifically, the Pearson correlation coefficient is used to calculate the correlations in streamflow between the different nodes and, hence, to identify the neighbors (i.e., links) for each and every node. The correlation threshold (T) can significantly influence the identification of the neighbors and, hence, the outcomes of the above methods. For instance, use of a very low correlation threshold (say, $T = 0.10$) normally yields too many links in the network (since the cross-correlation in streamflow between any two stations is normally greater than 0.10), while use of a very high correlation threshold (say, $T = 0.95$) normally yields only a few links in the network. It is, therefore, important to use at least a few different

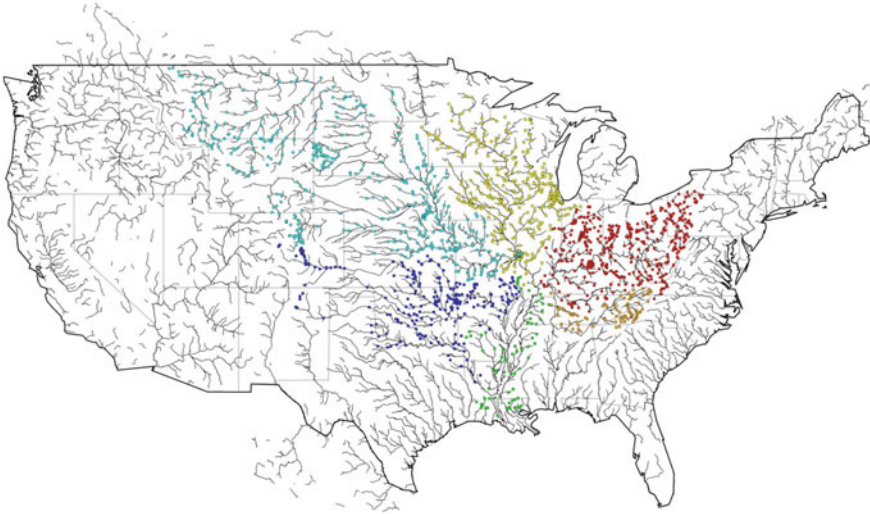


Fig. 3 Locations of 1663 streamflow stations in the Mississippi River basin considered in this study. The stations are colored according to their hydrologic region as follows: the Missouri River region (teal), the Upper Mississippi River region (yellow), the Ohio River region (red), the Tennessee River region (orange), the Arkansas-White-Red region (blue), and the Lower Mississippi River region (green)

threshold levels (but also preferably not too low or too high values) for more reliable interpretations and conclusions. To this end, four different threshold levels are considered: 0.70, 0.75, 0.80, and 0.85. The range of threshold herein (0.70–0.85) is chosen to better reflect the extent of correlations in streamflow, and is also partially based on our previous experiences on the analysis of hydrologic data using network-based methods; see Sivakumar and Woldemeskel [37, 38], Jha et al. [18], Fang et al. [13], Jha and Sivakumar [17], and Han et al. [16] for some additional details. For a given threshold, any node pair with a correlation coefficient above that threshold value is assigned a link. This means that there is generally an inverse relationship between the threshold value and the number of links; i.e., large number of links when the threshold is low and small number of links when the threshold is high.

4.1 Clustering Coefficient

Figure 4 shows the clustering coefficient (CC) values for the 1663 stations in the Mississippi River basin, for the above four different thresholds. For better illustration, the clustering coefficient values are presented in six different ranges: 0.76–1.00, 0.51–0.75, 0.26–0.50, 0.01–0.25, 0.00, and NA. Table 1 presents the number/percentage of stations that falls within these ranges. In Fig. 4 and Table 1,

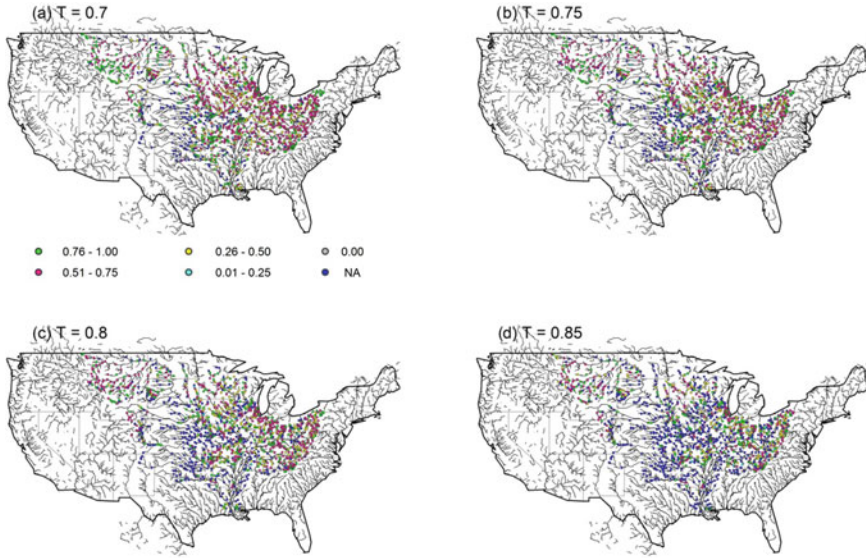


Fig. 4 Clustering coefficient values for the network of 1663 streamflow stations in the Mississippi River basin for four different correlation thresholds (T): **a** $T = 0.70$; **b** $T = 0.75$; **c** $T = 0.80$; and **d** $T = 0.85$

a clustering coefficient of 0.0 indicates a situation when there are more than one neighbor in the initial search (i.e., one or more links exist to calculate CC) but the neighbors are not connected among themselves, while a clustering coefficient of NA indicates a situation when there are no neighbors or only one neighbor in the initial search (i.e., there is no link to calculate CC).

The results presented in Fig. 4 and Table 1 indicate significant differences in clustering characteristics in the network with respect to the threshold values. In terms of the number of nodes falling under the six different CC ranges, the results follow either an increasing or a decreasing trend, depending upon the threshold. The number of nodes decreases with an increase in the threshold when $CC > 0.25$ (i.e., 0.76–1.00, 0.51–0.75, 0.26–0.50) and increases when $CC \leq 0.25$ (0.0–0.25, 0.0, NA), although the increase in nodes when CC is 0.0–0.25 is miniscule (see Table 1). It is also important to note that the number of nodes with a clustering coefficient value NA (i.e., nodes for which clustering coefficient cannot be calculated) remarkably increases from just 10% (170 nodes) when $T = 0.70$ to as high as 38% (630 nodes) when $T = 0.85$. The latter indicates that when T is high, calculation of the clustering coefficient is simply not possible for almost two-fifths of the number of stations, as there are either no neighbors or only one neighbor for such nodes. This clearly indicates the sensitivity of the clustering coefficient results to the correlation threshold and, hence, the need for caution in the analysis. The results also indicate that the connections are more sparse at higher threshold levels (i.e., nodes are less connected to each other); see also the degree distribution results in Sect. 4.3.

Table 1 Number and percentage of stations that fall under six different ranges of clustering coefficient values for the streamflow network for four different threshold levels (T)

T	Number and percentage of stations within each local clustering coefficient range						NA	Global clustering coefficient
	0.75–1.00	0.51–0.75	0.26–0.50	0.01–0.25	0			
0.7	446 27%	737 44%	276 17%	12 1%	22 1%	170 10%	0.588	
0.75	416 25%	658 40%	270 16%	14 1%	40 2%	265 16%	0.539	
0.8	386 23%	552 33%	253 15%	17 1%	47 3%	408 25%	0.484	
0.85	324 19%	370 22%	239 14%	19 1%	81 5%	630 38%	0.384	

The clustering coefficient results, including the nodes and their number with a clustering coefficient value of NA with respect to threshold, also offer some specific information as to where the spatial connections are stronger and where they are weaker. Regardless of the threshold, the clustering coefficient values are generally higher in the Missouri River, the Upper Mississippi River, the Ohio River, and the Tennessee River hydrologic regions when compared to those in the Arkansas-White-Red River and the Lower Mississippi River hydrologic regions. For example, at least for $T = 0.70$ and $T = 0.75$, the clustering coefficient values are greater than 0.5 for a significant proportion of stations in the former four regions (with some exceptions in the Upper Mississippi River region), and in some cases they are even greater than 0.75, while the latter two regions generally have clustering coefficient values less than 0.5. This may be construed to suggest that the connections of the stations in the former four regions with the rest of the network are generally stronger than the connections of the stations in the latter two regions with the rest of the network. Nevertheless, these interpretations need further verification and confirmation, as the clustering coefficient essentially measures the strength of connections between the first neighbors of a node (i.e., local density), which may or may not occur over the entire network.

The results also indicate that stations with higher clustering coefficient values exist in almost all of the regions (perhaps with the exception of the Arkansas-White-Red River region), for any of the four threshold levels considered. Similarly, stations with lower clustering coefficient values also exist in almost all of the regions, especially for higher threshold levels. These observations indicate that the strength of connection of a given station in the network does not necessarily depend on geographic proximity or the hydrologic region it belongs to, and that other factors are at play, including the role of river network formation. The results obtained from the classification of these 1663 stations, using community structure methods, also provide support to this interpretation; see Fang et al. [13] for details on classification.

The clustering coefficient values of the entire network, calculated as the average of the clustering coefficients for all the 1663 nodes, for the four different thresholds (i.e., $T = 0.70$, $T = 0.75$, $T = 0.80$, and $T = 0.85$) are 0.588, 0.539, 0.484, and 0.384, respectively. As expected, the clustering coefficient value decreases with an increase in the threshold value. These generally high clustering coefficient values, especially that for $T = 0.70$ (and also for $T = 0.75$), seem to suggest that the network is not a purely random graph, as the clustering coefficient values for random networks are typically very low (close to zero), essentially due to random distribution of links [45]. Indeed, for instance, when $T = 0.70$, the clustering coefficient value of an equivalent random network (i.e., a network with an equal number of nodes and links to that of the streamflow network) is found to be as low as 0.013. The streamflow network is also not a regular network, since the clustering coefficient for such fully connected networks is expected to be very close to 1.0. All these seem to suggest that the streamflow network in the Mississippi River basin may be a small-world network [45] or a scale-free network [2] or some other.

The reasonably high clustering coefficients for the streamflow network indicate that the network has high stability, but also low efficiency. The high network stability

implies that stations may be removed (randomly or otherwise) from the network without resulting in a significant loss of information. Which stations can be removed is an interesting question to ask. On one hand, it could be argued that stations with higher clustering coefficient values could be removed, since there are sufficient connections within its “neighboring” nodes to make up for the loss of information incurred by its removal, and that stations with low clustering coefficients should be kept, since there are not enough connections to recover the lost information. On the other hand, there could also be an argument against the removal of stations with very high clustering coefficients, since such stations are essentially the “dominant” ones (i.e., “supernodes”) in the network. We will address this issue in a future study, through investigating the effect of the removal of stations (randomly or according to some deterministic rules) on clustering coefficient results; see Jha and Sivakumar [17] for a preliminary study on this issue with a rainfall monitoring network.

4.2 Degree Distribution

Figure 5 presents the degree distribution results for the streamflow network of 1663 stations in the Mississippi River basin. The values are the complementary cumulative degree distribution values, defined as the fraction of nodes with degree at least k and denoted as $p(K \geq k)$. The plots show the results in the normal scale (Fig. 5a), semi-log scale (Fig. 5b), and log–log scale (Fig. 5c). The degree distribution exhibits a similar shape for all the above four thresholds (i.e., $T = 0.70, 0.75, 0.80, 0.85$). As expected, the use of a stricter threshold results in a lower maximum degree for the network. For example, the largest degree (i.e., the degree at which the degree distribution attains saturation) at $T = 0.70$ is around 100, while at $T = 0.85$, the highest degree is only half of that, to around 50.

The degree distribution results seem to resemble an exponential distribution over some sections and a power-law distribution over others (an exponential distribution should be roughly linear in a semi-log plot, while a power-law distribution appears roughly linear in a log–log plot). Further, the exponential distribution seems to be more fitting for low threshold levels, and the power-law distribution seems to appear more at high thresholds. Therefore, the degree distribution may be classified as a combination of exponential and power-law distributions, with a possible resemblance to an exponentially truncated power-law distribution [10]. This is another indication that the network is not a purely random graph or normal random graph, since the degree distribution for such a network is Poisson or Gaussian.

The present results also indicate that, at best, the most-connected station in this network is connected with only 6% (100 nodes) of the network size (1663 nodes) at $T = 0.7$. As the threshold increases to 0.85, this percentage reduces to around half, to around 3%. This highlights that the low connectivity of the nodes within the network; see Sect. 4.3 for further details.

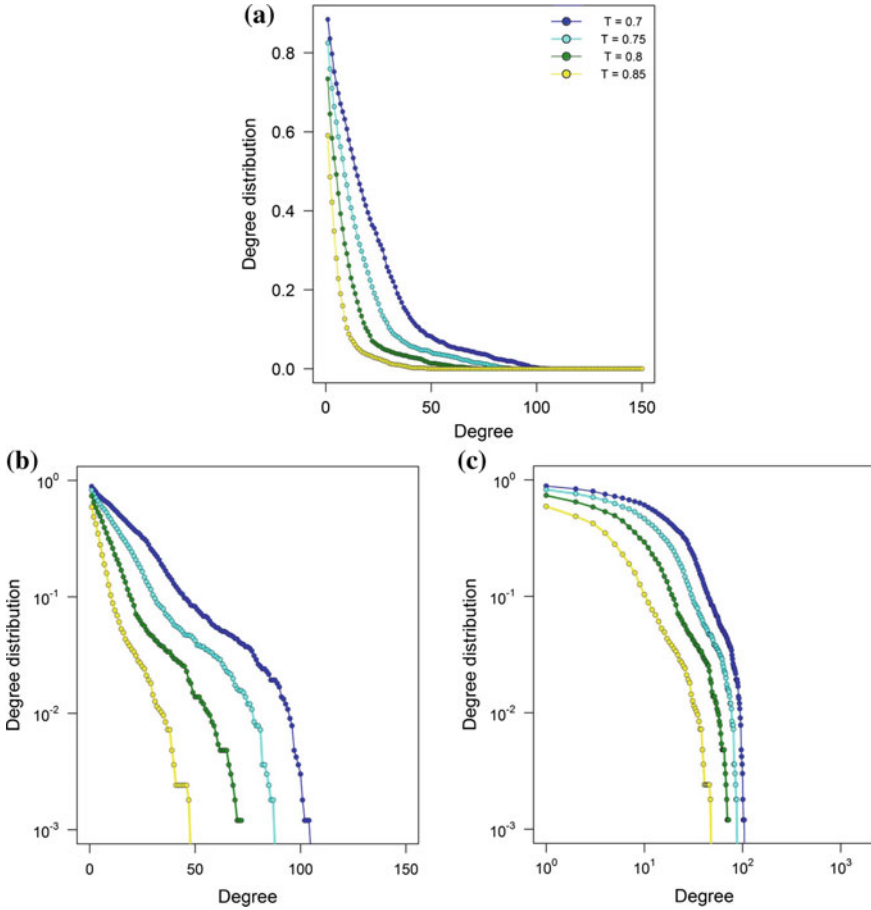


Fig. 5 Degree distribution for the network of 1663 streamflow stations in the Mississippi River basin for four different thresholds (T) (0.70, 0.75, 0.80, and 0.85): **a** normal scale; **b** semi-log scale; and **c** log-log scale

4.3 Shortest Path Length

The results from the application of the shortest path length method to the streamflow data from the 1663 stations in the Mississippi River basin are presented in Fig. 6, for all the four thresholds (T). Based on the shortest path lengths for the 1663 stations, the average shortest path length is also calculated. The average shortest path lengths are found to be 7.48, 8.36, 10.42, and 6.97, for $T = 0.70$, $T = 0.75$, $T = 0.80$, and $T = 0.85$, respectively. The efficiency of the network for the four thresholds are 0.13, 0.08, 0.04, and 0.01, and the number of unconnected node pairs are 30%, 47%, 78%, and 96%, respectively. The average shortest path length, efficiency, and unconnected node pairs are found to be very different from the ones obtained for an equivalent

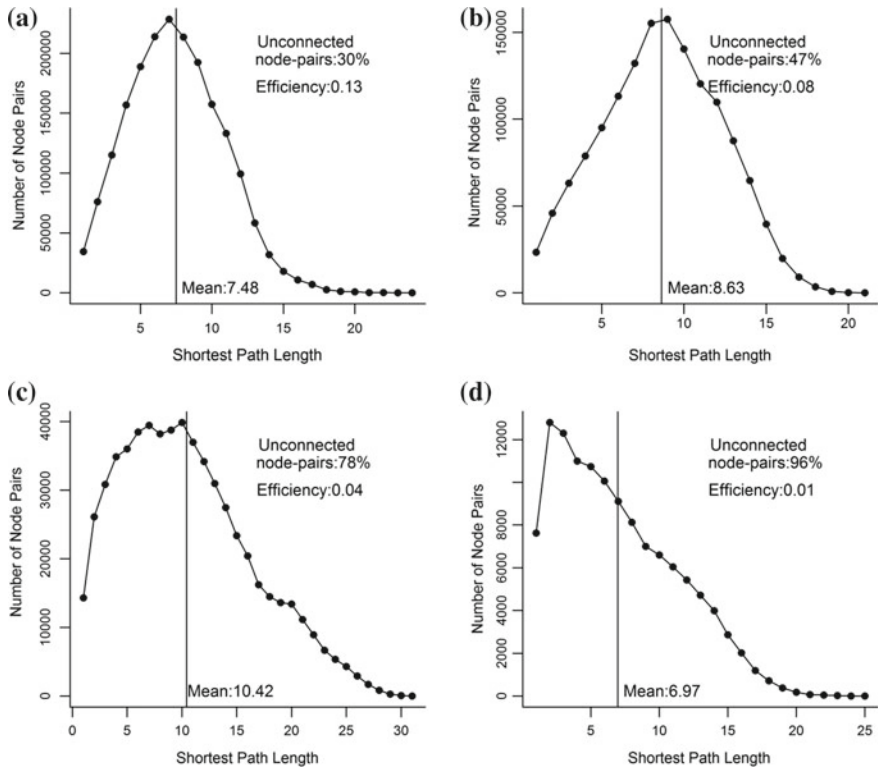


Fig. 6 Measures of average shortest path length, efficiency, and unconnected node pairs for the network of 1663 streamflow stations in the Mississippi River basin for four different thresholds: **a** $T = 0.70$; **b** $T = 0.75$; **c** $T = 0.80$; and **d** $T = 0.85$

random network. For instance, for $T = 0.70$, the average shortest path length for a random network is 2.75, efficiency is 0.375, and unconnected node pairs is less than 1%. These results suggest that the streamflow network is not a random graph, and support the results from the clustering coefficient method and the degree distribution method regarding the type of network.

The increase in the amount of unconnected node pairs with an increase in the threshold is clear and reflective of the role of threshold. This also supports the clustering coefficient results, where a significant increase in the number of stations with a clustering coefficient value of NA is observed when the threshold is increased. However, the results also offer another interesting observation. When T is increased from 0.80 to 0.85, despite an increase in the number of unconnected node pairs (from 78 to 96%), the average shortest path length decreases (from 10.42 to 6.97). This seems to suggest that when $T = 0.85$, there are more connections among the identified neighbors even when the neighbors may be fewer, when compared to when $T = 0.80$. This is understandable, since there may be situations when a small number

of stations have very strong connections among themselves. Nevertheless, when T increases from 0.80 to 0.85, the efficiency drops from 0.04 to 0.01, showing a more unconnected network as a whole. All these results indicate that the streamflow network is inefficient with particularly low levels of connectedness at higher thresholds. Thus, the propagation of information throughout the network does not occur easily.

5 Conclusions

Modeling and prediction of streamflow dynamics in large-scale river basins is a huge challenge, due to their enormous size, different hydroclimatic conditions, and significant heterogeneity in the catchment medium, among other factors. The present study has employed the concepts of complex networks to examine the spatial connections in streamflow in the Mississippi River basin, one of the largest river basins in the world. Application of the clustering coefficient, degree distribution, and shortest path length methods to daily streamflow data from a network of 1663 monitoring stations across the basin has offered some useful and interesting information regarding the properties of this network.

The results clearly indicate that streamflow stations in the Missouri River, Upper Mississippi River, Ohio River, and Tennessee River regions (i.e., northwestern, northern, and eastern parts) have much stronger connections with the rest of the network when compared to connections of the stations in the Arkansas-Red-White River and Lower Mississippi River regions (i.e., southwestern and southern parts) with the rest of the network. The results do not offer any evidence to suggest that the streamflow network is a purely random network (or a regular network), i.e., the connections in streamflow among the stations are not randomly distributed (or fully connected). The results, instead, seem to suggest that the distribution of connections in streamflow shows scale-free behavior in some parts of the network and exponential behavior in others. Further, scale-free distribution in the network is more evident when more stringent conditions in connections are imposed (i.e., very strong connections between the stations), while exponential distribution is more evident when the conditions in connections are more relaxed. The results also reveal that even the most-connected streamflow station is connected to only about 6% of the stations in the network even under relaxed conditions (i.e., when the threshold is on the lower side), thus suggesting that the streamflow network is inefficient, although, to a certain extent, stable. A significant portion of the network (over 95%) is unconnected when more stringent conditions of connections are imposed (i.e., when the threshold is on the higher side).

The results from the present study have important implications for water planning and management in the Mississippi River basin, and in large-scale river basins in general. For instance, identification of strongly connected/weakly connected regions in the basin offers crucial information as to whether new monitoring stations are necessary and, if yes, where they would be more effective/less effective. Indeed, identification of strongly connected/weakly connected regions also offers key information as to whether the existing data interpolation schemes would be effective, and

where, even before any steps to install new streamflow monitoring stations. Further, identification of the properties (e.g., clustering, degree distribution, shortest path length) of the streamflow network offers key information as to the type, and complexity, of model that is most suitable for representing the basin. These information, in turn, are essential from the perspectives of streamflow (and other data) monitoring, streamflow modeling and prediction, flood forecasting, and water resources assessment, in the entire river basin and in the subbasins. In this regard, there are also opportunities to construct the streamflow network in a better way. For instance, using the concepts of nonlinear dynamics and chaos, the single-variable streamflow time series can be reconstructed in a multidimensional phase space, which can then serve as a network to even better represent the connections, patterns, and dynamics in streamflow; see Yasmin and Sivakumar [46] for a very recent study. We will examine all these issues in our future studies.

Acknowledgements This study was supported by the Australian Research Council (ARC) Future Fellowship grant (FT110100328). Bellie Sivakumar acknowledges the financial support from ARC through this Future Fellowship grant.

References

1. Alexander JS, Wilson RC, Green WR (2012) A brief history and summary of the effects of river engineering and dams on the Mississippi River system and delta, p 43. US Geological Survey Circular 1375
2. Barabási A-L, Albert R (1999) Emergence of scaling in random networks. *Science* 286:509–512
3. Bouchaud J-P, Mézard M (2000) Wealth condensation in a simple model of economy. *Phys A* 282:536–540
4. Braga AC, Alves LGA, Costa LS, Ribeiro AA, de Jesus MMA, Tateishi AA, Ribeiro HV (2016) Characterization of river flow fluctuations via horizontal visibility graphs. *Phys A* 444:1003–1011
5. Chen J, Wu Y (2012) Advancing representation of hydrologic processes in the Soil and Water Assessment Tool (SWAT) through integration of the TOPographic MODEL (TOPMODEL) features. *J Hydrol* 420–421:319–328
6. Costa LDF, Rodriguez FA, Traviesco G, Villas Boas PR (2007) Characterization of complex networks: a survey of measurements. *Adv Phys* 56(1):167–242
7. Czuba JA, Foufoula-Georgiou E (2014) A network-based framework for identifying potential synchronizations and amplifications of sediment delivery in river basins. *Water Resour Res* 50:3826–3851
8. Czuba JA, Foufoula-Georgiou E (2015) Dynamic connectivity in a fluvial network for identifying hotspots of geomorphic change. *Water Resour Res* 51:1401–1421
9. Davis KF, D’Odorico P, Laio F, Ridolfi L (2013) Global spatio-temporal patterns in human migration: a complex network perspective. *PLoS ONE* 8(1):e53723. <https://doi.org/10.1371/journal.pone.0053723>
10. Estrada E (2012) *The structure of complex networks: theory and applications*. Oxford University Press, UK
11. Falcone JA (2011) GAGES-II: geospatial attributes of gages for evaluating streamflow. US Geological Survey, Reston, Virginia. http://water.usgs.gov/GIS/metadata/usgswrd/XML/gagesII_Sept2011.xml#Identification_Information

12. Falcone JA, Carlisle DM, Wolock DM, Meador MR (2010) GAGES: a stream gage database for evaluating natural and altered flow conditions in the conterminous United States. *Ecology* 91(2):621. Data Paper in Ecological Archives E091-045-D1. <http://esapubs.org/Archive/ecol/E091/045/metadata.htm>
13. Fang K, Sivakumar B, Woldemeskel FM (2017) Complex networks, community structure, and catchment classification in a large-scale river basin. *J Hydrol* 545:478–493
14. Girvan M, Newman MEJ (2002) Community structure in social and biological networks. *Proc Natl Acad Sci USA* 99:7821–7826
15. Halverson MJ, Fleming SW (2015) Complex network theory, streamflow, and hydrometric monitoring system design. *Hydrol Earth Syst Sci* 19:3301–3318
16. Han X, Sivakumar B, Woldemeskel FM, Guerra de Aguilar M (2018) Temporal dynamics of streamflow: application of complex networks. *Geosci Lett* 5:10
17. Jha SK, Sivakumar B (2017) Complex networks for rainfall modeling: spatial connections, temporal scale, and network size. *J Hydrol* 554:482–489
18. Jha SK, Zhao H, Woldemeskel FM, Sivakumar B (2015) Network theory and spatial rainfall connections: an interpretation. *J Hydrol* 527:13–19
19. Jothiprakash V, Kote SA (2011) Improving the performance of data driven techniques through data pre-processing for modelling daily reservoir inflow. *Hydrol Sci J* 56(1):168–186
20. Kiang JE, Stewart DW, Archfield SA, Osborne EB, Eng K (2013) A national streamflow network gap analysis. US Geological Survey Scientific Investigations Report 2013–5013, Reston, Virginia, USA
21. Konapala G, Mishra AK (2017) Review of complex networks application in hydroclimatic extremes with an implementation to characterize spatio-temporal drought propagation in continental USA. *J Hydrol* 555:600–620
22. Latora V, Marchiori M (2001) Efficient behavior of small-world networks. *Phys Rev Lett* 87(19):198701
23. Li T, Wang G, Chen J (2010) A modified binary tree codification of drainage networks to support complex hydrological models. *Comput Geosci* 36(11):1427–1435
24. Liljeros F, Edling C, Amaral LN, Stanley HE, Åberg Y (2001) The web of human sexual contacts. *Nature* 411:907–908
25. Miguens J, Mendes J (2008) Weighted and directed network on traveling patterns. *BioWire* 5151:145–154
26. Mishra AK, Coulibaly P (2009) Developments in hydrometric network design: a review. *Rev Geophys* 47, RG2001/2009
27. Naufan I, Sivakumar B, Woldemeskel FM, Raghavan SV, Vue MT, Liang S-Y (2018) Spatial connections in regional climate model rainfall outputs at different temporal scales: application of network theory. *J Hydrol* 556:1232–1243
28. Rinaldo A, Rigon R, Banavar JR, Maritan A, Rodriguez-Iturbe I (2014) Evolution and selection of river networks: Statics, dynamics, and complexity. *Proc Nat Acad Sci USA* 111(7):2417–2424
29. Rinaldo A, Banavar JR, Maritan A (2006) Trees, networks, and hydrology. *Water Resour Res* 42:W06D07. <https://doi.org/10.1029/2005wr004108>
30. Salas JD, Delleur JW, Yevjevich V, Lane WL (1995) Applied modeling of hydrologic time series. Water Resources Publications, Littleton, Colorado, USA
31. Seaber PR, Kapinos FP, Knapp GL (1987) Hydrologic unit maps. US Geological Survey, Denver
32. Serinaldi F, Kilsby CG (2016) Irreversibility and complex network behavior of streamflow fluctuations. *Phys A* 450:485–600
33. Singh VP (1997) The use of entropy in hydrology and water resources. *Hydrol Process* 11(6):587–626
34. Sivakumar B (2003) Forecasting monthly streamflow dynamics in the western United States: a nonlinear dynamical approach. *Environ Modell Softw* 18:721–728
35. Sivakumar B (2015) Networks: a generic theory for hydrology? *Stoch Environ Res Risk Assess* 29:761–771

36. Sivakumar B, Berndtsson R (2010) Advances in data-based approaches for hydrologic modeling and forecasting. World Scientific Publishing Company, Singapore
37. Sivakumar B, Woldemeskel FM (2014) Complex networks for streamflow dynamics. *Hydrol Earth Syst Sci* 18:4565–4578
38. Sivakumar B, Woldemeskel FM (2015) A network-based analysis of spatial rainfall connections. *Environ Modell Softw* 69:55–62
39. Sivakumar B, Woldemeskel FM, Fang K, Singh VP (2017) Network theory. In: Singh VP (ed) *Handbook of Applied Hydrology*. McGraw-Hill Education, Chapter 35, pp. 35-1–35-10
40. Tang Q, Liu J, Liu H (2010) Comparison of different daily streamflow series in US and China, under a viewpoint of complex networks. *Mod Phys Lett B* 24(14):1541–1547
41. Tongal H, Demirel MC, Booij MJ (2013) Seasonality of low flows and dominant processes in the Rhine River. *Stoch Environ Res Risk Assess* 27:489–503
42. Tsonis AA, Roebber PJ (2004) The architecture of the climate network. *Phys A* 333:497–504
43. Wang X, Hao G, Yang Z, Liang P, Cai Y, Li C, Sun L, Zhu J (2015) Variation analysis of streamflow and ecological flow for the twin rivers of the Miyun Reservoir Basin in northern China from 1963 to 2011. *Sci Total Environ* 536:739–749
44. Wasserman S, Faust K (1994) *Social network analysis*. Cambridge University Press, Cambridge
45. Watts DJ, Strogatz SH (1998) Collective dynamics of ‘small-world’ networks. *Nature* 393:440–442
46. Yasmin N, Sivakumar B (2018) Temporal streamflow analysis: coupling nonlinear dynamics with complex networks. *J Hydrol* 564:59–67
47. Zaliapin I, Foufoula-Georgiou F, Ghil M (2010) Transport on river networks: a dynamic tree approach. *J Geophys Res* 115:F00A15. <https://doi.org/10.1029/2009jf001281>
48. Zhao D, Shen F, Zeng J, Huang R, Yu Z, Wu QL (2016) Network analysis reveals seasonal variation of co-occurrence correlations between Cyanobacteria and other bacterioplankton. *Sci Total Environ* 573:817–825

Climate Change Impacts on Four Agricultural, Headwater Watersheds from Varying Climatic Regions of New Zealand



M. S. Srinivasan, Shailesh Kumar Singh and R. J. Wilcock

1 Introduction

Anthropogenic activities have resulted in changes to land surface and atmospheric composition, thereby affecting the energy balance of Earth and driving climate change [15]. Among others, climate change is predicted to result in increases in global average temperature, changes to precipitation patterns, and likely increases in the frequency of extreme weather events [14]. Such changes can potentially affect spatial and temporal occurrence—state, storage, flux, and, eventually, availability and use—of water resources. Climate change impacts on water resources have implications for both natural and human systems [1, 4, 5, 8, 13, 20, 39].

2 Climate Change Impacts on New Zealand

Conclusions from the fifth Intergovernmental Panel on Climate Change (IPCC) report indicate that the climate change impacts on New Zealand (NZ) are expected to be on similar lines as those projected in the fourth assessment report. A summary of climate change impacts on NZ climatic, hydrological and coastal systems can be found at <http://www.mfe.govt.nz/issues/climate/resources/impact-map/climate->

M. S. Srinivasan (✉)
National Institute of Water and Atmospheric Research Limited, 10 Kyle Street,
Christchurch 8011, New Zealand
e-mail: MS.Srinivasan@niwa.co.nz

S. K. Singh
National Institute of Water and Atmospheric Research Limited, Christchurch 8011,
New Zealand

R. J. Wilcock
National Institute of Water and Atmospheric Research Limited, Hamilton 3216, New Zealand

[change-impact-map-a3.pdf](#). The temperature increases could range from 0.2 to 1.7 °C by 2040 and from 0.1 to 4.6 °C by 2090 [23]. The MfE report (2016) also highlights marked differences in rainfall across the country: winter and spring seasons may bring more rainfall to the western parts of both islands, while the eastern parts might experience dry conditions. In summer, these trends may be reversed with the eastern parts of both islands experiencing more rainfall than western and central parts. The western part of South Island is likely to experience more extreme rainfall events, while the majority of the country may undergo more frequent drought events.

MfE [23] presents a more detailed discussion on the global climate models (GCMs) used to develop climate change projections for NZ. While a suite of GCMs are available, the models that best represented the current climate of NZ were chosen to simulate climate change projections. While IPCC fourth assessment GCMs used information on future projections of greenhouse concentrations as input, the IPCC fifth assessment included an additional scenario on future land use changes resulting from socio-economic changes. The investigation presented in the chapter does not account for land use change, hence was based on IPCC fourth assessment.

A suite of GCMs were applied to simulate twentieth-century climate in NZ, and the 12 best performing models were selected for further application [25]. The coarse output from GCMs was downscaled to NZ scale, and the methodology for downscaling temperature and precipitation is described in MfE [25], and the scientific details are provided in Mullan et al. [26]. The global climate change data were statistically downscaled to NZ, generating regression equations, stratified by season, to describe changes in monthly rainfall and temperature changes across NZ. The downscaled data consider large-scale climatic and circulation features only [23].

The ministry for Environment, based on IPCC published climate change projections [14], had developed procedures to derive climate change datasets for NZ and guidelines to apply them [24, 25]. The climate change datasets developed in accordance with [25] procedures have been used in several hydrological studies in NZ. These studies varied in spatial and seasonal scales—from regional (e.g. changes to seasonal snow cover across the Southern Alps of the South Island of NZ by [8]), large river basin (e.g. climate change impact on the hydrology of 1773-km² Rangitata River basin, South Island, NZ, by Woods et al. [39]) to local scale (e.g. climate change impact on irrigation demand and supply in a 180-km² irrigation scheme in Canterbury, NZ, by Srinivasan et al. [33]).

3 Hydrologic Modelling of Climate Change Projections

Hydrological models are useful tools in simulating, assessing, understanding and communicating climate change impacts on water resources. Hydrological models applied to assess climate change impacts have ranged from simple conceptual (e.g. [11, 17]) to comprehensive, physically based models [8, 33, 39]. Studies such as those reported in Velázquez et al. [36] have adopted a multi-model approach, where models applied varied in structure and process representation, from concep-

tual, lumped model to conceptual, process-based and distributed. They argued that such an approach would reduce the uncertainty arising from model selection and application.

Climate change in NZ, as elsewhere, is predicted to result in increases in temperature leading to changes in watershed-scale moisture storage and flux. Hydromad (Hydrological Model Assessment and Development; [2]), a hydrological modelling system containing a suite of soil moisture accounting (SMA) and runoff routing models, provides a framework where multiple models can be used independently in assessing watershed-scale storage and flux. The models within Hydromad were independently developed and tested (e.g. IHACRES Catchment Wetness Index model, [16]; IHACRES Catchment Moisture Deficit model, [10]; Sacramento Soil Moisture Accounting model, [7]; the GR4 J model, [30]; the Australian Water Balance model, [6]; the Single-Bucket model, [3]; the snow model, Kokkonen et al. [19]). Users can opt for model(s) based on input data availability and/or desired level of process complexity in watersheds of interest.

The goal of the study described here was to assess the climate change impacts on temperature, precipitation, and flows in four headwater, agricultural watersheds from diverse climatic regions of NZ. Earlier Wilcock et al. [37, 38] had identified that these four climatic regions could potentially undergo significant agricultural intensification in the coming years to decades, thereby impacting on land and water resources. A comprehensive field study was launched in 2001 to monitor flows and water quality in these watersheds, as they (the watersheds) were identified as representative of climate and land use of the respective climatic region [38]. The climate change impacts on these four watersheds were examined using a multi-model approach, as reported in Velázquez et al. [36]. A selection of SMA models from Hydromad was used. A scenario-based approach was applied, wherein a range of probable future climate change conditions was investigated, simulating an array of probable future outcomes. The specific objectives were to individually calibrate and validate the selected SMA models using flow observations from each watershed, and to assess the climate change impacts on watersheds' temperature, precipitation and flows using the validated models.

4 Methods and Materials

4.1 Study Watersheds

The study watersheds are spread across the length of the country over varying climatic regions, from warm subtropical (Toenepi) to cool temperate (Bog Burn) (Fig. 1). At all four watersheds, rainfall is uniformly distributed throughout the year though the prevailing weather system varies. The watersheds vary in topography, soils, temperature recorded, rainfall received and flows generated, but have a similar land cover (pasture) and land use practice (livestock grazing) (Table 1). A brief description

of the regional climate, adapted from National Institute of Water and Atmospheric Research Ltd (NIWA) [29], follows: the furthest north, North Island (NI) watershed Toenepi lies inland, sheltered by high country to the south and east, and is less windy than many other parts of NZ. Owing to its inland location, Toenepi experiences a wide range of temperature. Summers (January–March) are warm and dry with settled weather, and winters (June–August) are cool with unsettled weather. The Waiokura watershed (NI), because of its location, is exposed to weather systems originating from the Tasman Sea. This region often gets quite windy but has few climate extremes. Summer weather is warm and settled. Winter weather is unsettled. The headwaters of the Waiokura watershed descends steeply from the Taranaki mountain, before gradually sloping towards the coast. This watershed is characterized by a high density of ephemeral and first-order streams [38].

The Inchbonnie watershed is located on the West coast of the South Island (SI), between the Tasman Sea (West) and the Southern Alps (East). Even though the mean annual rainfall in this region is very high (upwards of 2,800 mm), dry spells do occur often during late summer and winter periods. Inchbonnie is the smallest of the four watersheds selected for the study but receives the most rainfall, and has the highest specific yield (flow per every unit area of the watershed) (see Table 1). The Bog Burn watershed is located within the cooler, temperate zone of SI. Cool coastal breezes from south dominate this region, and in the absence of a shelter such as a mountain range, this region is often subjected to the weather originating from and moving over the South Seas. Of the four, the Bog Burn watershed receives the least amount of rainfall, and its specific yield is 4% that of the Inchbonnie watershed.

4.2 *Time-Series Observations*

As a part of the field monitoring study initiated in 2001 [38], these four watersheds were instrumented with stage recorders (pumproTM) at the outlets and stream stages were recorded at 15-min intervals. Each monitoring site was visited 8–10 times annually for manual flow gauging, and site-specific rating curves were developed.

Precipitation and temperature data for each watershed were derived from a high-resolution daily climate data developed by NIWA. These data are available online, and are filed under “virtual climate network” within Cliflo [9]. The Virtual Climate Station (VCS) represents a network of approximately 5-km grid points across NZ for which daily precipitation (24-h total from 09:00) and temperature (maximum and minimum over 24 h from 09:00) data are interpolated from station observations. A thin plate smoothing spline model was used to derive daily rainfall based on observed meteorological data. More information on VCS data and interpolation procedures can be found in Tait and Woods [34] and Tait et al. [35].

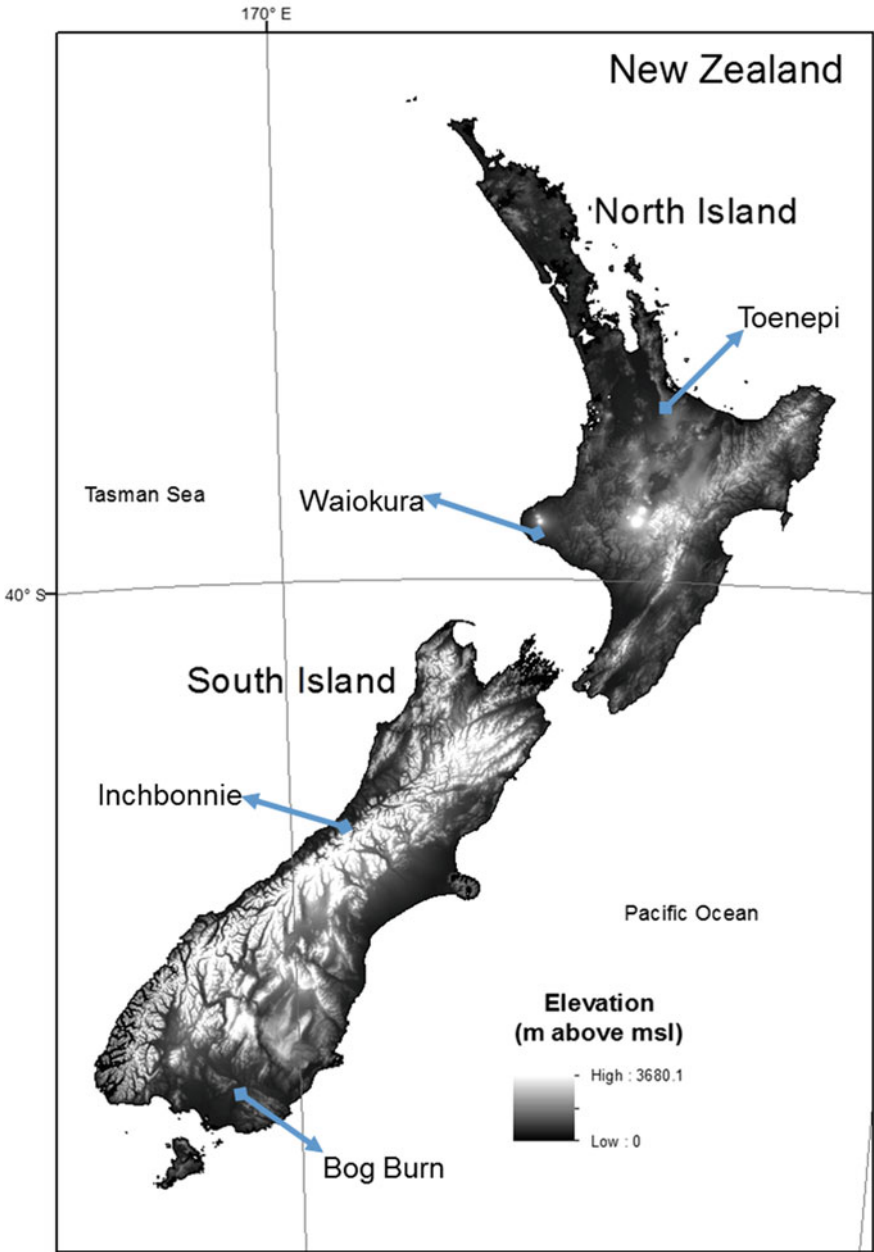


Fig. 1 Locations of the study watersheds. Key climatic, physical and hydrological characteristics are listed in Table 1

Table 1 Key physical, climatic and hydrological characteristics of the study watersheds. Watershed and hydrology data compiled and adapted from Wilcock et al. [37, 38]; Flow statistics based on observed flows. Rainfall data from Cliflo [9]; Air temperature, sun shine hours and prevailing wind direction from NIWA [29]

	Toenepi	Waiokura	Inchbonnie	Bog Burn
Area (km ²)	15.8	20.9	6.0	24.8
Slope (%)	0–11	1–20	0–12	0–12
Dominant land use (% of watershed area)	Grazed dairy pasture (83%)	Grazed dairy pasture (99%)	Grazed dairy pasture (100%)	Grazed dairy & sheep pasture (77%); rest in the pine plantation
Soil type	Volcanic origin—Topehaehae silt loam, Kiwitahi and Kereone yellow-brown loams, Morrinsville clay loam	Volcanic origin—Egmont brown loam	Freely draining stony soil—Harihari silt loam	Poorly draining with extensive mole and pipe drains; Taringatura silt loam, Mossburn silt loam, Pukemutu silt loam
Rainfall (mm y ⁻¹)	1,160	1,250	4,800	900
Monthly average (mm)	100 (<i>Summer, Jan.–Mar.</i>);	100;	210;	90;
	130 (<i>Winter, Jun.–Aug.</i>)	135	240	90
Average air temperature (°C)	21–26 (<i>Summer</i>)	21–26;	17–22;	16–23;
	10–14 (<i>Winter</i>)	10–14	10–14	8–12
Annual average sunshine hours	2100	2000	1900	1600
Prevailing wind direction	Southwest	Northwest	North–Northeast; Southwest	South–Southwest
Duration of observed flow records	Jun. 2000–Sep. 2009	May 2001–Apr. 2010	May 2004–Apr. 2010	May 2001–Feb. 2010
Flow range (mm d ⁻¹)	0–38.2	0.1–30.2	0.2–308.5	0.1–41.8
Mean flow (mm d ⁻¹)	1.2	1.8	5.2	1.0
Median (mm d ⁻¹)	0.4	1.5	1.4	0.5
95 percentile flow (mm d ⁻¹)	5.0	4.0	17.3	3.8
Specific yield (mm km ⁻² y ⁻¹)	27.7	31.4	377.2	14.7

4.3 *Climate Change Data*

Of the 17 global climate models described in [14] for developing regional climate change datasets, 12 were found to perform satisfactorily in predicting the climate in NZ and South Pacific region [24, 25, 27]. MfE had published procedures to derive climate change datasets based on these twelve models for two 20-year future periods—1 Jan. 2030–31 Dec. 2049 (termed “2040” hereafter) and 1 Jan. 2080–31 Dec. 2099 (“2090”) [24, 25]. Climate-change induced changes to precipitation and temperature were applied to data from 1 Jan. 1980–31 Dec 1999 (“1990”) period to derive data for 2040 and 2090 periods. Thus, the datasets from 1990, 2040 and 2090 have the same resolution, spatially (~5 km grid) and temporally (daily). The down-scaled temperature change data for climate change scenarios represent the change in mean temperatures from the 1990 condition. Precipitation data for climate change scenarios were derived in four steps. In step 1, daily precipitation from 1990 condition was adjusted using monthly offset described in Tables 2 and 3 of MfE (2008; pages 19 and 20) for 2040 and 2090 conditions. In step 2, the number of rain days per year was altered based on predicted warming. For every degree of warming, 7 fewer rain days are predicted. Days with the lowest precipitation recorded under 1990 condition were reset to days with zero precipitation in 2040 and 2090. In step 3, increases to precipitation resulting from increases in temperature were applied to 1990 precipitation data from step 2. For every degree rise in temperature, the water vapour saturation levels and, hence, the precipitation were increased by 8%. In step 4, the annual and monthly precipitation estimated in step 3 were compared against those presented in MfE (2008) to ensure the changes were consistent. More details on this downscaling procedure can be found in the MfE report [24]; pages 22–24).

The published MfE procedures cover a spectrum of greenhouse emission scenarios. A description of these emission scenarios can be found in Reisinger [31] and MfE [24]. In this study, between 2040 and 2090, three emission scenarios were considered, B1 (low emission; an increase in forest cover over the current conditions, and introduction and adaptation of clean and resource-efficient technologies), A1B (medium or middle-of-the road emission; a balance across all emission sources), and A1FI (high emission; a fossil-fuel intensive future). For each emission scenario, an averaged dataset from the 12 GCMs were used. Based on a hydrological modelling study in a large river basin in NZ, Woods et al. [39] suggested that where resources are not limited, data from the 12 models should be considered individually. However, in this study, as had been done previously in Srinivasan et al. [33] and Woods et al. [39], for lack of sufficient resources, for each emission scenario dataset averaged from the twelve GCMs was used for modelling.

Table 2 Statistical analyses of Soil Moisture Accounting models calibrated and validated in the study watersheds. Nash-Sutcliffe coefficient is based on daily flows. Calibration period, 1 Jan. 2004–31 Dec. 2008, validation period, 1 Jan. 2009–31 Dec. 2011

Model	Nash-Sutcliffe coefficient											
	Toenepi			Waiokura			Inchbonnie			Bog Burn		
	Calibration	Validation		Calibration	Validation		Calibration	Validation		Calibration	Validation	
Catchment Wetness Index (CWI)	0.78	0.83		0.79	0.89		0.65	0.64		0.66	0.57	
Catchment Moisture Deficit (CMD)	0.82	0.80		0.79	0.86		0.67	0.68		0.58	0.55	
Single-Bucket (SB)	0.84	0.77		0.79	0.79		0.66	0.66		0.66	0.60	
Sacramento Soil Moisture Accounting (SSMA)	0.47	0.41		0.59	0.57		0.63	0.64		0.43	0.35	
Australian Water Balance (AWB)	0.82	0.49		0.78	0.87		0.69	0.69		0.60	0.55	

Table 3 Changes in daily and seasonal rainfall characteristics in 2040 (“2030–49”) and 2090 (“2080–99”) over 1990 (“1980–99”). All statistics are based on 20-year daily data from each time period. Mean daily rainfall statistics includes only non-zero values. B1—Low emission; A1B—Medium emission; A1FI—High emission. Growing season—Oct.–Mar.; Dormant season—Apr.–Sep.

	1990 conditions		2040 conditions		2090 conditions	
	Growing	Dormant	Growing	Dormant	Growing	Dormant
Watershed			B1, A1B, A1FI	B1, A1B, A1FI	B1, A1B, A1FI	B1, A1B, A1FI
	<i>Mean daily rainfall (mm)</i>		<i>Percent change in mean rainfall over 1990 conditions^a</i>			
Toenepi	9.1	8.9	3.3, 5.3, 8.4	3.1, 5.0, 7.4	7.2, 11.9, 19.1	7.1, 11.5, 17.1
Waiokura	6.2	5.6	2.8, 4.6, 7.0	4.3, 5.5, 8.3	5.4, 8.6, 14.2	6.9, 11.0, 16.8
Inchbonnie	13.1	13.1	3.1, 4.7, 6.6	7.2, 11.6, 17.2	5.0, 7.3, 10.8	13.9, 21.4, 32.4
Bog Burn	6.7	5.8	4.0, 6.2, 8.9	6.1, 9.4, 13.4	8.2, 13.8, 19.5	11.9, 19.4, 30.0
	<i>Maximum daily rainfall (mm)</i>		<i>Percent change in maximum rainfall over 1990 conditions</i>			
Toenepi	137.8	99.1	9.4, 9.9, 14.5	5.8, 9.0, 13.2	13.8, 21.6, 32.3	12.1, 18.9, 28.1
Waiokura	93.7	58.0	6.3, 9.7, 14.2	5.8, 8.9, 13.0	12.9, 20.2, 29.9	13.5, 21.1, 31.4
Inchbonnie	153.5	155.8	5.7, 8.8, 12.8	15.4, 24.1, 35.4	11.9, 18.3, 26.6	28.3, 45.0, 68.2
Bog Burn	120.4	67.0	4.4, 6.8, 9.8	6.1, 9.5, 16.1	11.8, 18.5, 27.5	15.6, 27.6, 44.2
	<i>Seasonal total rainfall (mm)</i>		<i>Percent change in seasonal total rainfall over 1990 conditions</i>			
Toenepi	472.7	589.9	0.2, 0.3, 0.4	0.0, 0.0, 0.1	−1.4, −2.2, −3.3	0.4, 0.6, 0.9
Waiokura	517.7	593.2	0.5, 0.8, 1.2	−0.6, 1.8, 2.5	−0.6, −1.0, −1.5	1.6, 2.4, 3.6
Inchbonnie	1524.4	1575.1	0.9, 1.4, 1.9	4.6, 8.5, 13.2	0.2, 0.1, −0.3	10.0, 15.5, 22.7
Bog Burn	502.7	424.5	1.3, 1.9, 2.8	3.9, 6.0, 8.6	1.9, 2.7, 3.8	6.9, 10.7, 15.6

^aPositive values—greater than that of 1990; negative values—less than that of 1990

4.4 Scenario Approach

Using a scenario approach, the multiple models (the models used are identified in the next section) from Hydromad were calibrated and validated using observed (flow) and VCS (interpolated observations of precipitation and temperature) data and the validated models were then applied to 1990, and to multiple probable climate change scenarios (B1, A1B, A1FI) from 2040 to 2090. The scenario approach assumes no change in the relationship between drivers (precipitation and temperature) and responses (watershed storage and flows) under all conditions, thereby providing a common ground to compare multiple responses resulting from a range of drivers. To further support this approach, the land use and land cover in the study watersheds were assumed to remain the same for all scenarios.

4.5 Hydromad Modelling Framework

The Hydromad modelling framework offers a range of SMA and routing models within a powerful R environment, and is an open-source software. Hydromad allows calibration and validation of models using user-defined objective functions. Since the watersheds considered in this study were small, primarily composed of ephemeral and first- and second-order streams, following a preliminary assessment and testing of all routing models, only one routing model—the exponential components transfer function model—was considered. This routing model was paired individually with five different SMA models, the Catchment Moisture Deficit (CMD), the Catchment Wetness Index (CWI), the Single-Bucket (SB), the Sacramento Soil Moisture Accounting (SSMA), and the Australian Water Balance (AWM). All are daily time-stepping models, and treat watersheds as lumped units (i.e. the smallest computational unit is watershed; AWM is an exception to this). The SMA models partition the input rainfall into storage and effective rainfall, and each model applies its own procedure in computing the storage. Depending on the SMA model chosen, the storage may become available for evaporation, stream flow, lateral drainage and percolation. The effective rainfall is routed to the watershed outlet using the routing model.

A description of Hydromad SMA and routing models is available at <http://hydromad.catchment.org/> (last accessed on 17 March 2018). A brief description of SMA models used in this study is presented here. CMD model uses a mass balance approach to calculate effective rainfall based on watershed-scale (soil) moisture deficit and evaporative losses, both of which are expressed in the same units as rainfall. Evaporative losses are estimated internally using input temperature. Effective rainfall is a direct function of moisture deficit. CWI model uses a watershed-scale wetness index to represent watershed-scale moisture conditions. The wetness index is not a physical measure and is watershed specific. A high wetness index results in a large effective rainfall. The effective rainfall is calculated as a product of input rainfall and a storage index, which is a function of wetness index.

The SB model uses a single soil layer with defined storage. Rainfall in excess of soil storage results in effective rainfall. Evaporation is optional and has to be supplied as input. The SSMA model is the most sophisticated of models considered in this study. It includes multiple soil zones (upper and lower), with lateral flow, percolation and evaporation simulated from each zone, and a provision to include impervious areas. Lateral drainage from upper and lower soil zones and storage-excess rainfall constitute effective rainfall. The AWM model is a three-bucket model, where a watershed can be represented as many as three segments with varying storages. User defines the storage and areal extents of the segments. Saturation excess based on storage and evaporative losses from each segment are cumulated to estimate effective rainfall.

During calibration, for a given watershed, the SMA and routing models were operated as paired models and parameters were adjusted to get the best fit between modelled and observed flows. Each model pair was calibrated individually in every watershed using the default PORT algorithm [12], and the Nash-Sutcliffe (NS) coefficient [28] as the objective function and modelled flows as the evaluation variable. Within each model pair, the effective rainfall routing (routing effective rainfall as flow to watershed outlet) and Soil Moisture Accounting (partitioning input rainfall into effective rainfall and watershed storage) parameters were adjusted to fit modelled flows to those observed. Thus, for a given watershed, the same routing model may have a different parameter set depending on the SMA model it is paired with. Both calibration and validation included a 3-month warm up period and data from that period were not used in assessing the model performance.

4.6 Data Preparation and Analysis

During calibration and validation, daily VCS precipitation and temperature data from 2004 to 2011 were used to drive the models (calibration, 1 Jan. 2004 to 31 Dec. 2008; validation, 1 Jan. 2009 and 31 Dec. 2011). Spatially averaged precipitation and temperature data within each watershed were used to reduce the impact of uncertain spatial forcing data. Two models were selected based on their performance during calibration and validation and data requirements/availability for further application to 1990, 2040 and 2090 periods. Model outputs from multiple emission scenarios from 2040 to 2090 were compared against 1990 to assess the climate change impact. Changes to flows at watershed outlet and watershed internal state (moisture conditions) were compared.

Because the climate change datasets were derived from spatially diffuse global-scale models and from temporally coarse annual to monthly time-series temperature and precipitation offsets, the model outputs were assessed at appropriate scales. Spatially, outputs were assessed at the watershed scale, and temporally at seasonal scale. The seasonal scale was aligned with grazing season, as the study watersheds are primarily under grazing (see Table 1). October through March period (termed as “growing season” hereafter) is characterized by intensive grazing, wherein each

paddock may get grazed as frequently as every 21 days. April through September period is characterized by less intensive grazing, as soil and climatic conditions are less conducive for pasture growth and grazing. (“dormant season”).

In NZ, the 7-day mean annual low flow is a standard metric used to illustrate the severity of low flows and dry conditions in watersheds (e.g. Scarf et al. [32]). In this study, since the data were analysed at a seasonal scale, the 7-day mean statistics were calculated at the same scale. The 7-day mean seasonal statistics includes the 7-d mean seasonal low flow (7-d MSLF) based on two selected models CMD and CWI, the 7-d mean seasonal high (soil) moisture deficit (7-d MSHMD) based on CMD, and the 7-d mean seasonal low wetness index (7-d MSLWI) based on CWI. The 7-day statistics are indicative of the severity of dry conditions in the watershed, and are expressed using a different metric.

5 Results

5.1 Calibration and Validation of Model Pairs

The five SMA models in combination with one routing model were calibrated and validated using daily data in the four watersheds. On a daily time scale, at 3 out of 4 watersheds, the SB model outperformed, though marginally, other models (see NS coefficient, Table 2). At the fourth, the Inchbonnie watershed, where frequent rainfall events would have resulted in saturated soil conditions and saturation excess runoff, the 3-bucket AWB model, a saturation excess model, outperformed others.

CMD and CWI models were the next best performing models to the SB model in all watersheds (see Table 1 and Fig. 2 for model performance). The SB and CMD models use similar water balance approach. In the SB model, evaporation is optional, and has to be provided by the user. In CMD model, evaporation is calculated from input temperature data. Since temperature data are readily available for all climate change scenarios, CMD model, along with CWI, was chosen for assessing climate change impact in the four watersheds. Both CMD and CWI models simulate daily flows at watershed outlets. As the internal watershed state, CMD model generates daily, watershed-scale (soil) moisture deficit, and CWI generates daily, watershed-scale wetness index.

A comparison of effective rainfall in the four watersheds during calibration and validation periods indicated that the differences between CMD and CWI models were small. At Toenepi, the differences were 3.6% (calibration) and 6.5% (validation) of seasonal total rainfall. The differences at the other watersheds were 0.8 (calibration) and <0.1% (validation) for Waiokura, 3.0 and 8.6% for Inchbonnie and 3.2 and 8.6% for Bog Burn. There was no consistent relationship between models, watersheds and effective rainfall generated.

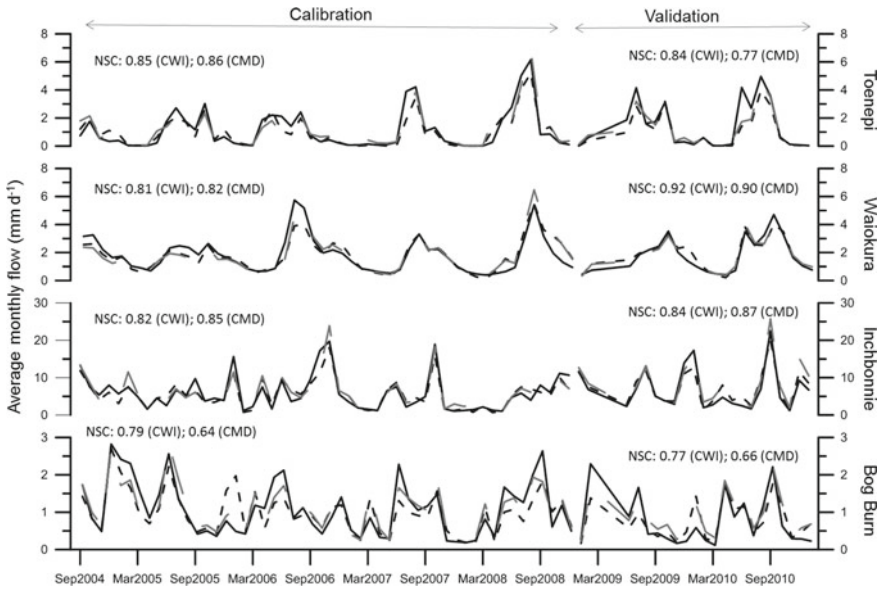


Fig. 2 Model performance in the four study watersheds during calibration and validation periods. CWI is catchment wetness index model flows (grey dashed line) and CMD is Catchment Moisture Deficit model flows (dark dotted line). Observed flows are shown as a black continuous line. NSC (Nash-Sutcliffe Coefficient) based on monthly average data

5.2 Climate Change Impacts on Precipitation and Temperature

As predicted, at all four watersheds, climate change resulted in changes to temperature and precipitation in 2040 and 2090 scenarios over 1990. Maximum (Fig. 3) and minimum (data not shown) temperatures followed similar increasing trends over seasons for all four watersheds. As moved from low (B1) to high (A1FI) emission scenarios, and from 2040 to 2090, the increases in temperatures are predicted to become larger. Generally, the SI watersheds (Inchbonnie and Bog Burn) are predicted to experience greater temperature increases than those in NI (Toenepi and Waiokura) (Fig. 3), and Inchbonnie is predicted to record maximum increases. The cool temperate Bog Burn watershed is expected to record a greater increase in temperature than the warm, subtropical Toenepi watershed. In both islands, the temperature increases under climate change are predicted to be larger during dormant (April–September) than growing (October–March) season. Both under 2040 and 2090 scenarios, the winter months (June and July) are predicted to record maximum increases in temperatures (same for minimum temperature, data not shown). Since none of the four watersheds receive snowfall, an increase in winter temperature is unlikely to impact snow processes. With climate change, though the increases in summer temperatures

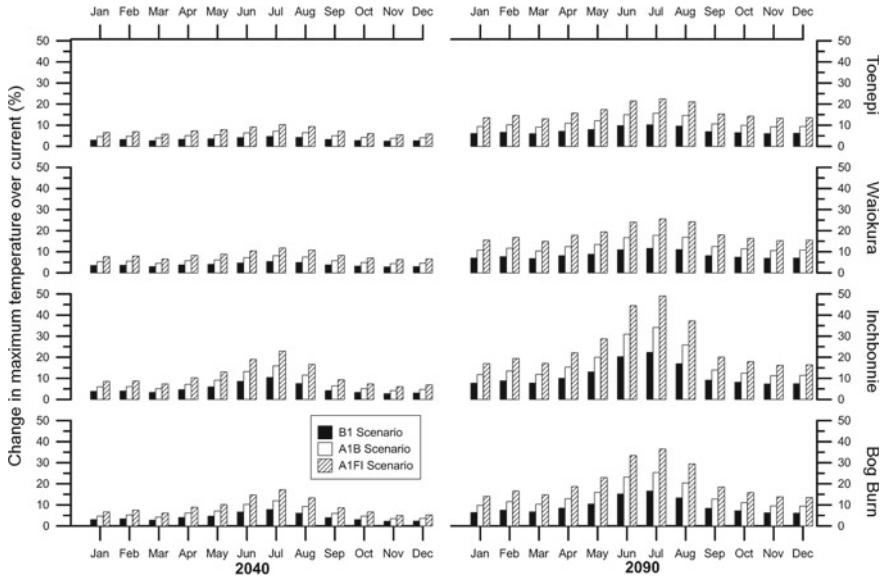


Fig. 3 Changes in monthly maximum temperatures in 2040 (“2030–49”) and 2090 (“2080–99”) over 1990 (“1980–99”) for three different emission scenarios. B1—Low emission; A1B—Medium emission; A1FI—High emission. Growing season—Oct.–Mar.; Dormant season—Apr.–Sep.

are predicted to be smaller than in winter, nevertheless they could rise by as much as 8–15% in 2090 over 1990 levels.

While the changes in temperature under all future scenarios are trending up, the changes in precipitation are mixed (Table 3). In all four watersheds, the mean (includes non-zero rainfall only) and maximum daily rainfall are predicted to go up for all climate change scenarios over 1990 but this trend was not always true for seasonal total rainfall. The increases to the mean and maximum daily rainfall are predicted to be greater during dormant than growing season in the SI watersheds, a trend similar to that of temperature. However, such seasonal trends in rainfall are not observable in the NI watersheds. Also, in the SI watersheds, the differences in seasonal rainfall (compare 2040 and 2090, dormant vs growing seasons for all scenarios; Table 3) are consistently greater than those predicted for the NI watersheds. During the dormant season of 2090, the mean rainfall of the two SI watersheds is predicted to go up by 33% over the 1990 levels. The Toenepi and Bog Burn watersheds located on either ends of the country, are likely to record the largest increases in the mean daily rainfall during the growing seasons of 2040 and 2090. At Inchbonnie, where the mean and maximum daily rainfall were very similar between seasons in 1990, with the onset of climate change, would vary widely with the season. Of the four, the Inchbonnie watershed is predicted to record the largest increases in rainfall during the dormant season and the smallest during the growing season.

Increases in mean and maximum daily rainfalls under climate change scenarios did not always result in increases in seasonal total rainfall. The NI watersheds showed a mixed trend. At Toenepi, the changes could go either way—more seasonal total rainfall in 2090 and less in 2040, compared to 1990. At Waiokura, compared to 1990, the 2090 growing season is predicted to record a decrease in the seasonal total rainfall but the 2090 dormant season may record an increase. The two SI watersheds, except for 2090 A1FI scenario growing season at Inchbonnie, are set to record increases in seasonal total rainfall under climate change. The increases predicted for the dormant season can be several times larger than those of growing season (compare Bog Burn 2040 and Inchbonnie 2090 for all scenarios, Table 3), a trend similar to those of mean and maximum daily rainfall.

Changes to the frequency of wet days (days it rained) were analysed to further understand the rainfall input to the watersheds (Table 4). All four watersheds are predicted to experience decreases in the frequency of wet days under climate change and the decreases are likely to be greater during growing than dormant seasons (exception to this, Toenepi, Waiokura and Inchbonnie 2040B1 scenario). An analysis of the frequency of days with 30 mm, or more, of rainfall indicated that under climate change there is a positive increase in intense rainfall events in all watersheds over 1990 (data not shown here), and the increases are predicted to be greater during dormant than growing seasons. The frequency of extended dry (no rain for 7 consecutive days or more) and wet (rains for 7 consecutive days or more) spells in the study watersheds were analysed (Table 4). For all scenarios in 2040 and 2090, and for all watersheds, extended dry spells are predicted to increase and extended wet spells to decrease. During the growing season, the SI watersheds are predicted to record more dry spells than those in NI, while the trends are mixed during the dormant season. Also, under climate change, the far end watersheds, Toenepi and Bog Burn are predicted to have fewer wet spells than Inchbonnie and Waiokura watersheds.

5.3 Climate Change Impacts on Flows and Internal Watershed Conditions

The two selected models, CWI and CMD, along with a routing model, were applied to simulate flows and watershed-scale moisture conditions in the four watersheds under 1990, 2040 and 2090 conditions. The outputs from the models were analysed separately. The modelled flows were analysed for mean and maximum statistics (Table 5). At both NI watersheds and at Bog Burn, for 2040 and 2090, both models predicted the mean daily flows to decrease under climate change scenarios. The two NI watersheds are likely to undergo a greater decrease than the Bog Burn watershed. The Inchbonnie watershed is predicted to record an increase in the mean daily flow during the dormant season under climate change. Of all the four watersheds, under climate change, the Bog Burn is predicted to record minimal changes in the mean daily flow over 1990.

Table 4 Statistical comparison of rainfall data influencing watershed moisture conditions in 2040 (“2030–49”) and 2090 (“2080–99”) over 1990 (“1980–99”). All statistics are based on 20-year daily data from each time period. Mean daily rainfall statistics includes only non-zero values. B1—Low emission; A1B—Medium emission; A1FI—High emission. Growing season—Oct.–Mar.; Dormant season—Apr.–Sep.

	1990 conditions		2040 conditions		2090 conditions	
	Growing	Dormant	Growing	Dormant	Growing	Dormant
Watershed			B1, A1B, A1FI	B1, A1B, A1FI	B1, A1B, A1FI	B1, A1B, A1FI
	<i>Number of wet days per year</i>		<i>Percent change in the number of wet days over 1990 conditions^a</i>			
Toenepi	52.1	67.1	-3.2, -4.9, -7.6	-3.4, -5.1, -6.9	-8.3, -12.5, -18.6	-6.6, -10.1, -14.1
Waiokura	84.0	107.6	-2.1, -3.5, -5.2	-4.6, -3.4, -5.1	-5.5, -8.6, -13.5	-4.7, -7.5, -10.9
Inchbonnie	116.6	120.2	-2.0, -3.1, -4.2	-3.0, -3.0, -3.4	-4.4, -6.6, -9.8	-3.4, -4.8, -7.2
Bog Burn	75.5	73.8	-2.5, -3.8, -5.5	-2.0, -3.1, -4.1	-5.7, 9.5, -12.9	-4.3, -6.8, -10.5
	<i>Instances no rain for ≥7 days together</i>		<i>Percent change in instances with no rain for ≥7 days together</i>			
Toenepi	9.6	7.8	2.1, 3.1, 6.8	2.6, 4.5, 6.4	7.3, 8.4, 9.4	5.1, 7.7, 9.6
Waiokura	6.0	4.2	1.7, 1.7, 5.0	3.6, 9.5, 13.1	6.7, 11.7, 18.3	11.9, 13.1, 20.2
Inchbonnie	3.3	3.6	1.5, 4.5, 9.1	1.4, 4.2, 9.7	10.6, 19.7, 33.3	9.7, 12.5, 13.9
Bog Burn	5.5	6.9	1.8, 3.6, 9.1	2.9, 5.1, 5.8	10.0, 19.1, 24.5	5.8, 9.4, 12.3
	<i>Instances rainfall predicted for ≥7 consecutive days</i>		<i>Percent change in the number of instances with rainfall predicted for ≥7 consecutive days</i>			
Toenepi	1.3	2.6	-34.6, -34.6, -38.5	-7.8, -17.6, -21.6	-38.5, -42.3, -46.2	-21.6, -31.4, -47.1
Waiokura	7.3	21.3	-8.9, -14.4, -22.6	-10.4, -12.9, -21.9	-26.7, -32.9, -40.4	-18.1, -33.6, -43.5
Inchbonnie	28.9	33.4	-10.4, -16.1, -18.5	-5.2, -8.7, -12.0	-18.4, -18.4, -34.7	-11.2, -18.0, -28.2
Bog Burn	1.5	3.1	-20.0, -20.0, -26.7	-9.8, -21.3, -21.3	-26.7, -33.3, -63.3	-21.3, -26.2, -36.1

^aPositive values—greater than that of 1990; negative values—less than that of 1990

Table 5 Changes in flow conditions in 2040 (“2030–49”) and 2090 (“2080–99”) over 1990 (“1980–99”). All statistics are based on 20-year daily flow data from each time period. CWI—Catchment Wetness Index model; CMD—Catchment Moisture Deficit model. B1—Low emission; A1B—Medium emission; A1FI—High emission. Growing season—Oct to Mar; Dormant season—Apr.–Sep.

		1990 conditions		2040 conditions		2090 conditions	
		Growing	Dormant	Growing	Dormant	Growing	Dormant
Watershed	Model			B1, A1B, A1FI	B1, A1B, A1FI	B1, A1B, A1FI	B1, A1B, A1FI
		<i>Mean daily flow (mm)</i>		<i>Percent change in mean daily flow over 1990 conditions^a</i>			
Toenepi	CMD	0.5	1.2	−9.1, −13.3, −18.2	−6.0, −8.9, −12.3	−19.4, −26.4, −33.5	−12.2, −17.5, −23.1
	CWI	0.7	1.6	−7.5, −10.8, −14.3	−8.0, −11.8, −16.4	−15.9, −21.2, −25.4	−15.8, −22.7, −30.1
Waiokura	CMD	0.8	1.1	−3.6, −5.3, −7.3	−3.0, −4.4, −6.2	−9.1, −12.9, −17.0	−8.4, −12.3, −16.5
	CWI	0.8	1.0	−4.8, −7.0, −9.5	−5.0, −7.4, −10.2	−11.2, −15.7, −20.1	−11.9, −17.1, −22.5
Inchbonnie	CMD	4.3	6.1	−1.1, −1.7, −2.4	3.8, 5.9, 8.6	−5.7, −8.5, −11.7	4.0, 6.4, 9.9
	CWI	4.8	5.8	1.9, 2.8, 4.1	8.2, 12.8, 18.8	0.5, 0.7, 1.1	13.0, 20.9, 32.1
Bog Burn	CMD	0.8	1.1	−0.9, −1.3, −1.6	−0.3, −0.4, −0.4	−3.7, −5.2, −6.2	−4.1, −5.5, −6.5
	CWI	0.8	1.4	−1.1, −1.4, −1.4	−2.4, −3.5, −5.1	−2.9, −2.9, −1.4	−8.5, −12.2, −15.9
		<i>Maximum daily flow (mm)</i>		<i>Percent change in maximum daily flow over 1990 conditions</i>			
Toenepi	CMD	4.8	6.7	−1.6, −2.4, −3.2	−0.3, −0.3, −0.1	−3.3, −4.0, −3.3	0.5, 1.4, 3.0
	CWI	5.2	7.7	−1.9, −2.4, −2.4	−3.8, −5.2, −6.8	−3.1, −2.1, 3.6	−6.2, −8.0, −8.4

(continued)

Table 5 (continued)

		1990 conditions		2040 conditions		2090 conditions	
		Growing	Dormant	Growing	Dormant	Growing	Dormant
Waiokura	CMD	2.2	2.5	-0.6, -0.7, 0.7	-1.3, -1.8, 2.4	-2.1, -2.6, 2.5	-3.0, -4.0, 4.5
	CWI	2.2	2.5	-1.3, -1.8, 2.1	-3.3, -4.8, 6.4	-3.9, -4.6, 4.1	-6.9, -9.1, 10.6
Inchbonnie	CMD	48.1	52.0	4.5, 6.9, 10.2	9.5, 15.0, 22.5	8.5, 13.0, 18.6	19.1, 31.3, 51.1
	CWI	52.8	56.2	7.6, 12.0, 17.9	14.0, 23.0, 36.3	14.1, 22.4, 33.6	29.6, 51.4, 86.2
Bog Burn	CMD	7.0	5.5	4.0, 6.2, 9.1	3.8, 6.1, 9.2	8.0, 12.8, 19.9	5.7, 10.2, 17.4
	CWI	7.7	7.3	5.6, 9.1, 14.0	2.3, 3.7, 5.5	13.4, 22.4, 35.8	1.7, 3.8, 8.8
		<i>Runoff-rainfall ratio</i>		<i>Percent change in runoff-rainfall ratio over 1990 conditions</i>			
Toenepi	CMD	0.2	0.4	-9.0, -13.2, 18.1	-5.9, -8.9, 12.4	-17.9, -24.4, -30.9	-12.5, -18.0, -23.8
	CWI	0.3	0.5	-7.6, -10.8, 14.3	-8.0, -11.8, 16.5	-14.4, -19.0, -22.3	-16.1, -23.1, -30.8
Waiokura	CMD	0.3	0.3	-4.1, -6.0, 8.3	-2.4, -6.1, 8.5	-8.5, -11.9, 15.6	-9.8, -14.3, 19.4
	CWI	0.3	0.3	-5.2, -7.6, 10.4	-4.4, -9.0, 12.5	-10.5, -14.6, -18.6	-13.3, -19.0, -25.2
Inchbonnie	CMD	0.5	0.7	-2.0, -3.1, 4.3	-0.7, -2.4, 4.1	-6.0, -8.7, 11.5	-5.4, -7.9, 10.4
	CWI	0.6	0.7	0.9, 1.4, 2.2	3.5, 4.0, 5.0	0.3, 0.7, 1.4	2.7, 4.7, 7.7
Bog Burn	CMD	0.3	0.5	-2.2, -3.3, 4.4	-4.1, -6.0, 8.3	-5.5, -7.8, 9.8	-10.3, -14.6, -19.2
	CWI	0.3	0.6	-2.3, -3.3, 4.0	-6.0, -9.0, 12.6	-4.7, -5.5, 5.0	-14.5, -20.8, -27.3

^aPositive values—greater than that of 1990; negative values—less than that of 1990

The maximum daily flow statistics present a very different picture of NI and SI watersheds (Table 5). The SI watersheds are predicted to record increases in the maximum daily flow which is in line with an increase in maximum daily rainfall under climate change scenarios (see Table 3). In the Inchbonnie watershed, under climate change, the maximum daily flows are predicted to increase by as much as 51–86% over 1990 (see Table 5, CWD and CWI output for 2090 A1FI dormant season). In the NI watersheds, increases in the maximum daily rainfall under climate change scenarios (Table 3) may not translate into increases in maximum daily flows (Table 5).

With exception of CWI model prediction in the Inchbonnie watershed, the runoff–rainfall (RR) ratios are predicted to decline in 2040 and 2090 over 1990 for all scenarios and in all four watersheds (Table 5). This ratio represents the proportion of rainfall becoming runoff, and here it is calculated as a ratio of total runoff to total rainfall over a season. A reduction in RR ratio, when there is a predicted increase in mean, maximum and seasonal total rainfall (Table 3) indicates that less rainfall could be becoming runoff in 2040 and 2090. Thus, an increase in seasonal total rainfall does not directly translate into an increase in seasonal total flow. In Waiokura and Bog Burn watersheds, the dormant seasons are likely to record larger decreases in RR ratios than growing seasons. At Toenepi and Inchbonnie watersheds, the two model predictions did not match, and, hence, no specific trends could be deciphered.

Differences in the methods used to estimate watershed storage and effective rainfall may have resulted in differences in CMD and CWI outputs. At Inchbonnie, there was a mismatch in the predicted mean daily flow trends between CWI and CMD models for the growing seasons of 2040 and 2090. Similarly, in the NI watersheds and at Bog Burn, CMD model predicted a larger decrease in the mean daily flow during the growing season, while CWI model predicted that to happen during the dormant season. In the Inchbonnie watershed, CMD model predicted a decrease in RR ratios under climate change scenarios but CWI model predicted an increase. However, unlike others, in the Inchbonnie watershed, the changes to RR ratios under climate change scenarios were small compared to 1990.

The duration and frequency of modelled flows were analysed for all watersheds (Fig. 4 CMD model simulations; Fig. 5 CWI model simulations). For clarity and readability, data from scenarios B1 and A1FI are shown in those figures and the flow duration curves for A1B scenario lie in between the two shown. Generally, under climate change, the SI watersheds show less deviation in flow frequencies from 1990. The NI watersheds showed an increasingly greater deviation in flow frequencies as moved from 1990 to 2040 and 2090. While the frequencies of high flows do not appear to increase significantly, the frequencies and magnitude of low flows could be significantly different under climate change scenarios compared to 1990. At both NI watersheds, CWI model predicted a greater frequency of very low flows than CMD model. Both models predicted the Toenepi watershed to record flows that are in the order of 0.01 mm d^{-1} , and less, at greater frequencies than occurred in 1990. None of the other watersheds were predicted to record such low flows. Also, at the Toenepi watershed, in 2040 and 2090, the growing seasons may undergo low flows at a greater frequency than the dormant seasons (Fig. 5, CWI model).

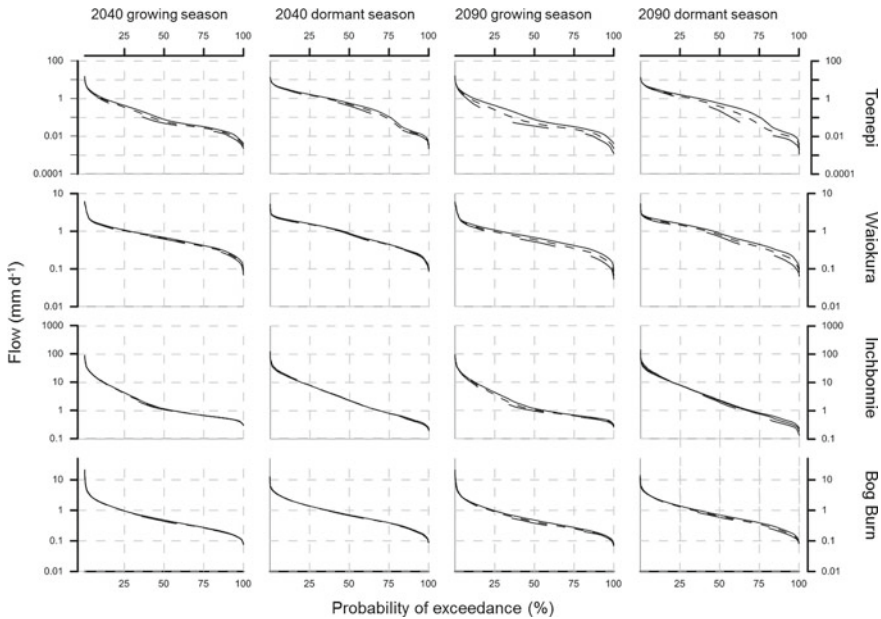


Fig. 4 Seasonal flow duration curves for 1990 (“1980–99”), 2040 (“2030–49”) and 2090 (“2080–99”) based on Catchment Moisture Deficit model. Data from B1 (shorter dotted line) and A1FI (long dashed line) along with 1990 (solid black line) are shown. Vertical and horizontal grey lines are guides. For the A1B scenario not shown here, the flow duration curves fell between B1 and A1FI

To further understand the extent and severity of dry spells under climate change scenarios, flows (Table 6) and internal watershed conditions (Fig. 6, CMD model moisture deficit; Fig. 7, CWI model wetness index) were analysed. All 7-day statistics indicate that the four watersheds are to become increasingly dry under climate change, despite increases in mean and maximum rainfall (in the case of 7-d increasing soil moisture deficit). The NI watersheds are likely to undergo more severe dry spells than those in SI. The Toenepi watershed is predicted to see the largest decrease in 7-d MSLF (low flow) under climate change. The Inchbonnie watershed is predicted to experience moisture deficits that can be five times as great as those predicted for other watersheds (see Table 6; Inchbonnie A1FI scenarios, 2090 dormant season), though, in absolute numbers, the Toenepi watershed could be recording the largest deficit (Table 6, Figs. 6 and 7).

Under climate change scenarios, the four watersheds are also likely to stay drier for longer periods than they did in 1990. Soil moisture deficits are predicted to get larger as moved from 1990, 2040–2090 (Fig. 6). Also, unlike flows, under climate change, the watersheds are likely to be drier during growing than the dormant season (Figs. 6 and 7). Of the four watersheds, the moisture deficit changes under climate change are likely to be the least in the Bog Burn watershed (<100 mm for all climate change scenarios; see Fig. 6) and the most in the Inchbonnie watershed.

Table 6 Comparison of the severity of dry conditions—flows and internal watershed soil moisture conditions in 2040 and 2090 over 1990 condition. All statistics are based on 20-year daily data from each time period for two Soil Moisture Accounting models, CWI and CMD. BI—Low emission; AIB—Medium emission; AIFI—High emission. Growing season—Oct.–Mar.; Dormant season—Apr.–Sep.

Watershed	Model	1990 conditions		2040 conditions		2090 conditions	
		Growing	Dormant	Growing	Dormant	Growing	Dormant
		7-day mean seasonal low flow (mm d ⁻¹)		Percent change in 7-day mean annual seasonal low flow over 1990 conditions ^a			
Toenepi	CMD	0.0	0.0	-14.2, -19.5, -24.9	-12.3, -17.5, -23.2	-24.8, -32.3, -40.0	-23.9, -35.8, -44.1
	CWI	0.0	0.1	-14.0, -19.8, -26.4	-9.4, -14.5, -19.4	-29.6, -41.8, -51.1	-24.6, -34.8, -43.4
Waiokura	CMD	0.3	0.3	-6.6, -9.8, -13.5	-3.4, -5.1, -7.1	-16.5, -23.5, -31.4	-15.1, -22.0, -29.7
	CWI	0.3	0.3	-5.6, -8.4, -11.7	-3.2, -4.6, -6.4	-14.0, -19.8, -25.9	-12.4, -17.4, -22.6
Inchbonnie	CMD	0.5	0.5	-1.0, -1.5, -2.0	-2.4, -3.9, -5.9	-5.3, -7.8, -10.1	-12.5, -18.3, -27.9
	CWI	0.5	0.5	2.3, 3.7, 5.6	1.9, 3.0, 4.4	1.4, 2.6, 4.4	-0.6, -0.8, -0.3
Bog Burn	CMD	0.2	0.2	-1.6, -2.6, -3.4	-3.2, -4.9, -6.7	-6.5, -9.4, -11.7	-9.9, -14.3, -18.3
	CWI	0.2	0.2	-2.9, -4.6, -6.5	-4.2, -6.6, -8.9	-9.6, -13.2, -16.5	-12.0, -16.2, -19.7
		7-day mean seasonal high moisture deficit (mm)		Percent change in 7-day seasonal high moisture deficit over 1990 conditions			
Toenepi	CMD	114.1	101.1	1.8, 2.8, 3.9	1.9, 2.9, 4.0	4.5, 6.8, 9.5	5.2, 7.7, 10.5
	CWI	109.3	98.3	1.6, 2.5, 3.5	1.1, 1.7, 2.4	4.0, 6.1, 8.7	3.7, 5.7, 8.0
Waiokura	CMD	123.2	78.2	6.5, 10.3, 15.2	6.7, 10.2, 14.7	15.8, 24.1, 34.6	20.9, 33.0, 47.8
	CWI	60.3	53.0	1.4, 2.2, 3.2	2.3, 3.5, 5.0	3.9, 5.9, 8.6	5.1, 7.7, 10.9
		7-day mean seasonal low wetness index		Percent change in 7-day seasonal low wetness index over 1990 conditions			
Toenepi	CWI	0.6	12.4	-46.0, -60.6, -76.3	-22.0, -32.6, -44.1	-76.9, -87.8, -94.9	-46.5, -63.7, -79.8
	CWI	2.7	12.0	-25.8, -36.8, -48.4	-14.1, -21.1, -29.4	-49.1, -65.6, -80.3	-33.3, -48.0, -62.6
Inchbonnie	CWI	26.9	56.1	-9.1, -14.2, -20.5	-2.9, -4.5, -6.6	-22.2, -32.7, -44.4	-11.8, -17.9, -25.9
	CWI	0.6	7.9	-33.4, -42.5, -52.3	-22.3, -32.5, -44.2	-59.1, -73.5, -87.7	-43.7, -60.9, -75.7

^aPositive values—greater than that of 1990; negative values—less than that of 1990

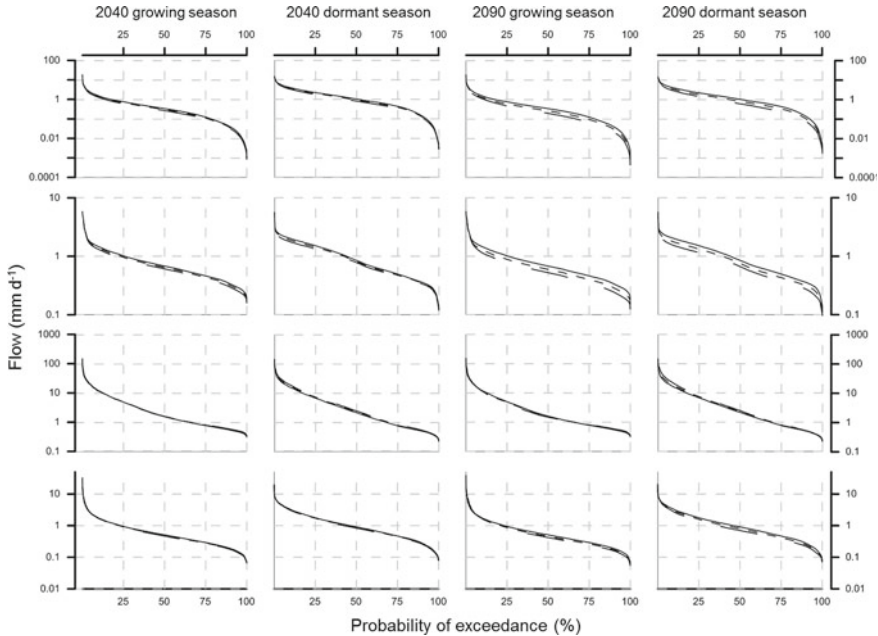


Fig. 5 Seasonal flow duration curves for 1990 (“1980–99”), 2040 (“2030–49”) and 2090 (“2080–99”) based Catchment Wetness Index model. Data from B1 (shorter dotted line) and A1FI (long dashed line) along with 1990 (solid black line) are shown. Vertical and horizontal grey lines are guides. For the A1B scenario not shown here, the flow duration curves fell between B1 and A1FI

6 Discussion

The major challenge in assessing climate change impact on water resources is uncertainty. According to Kay et al. [17], uncertainties can occur anywhere from downscaling procedures applied to global climate change datasets, representing inter-annual changes in climate systems to selecting hydrological models that can be parameterised for current and future conditions equally realistically. Added to these uncertainties, prediction of climate in NZ, an island surrounded by enormous water bodies is further complicated by the country’s location and orographic effects [18]. In NZ, at a seasonal scale, only half of the temperature variability during a growing season (September to March) and less than a third of rainfall variability for any season are predictable [21, 22]. Thus, any water resources assessment under climate change needs to take into account for these regional uncertainties. The uncertainty arising from downscaling of global climate change datasets to NZ and the suitability of global models to derive regional climate change data for NZ are discussed in Mullan and Dean [27] and MfE [24], and hence, not covered here.

The VCS data from 1990 (1980–99) were used to derive climate change data for 2040 (2030–49) and 2090 (2080–99). The 1990 VCS data were interpolation of

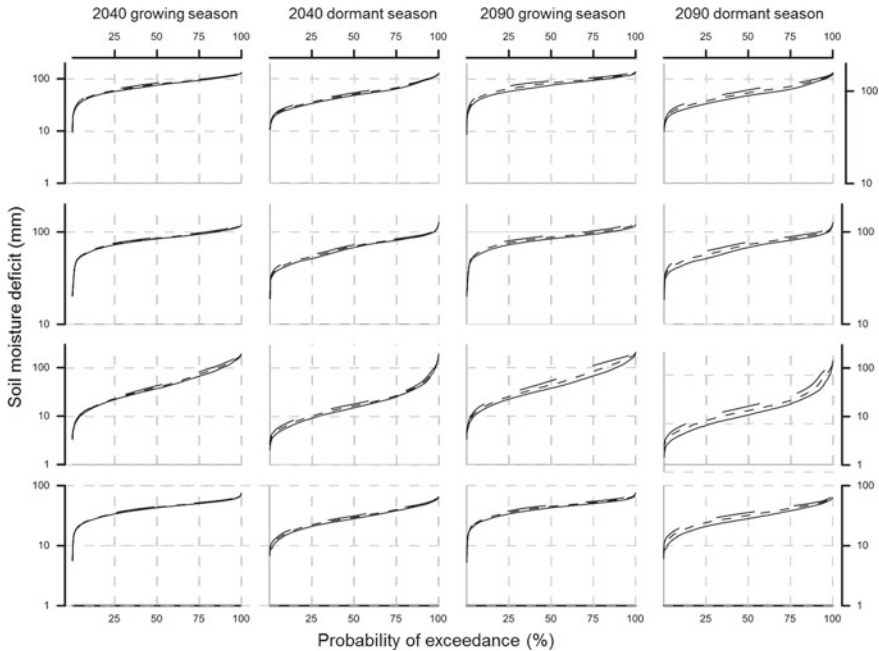


Fig. 6 Seasonal soil moisture deficit curves for 1990 (“1980–99”), 2040 (“2030–49”) and 2090 (“2080–99”) based Catchment Moisture Deficit model. Data from B1 (shorter dotted line) and A1FI (long dashed line) along with 1990 (solid black line) are shown. Vertical and horizontal grey lines are guides. For the A1B scenario not shown here, the flow duration curves fell between B1 and A1FI

station observations during that period, and thus includes the inter-annual variability. The derived dataset for 2040 and 2090 may thus include the same inter-annual variability as those of 1990. In the absence of any specific knowledge of inter-annual variability during those future periods, variability from 1990 was applied to 2040 and 2090. While processing the climate change datasets from 2040 to 2090, averages over the 20-year periods were compared against 1990 periods. Such averaging of long-term dataset might have reduced any differences arising from inter-annual variability.

In this study, multi-model and scenario approaches were used to reduce the uncertainty arising from the hydrological representation of watersheds. The multi-model approach examined watershed response to a given set of input conditions using more than one model. Also, calibration and validation using same observed flow and VCS datasets for all models allowed consistent training of the models and selection of parameters specific to watersheds and hydrological conditions specific to that period. By maintaining the model representation of watersheds and parameter selection same across the given hydrological conditions, the scenario approach assumed a similar level of uncertainty arising from model representation of input–output relationships.

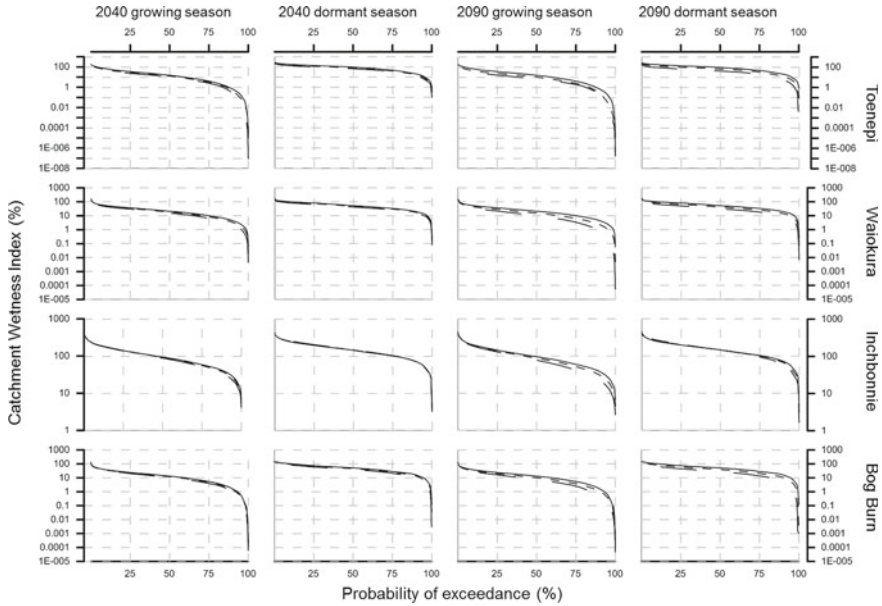


Fig. 7 Seasonal catchment wetness index curves for 1990 (“1980–99”), 2040 (“2030–49”) and 2090 (“2080–99”) based catchment wetness index model. Data from B1 (shorter dotted line) and A1FI (long dashed line) along with 1990 (solid black line) are shown. Vertical and horizontal grey lines are guides. For the A1B scenario not shown here, the flow duration curves fell between B1 and A1FI

Under climate change scenarios all four watersheds recorded increases in temperatures and changes to seasonal rainfall patterns over 1990. These are consistent with those highlighted in MfE report (2008). However, the magnitude of change varied between watersheds as moved across the country. The SI watersheds Inchbonnie and Bog Burn recorded greater increases in temperatures than the NI watersheds, Toenepi and Waiokura. As temperature increases, so does the ability of air to hold more water vapour. A positive increase in observed global change in water vapor of about 3.5% in the past 40 years, consistent with that of observed temperature change of about 0.5 °C during the same period has been observed [15].

The cool, temperate Bog Burn watershed is predicted to record greater increases in temperatures under climate change scenarios than the warm, subtropical Toenepi watershed. More intense rainfall events and larger seasonal total rainfall are predicted to occur under climate change scenarios in Bog Burn than in Toenepi. Both Toenepi and Bog Burn watersheds record fewer wet spells compared to Inchbonnie and Waiokura watersheds. Under climate change scenarios, as these wet spells are predicted to decrease in frequency, both Toenepi and Bog Burn may undergo extended dry spells. Thus, even though it is expected to undergo less warming than Bog Burn, Toenepi could undergo longer and more severe dry spells than Bogburn.

Under climate change scenarios, a warmer dormant (April—September), season is predicted to record more rainfall than a less warm growing (October—March) season in all four watersheds. The growing seasons are predicted to have fewer wet days, longer dry spells and fewer wet spells than the dormant seasons, thereby resulting in a greater decrease in flows and watershed storage. In the SI watersheds, where a greater temperature increases than NI watersheds are predicted, the seasonal differences in rainfall input, and flow and watershed storage response could be greater. The SI watersheds are predicted to record greater increases in the mean and maximum daily rainfall, seasonal total rainfall, and maximum daily flow than NI watersheds. In 2040 and 2090, the dormant seasons, specifically the winter months of June and July, are predicted to undergo the largest increases in temperature, and hence, the mean and maximum daily rainfall, as the capacity for air to hold more water vapour. The SI watersheds are predicted to record an increase in the seasonal total rainfall while the NI watersheds are predicted to record a decrease. While the temperature increases under climate change scenarios may result in fewer wet days in both islands, the rainfall increases resulting from temperature increases are not sufficiently large to enough in the NI watersheds to increase the seasonal total rainfall. While the rainfall events may become intense in both islands, the NI watersheds are likely to go through more dry spells (days with no rainfall for 7 days or more), thereby resulting in decreases in seasonal total rainfall. This also may result in the NI watersheds recording a larger decrease in mean flow under climate change scenarios than those in SI.

The watersheds from both islands are predicted to record changes in flows under climate change scenarios. Owing to drier conditions under climate change scenarios over 1990 conditions, the NI watersheds are predicted to record decreases in mean and maximum daily flows under climate change scenarios over 1990 conditions, while the maximum daily flows are predicted to increase in SI watersheds. Despite a larger mean and maximum daily rainfall under climate change scenarios, all watersheds are expected to convert less rainfall to runoff seasonally (exception to this is Inchbonnie watershed, CWI model simulations predicted an increase in flow and an increase in runoff–rainfall ratio). A combination of intense rainfall and long dry spells may result in extreme variability in flows, with intense events resulting in a greater probability of infiltration-excess runoff, and thus flow, while the dry spells may plunge the watersheds to very low flow conditions. The 7-day mean flow and soil moisture statistics indicate that, while all four watersheds are getting drier under climate change scenarios, the NI watersheds could be drier than SI watersheds. Such extreme variability in flow conditions may have implications to in-stream processes influencing water quality and ecology of these watersheds.

7 Conclusions

Climate change is predicted to result in increases in temperatures and changes to precipitation in New Zealand watersheds. The changes in temperature and rainfall

were predicted to increase from low (B1) to high (A1FI) emission scenarios, and from 1990 (“1980–99”), 2040 (“2030–49”) to 2090 (“2080–99”). Some of the key predictions for the four study watersheds under climate change scenarios are

- South Island (SI) watersheds (Inchbonnie and Bog Burn) may record greater increases in temperature, mean and maximum daily rainfalls, seasonal total rainfall and maximum daily flow than North Island (NI) watersheds (Toenepi and Waiokura). In the NI watersheds, increases in the maximum daily rainfall may not translate into increases in maximum daily flow.
- The cool, temperate Bog Burn watershed may record greater increases in temperature than the warm, subtropical Toenepi. However, Toenepi may undergo more dry spells due to extended periods of no rainfall.
- With exception of CWI (Catchment Wetness Index) model prediction in the Inchbonnie watershed, the runoff–rainfall (RR) ratios are predicted to decline in 2040 and 2090 over 1990 in all four watersheds.
- The frequency of high flows may not increase significantly but the frequency and magnitude of low flows could be significantly affected. The NI watersheds are likely to undergo more severe low flow conditions than those in SI.
- In all watersheds, dormant season (April–September) are predicted to record larger temperature and rainfall increases than growing season (October–March). Growing seasons are predicted to experience fewer wet days (rain days), longer dry spells (no rain for 7 consecutive days or more) and fewer wet spells (rains for 7 consecutive days or more) than dormant seasons, thereby experiencing greater decreases in flows and watershed storage.
- Of the four, the Inchbonnie watershed is predicted to record the largest increases in rainfall during the dormant season and the smallest during the growing season.

All four watersheds are dominantly dairy grazed, and suboptimal soil moisture conditions may negatively impact pasture growth. Under climate change conditions, since the states and stores of available water are spatially and temporally different over the current conditions, water use might also differ from current conditions. To sustain production, farmers and producers may need to explore other measures such as reducing stock density, importing feed, adapting to drought-resistant pasture species and/or increasing water storage to counter dry spells, all of which may result in significant to transformative changes to agricultural practices, farmer water use behaviour and farm economy.

Acknowledgements The authors would like to thank Einar Hreinsson and Christian Zammit, NIWA-Christchurch, and the Climate Variability and Change team, NIWA-Greta Point, for their assistance in compiling the climate change data for this study. We acknowledge the New Zealand Ministry of Business, Innovation and Employment for funding the programme Justified Irrigation (CO1X1617) that provided partial support in developing the work presented here.

References

1. Andreasson J, Bergstorm S, Carlsson B, Graham LP, Lindstrom G (2004) Hydrological change—Climate change impact simulations for Sweden. *Ambio* 33:228–234
2. Andrews FT, Croke BFW, Jakeman AJ (2011) An open software environment for hydrological model assessment and development. *Environ Model Softw* 26:1171–1185
3. Bai Y, Wagener T, Reed P (2009) A top-down framework for watershed model evaluation and selection under uncertainty. *Environ Model Softw* 24:901–916
4. Bates BC, Kundzewicz ZW, Wu S, Palutikof JP (eds) (2008) Climate change and water. Technical paper of the Intergovernmental Panel on Climate Change, IPCC Secretariat, Geneva, 210 pages
5. Boe J, Terray L, Martin E, Habets F (2009) Projected changes in components of the hydrological cycle in French river basins during the 21st century. *Water Resour Res* 45:W08426
6. Boughton W (2004) The Australian water balance model. *Environ Model Softw* 19:943–956
7. Burnash RJC (1995) The NWS river forecast system-catchment modeling. In: Singh VP (ed) *Computer models for watershed hydrology*. CAB Direct, Oxfordshire, United Kingdom, pp 311–366. ISBN 0-918334-91-8
8. Clark MP, Hreinsson EO, Martinez G, Tait A, Slater AG, Hendrikx J, Owens I, Gupta H, Schmidt J, Woods R (2009) Simulations of seasonal snow for the South Island, New Zealand. *J Hydrol (NZ)* 48:41–58
9. Cliflo (2013) The national climate database. <http://cliflo.niwa.co.nz/>. Accessed 14 Dec 2013
10. Croke BFW, Jakeman AJ (2004) A catchment moisture deficit module for the ihacres rainfall-runoff model. *Environ Model Softw* 19:1–5
11. Dibike YB, Coulibaly P (2005) Hydrologic impact of climate change in the Saguenay watershed: comparison of downscaling methods and hydrologic models. *J Hydrol* 307:145–163
12. Gay MD (1990) Usage summary for selected optimization routines. Computing Science Technical Report No. 153. AT&T Bell Murray Hill, NJ 07974, USA
13. Hassan Z, Harun S (2011) Hydrological response of a catchment to climate change in the Kurau River basin, Perak, Malaysia. In: Proceedings of 3rd international conference on managing rivers in the 21st century: sustainable solutions for global crisis of flooding, pollution and water scarcity. 6–9 Dec 2011, Penang, Malaysia, pp 216–225
14. IPCC (Intergovernmental Panel on Climate Change) (2007) The physical science basis. Contribution of working group I to the fourth assessment report of the intergovernmental panel on climate change. In: Solomon S, Qin D, Manning M, Chen Z, Marquis M, Averyt KB, Tignor M, Miller HL (eds) Cambridge University Press, Cambridge, United Kingdom and New York, NY, USA, 996 pages
15. IPCC (Intergovernmental Panel on Climate Change) (2013) Working group I contribution to the IPCC fifth assessment report: the physical science basis. Final draft underlying scientific-technical assessment. In: Christensen J, Kanikicharla KK (eds). http://www.climatechange2013.org/images/uploads/WGIAR5_WGI-12Doc2b_FinalDraft_TechnicalSummary.pdf. Accessed 14 Dec 2013
16. Jakeman AJ, Hornberger GM (1993) How much complexity is warranted in a rainfall-runoff model? *Water Resour Res* 29:2637–2649
17. Kay AL, Davies HN, Bell V, Jones RG (2009) Comparison of uncertainty sources for climate change impacts: flood frequency in England. *Clim Change* 92:41–63. <https://doi.org/10.1007/s10584-008-9471-4>
18. Kenny G (2010) Adaptation in agriculture: lessons for resilience from eastern regions of New Zealand. In: Nottage RAC, Wratt DS, Bornman JF, Jones K (eds) *Climate change adaptation in New Zealand: future scenarios and some sectoral perspectives*. New Zealand Climate Change Centre, Wellington, New Zealand, pp 56–69
19. Kokkonen T, Koivusalo H, Jakeman A, Norton J (2006) Construction of a degree-day snow model in the light of the “ten iterative steps in model development”. In: Voinov A, Jakeman

- AJ, Rizzoli AE (eds) Proceedings of the IEMSs third biennial meeting: summit on environmental modelling and software. International Environmental Modelling and Software Society, Burlington, USA
20. Kundzewicz ZW, Mata LJ, Arnell NW, Doll P, Jimenez B, Miller K, Oki T, Sen Z, Shiklomanov I (2008) The implications of projected climate change for freshwater resources and their management. *Hydrol Sci J* 53:3–10
 21. Madden RA, Kidson JW (1997) The potential long-range predictability of temperature over New Zealand. *Int J Climatol* 17:483–495
 22. Madden RA, Shea DJ, Katz RW, Kidson JW (1999) The potential long-range predictability of precipitation over New Zealand. *Int J Climatol* 19:405–421
 23. MfE (Ministry for the Environment) (2016) Climate change projections for New Zealand: atmosphere projections based on simulations from the IPCC fifth assessment. Ministry for the Environment, Wellington, 127 pages. ISBN: 978-0-908339-44-0; Publication number: ME 1247
 24. MfE (Ministry for the Environment) (2010) Tools for estimating the effects of climate change on flood flow: a guidance manual for local government in New Zealand. Ministry for the Environment, Wellington, New Zealand. Report CHC2008-110, 93 pages
 25. MfE (Ministry for the Environment) (2008) Climate change effects and impacts assessment: a guidance manual for local government in New Zealand, 2nd edn. Wellington, New Zealand. <http://www.mfe.govt.nz/publications/climate/climate-change-effect-impacts-assessments-may08/index.html>. Accessed 15 Dec 2010
 26. Mullan AB, Thompson CS, Woods RA (2001) Future climate and river flow scenarios. NIWA Client Report No. WLG 2001/26. 46 p
 27. Mullan AB, Dean S (2009) AR4 climate model validation and scenarios for New Zealand. In: Presented at 9th international conference on Southern hemisphere meteorology and oceanography, Melbourne, 9–13 Feb 2009. Available from http://www.bom.gov.au/events/9icshmo/program_4.sthml. Accessed 6 Dec 2013
 28. Nash JE, Sutcliffe JV (1970) River flow forecasting through conceptual models Part I: a discussion of principles. *J Hydrol* 10:282–290
 29. NIWA (National Institute of Water and Atmospheric Research Limited) (2013) Overview of New Zealand climate. <http://www.niwa.co.nz/education-and-training/schools/resources/climate/overview>. Accessed 14 Dec 2013
 30. Perrin C, Michel C, Andreassian V (2003) Improvement of a parsimonious model for streamflow simulation. *J Hydrol* 279:275–289
 31. Reisinger A (2009) Climate change 101: an educational resource. Science-impacts-adaptation-mitigation-decision-making challenges. Institute of Policy Studies and New Zealand Climate Change Research Institute, School of Government, Victoria University of Wellington, Wellington, New Zealand, 303 pages
 32. Scarf W (2007) Seven-day mean annual low flow and mean annual flow mapping of the Waipara River catchment, North Canterbury. Report No. U08/10 ISBN 978-1-86937-779-3. Environment Canterbury, Christchurch, New Zealand. 47 pages. <http://ecan.govt.nz/publications/Reports/seven-day-mean-annual-low-flow-mean-annual-flow-mapping-waipara-river.pdf>. Accessed 12 Jan 2014
 33. Srinivasan MS, Schmidt J, Poyck S, Hreinsson E (2011) Irrigation reliability under climate change scenarios: a modelling: investigation in a river-based irrigation scheme in New Zealand. *J Am Water Resour Assoc* 47:1261–1274. <https://doi.org/10.1111/j.1752-1688.2011.00568.x>
 34. Tait A, Woods R (2007) Spatial interpolation of daily potential evapotranspiration for New Zealand using a spline model. *J Hydrometeorol* 8:430–438
 35. Tait A, Henderson R, Turner R, Zheng X (2006) Thin plate smoothing spline interpolation of daily rainfall for New Zealand using a climatological rainfall surface. *Int J Climatol* 26:2097–2115
 36. Velázquez JA, Schmid J, Ricard S, Muerth MJ, Gauvin St-Denis B, Minville M, Chaumont D, Caya D, Ludwig R, Turcotte R (2013) An ensemble approach to assess hydrological models' contribution to uncertainties in the analysis of climate change impact on water resources. *Hydrol Earth Syst Sci* 17:565–578

37. Wilcock RJ, Monaghan RM, Quinn JM, Srinivasan MS, Houlbrooke DJ, Duncan MJ, Wright-Stow AE, Scarsbrook MR (2013) Trends in water quality of five dairy farming streams in response to adoption of best practice and benefits of long-term monitoring at the catchment scale. *Mar Freshw Res* 64:401–412
38. Wilcock RJ, Monaghan R, Srinivasan MS, Wright-Stow AE (2012). Best practice catchments for sustainable dairy farming: review of a long-term monitoring study of water quality trends. National Institute of Water & Atmospheric Research Client report, HAM2012-071. Hamilton, New Zealand. 58 pages
39. Woods R, Tait A, Mullan B, Hendrikx J, Dietrich J (2008) Projected climate and river flow for the rangitata catchment for 2040. National Institute of Water & Atmospheric Research Report CHC2008-097, Christchurch, New Zealand. 36 pages